An Electrospun Nonwoven-Hydrogel Scaffold for Application in Spinal Cord Injury Repair

Benjamin Harry Golland

Submitted in accordance with the requirements for the degree of Doctor of Philosophy

The University of Leeds
Institute of Medical and Biological Engineering
School of Design

March 2021

The candidate confirms that the work submitted is his own and that appropriate credit has been given where reference has been made to the work of others.

Acknowledgements

My biggest thanks goes to my wife, Faye. Not only did she put up with a long distance relationship between Leeds and London for two years and moved to Leeds for a further two years, but she also spent the last year watching TV on her own of an evening whilst I wrestled with this thesis. Your love and support is all I need.

Big thanks are also extended to Richard Hall, Giuseppe Tronci and, most of all, Steve Russell for the support and guidance over the last five years. On every occasion I went into a supervisory meeting confused and overwhelmed, I came out with clarity and options forward. I believed from my first meeting with Steve his enthusiasm would get me through the next five years. Whilst the viva is still to go, I can almost say I was right.

Big thanks also go to the CDT TERM cohort of 2015. Without the opportunity to complain about experiments not working, thesis writing not really happening, and all the extra stuff we had to do as a group that we loved to hate, I'd have gone mad. I've made some friends I know will last a lifetime.

Thanks also go to the CDT TERM programme in general, especially Joanne Tipper and Claire Brockett. What a fantastic opportunity the last five years has been and thank you for providing such a holistic programme.

Thanks are also extended to the team at The Electrospinning Company, without whom I would not have produced such a huge amount of electrospun material for this research; to the team at Medipex, who gave me invaluable experience in how innovations are taken out of the lab; and the team at Mercia, who gave me such an honest view of how innovation is supported in business. It was this extra activity that made my research time all the more enriching.

Thanks also to all the staff and students in the Institute of Medical and Biological Engineering, School of Design and Oral Biology who helped me in some way during this research. Each contribution, however small, is deeply appreciated.

Lastly, I would like to dedicate this thesis to my parents who have always encouraged me academically. The journey has been even more fulfilling than the destination.

Abstract

Injury to the spinal cord is devastating for patients and no routine procedure currently exists to promote functional recovery. To this end, composite scaffolds of nonwovens and hydrogels have emerged as a leading research theme for spinal cord injury repair. Despite this, a limited number of biomaterials have been investigated to date for composite nonwoven-hydrogel scaffolds.

Recently, the electrospinning of poly(ε-caprolactone) (PCL) and the self-assembling peptide (SAP) P_{11}-8 indicated the utility of SAPs as biomaterials could be extended to a more clinically practical form, as a dry fibre web rather than a hydrogel. Similarly, previous studies of a glycidyl methacrylate (GMA)-functionalised collagen (collagen-GMA) hydrogel, for wound dressing and regenerative scaffolds, indicated the hydrogel system was biocompatible and could be tuned with regards to mechanical and degradation properties. However, neither had been optimised or combined for spinal cord tissue regeneration.

Accordingly, the aim of the work herein was to investigate the manufacture, structure and properties of composite scaffolds comprising aligned P_{11}-8 peptide-enriched PCL (PCL/P_{11}-8) fibres and a biomimetic collagen-GMA hydrogel, both optimised for spinal cord injury repair.

Initially, the feasibility of electrospinning aligned fibre webs of PCL/P_{11}-8 was confirmed for the first time, producing a web of submicron diameter fibres (~400 nm) that coexisted with a network of nanoscale diameter fibres (~20 nm). Whilst alignment in the direction of axis rotation of the electrospinning collector was confined to the submicron network and not the nanoscale network, neurites from PC12 cells, a rat pheochromocytoma cell line, extended in the direction of the aligned submicron network. Further, the utility of the SAP and the nanoscale network reversed the wetting performance of the web and produced a concentration-dependent effect on stiffness in the cross direction.

Secondly, cells were encapsulated in a single-phase UV-cured collagen-GMA hydrogel for the first time and shown to be viable, as well as extend neurites in multiple planes. Further, hydrogels were shown to have shear properties optimised

for cell viability and growth, whilst compressive properties mimicked native spinal cord tissue.

Lastly, aligned electrospun PCL/P_{11}-8 fibre webs were combined with collagen-GMA hydrogel for the first time to produce a composite nonwoven-hydrogel scaffold integrated at the fibre level. Neurite extension was observed in the combined scaffold, as well as in a more clinically relevant “off-the-shelf” lyophilised form. To enhance cell infiltration, laser ablation was used to introduce controlled porosity into the scaffold, the distribution of which correlated with the degree of cell infiltration up to around 25% porosity, after which no further improvement was observed. Further, the utility of non-ablated PCL/P_{11}-8 as an outer layer preventing non-native cell infiltration was highlighted in a proof-of-principle co-culture of PC12 and L929 cells.

Table of Contents

Acknowledgements III

Abstract I

List of Figures VIII

List of Tables XI

List of Abbreviations XII

Chapter 1 Introduction 1

1.1 Spinal Cord Injury 1

1.2 Current Management of Spinal Cord Injury 3

1.3 Challenges of Existing Treatment Methods 4

1.3.1 Neuro-Spinal Scaffold 4

1.3.2 NeuroRegen Scaffold 7

1.3.3 Summary 8

1.4 Aims and Objectives 9

Chapter 2 Review of the Literature 11

2.1 Introduction 11

2.2 Anatomy of the Spinal Cord 11

2.2.1 Macroscale Anatomy 12

2.2.2 Microscale Anatomy 14

2.3 Spinal Cord Injury 23

2.3.1 Primary Injury 24

2.3.2 Secondary Biological Response 24

2.4 Regenerative Medicine 28

2.4.1 Design of Regenerative Scaffolds 30

2.4.2 Electrospinning 37

2.5 Scaffold-Mediated Spinal Cord Repair 44

2.5.1 Electrospun Nonwoven Scaffolds 44

2.5.2 Hydrogel Scaffolds 47
2.5.3 Composite Nonwoven-Hydrogel Scaffolds 50
2.6 Summary 62
Chapter 3 Materials and Methods 64
3.1 Materials and Equipment 64
3.1.1 Equipment 64
3.1.2 Chemicals 65
3.1.3 Consumables 66
3.1.4 Cells 66
3.1.5 Antibodies 67
3.2 Experimental Methods 67
3.2.1 Manufacture of Electrospun Nonwoven Scaffolds 67
3.2.2 Manufacture of Collagen-GMA Hydrogel 69
Chapter 4 Manufacture and Structure of Aligned Fibre Scaffolds 73
4.1 Introduction 73
4.2 Materials and Methods 73
4.2.1 Manufacture of Electrospun Nonwoven Scaffolds 73
4.2.2 Fibre Characterisation 74
4.2.3 High Performance Liquid Chromatography 74
4.2.4 Mass Spectrometry 76
4.3 Results and Discussion 77
4.3.1 Electrospinning of Aligned PCL Fibre Nonwovens and the Effect of Collector Surface Velocity on Fibre Diameter 77
4.3.2 Electrospinning Collector Surface Velocity and the Effect on Fibre Alignment 80
4.3.3 Electrospinning of Aligned PCL/P_{11}-8 Fibre Nonwovens and the Effect of SAP on Fibre Diameter 81

4.3.4 Electrospinning of Aligned PCL/P_{11}-8 Fibre Nonwovens and the Effect of SAP on Fibre Alignment 85
4.3.5 Detection of SAP in the Nonwoven Web Post-Electrospinning..... 87
..... 89
4.3.6 Quantification of SAP Post-Electrospinning..... 90
4.4 Summary..... 94
Chapter 5 Physical Characterisation and *in vitro* Neurite Extension of Aligned Fibre Scaffolds 96
5.1 Introduction 96
5.2 Materials and Methods..... 97
5.2.1 Manufacture of Electrospun Nonwoven Scaffolds 97
5.2.2 Neurite Extension 97
5.2.3 Tensile Testing 98
5.2.4 Wettability..... 100
5.3 Results and Discussion..... 101
5.3.1 Neurite Extension and the Importance of an Aligned Submicron Fibre Network 101
5.3.2 Nanoscale Fibres and their Impact on Macroscale Scaffold Stiffness 105
5.3.3 The Effect of SAP on the Wettability of PCL/P_{11}-8 Electrospun Fibre Webs…..... 110
5.4 Summary..... 115
Chapter 6 Manufacture and Optimisation of Hydrogel Properties 116
6.1 Introduction 116
6.2 Materials and Methods..... 117
6.2.1 Manufacture of Collagen-GMA Hydrogel..... 117
6.2.2 Degree of Functionalisation of Collagen-GMA..... 118
6.2.3 Rheology of Collagen-GMA Hydrogel..... 119
6.2.4 Compression of Collagen-GMA Hydrogel..... 119

6.2.5 Cell Viability of PC12 Cells in Collagen-GMA Hydrogel 120
6.2.6 Neurite Extension of PC12 Cells in Collagen-GMA Hydrogel 121
6.3 Results and Discussion 121
6.3.1 Achieving Three-Dimensional Cell Encapsulation by Prioritising Cell Viability.. 121
6.3.2 Hydrogel Stiffness and the Effect of Collagen-GMA Weight Percent.. 128
6.3.3 Hydrogel Stiffness, Cell Viability and the Effect of UV-Irradiation Time….. 133
6.3.4 Hydrogel Compression and the Effect of Collagen-GMA Weight Percent…. 137
6.4 Summary 144
Chapter 7 146
Manufacture and Characterisation of a Composite Nonwoven-Hydrogel Spinal Cord Scaffold 146
7.1 Introduction 146
7.2 Materials and Methods 147
7.2.1 Manufacture of Dry Collagen-GMA Hydrogel 147
7.2.2 Manufacture of the Composite Nonwoven-Hydrogel Scaffold 148
7.2.3 Cell Viability of PC12 Cells in Lyophilised Collagen-GMA Hydrogel... 149
7.2.4 Neurite Extension of PC12 Cells in Composite Nonwoven-Hydrogel Scaffolds 149
7.2.5 Liquid Wicking Rate of Collagen-GMA Hydrogel-Forming Solution into Electrospun PCL and PCL/P_{11}-8 150
7.2.6 Dry Mass of Composite Nonwoven-Hydrogel Scaffolds 150
7.2.7 Laser Ablation of PCL/P_{11}-8 Nonwoven 151
7.2.8 PC12 Cell Infiltration Assay of Laser-Ablated Composite Nonwoven-Hydrogel Scaffold 151
7.2.9 L929 Cell Exclusion Assay of Non-Ablated PCL/P_{11}-8 152

7.3 Results and Discussion 153
7.3.1 Neurite Extension in the Composite Nonwoven-Hydrogel Scaffold and the Effect of Surrounding Material on the Alignment of Neurites 153
7.3.2 Cell Infiltration in the Composite Nonwoven-Hydrogel Scaffold and the Effect of Laser Ablation on Nonwoven Porosity 159
7.3.3 Proof of Principle for PCL/P_{11}-8 as a Cell-Impermeable Layer for Preventing Non-Native Cell Infiltration in a Composite Nonwoven-Hydrogel Scaffold 164
7.3.4 Integration of Collagen-GMA Hydrogel with PCL and PCL/P_{11}-8 at the Fibre Level and the Effect of SAP on Hydrogel Absorption 168
7.3.5 Dehydration of Collagen-GMA and the Effect of Methodology on Retaining Pore Structure 173
7.3.6 Refinement of Laser Ablation Parameters 178
7.4 Summary 183
Chapter 8 185
Conclusion 185
8.1 General Conclusions 185
8.2 Recommendations for Further Work 188
References 190

List of Figures

Figure 1.1 Neuro-Spinal and NeuroRegen scaffolds. 5
Figure 2.1 Macroscale anatomy of the spinal cord 12
Figure 2.2 Neurons and neuroglia 15
Figure 2.3 Spinal cord ECM 22
Figure 2.4 Composition of the spinal injury scar 26
Figure 2.5 Repeating chemical structure of PCL 32
Figure 2.6 Chemical structure of P_{11}-8 33
Figure 2.7 Collagen functionalised with the vinyl-bearing moieties..... 35
Figure 2.8 Diagram of the electrospinning process 38
Figure 3.1 Electrospinning setup used to produce nonwoven fibre webs of PCL and PCL/P_{11}-8 68
Figure 3.2 Diagram of collagen extraction, functionalisation with GMA and photo-activation to form collagen-GMA .....**Error! Bookmark not defined.**
Figure 4.1 Diagram of the HPLC system used to detect and quantitate P_{11}-8..... 75
Figure 4.2 Diagram of the mass spectrometer used to identify P_{11}-8 77
Figure 4.3 Aligned electrospinning of PCL 79
Figure 4.4 SEM images of electrospun PCL and PCL/P_{11}-8 nonwovens..... 82
Figure 4.5 Fibre diameter distribution of PCL-only and PCL/P_{11}-8 nonwoven webs 84
Figure 4.6 SEM images and graphs showing alignment of the submicron and nanoscale networks..... 86
Figure 4.7 Detection and quantitation of P_{11}-8 in PCL/P_{11}-8 nonwoven 89
Figure 4.8 Mass spectrum of the HPLC peak at 15 minutes retention time 90
Figure 4.9 Mass spectrum of P_{11}-8 from C.S. Bio, the peptide manufacturer 91
Figure 5.1 Diagram of the wettability test method..... 100
Figure 5.2 Confocal images and graphs showing neurite extension of PC12 cells after 14 days compared to alignment of the underlying nonwoven fibre web 102
Figure 5.3 Graphs showing the Young's modulus of aligned PCL and aligned PCL/P_{11}-8 at 10, 20 and 40 mg ml^{-1} 107
Figure 5.4 Wettability of PCL/P_{11}-8 aligned nonwoven 111
Figure 6.1 Neurite extension of PC12 cells in collagen-GMA hydrogel 122
Figure 6.2 Cell viability of PC12 cells encapsulated in collagen-GMA hydrogel 123

Figure 6.3 PC12 cell distribution in collagen-GMA hydrogel..... 124
Figure 6.4 Mechanical properties in shear of collagen-GMA hydrogel at varying weight percent (wt%)..... 129
Figure 6.5 Shear modulus values of collagen-GMA hydrogel at varying weight percent (wt%) 131
Figure 6.6 Mechanical properties in shear of collagen-GMA hydrogel at varying UV-irradiation time..... 134
Figure 6.7 Mechanical properties in compression of collagen-GMA hydrogel at varying weight percent (wt%) 138
Figure 6.8 Key compression properties of collagen-GMA hydrogel at varying weight percent (wt%) 139
Figure 6.9 Mechanical properties in compression of collagen-GMA hydrogel at varying weight percent (wt%) up to 0.5 strain.....**Error! Bookmark not defined.**
Figure 7.1 Diagram showing the scaffold manufacturing process 148
Figure 7.2 Neurite extension of PC12 cells in the composite nonwoven-hydrogel scaffold..... 154
Figure 7.3 Neurite extension of PC12 cells in lyophilised composite nonwoven-hydrogel scaffold 157
Figure 7.4 Porosity introduced into the electrospun nonwoven using laser ablation and its effect on cell infiltration into the underlying collagen-GMA hydrogel..... 161
Figure 7.5 Neurite extension of PC12 cells and exclusion of L929 cells..... 166
Figure 7.6 SEM images of composite nonwoven-hydrogel scaffolds..... 168
Figure 7.7 Total dry mass of composite nonwoven-hydrogel scaffolds ..... **Error! Bookmark not defined.**
Figure 7.8 Liquid wicking rate of collagen-GMA hydrogel-forming solution into electrospun nonwoven 171
Figure 7.9 SEM images of dry collagen-GMA hydrogel..... 174
Figure 7.10 Mechanical properties in shear of collagen-GMA hydrogel lyophilised and rehydrated versus pre-hydrated .....**Error! Bookmark not defined.**
Figure 7.11 Cell viability of PC12 cells in lyophilised collagen-GMA hydrogel..... 177
Figure 7.12 PC12 cells in lyophilised collagen-GMA hydrogel 178
Figure 7.13 Laser ablation of electrospun PCL/P_{11}-8 nonwoven 179
Figure 7.14 SEM images of laser-ablated PCL/P_{11}-8 electrospun nonwoven..... 180

Figure 7.15 Effect of the laser power on pore area and the link between intended input and actual output for inter-pore distance 182

List of Tables

Table 1.1 Table showing the ASIA Impairment Scale for classifying severity of SCI . 6
Table 3.1 Equipment used herein, including supplier information. 64
Table 3.2 Chemicals and reagents used herein, including supplier information. 65
Table 3.3 Consumables used herein, including supplier information. 66
Table 3.4 Antibodies used herein, including supplier information. 67
Table 5.1 Table showing the ultimate tensile strength (UTS) values for PCL and PCL/P_{11}-8 at 40, 20 and 10 mg ml^{-1} in both the MD and CD 106
Table 6.1 Collagen-GMA hydrogel production protocol as detailed in Kirk (2018) and Tronci et al. (2013) 125
Table 6.2 The altered Collagen-GMA hydrogel production protocol used in herein127
Table 6.3 Table of storage, loss and complex shear modulus values of collagen-GMA hydrogel at varying weight percent (wt%) 132

List of Abbreviations

% s^{-1}	Percentage per second
°	Degrees
°C	Degrees centigrade
µm	Micrometre
3D	Three-dimensional
4VBC	4-vinylbenzyl chloride
ANOVA	Analysis of variants
ASIA	American Spinal Injury Association
ATCC	American Type Culture Collection
ATP	Adenosine triphosphate
ATR-FTIR	Attenuated Total Reflection-Fourier Transform Infrared Spectroscopy
BBB	Basso-Beattie-Bresnahan
BCA	Bicinchoninic acid
BDNF	Brain-derived neurotrophic factor
BMMC	Bone marrow mononuclear cells
BMS	Basso-Mouse Scale
BMSCs	Bone marrow-derived mesenchymal stem cells
C1q	Complement component 1q
$CaCl_2$	Calcium chloride
CD	Cross direction
CH_3COOH	Acetic acid
ChABC	Chondroitinase ABC
CHN	Carbon-Hydrogen-Nitrogen analysis
CHO-K1	Chinese Hamster Ovary cell line
CNPase	2',3'-Cyclic-nucleotide 3'-phosphodiesterase
CNS	Central nervous system
CO_2	Carbon dioxide
CSF	Cerebrospinal fluid
CSPG	Chondroitin sulfate proteoglycan
DAMP	Damage-associated molecular pattern
DAPI	4,6-diamidino-2-phenylindole
DCML	Dorsal column-medial lemniscal
DIKVAV	Amino acid sequence; aspartic acid-isoleucine-lysine-valine-alanine-valine
DMEM	Dulbecco's modified Eagle's medium
DMSO	Dimethyl sulfoxide
DNA	Deoxyribonucleic acid
DRG	Dorsal rot ganglion
drNPC	Directly reprogrammed neural progenitor cells
DSC	Differential Scanning Calorimetry
ECACC	European Collection of Authenticated Cell Cultures
ECM	Extracellular matrix
EDX	Energy Dispersive X-ray spectroscopy
EHS	Engelbreth-Holm-Swarm
FBS	Foetal bovine serum
FDA	US Food & Drug Administration
FITC	Fluorescein isothiocyanate
Fmoc	Fluorenylmethyloxycarbonyl
FTIR	Fourier Transform Infrared Spectroscopy
GAG	Glycosaminoglycan
GAP-43	Growth Associated Protein 43
GDNF	Glial cell line-derived neurotrophic factor
GelMA	Methacrylated gelatin
GFAP	Glial fibrillary acidic protein
GMA	Glycidyl methacrylate

h	Hour
HA	Hyaluronic acid
HA-MA	Methacrylated hyaluronic acid
HAMC	Hyaluronan-methylcellulose
HCl	Hydrochloric acid
hESC	Human embryonic stem cell
HFIP	1,1,1,3,3,3-hexafluoro-2-propanol
hMSCs	Human mesenchymal stem cells
hNSCs	Human neural stem cells
HOV	Homogeneity of variance
HPECs	Human placental endothelial cells
HPLC	High performance liquid chromatography
hUCB-MSC	Human umbilical cord mesenchymal stem cells
hUMSCs	Human umbilical mesenchymal stem cells
I2959	2-Hydroxy-1-[4-(2-hydroxyethoxy)phenyl]-2-methylpropan-1-one
IL-1α	Interleukin-1 alpha
IPC	Interfacial polyelectrolyte complexation
iPSC	Induced pluripotent stem cell
J cm^{-2}	Joules per centimetre squared
kPa	Kilopascal
L929	Mouse fibroblast cell line
LAP	Phenyl-2,4,6-trimethylbenzoylphosphinate
m s^{-1}	Metres per second
M.O.M.	Mouse on Mouse
MAG	Myelin-associated glycoprotein
MAP2	Microtubule Associated Protein 2
MD	Machine direction
mg ml^{-1}	Milligram per millilitre
miRNA	Micro ribonucleic acid
ml	Millilitre
ml h^{-1}	Millilitre per hour
mm	Millimetre
mm^2	Millimetre squared
MSC	Mesenchymal stem cells
mW cm^{-2}	Milliwatts per centimetre squared
N	Newton
$NaHCO_3$	Sodium hydrogen carbonate
NaOH	Sodium hydroxide
NF	Neurofilament
ng ml^{-1}	Nanogram per millilitre
NGF	Nerve growth factor
NHS	National Health Service
NLI	Neurological level of injury
nm	Nanometre
NPC	Neural progenitor cell
NS/PG	Neural stem/progenitor cell
NSC	Neural stem cell
NT-3	Neurotrophin-3
OMgp	Oligodendrocyte myelin glycoprotein
OPC	Oligodendrocyte precursor cell
P(CL:DLLA)	Poly(3-caprolactone-co-D,L-lactide)
Pa	Pascal
PBS	Phosphate buffered saline
PC12	Rat pheochromocytoma cell line
PCL	Poly(ε-caprolactone)
PCLEEP	Poly(ε-caprolactone-co-ethyl ethylene phosphate)
PDGFRa	Platelet Derived Growth Factor Receptor Alpha
PDL	Poly-D-lysine

PEGDA	Poly(ethylene glycol) diacrylate
PEG-PLL	Poly(ethylene glycol)-poly(L-lysine)
PEO	Polyethylene oxide
PEUU	Poly(ester urethane)urea
PEUUR	Poly(esterurethane urea)
PLA	Polylactic acid
PLGA	Poly(lactic-co-glycolic acid)
PLLA	Poly(L-lactic acid)
PLP	Proteolipid protein
PNN	Perineuronal net
PNS	Peripheral nervous system
PPARα	Peroxisome proliferator-activated receptor alpha
PRP	Platelet-rich plasma
PVA	Poly(vinyl alcohol)
PVDF-TrFE	Polyvinylidene fluoride-trifluoroethylene
QQRFOWOFEQQ	Amino acid sequence; CH_3CO-glutamine-glutamine-arginine-phenylalinine-ornithine-tryptophan-ornithine-phenylalinine-glutamate-glutamine-glutamine-NH_2
rad	Radians
rad s^{-1}	Radians per second
RADA16-I-BMHP1	Self-assembling peptide with conjugated Bone Marrow Homing Peptide 1; RADARADARADARADAG-GPFSSTKT
RPM	Revolutions per minute
RPMI	Roswell Park Memorial Institute
s	Second
SAP	Self-assembling peptide
SC	Schwann cell
SCI	Spinal cord injury
SCIC	Spinal Cord Injury Centre
SE	Standard error of the mean
SEL	Spinal ependymal layer
SEM	Scanning electron microscope
SH-SY5Y	Human neuroblastoma cell line
SMCs	Smooth Muscle Cells
SPIONs	Superparamagnetic iron oxide nanoparticles
STT	Spinothalamic tract
TEA	Triethylamine
TG-DTA	Thermogravimetry–Differential Thermal Analysis
TiO_2	Titanium dioxide
TMZ	Temozolomide
TNBS	2,4,6-trinitrobenzene sulfonic acid
TNFα	Tumour Necrosis Factor alpha
TNP	Trinitrophenol
UTS	Ultimate Tensile Strength
UV	Ultraviolet
UV/Vis	Ultraviolet/Visible
V	Voltage
v/v	Volume per volume
W	Watts
W cm^{-2}	Watts per centimetre squared
wt%	Weight percent
XPS	X-ray Photoelectron Spectroscopy
β-CD	Beta Cyclodextrin
β-NGF	Beta Nerve Growth Factor

Chapter 1

Introduction

1.1 Spinal Cord Injury

The UK Spinal Cord Injury (SCI) population is crudely estimated at 40,000 people (BMJ, 2016) with the incidence rate close to 1000 new cases per year (NHS England, 2013). Despite the relatively small number of patients, this results in a cumulative cost to the National Health Service (NHS) estimated at £1 billion (Spinal Research, 2015). More surprising, this figure is now thought overly conservative and is under revision (Spinal Research, 2015).

SCI is a term inclusive of all damage to the spinal cord, including the tapered end (conus medullaris) and inferior bundle of nerves (cauda equina) (Cramer and Darby, 2014). This damage prevents the spinal cord from being able to perform its primary task of information transmission between the CNS and periphery, and impairs the overall purpose of the nervous system, of adequately responding to the environment and controlling homeostasis (Tortora and Derrickson, 2014). As such, patients are condemned to a host of physical impairments that are still managed crudely and a mental burden that often weighs greater than any physical loss.

SCI is categorised into either traumatic SCI, if caused by an impact over a short period of time, or non-traumatic, if pathology-associated or progressive (WHO, 2013). The vast majority of reported SCI is traumatic, with road traffic accidents the leading cause worldwide, but falls and violence also contribute significantly (WHO, 2013). Unlike progressive diseases, the sudden impact of these events results in up to 30% of patients presenting clinically relevant signs of depression (WHO, 2013); a reaction augmented by societies that are ill-equipped to fully include those with SCI.

Non-traumatic SCI is considered under-reported but increasing, partly due to the ageing population (Van Den Berg et al., 2010; New et al., 2014). Most regions where

data is available report at least a two-thirds majority in paraplegia over tetraplegia for non-traumatic SCI (New et al., 2014). Tumour growth and degenerative diseases, such as osteoarthritis, are leading causes in developed nations and infectious diseases, like tuberculosis and HIV, have higher incidence in developing nations (WHO, 2013; New et al., 2014).

There is also an imbalance with regards to gender amongst traumatic SCI incidence. In the adult population, males are more likely to suffer an accident resulting in SCI – an observation not seen in the paediatric population – and likely a reflection of social behaviour, such as alcohol consumption (WHO, 2013). Two age-related peaks are also observed; young adults, again likely from typical social behaviour, such as extreme sports, and the elderly from falls (WHO, 2013). Understanding this evolving injury profile can help tailor future preventative measures and influence legislation to reduce these peaks.

However, prevention is no longer applicable for those already injured and SCI patients are more likely to die prematurely than the general population; augmented with a more serious injury (WHO, 2013). Before this, treatment, care and the associated cost is required for the rest of an individual's life, which is also augmented with injury severity. In the USA, lifetime costs for a 25 year old with paraplegia have been estimated at $2.3 million and $4.6 million for tetraplegia (NSCISC, 2013). It should also be noted these costs do not factor in the personal financial loss or immeasurable cumulative economic deficit from SCI (WHO, 2013).

Whilst life expectancy and quality of life continues to improve in developed nations, there is still a higher prevalence of death by influenza, pneumonia, suicide and heart disease amongst the SCI population (WHO, 2013). Further, preventable secondary conditions such as urosepsis, renal failure and infections from pressure ulcers are still leading causes of death in developing nations (WHO, 2013). This symptom of an underdeveloped healthcare infrastructure, alongside poor reporting standards and a less regulated society, means global incidence for SCI is in the region of 250,000-500,000 each year (WHO, 2013).

As no treatment to restore spinal cord function yet exists, management of each individual symptom is required – from mobility to bowel and bladder control to breathing – alongside associated complications, such as pressure ulcers from

immobility. This is the underlying cause behind high treatment costs as care, equipment and time is dedicated to individual symptom management over the lifetime of a patient. Whilst this is currently the only option, the loss of independence associated with this treatment model also contributes to depression.

1.2 Current Management of Spinal Cord Injury

Current management of SCI is confined to management of symptoms, without treating the injury itself or restoring function of the spinal cord. In the UK, eleven Spinal Cord Injury Centres (SCICs) are designed to give specialist treatment, care and rehabilitation to SCI patients (MASCIP, 2020). Even though the vast majority of injuries to the spinal cord are contusion injuries with micro-haemorrhages and swelling – most as a result of a burst fracture to the spine – there is no set treatment pathway for patients. Some treating clinicians prefer a conservative approach; allowing recovery to initiate through immobilisation. Others prefer an operative strategy; removing bony fragments and stabilising the spinal column. The opposing strategies coexist at present because no randomised control trial has yet been designed and run to investigate which strategy results in a more positive patient outcome (O'Connor, 2016).

As no treatment to promote functional recovery yet exists, symptoms and complications are still managed individually and crudely. For example, immobility can be addressed using wheelchairs, bladder movement with a catheter, and breathing difficulties with a ventilator (NHS, 2017). Regular physiotherapy is generally required to avoid muscle spasticity and spasms, but oral medication or local injections of muscle relaxants may be required for more severe cases (NHS, 2017).

Neuropathic pain is also managed using medication, such as amitriptyline and pregabalin – with side effects that range from the uncomfortable (dry mouth) to the unpleasant (vision impairment) to the distressing (suicidal thoughts) (NHS, 2017). Depression is observed in up to 30% of SCI patients (WHO, 2013), another symptom managed using drugs, but generally prescribed alongside counselling (NHS, 2017).

Some complications of SCI are managed more easily. Pressure ulcers are developed from abnormal pressure or shear force on soft tissue, which disrupts

blood flow and results in an impeachment of oxygen directly to the site, as well as the potential for reperfusion injury if the period of ischaemia ends (National Pressure Ulcer Advisory Panel et al., 2014). Through regular movement of the patient, pressure ulcers can be avoided, but if they do occur must be washed and bandaged to avoid infection and promote healing (National Pressure Ulcer Advisory Panel et al., 2014).

Other complications require the aid of specialist medical services, such as fertility clinics for freezing sperm (NHS, 2017), whilst others are seriously life-threatening. Autonomic dysreflexia is the raising of blood pressure in response to abnormal functioning of the autonomic nervous system (NHS, 2017). Common to tetraplegics, this can be caused by blockages in bowel or bladder drainage and must be identified and dealt with immediately.

Managing these symptoms is time and energy consuming. Physical impairments lead to dependency on others or machines, whilst the mental burden manifests as embarrassment, anxiety and depression. When this is considered alongside the lack of integration for SCI patients within society, the necessity for an effective treatment is evident. A solution that restores tissue function may overcome all of the current challenges.

1.3 Challenges of Existing Treatment Methods

To date, no therapy is used in routine practice with the purpose of restoring spinal cord function (Ashammakhi et al., 2019). Historically, clinical trials have investigated the benefit of drugs for treating SCI with largely negative or disappointing outcomes (Hawryluk et al., 2008). Implantable scaffolds are a relatively recent research avenue, and only two biomaterial scaffolds have been implanted into humans to date; the Neuro-Spinal scaffold (Theodore et al., 2016; Layer et al., 2017; Kim et al., 2021) and the NeuroRegen scaffold (Xiao et al., 2016; Zhao et al., 2017; Xiao et al., 2018; Chen et al., 2020; Deng et al., 2020)..

1.3.1 Neuro-Spinal Scaffold

The Neuro-Spinal scaffold (Fig. 1.1A) has been implanted into 16 acute SCI patients successfully to date as part of a single study (Kim et al., 2021). The scaffold consists

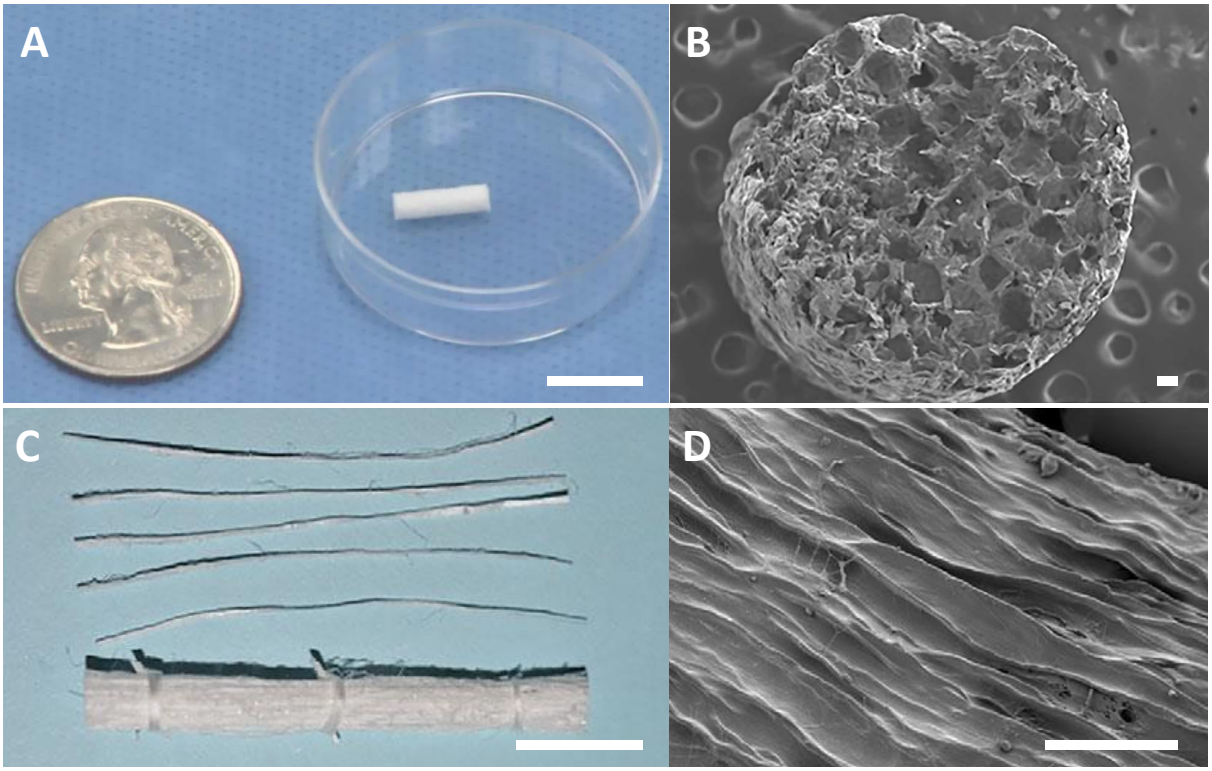

Figure 1.1 Neuro-Spinal and NeuroRegen scaffolds. Only two scaffolds have been implanted into humans for regeneration of the spinal cord to date. (A) Image of the Neuro-Spinal scaffold made of salt-leached PLGA conjugated to poly(L-lysine) and (B) an SEM image of the microscale porosity (reprinted from Theodore et al., 2016; reproduced by permission of Oxford University Press). (C) Image of the NeuroRegen scaffold made of collagen from decellularised bovine aponeurosis and (D) an SEM image of the microscale aligned channels at the microscale (reprinted from Xiao et al., 2016; reproduced by permission of Springer Nature). Image scale bars are 10 mm; SEM image scale bars are 100 µm.

of a highly porous, salt-leached matrix made from the polymer poly(lactic-co-glycolic acid) (PLGA) conjugated to poly(L-lysine) (Fig. 1.1B) that has shown promise in preclinical testing (Teng et al., 2002; Pritchard et al., 2010; Guest et al., 2018).

For acute patients, an opportunity for implantation presents itself during decompression and fixation, performed routinely by some clinicians, and before scarring takes place. All patients had a thoracic injury and were rated A on the ASIA Impairment Scale, which is used to classify severity of injury (Table 1.1), and thus showed no sensory or motor function in the lower sacral region.

The main aim for the study was to evaluate "*probable benefit for safety and neurological recovery*" as measured by the primary outcome of an improvement in ASIA score (Kim et al., 2021). Secondary outcomes included improvement in the

Grade	Type of Injury	Description of Injury
A	Complete	No sensory or motor function is preserved in the sacral segments S4-S5.
B	Sensory Incomplete	Sensory but not motor function is preserved below the neurological level of injury (NLI) and includes the sacral segments S4-S5 AND no motor function is preserved more than three levels below the motor level on either side of the body.
C	Motor Incomplete	Motor function is preserved at the most caudal sacral segments for voluntary anal contraction (VAC) OR the patient meets the criteria for sensory incomplete status (as above), AND has some sparing of motor function more than three levels below the ipsilateral motor level on either side of the body.
D	Motor Incomplete	Defined as above with half or more of key muscle functions below the NLI having at least active movement and full range of motion against gravity (muscle grade ≥ 3).
E	Normal	If sensation and motor function are graded as normal in all segments AND the patient had prior deficits.

Table 1.1 Table showing the ASIA Impairment Scale for classifying severity of SCI.

most caudal level of sensory and motor function – termed the neurological level of injury (NLI) – and appearance of complications such as cysts or scars.

Three month post-operative assessment in the first patient indicated some motor and sensory function had returned below the level of injury (Theodore et al., 2016), and improvement in ASIA score in five of nine patients was detailed in an interim report (Layer et al., 2017).

Following the end of recruitment, out of sixteen patients enrolled and successfully followed up at six months, seven (44%) had improved ASIA score, indicating a downgrade in severity of injury from no sensory or motor function in the lower sacral levels to some sensory or some motor function. This is well above the 16-21% spontaneous improvement determined from historical records (Zariffa et al., 2011; B.A. Lee et al., 2016; Aimetti et al., 2019) and the 25% benchmark the group had set themselves.

These results have indicated the potential benefits of implanting the Neuro-Spinal scaffold outweigh the risks and support further clinical investigation, with a

randomised control trial now recruiting (ClinicalTrials.gov; NCT03762655). However, whilst the improvement in ASIA score is promising and future follow-up may observe further improvement, the results for the secondary endpoints was underwhelming. Changes in NLI were not clinically significant, sensory changes and appearance of complications were similar to historic averages, and significant motor recovery was still regarded as unattainable.

1.3.2 NeuroRegen Scaffold

Similar results have also been recorded for the NeuroRegen scaffold (Fig. 1.1C). The NeuroRegen scaffold is made of collagen from decellularised bovine aponeurosis (Lin et al., 2006) (Fig. 1.1D) that has been evaluated preclinically over the last decade (Han et al., 2009; Han et al., 2010; Fan et al., 2010; Li et al., 2013; Han et al., 2015; Xing Li et al., 2015), and implanted into both acute (Xiao et al., 2018; Chen et al., 2020) and chronic (Xiao et al., 2016; Zhao et al., 2017) SCI patients.

Recently, the one-year follow-up was published of a phase I clinical trial (ClinicalTrials.gov; NCT02510365) focused on acute cervical SCI patients implanted with the NeuroRegen scaffold with human umbilical cord mesenchymal stem cells (hUCB-MSCs) (Deng et al., 2020). Out of 40 patients, half were implanted with the scaffold and half used as a control group with no scaffold or cells.

Remarkably, 11 of the patients in the treatment group (55%) showed improved ASIA score versus none in the control group. Further, partial control over urination and defecation returned for some patients as well as some motor control, with one patient even regaining movement in the left little finger. Nerve fibre regeneration was also observed via MRI, along with an increase in cord size and decrease in cavity size.

Of similar significance, two patients with acute complete SCI, which were also implanted with hUCB-MSCs as part of the same clinical trial, achieved reclassification of ASIA score from A to C (Xiao et al., 2018). The thoracic patient regained the ability to walk with the aid of a hip brace and regained some sensory and motor control of the bowel and bladder. The cervical patient regained the ability

to move his legs and toes under control, as well as some sensory function in the bowel and bladder.

Whilst this is promising, weaker results have been observed for the NeuroRegen scaffold implanted into six acute SCI patients with autologous bone marrow mononuclear cells (BMMCs) (Chen et al., 2020). No improvement in ASIA score was observed for any of these patients after three years, though some defecation, erection and sweating function did return.

Similarly, even weaker results have been recorded for the NeuroRegen scaffold implanted into chronic SCI patients. Chronic SCI patients are considered stable, with the spinal injury scar presenting an occlusion, and as such resection of the scar was undertaken. Despite resection and implantation, no improvement in ASIA score was recorded for five chronic patients implanted with BMMCs after one year, but some sensory, erection and sweating function did return (Xiao et al., 2016). Further, no improvement in ASIA score was recorded for eight patients implanted with hUCB-MSCs after one year, but some improvement in sensation level, motor signalling and sweating did return (Zhao et al., 2017).

The results above indicate the NeuroRegen scaffold is safe to implant and likely does have some regenerative effect. Whilst there is evidence this is influenced by stem cell source and injury type, a randomised controlled clinical trial would be welcome to further understand the regenerative capacity of the scaffold and combined cell therapy. As it stands, it remains unclear why around half of acute patients and all chronic patients do not see significant improvement following implantation, resulting in a reclassification of injury.

1.3.3 Summary

The limited regeneration observed from the minimal clinical data above may be due to the lack of a mechanically optimised environment for cell survival and tissue regeneration that has become an important research avenue of regenerative medicine (Bartlett et al., 2016). When partnered with directional cues, this could be a more potent promoter of regeneration than directional cues on their own, used in the NeuroRegen scaffold (Xiao et al., 2016; Zhao et al., 2017; Xiao et al., 2018; Chen et al., 2020; Deng et al., 2020), or a porous environment lacking both mechanical

optimisation and directional cues, as in the Neuro-Spinal scaffold (Theodore et al., 2016; Layer et al., 2017; Kim et al., 2021). Addressing these emerging design requirements, biomimetic composite scaffolds comprising of both fibres and hydrogels are amongst the most promising.

Recently, the incorporation of self-assembling peptides (SAP) with a degradable polymer made into electrospun nonwoven fibre networks have been shown to provide beneficial properties with respect to hard tissue repair; specifically P_{11}-8 peptides and poly(ε-caprolactone) (PCL) polymer (PCL/P_{11}-8) (Gharaei et al., 2016; Gharaei, 2017; Gharaei et al., 2020). However, such scaffolds have only been produced and studied with randomly oriented fibres, rather than the highly aligned geometry needed for spinal cord tissue regeneration (Milbreta et al., 2016; Yao et al., 2016; Y.S. Lee et al., 2017; Du et al., 2017; Yao et al., 2018; Wang et al., 2018).

Similarly, collagen with glycidyl methacrylate (GMA) moieties conjugated to its backbone (collagen-GMA) is able to form a photo-crosslinked hydrogel that has shown beneficial properties as a wound dressing material and as a regenerative scaffold (Tronci et al., 2013; Tronci et al., 2015), but has not been investigated on its own for three-dimensional cell culture in general, especially for neural cells or spinal cord tissue. If an aligned electrospun nonwoven of PCL/P_{11}-8 could be produced and partnered with an optimised collagen-GMA hydrogel capable of three-dimensional cell culture, it was hypothesised their respective properties and integration as a scaffold would be beneficial for SCI repair.

Accordingly, understanding the feasibility of manufacturing novel composite scaffolds containing PCL/P_{11}-8 fibres and collagen-GMA hydrogel could provide the basis of an improved regenerative scaffold strategy for spinal cord repair.

1.4 Aims and Objectives

Given current challenges in the treatment and restoration of function in spinal cord injuries, the overall aim of this work was to investigate the manufacture, structure and properties of scaffolds comprising aligned PCL/P_{11}-8 peptide fibres and a biomimetic collagen-GMA hydrogel material. The purpose of the study was therefore to investigate the structure-property relationships of PCL/P_{11}-8 and collagen-GMA as

individual materials, aiming to accomplish a novel SCI repair scaffold via their integration into a single composite system.

The specific objectives were:

- To critically review the literature relating to spinal cord injury and the harnessing of regenerative strategies involving fibre and hydrogel scaffolds.
- To investigate the feasibility of producing a highly aligned web of PCL/P_{11}-8 for the first time.
- To characterise aligned PCL/P_{11}-8 electrospun nonwovens, including investigating the effect of electrospinning parameters and SAP concentration on web properties.
- To study collagen-GMA hydrogel mechanical properties at a scale relevant to cells and tissue for SCI regeneration.
- To investigate the properties of composite scaffolds of PCL/P_{11}-8 nonwoven and collagen-GMA hydrogel in terms of directional neurite extension, desired cell infiltration, and preventing non-native cell infiltration following implantation.

Chapter 2

Review of the Literature

2.1 Introduction

This chapter reports a critical review of the literature relevant for producing a composite nonwoven-hydrogel scaffold of electrospun PCL/P_{11}-8 nonwoven and collagen-GMA hydrogel for spinal cord tissue regeneration. To understand the requirements for spinal cord tissue regeneration, an introduction to spinal cord tissue is provided, including the macroscale and microscale anatomy, and the structural and chemical changes to this environment following SCI. Next, the process of regenerative medicine is introduced, along with the design and manufacturing processes for a composite nonwoven-hydrogel scaffold designed for SCI repair. Finally, findings from the literature on nonwovens and hydrogels in isolation for spinal cord tissue regeneration are provided, as well as composite nonwoven-hydrogels. Accordingly, the purpose of this chapter was to introduce the requirements for spinal cord tissue regeneration, understand the approaches already undertaken in the literature and how this should inform the aims and objectives of the work herein.

2.2 Anatomy of the Spinal Cord

The spinal cord, along with the brain, is part of the central nervous system (CNS) (Fig. 2.1A). The CNS controls most functions of the body, and works in conjunction with the peripheral nervous system (PNS) to allow the body to respond to the environment; whether this means engaging with surroundings or maintaining homeostasis (Tortora and Derrickson, 2014). Of this broad definition, the main function of the spinal cord is information transmission between the CNS and periphery. This is reflected in the anisotropic macroscale tissue morphology,

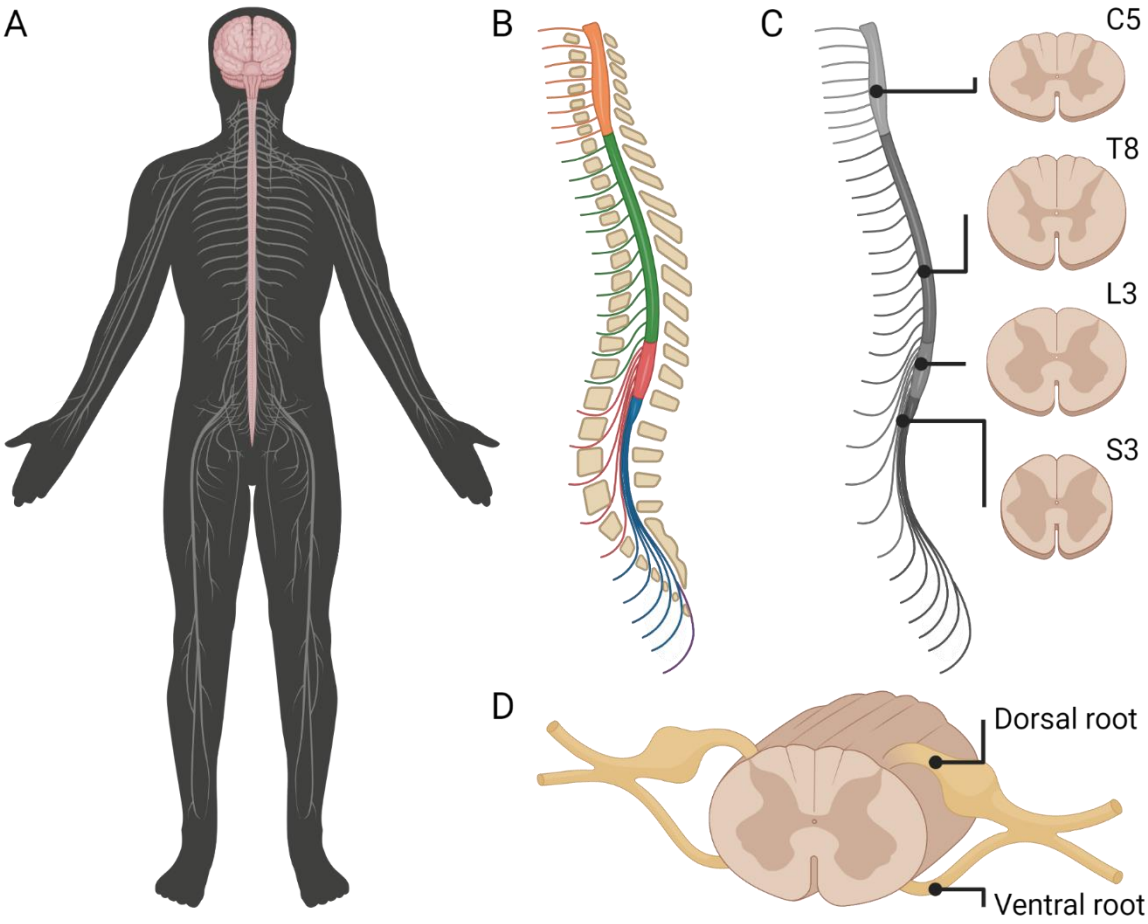

Figure 2.1 Macroscale anatomy of the spinal cord. (A) The spinal cord and brain (pink) comprise the CNS, with the PNS comprising the rest of the nervous system (grey). (B) The spinal cord is comprised of thirty-one segments; eight cervical (C1-8, yellow); twelve thoracic (T1-12, green); five lumbar (L1-5, pink); five sacral (S1-5, blue); and one coccygeal (purple). (C) The proportions of grey (dark pink) and white matter (light pink) change depending on the position. (D) Spinal nerves connect to the spinal cord, with the dorsal root containing sensory neurons and the ventral root containing motor neurons. Created with BioRender.com.

extending from the brain through the spinal column, and the anisotropic microscale cell morphology, with neuronal axons highly aligned rostral to caudal.

2.2.1 Macroscale Anatomy

The spinal cord extends from the base of the brain, through the spinal canal of the vertebrae, and finishes around the second lumbar vertebra (L2) (Watson and Kayalioglu, 2009; Cramer and Darby, 2014). Morphologically, it is a flattened cylinder around 42-45 cm in length in the average adult and comprised of thirty-one

segments; eight cervical (C1-8); twelve thoracic (T1-12); five lumbar (L1-5); five sacral (S1-5); and one coccygeal (Fig. 2.1B) (Watson and Kayalioglu, 2009; Cramer and Darby, 2014).

These segments are not uniform in diameter, with two notable enlargements. The first enlargement exists between C3-T2 (Cramer and Darby, 2014), with C5 being the largest cross-sectional area of the whole cord (Ko et al., 2004), and a second enlargement exists between L1-S3 (Cramer and Darby, 2014), peaking at L4 (Ko et al., 2004). The enlargements are due to a higher density of neuron cell bodies in these areas, as these regions are responsible for innervating the increased area associated with the upper and lower extremities, respectively (Cramer and Darby, 2014).

Whilst the spinal cord changes in cross-sectional size through its length, there are two distinct regions found throughout. Spinal cord tissue is segregated into grey and white matter, the proportions of which change depending on the position (Fig. 2.1C). Grey matter contains neuron cell bodies, dendrites and axons that emerge from the cell bodies, neuroglial cells that support the neurons through ECM construction, and capillaries for the delivery of oxygenated blood (Watson and Kayalioglu, 2009; Cramer and Darby, 2014). White matter surrounds the majority of grey matter and is largely made up of axons running in the axial plane, supportive neuroglia and capillaries (Cramer and Darby, 2014).

The tissue itself is encased by the meninges; a set of three protective membranes (Watson and Kayalioglu, 2009). The dura mater is the outermost layer, followed by the arachnoid mater and the pia mater, and with the subarachnoid space between the latter two filled with cerebrospinal fluid. Adipose tissue fills the remaining foramen of the spinal canal, exterior to the dura mater.

Connecting this central tissue to the periphery are thirty-one pairs of spinal nerves, each associated with one of the thirty-one spinal cord segments (Fig. 2.1D) (Cramer and Darby, 2014). Spinal nerves branch into the ventral and dorsal roots as they approach the spinal cord and further subdivide into 6-8 rootlets which attach to the spinal cord at the ventrolateral and dorsolateral sulcus (Watson and Kayalioglu, 2009). The dorsal root contains sensory neurons from the skin, tissue and organs with the cell bodies of these neurons located in the dorsal root ganglion (DRG)

(Cramer and Darby, 2014). The ventral root contains motor neurons that innervate muscles and glands (Cramer and Darby, 2014).

2.2.2 Microscale Anatomy

The microscale anatomy consists of cells and extracellular matrix (ECM). Cells of spinal cord tissue include neurons and supporting neuroglia, which enable tissue function. ECM refers to the non-cellular component of tissue which provides physical structuring and support for cells, as well as biochemical and biomechanical signals. Again, anisotropy of the tissue is observed at this scale as well.

2.2.2.1 Neurons

Neurons are the electrically excitable cells that allow nerve impulses to propagate along them and facilitate information transmission in the spinal cord (Tortora and Derrickson, 2014). Neurons generally have three main cell parts; the cell body, containing characteristic Nissl bodies (clusters of rough endoplasmic reticulum and free ribosomes) that give grey matter its grey colour; multiple dendrites, the highly branched input processes of the cell; and an axon, the single output process.

The action of nerve impulses is well characterised (Tortora and Derrickson, 2014). Briefly, these are rapid waves of changing electrical potential due to the movement of sodium and potassium ions across the plasma membrane. The non-decremental repetition of this event in adjacent downstream portions of the axon, and the refractory period in the adjacent upstream portion, propagates the action potential along the axon and prevents backward propagation.

The adult mammalian spinal cord consists of three types of neuron; ascending tract sensory neurons that project to the brain via the dorsal horn; spinal interneurons that project to other neurons within the spinal cord; and spinal motor neurons that project to skeletal muscles (somatic) or cardiac muscles, smooth muscles and glands (visceral), the latter also known as preganglionic neurons as they signal via peripheral neurons rather than direct innervation (Zholudeva et al., 2018).

Ascending Tract Sensory Neurons

Ascending tract sensory neurons refer to the bundles of pseudo-unipolar sensory neurons that send information from the periphery to the brain (Fig. 2.2A) (Chandar and Freeman, 2014). They can be characterised as ‘unconscious’ and ‘conscious’

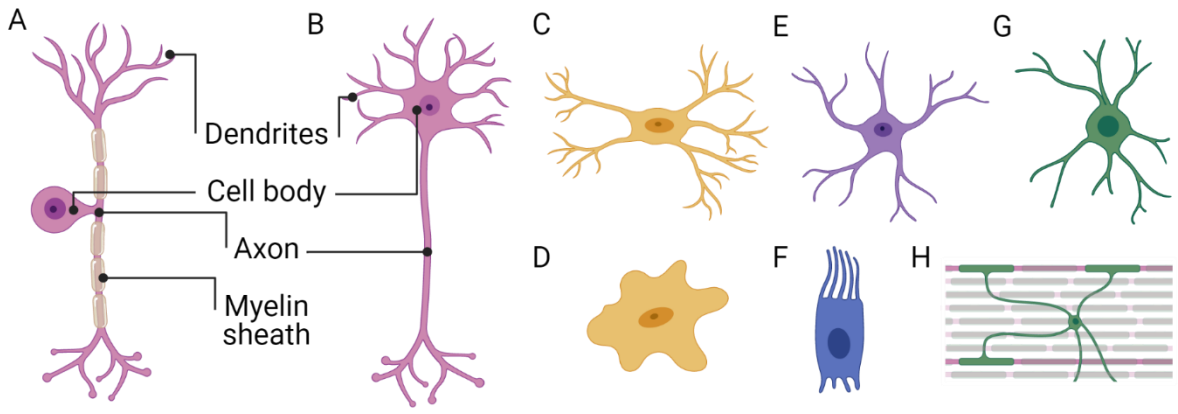

Figure 2.2 Neurons and neuroglia. (A) Pseudo-unipolar neuron, similar to sensory neurons (shown myelinated). (B) Multi-polar neuron, similar to interneurons and motor neurons (shown non-myelinated). (C) Ramified morphology of microglia. (D) Amoeboid morphology of microglia. (E) Astrocyte morphology. (F) Ependymocyte morphology. (G) Oligodendrocyte morphology. (H) Oligodendrocytes are able to myelinate multiple axons, creating myelinated internodes and gaps called nodes of Ranvier. Created with BioRender.com.

depending on the specific white matter tract. Unconscious tracts are found in the spinocerebellar tracts and transmit unconscious proprioceptive signals from the muscles to the brain. Conscious tracts are found in the dorsal column-medial lemniscal (DCML) pathway, responsible for fine touch, vibration and proprioception; and the spinothalamic tract (STT), responsible for crude touch, pressure, pain and temperature.

Damage to the DCML and STT is associated with neuropathic pain after SCI (Cruz-Almeida et al., 2012) and recent work has suggested transcriptional changes in these cells could be responsible for the characteristic poor axonal regeneration, due to a downregulation in lipid metabolism (Ewan et al., 2021). It may also be influenced by satellite cells – glial cells found in the DRG – via signalling through the nuclear receptor peroxisome proliferator-activated receptor alpha (PPARα) that is activated following peripheral nerve injury but not SCI, and agonists such as the FDA-approved fenofibrate may have therapeutic potential (Avraham et al., 2020)

Spinal Interneurons

Spinal interneurons are multi-polar instead (Fig. 2.2B) and process sensory information from sensory neurons and elicit effector response through motor neurons (Zavvarian et al., 2020). Spinal interneurons can be classified into local and

propriospinal; local spinal interneurons play a role in neural oscillations and reflexes, whereas propriospinal neurons connect different spinal segments, and can be short or long depending on whether they connect adjacent segments or more distant segments. They can also be classified as inhibitory or excitatory, based on whether they release neurotransmitters such as glycine or glutamate, respectively. Tens of subtypes of interneurons are believed to exist, indicating specialisation and specificity on an individual and regional level (Sagner and Briscoe, 2019).

Spinal interneurons sprout new processes, reorganise connectivity and change phenotype in response to injury, disease, and adaptive or maladaptive changes (Zholudeva et al., 2018). This function and neuroplasticity makes them therapeutic targets. Current research avenues include activity-based therapies, neural interfacing with direct electrical stimulation, and transplantation of spinal interneuron precursor cells (Zholudeva et al., 2018; Zavvarian et al., 2020).

Spinal Motor Neurons

Spinal motor neurons are also multi-polar (Fig. 2.2B) and are the longest known cell type, extending up to several meters in mammals via the ventral horns (Stifani, 2014). Somatic spinal motor neurons innervate skeletal muscles and can be further subdivided into alpha (contraction), beta (contraction and proprioception) and gamma (proprioception). Visceral motor neurons relay information to ganglionic neurons of the PNS as part of the autonomic nervous system, controlling smooth muscle, cardiac muscle and glands.

Due to the lack of alternative routes to convey commands from the CNS to the periphery, spinal motor neurons have been described as the "*the ultimate and irreplaceable component of the neuronal circuitry*" (Stifani, 2014). Despite atrophy to the area caudal to the spinal injury and reduced synaptic input to motor neurons, synaptogenic potential has been shown to remain and indicates that methods of restoring the input could be therapeutic (Yokota et al., 2019), as well as transplantation of iPSC-derived motor neurons (Trawczynski et al., 2019).

2.2.2.2 Neuroglia

Neuroglia is the collective name for the non-neuronal cells of the nervous system. Together, neuroglia play a key role in maintaining homeostasis and enabling the

primary function of information transmission. Neuroglia of the CNS include microglia, astrocytes, ependymocytes and oligodendrocytes (Tortora and Derrickson, 2014).

Microglia

Microglia are the resident mononuclear phagocytes of the CNS (Sierra et al., 2019; Garaschuk and Verkhratsky, 2019). In the adult CNS, microglia are homogeneously distributed throughout the tissue and have a highly branched 'ramified' morphology (Fig. 2.2C). The ramified morphology allows microglia to move their processes without moving the cell body to sample the immediate environment around themselves (Kettenmann et al., 2011; Garaschuk and Verkhratsky, 2019). This includes contacting neuronal cell bodies, blood vessels and astrocytes (Nimmerjahn et al., 2005), and as part of the astroglial cradle that supports synapse functioning (Verkhratsky and Nedergaard, 2014).

In this way, microglia are both part of the cytoarchitecture and play a functional role in modulating physiological processes and responding to pathology (Garaschuk and Verkhratsky, 2019). For example, microglia secrete factors, such as BDNF (Coull et al., 2005) and ATP (Pascual et al., 2012), that modulate neural and glial cell activity respectively, as well as modulating neurogenesis (Sierra et al., 2010). Microglia are also involved in synaptic stripping – the removal of silent, redundant or damaged synapses via physiological phagocytosis (Sierra et al., 2010). These processes are mediated by the array of receptors found in microglia, including those for neurotransmitters and neuromodulators, immune and phagocytic responses, and those that are triggers for pathogens or damage (Garaschuk and Verkhratsky, 2019).

However, in response to injury the cell morphology of microglia switches to an activated 'amoeboid' state (Fig. 2.2D) (Nimmerjahn et al., 2005; Davalos et al., 2005). The processes present during the steady-state retract and resorb into the cell body and new processes capable of facilitating motility of the whole cell emerge (Stence et al., 2001; Parakalan et al., 2012). Together, these two phenotypes allow microglia to form a vigilant and responsive protection of the CNS.

Of note, microglia can also become senescent in response to injury, where they are no longer able to perform the neuroprotective or phagocytic duties associated with the above two phenotypes (Streit et al., 2014; Bachstetter et al., 2015; Garaschuk and Verkhratsky, 2019). This is believed to occur in response to progressing

pathologies, with cells losing the ability to respond to the overexpression of inflammatory factors following disease or injury (Garaschuk and Verkhratsky, 2019).

Further, other microglial phenotypes associated with injury and disease are also found in the CNS – including hypertrophic, rod-like and satellite microglia – but as these are not regionally distributed within the spinal cord they have not been detailed herein (Garaschuk and Verkhratsky, 2019).

Astrocytes

Astrocytes are also distributed homogeneously throughout the CNS, forming a network between themselves, neurons and the vasculature (Sofroniew and Vinters, 2010). They have two main subtypes; protoplasmic astrocytes are found in the grey matter and have short, branched processes; versus fibrous astrocytes that are found in the white matter and have longer, unbranched processes (Fig. 2.2E) (Tortora and Derrickson, 2014). For a comprehensive list of astrocyte functions, see Kimelberg and Nedergaard (2010), but of main importance is their role in synapse functioning, functioning of nodes of Ranvier and control of the vasculature, including CNS energy.

Processes from astrocytes envelope synapses, forming tripartite structures that control the fluid (Simard and Nedergaard, 2004), ion (Obara et al., 2008), pH (Obara et al., 2008) and neurotransmitter recycling or dissipation (Seifert et al., 2006) that are all essential for synapse function (Sofroniew and Vinters, 2010; Kimelberg and Nedergaard, 2010).

To do so, astrocytes interact with neuronal synapses through a whole host of contact-mediated and secreted cues that control synapse formation (Christopherson et al., 2005), alter density of specific receptors (Stellwagen et al., 2005; Stellwagen and Malenka, 2006; Hennekinne et al., 2013) and thus affect function (Allen and Eroglu, 2017). For example, release of ATP is suspected to modulate expression of proteins, such as PSD95, involved in forming trans-synaptic columns that align presynaptic neurotransmitter release sites and their opposing postsynaptic targets (Tang et al., 2016; Broadhead et al., 2020).

Astrocytes also contact the majority of nodes of Ranvier in the spinal cord (Serwanski et al., 2017) and secrete ECM proteins or cell adhesion molecules which promote stabilisation of the nodes or affect node channel architecture (Lubetzki et

al., 2020). They have also been shown to secrete thrombin protease inhibitors that affect myelin sheath thickness, increasing node length and thus affect conduction velocity in the CNS (Dutta et al., 2018).

Astrocyte processes also surround all blood vessels in the CNS, but of particular importance is their interaction with precapillary arterioles, which are surrounded by smooth muscle and can control blood flow (Kimelberg and Nedergaard, 2010). Astrocytes regulate blood flow by releasing mediators such as prostaglandins, nitric oxide and arachidonic acid (Iadecola and Nedergaard, 2007). Although, astrocytes are not believed to take part directly in the blood-CNS barrier, as evidenced by the lack of leakage following ablation of astrocytic endfeet (Kubotera et al., 2019).

This interconnectivity between capillaries and key energy-consuming sites makes astrocytes appropriate energy distributors and stores (Sofroniew and Vinters, 2010). Astrocytes not only store glycogen close to these sites (Phelps, 1972), but the astrocyte-neuron lactate shuttle hypothesis – in which glucose is taken up by the astrocyte processes and converted to lactate via aerobic glycolysis for use as the principal energy of neurons – is also widely accepted (Kimelberg and Nedergaard, 2010). However, it is worth noting the existence of the lactate shuttle is still a highly debated topic (Barros and Weber, 2018; Bak and Walls, 2018).

Ependymocytes

Ependymocytes are the most plentiful cell type found in the spinal ependymal layer (SEL) – the lining of the central canal of the spinal cord, but are also found in the ventricles of the brain (Moore, 2016). Ependymocytes have a cuboidal morphology, with characteristic microvilli and elongated cilia (Fig. 2.2F) (Del Bigio, 2010).

Their location and morphology enable their primary function of producing, monitoring and circulating cerebrospinal fluid (CSF), which itself nourishes, removes waste and protects the CNS (Spector et al., 2015; Telano and Baker, 2018). In doing so, they also form the blood-CSF barrier and play a role in modulating fluid (Venero et al., 1999) and ion (Kanaka et al., 2001) concentration, as well as trophic and metabolic activity (Del Bigio, 2010; Moore, 2016).

Whilst renewal of ependymocytes in healthy adult tissue is slow (Barnabé-Heider et al., 2010) and could be affected by age and injury (Xiaofei Li et al., 2016), there is evidence that mature ependymocytes express neural stem cell markers, such as

nestin and Sox2; are capable of self-renewal *in vivo* (Meletis et al., 2008); and have the ability to form astrocytes and oligodendrocytes in response to injury (Meletis et al., 2008), as well as motor neurons *in vitro* (Barnabé-Heider et al., 2010). As such, they are believed to be a potential stem cell niche within the CNS, with therapeutic potential (Moore, 2016).

It is worth noting ependymocytes are not the only cell type found in the SEL, which also consists of tanycytes that provide contact between the CSF and blood vessels; CSF-contacting neurons that are believed to be a type of sensory neuron detecting changes in CSF composition, pressure and flow; and supraependymal cells that possibly play a role in immunosurveillance (Moore, 2016). Further, recent MRI images have indicated the central canal appears to be occluded rather than patent in the adult spinal cord, with ependymocytes forming dense clusters reminiscent of ependymal tumours, the formation and function of which is yet to be characterised (Garcia-Ovejero et al., 2015).

Oligodendrocytes

Oligodendrocytes are the myelinating cells of the CNS and have long unbranched processes that wrap around and insulate axons (Fig. 2.2G) (Tortora and Derrickson, 2014). Myelin itself is a specialised extension of the oligodendrocyte process cell membrane that forms internodes a few hundred microns in length on multiple axons, separated by spaces known as nodes of Ranvier that are less than a micron in length (Fig. 2.2H) (Baumann and Pham-Dinh, 2001). The majority of axons in the spinal cord are myelinated, with the number in the tens of thousands per square millimetre (Saliani et al., 2017), and it is this density of myelin that is responsible for the white colour of white matter (Tortora and Derrickson, 2014).

Myelination is a complex series of events, involving proliferation and migration of oligodendrocyte precursor cells (OPCs), recognition of axons to be myelinated, differentiation of OPCs to mature oligodendrocytes, ensheathment, reorganisation of membrane components, myelin compaction, and formation of nodes of Ranvier (Krawczyk-Marc et al., 2019)

The nodes of Ranvier are the regions that enable saltatory conduction and therefore expedite impulse transmission (Bjartmar et al., 1994).The myelin sheath enables saltatory conduction through its structure, thickness, low water content and high lipid

content (Baumann and Pham-Dinh, 2001). Further, previously evenly distributed sodium channels in the axon become redistributed to the nodes of Ranvier (Kaplan et al., 1997; Waxman, 1997), with potassium channels clustered in the juxtaparanodal region close by (Baumann and Pham-Dinh, 2001; Nave, 2010), enabling depolarisation and repolarisation at the nodes. In doing so, conduction velocity increases from 0.5-10 m s^{-1} in unmyelinated axons up to 150 m s^{-1} for myelinated axons (Purves et al., 2001), whilst reducing the energy requirement (Zalc, 2000).

Further roles for oligodendrocytes in trophic support of neurons are only beginning to be understood (Nave, 2010). Whilst it has been known for some time that a lack of proteolipid protein (PLP), a key myelin protein, is required for axonal health (Readhead et al., 1994; Griffiths et al., 1998), only recently has evidence supported oligodendrocytes involvement in energy metabolite provision to neurons via the lactate shuttle (Philips and Rothstein, 2017) and an influence over intra-axon vesicle transport via exosomos (Frühbeis et al., 2020).

These functions may also be linked to specific subtypes of oligodendrocytes. Historic subtyping has been based on location in the CNS and morphological differences (Pérez-Cerdá et al., 2015) or from the density of the cytoplasm as a sign of maturity (Wawrzyniak-Gacek, 2002). However, more recent single-cell sequencing techniques have indicated oligodendrocytes could exist as different functional types or in functional states based on the stage of myelination (Duncan et al., 2018; Kamen et al., 2021).

2.2.2.3 The Extracellular Matrix

There are three main regions that are defined as extracellular matrix (ECM) within the CNS (Fig. 2.3). The first are basement membranes which surround blood vessels; the second are condensed regions known as perineuronal nets (PNNs) that cluster around cell bodies, dendrites and the start of the axon; and third, diffusely spread as interstitial matrix between parenchyma (Lau et al., 2013).

The basement membrane serves as a structural support that provides an anchor for cellular components and the rest of the ECM to the vasculature. The structural protein collagen type IV acts as a flexible scaffold to which the glycoproteins laminin and fibronectin are attached (Burnside and Bradbury, 2014).

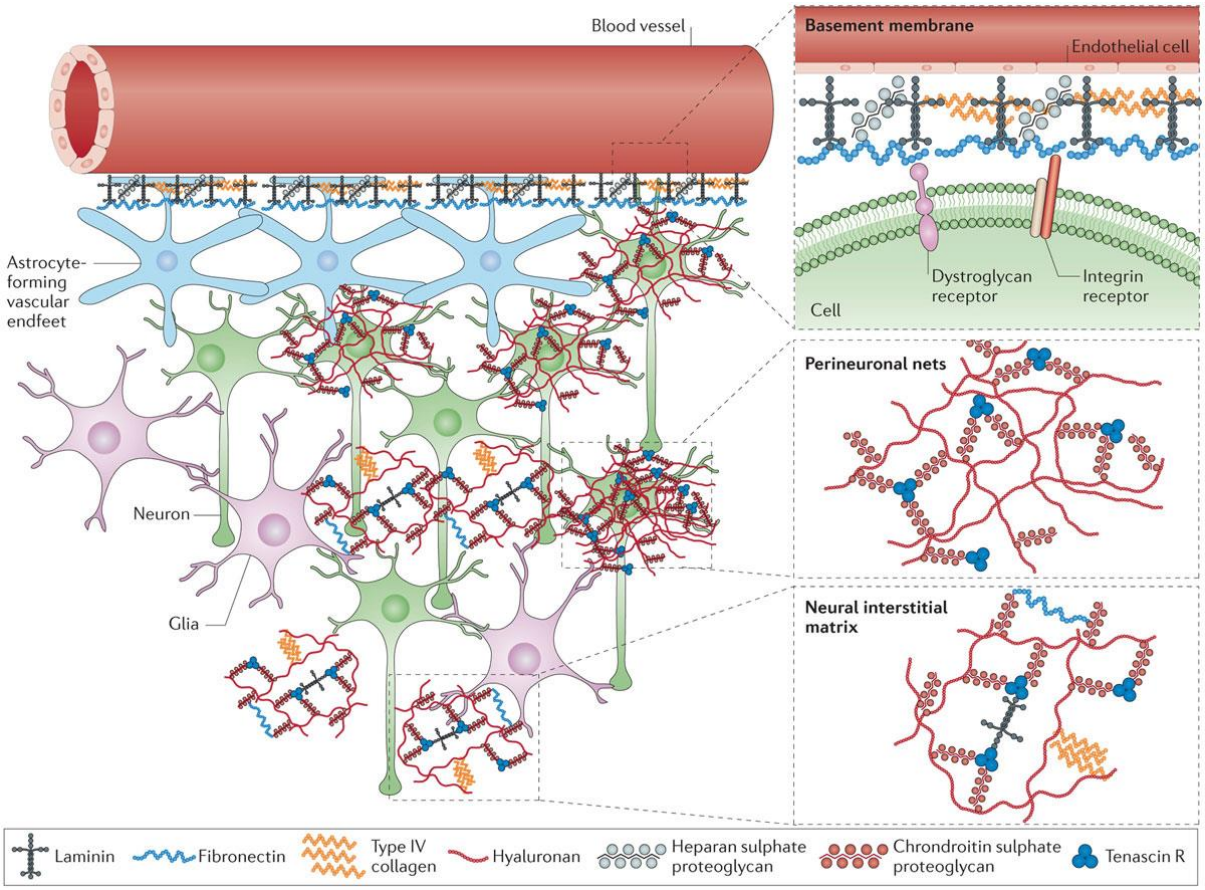

Figure 2.3 Spinal cord ECM. Spinal cord ECM has three main regions; basement membrane, perineuronal nets (PNNs) and interstitial matrix. Basement membrane surrounds blood vessels and is comprised of collagen type IV, fibronectin, laminin and heparan sulphate proteoglycans; PNNs cluster around cell bodies, dendrites and the start of the axons and are comprised of hyaluronan, chondroitin sulphate proteoglycans and tenascin R; and interstitial matrix fills the remaining space, comprised of the same components as PNNs as well as collagen type IV and laminin (reprinted from Lau et al., 2013; reproduced by permission of Springer Nature).

Laminin polymerises laterally, providing cell adhesion properties via integrins and syndicans between blood vessels, neurons and glia (Burnside and Bradbury, 2014). Specific laminin isoforms interacting with specific integrins, such as laminin-1 interacting with α3β1 or α7β1 and laminin-10 interacting with α6β1, have been shown to promote neurite outgrowth of rat DRG independent of neural growth factor (Plantman et al., 2008). Glycosaminoglycan (GAG)-rich fibronectin is also able to bind integrins, as well as heparan sulphate proteoglycans found on the cell surface and in basement membranes (Sarrazin et al., 2011).

PNNs have a role in synaptic stabilisation. Within the spinal cord they can be found on 30% of motor neurons in the ventral horn, 50% of large interneurons in the intermediate grey area and 20% of sensory neurons in the dorsal horn (Burnside and Bradbury, 2014). PNNs are largely comprised of hyaluronan, chondroitin sulfate proteoglycans (CSPGs) and tenascin R (Kwok et al., 2011). Hyaluronan is an anionic non-sulfated GAG that provides a backbone for attachment of CSPGs that have a structural and cell adhesive role, alongside their ability to restrict nerve growth. CSPGs are overexpressed by activated astrocytes following injury and contribute to the chemically inhibitive effects of the spinal injury scar to axon growth (Silver and Miller, 2004). Tenascins are an additional glycoprotein, of which tenascin R helps form PNN structures (Burnside and Bradbury, 2014). It is exclusive to CNS ECM and produced by oligodendrocytes and some neurons to aid PNN formation (Burnside and Bradbury, 2014).

Lastly, the interstitial matrix that fills the gaps distal to blood vessels between neurons and glial cells is largely made up of the same components as PNNs, with collagen type IV and laminin also featuring (Lau et al., 2013). The major difference is the density of the matrix is much higher for PNNs and greatly reduced in the interstitial space (Lau et al., 2013).

Overall, the CNS ECM has been specialised to contain high amounts of proteoglycans and glycoproteins, which differs to other tissues that tend to contain more fibrillar collagens and fibronectin. This may contribute to the high water content of the CNS and the resulting mechanically weak matrix (Bartlett et al., 2016).

2.3 Spinal Cord Injury

SCI can be thought of as a temporal sequence of events that dramatically alters the structure of the spinal cord, and therefore its ability to function. This change in structure can be observed at the macroscale and at the microscale, involving both cells and the ECM. Following primary injury, a secondary biological response occurs, which can be subdivided into overlapping acute, subacute and chronic phases (Oyinbo, 2011).

2.3.1 Primary Injury

Primary injury to the spinal cord refers to the nature of the injury itself and can be grouped into one of four mechanisms; impact with persistent compression; impact with transient compression; distraction; and transection (Dumont et al., 2001). The majority of SCI cases are traumatic blunt contusion injuries, which fall into the impact with persistent compression category (Norenberg et al., 2004; Alizadeh et al., 2019). At the macroscale, this compression of the tissue is caused by burst fracture fragments of bone or disc dislocating and compressing the spinal cord (Alizadeh et al., 2019). At the microscale, axons and blood vessels are sheared, with the axon portion distal to the injury eventually breaking down; a process known as Wallerian degeneration (Tran et al., 2018; Bradbury and Burnside, 2019). Whilst the spinal cord can also be transected, this is a much rarer event and constitutes the minority of injuries; highlighted by 59% of a retrospective collection of explants showing no laceration or maceration at all (Norenberg et al., 2004).

2.3.2 Secondary Biological Response

After the primary injury itself, the secondary biological response to the injury begins. This is a hugely complex series of events that continuously alters over time and is influenced by injury severity. This has been well detailed elsewhere (Oyinbo, 2011; Tran et al., 2018; Bradbury and Burnside, 2019), but the following constitutes a summary of the main events.

The acute phase occurs seconds to minutes immediately following injury. At the systemic level, hypotension can occur due to vasculature rupture and breach of the blood-spinal cord barrier, as well as spinal shock – the characteristic feature of loss of function below the injury point. At the local level, necrotic cell death from direct injury occurs – and due to the rupture at both the cell and tissue levels – oedema, ischaemia, and a chaotic imbalance of ions and signalling molecules follows.

The subacute phase follows in the minutes to weeks after injury. Many of the events observed in the acute stage continue, but the subacute stage is also characterised by other events, such as the immune system-mediated inflammation in an attempt to clear cell debris; damage to lipids, proteins and nucleic acids through free radical accumulation; excitotic apoptosis of axons from influx of calcium due to the release

of the neurotransmitter glutamate; demyelination of surviving axons; and the start of astrogliosis – the process which leads to spinal injury scar formation.

The chronic phase occurs months to years after injury. Again, events such as demyelination and apoptosis continue into the chronic stage of SCI, but which is also characterised by other events, such as formation of the spinal injury scar; attempted regenerative processes, such as neuron sprouting; and extraordinary complications, such as post-traumatic syringomyelia.

Together, the acute, subacute and chronic stages of the secondary biological response represent the body's attempt, from seconds to years, to deal with the catastrophic primary injury. The fact the acute phase is limited to seconds to minutes after primary injury, and specialised care cannot be administered until hours to days, means it has been recognised this is not feasibly part of the therapeutic window (Oyinbo, 2011). As such, much attention has been paid to understanding the formation of the spinal injury scar – that begins in the subacute phase and becomes a hallmark of the chronic stage – as the injury environment to which interventions would be targeted.

2.3.2.1 Inflammation and Astrogliosis

During the acute and subacute phase of the secondary biological response, mass necrosis and apoptosis occurs (Tran et al., 2018). This causes the release of moieties that are normally only found within cells, such as ATP, histones and interleukins, as well as scattering cellular debris. These endogenous moieties, collectively termed alarmins, and further grouped as damage-associated molecular patterns (DAMPs) when included with cellular debris and other exogenous triggers, trigger the reaction of all manner of cells to the injury (Fig. 2.4A) (Bianchi, 2007; Tran et al., 2018).

A key cell group activated by these molecules are those of the immune system. Circulating monocytes that are not normally found in the CNS, but now find themselves there due to the breach of the blood-spinal cord barrier, are recruited to the injury site and adopt an increasingly pro-inflammatory 'M1' phenotype (Tran et al., 2018; Bradbury and Burnside, 2019). In this state, macrophages are activated in such a manner to attempt to deal with the injury. This is done by phagocytosing debris and upregulating factors that promote this behaviour by attracting other

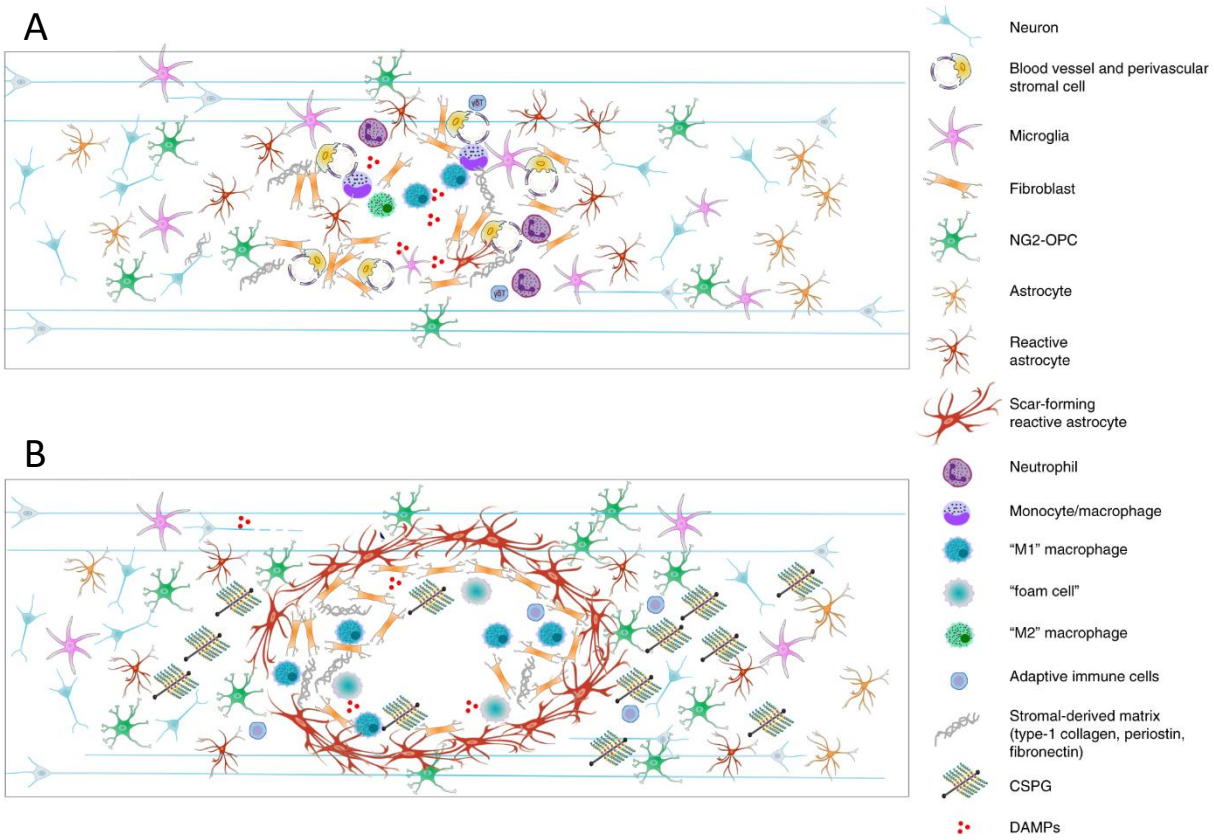

Figure 2.4 Composition of the spinal injury scar. (A) During the acute phase, cell death and damage lead to release of DAMPs. These activate invading monocytes, microglia and astrocytes. (B) During the chronic phase, the tissue is remodelled into the characteristic spinal injury scar. A glial border of reactive astrocytes, OPCs and some microglia surrounds a core of pericyte-derived fibroblasts, immune cells, and a cystic cavity of CSPGs and ECM components (reprinted from Bradbury and Burnside, 2019; reproduced by permission of Springer Nature).

immune cells to the site. Whilst this may seem useful, it leads to invasion of non-native immune cells into the CNS, which also produce reactive oxygen species normally used for killing pathogens, and adds to the increasingly toxic environment.

Further, microglia are also activated and begin to secrete three factors in particular; Il-1α, TNFα, and C1q (Liddelow et al., 2017). These factors together are believed to be responsible for the activation of astrocytes into a neurodegenerative 'A1' phenotype (Zamanian et al., 2012), beginning a process of gene expression, hypertrophy, and remodelling termed astrogliosis that partially defines the spinal injury scar (Sofroniew, 2015; Li et al., 2020).

2.3.2.2 Spinal Injury Scar

The activation of immune cells, astrocytes and other cells in the CNS begins a remodelling process with the end result being a characteristic spinal injury scar (Fig. 2.4B). Reactive astrocytes make up the majority of the spinal injury scar border, but are also joined by OPCs and microglia, which all migrate to the periphery of the injury and become the dividing line between the inflammation, fibrosis and cavitation at the injury site and the rest of the spinal cord (Tran et al., 2018; Bradbury and Burnside, 2019).

The core is mainly composed of pericyte-derived fibroblasts, immune cells and the fibronectin, collagen and laminin they are promoted to deposit (Tran et al., 2018; Bradbury and Burnside, 2019). These exist around a cystic cavity that develops at the epicentre of the injury, which is further defiled by a gradient of CSPGs that radiates from the lesion, having been deposited by astrocytes (Tran et al., 2018). It is this mixture of chemical inhibition and physical blockage that promotes axon dieback and prevents subsequent regeneration.

2.3.2.3 Axon Dormancy

Whilst CSPGs are part of the native spinal cord ECM, their upregulation and subsequent high concentration within the spinal injury scar inhibits axon regeneration and promotes dormancy (Tran et al., 2018). These axons form dynamic dystrophic endbulbs that were first observed by Ramón y Cajal (Ramón y Cajal, 1928), and stall due to receptor-mediated over-adhesion to the CSPGs (Busch et al., 2010; Filous et al., 2014; Lang et al., 2015; Tran et al., 2018).

Other molecules that are also inhibitory to neurons include the myelin-associated molecules Nogo A, myelin-associated glycoprotein (MAG) and oligodendrocyte myelin glycoprotein (OMgp) (Niederöst et al., 2002; Schwab and Strittmatter, 2014). Further, an increased sensitivity to the chemo-repellent semaphorin-3 secreted by fibroblasts is also observed, through upregulation of the neuropilin-1 receptor by neurons in response to injury (Pasterkamp et al., 1999; De Winter et al., 2002). The appearance of semaphorin-3 along with ephrin-B2 expression by astrocytes, which are associated with cell movement and tissue construction, aides scar formation (Bundesen et al., 2003).

It should be kept in mind the spinal injury scar in-part serves to isolate the injury by re-establishing the blood-spinal cord barrier to prevent further immune response and degeneration (Faulkner et al., 2004; Tran et al., 2018; Bradbury and Burnside, 2019). However, it is the loss of native structure from initial injury and subsequent reorganisation of cells and ECM to form the spinal injury scar that causes loss of function.

Further, a complex mixture of chemical signals – that are not normally present in such abundance – contaminate the spinal cord and stop normal functioning of axons and glial cells, and adversely affects any subsequent capacity for regeneration. Over time, this mass can also solidify and become a physical barrier to regeneration, which is augmented by more severe lesions that breach the meninges and feature connective tissue ingrowth (Silver and Miller, 2004).

Ultimately, the development of the spinal injury scar prevents transmission of impulses between the CNS and periphery. As such, excision of the chronic spinal injury scar (Xiao et al., 2016; Zhao et al., 2017) or delivery of a solution in the subacute phase before scar development (Theodore et al., 2016; Layer et al., 2017; Xiao et al., 2018; Chen et al., 2020; Deng et al., 2020; Kim et al., 2021) may be the only option to avoid this obstacle to regeneration.

2.4 Regenerative Medicine

A solution designed to regenerate tissue and recover tissue function sits within the field of regenerative medicine, which has been identified as one of the technologies in which the UK is set to become a global leader (BEIS, 2013). The term ‘regenerative medicine’ was popularised in the late 1990s and is attributed to the American scientist William Haseltine, who introduced many to the emerging fields of gene therapy, stem cell therapy, tissue engineering and biomechanical prosthetics, which he grouped under one phrase (Fahy, 2002). Today, regenerative medicine is defined as “the branch of medicine that develops methods to regrow, repair or replace damaged or diseased cells, organs or tissues”, and thus whilst the fields above have emerged as major areas in their own right, are still encompassed by the definition and goals of regenerative medicine (Nature, 2020). Regarding SCI specifically, whilst leading research themes for restoring or enhancing function

include wireless electrode-tissue implants (Capogrosso et al., 2016), electrical stimulation – both alone (Barra et al., 2020) and partnered with physiotherapy regimes (Kissane et al., 2019), and regenerative medicine-based strategies (Ashammakhi et al., 2019), only the latter holds promise for complete recovery of tissue function. This is especially true for severe injuries.

However, by the above definition a regenerative medicine-based strategy for SCI could take many forms and it is worth noting we are still in the early research phases of understanding which, if any, could be fruitful. As such, there is value in continued research in gene therapy-, stem cell therapy- and biomaterials-based approaches, as well as combinations of these together and with technological and rehabilitation advances, to regenerate spinal cord tissue and restore nervous function.

One idealised clinical scenario for a regenerative medicine-based approach to SCI is for a regenerative scaffold to be implanted into the spinal cord that could serve a spatial, chemical, biomechanical, and even temporal regenerative function. The regenerative scaffold could be implanted on its own to utilise local cell populations, or alongside cells and signalling molecules incorporated during production or at the point of implantation. It could also be implanted alongside other drugs for controlling or augmenting the injury or regeneration, as well as forming part of a more holistic treatment strategy. Regardless of the other elements, the scaffold itself forms an integral part of such an approach, with material choice and scaffold design capable of influencing cellular behaviour and performance. These factors can be tailored for tissue regeneration in the spinal cord.

Of note, regenerative medicine is closely associated with the term ‘tissue engineering’, which was also popularised during the 1990s as “an interdisciplinary field which applies the principles of engineering and life sciences toward the development of biological substitutes that restore, maintain, or improve tissue function” (Langer and Vacanti, 1993). A key difference is tissue engineering focuses on growth of tissue outside of the body for subsequent implantation. As the focus of the work herein was not for growth of spinal cord in the lab, but development of a scaffold that could be implanted for regeneration, the term ‘regenerative scaffold’ has been used throughout. Though, it should be noted the regenerative scaffold described herein may be utilisable as a tissue engineering scaffold for lab-grown

spinal cord, if investigated with appropriate cells and signalling molecules, which together are considered the three essential parts of the ‘tissue engineering triad’ (Bell, 2000).

2.4.1 Design of Regenerative Scaffolds

Scaffold design has two main components; material choice and scaffold structure. Whilst materials for tissue regeneration must be biomaterials, this represents a variable with lots of choice. Different materials provide different mechanical and chemical characteristics to the scaffold which can be tailored to the desired function.

The structure or form the biomaterials take is the second key component of scaffold design. Cells respond to the surrounding physical environment, and therefore the influence of structure on cell morphology and regenerating tissue should be considered, so as to recapitulate native structure. Regarding spinal cord, which has a tight link between structure and function, promoting alignment of cells and tissue is a necessity.

2.4.1.2 Biomaterials

A biomaterial is defined as “a substance that has been engineered to... direct, by control of interactions with components of living systems, the course of any therapeutic or diagnostic procedure” (Elsevier, 2020). Biomaterials must be biofunctional, biocompatible and account for structure and function of surrounding tissue for a sufficiently long period without losing their intended function (Hudecki et al., 2019).

However, beyond these base needs, the list of properties and the source materials they come from is vast. Biomaterials can be organic or synthetic, biostable or bioresorbable, bioinert or bioactive. The real benefit is in combining biomaterials as a way of introducing different characteristics and tuning properties for desired function. The work herein utilises PCL, P_{11}-8 self-assembling peptides and collagen-GMA, which are described below.

Poly(ε-caprolactone)

Poly(ε-caprolactone) (PCL) is a synthetic aliphatic polyester (Fig. 2.5) that has been widely investigated for drug delivery, wound dressing and regenerative medicine applications, including bone, cardiovascular, skin and nervous tissue (Woodruff and

Hutmacher, 2010; Suwantong, 2016; Janmohammadi and Nourbakhsh, 2019). Specifically for SCI repair, PCL has been investigated as part of aligned electrospun scaffolds (Horne et al., 2010; Daud et al., 2012; Xinghan Li et al., 2015), and more recently as part of composite nonwoven-hydrogel scaffolds for SCI repair (Hyysalo et al., 2017) and other neural tissue regenerative applications (McMurtrey, 2014; Huang et al., 2016; Shelke et al., 2016; S.J. Lee et al., 2017).

PCL has general characteristic properties that are favourable for biomedical engineering applications, such as tuneable degradation kinetics and mechanical properties, especially due to the good blend compatibility with other materials and co-polymerisation with other polymers for further tailoring (Woodruff and Hutmacher, 2010). This is further enhanced when considered alongside the favourable properties for manufacturing, including good solubility, low melting point (~60 °C) and inexpensive production routes (Woodruff and Hutmacher, 2010).

Further, PCL degradation has been characterised, with no accumulation measured *in vivo* (Pitt et al., 1981; Sun et al., 2006). The process begins with hydrolysis of the polymer chains, followed by erosion of material and phagocytic ingestion (Pitt and Schindler, 1984; Woodward et al., 1985; Woodruff and Hutmacher, 2010). As such, PCL is believed to be completely bioresorbable.

However, degradation is significantly slower than other widely used bioresorbable polymers, such as polylactic acid (PLA), poly(L-lactic acid) (PLLA) and poly(D,L-lactic-co-glycolic acid) (PLGA) (Engelberg and Kohn, 1991). This is partly due to the repeating molecular structure of five nonpolar methylene groups and a polar ester group (Fig. 2.5) that make PCL highly hydrophobic (Davison et al., 2014; Kwansa and Freeman, 2015).

As such, PCL stands out as a candidate material for long term implantable medical device applications. This is reflected in its utilisation in FDA-approved medical devices already on the market, including Osteoplug™ and Osteomesh™ bone tissue regenerative products (Osteopore, 2020), and the NEUROLAC® peripheral nerve guide conduit (Polyganics, 2020). For these reasons, it has been chosen as an ideal polymer to serve as a structural guide for promoting regeneration of spinal cord in the electrospun composite nonwoven-hydrogel scaffold herein.

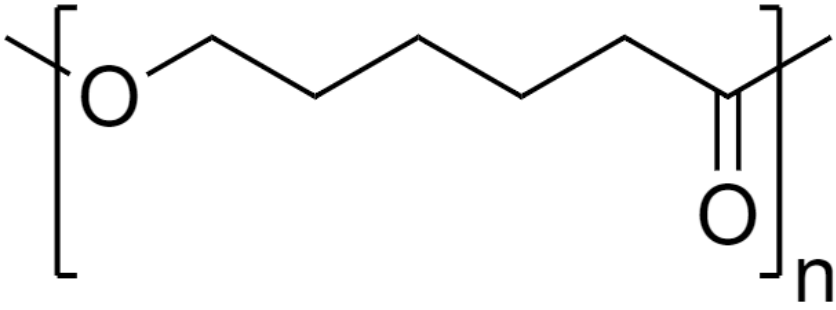

Figure 2.5 Repeating chemical structure of PCL. PCL features a polar ester group and five non polar methylene groups, giving PCL its hydrophobicity.

P_{11}-8 Self-Assembling Peptide

Recently, a polymer blend, which is defined as a combination of two or more polymers mixed at the molecular scale to obtain a single phase (Visakh et al., 2016), of PCL and the self-assembling peptide P_{11}-8 and their co-electrospinning has yielded a web with connected nanoscale and submicron networks (Gharaei et al., 2016) that was evaluated for bone tissue regeneration (Gharaei, 2017; Gharaei et al., 2020). Surface contact wettability of the resulting web could be modulated in a concentration-dependent manner and supported L929 cells.

Further, the authors showed the peptide could simply be added into the spinning solution, having considered the choice of solvent to 1,1,1,3,3,3-hexafluoro-2-propanol (HFIP) to prevent hydrogen bonding and hydrophobic interactions in solution (Aggeli et al., 1997; Gharaei et al., 2016). An even distribution of peptide was observed throughout the web and the self-assembly from monomeric form to beta-sheets was confirmed using circular dichroism and Fourier-transform infrared spectroscopy (Gharaei et al., 2016).

The inspiration for incorporating P_{11}-8 into electrospun fibre webs was to utilise their biophysical ECM mimicry, but overcome the poor mechanical strength, difficulty handling and difficulty fixating such materials for tissue regenerative applications. Up until their incorporation into electrospun nonwovens, P_{11}-*X* peptides had been exclusively evaluated as hydrogel-forming materials (Aggeli et al., 1997; Aggeli et al., 2001; Aggeli et al., 2003; Davies et al., 2006; Carrick et al., 2007; Maude et al., 2011).

Criteria for the rational design of the P_{11}-*X* beta-sheet forming *de novo* 11 amino acid peptides was deduced more than 20 years ago and shown to produce hydrogels that respond to chemical and physical triggers (Aggeli et al., 1997; Aggeli et al., 2003; Carrick et al., 2007). Of the P_{11}-*X* peptides, P_{11}-8 has the amino acid sequence CH_3CO-glutamine-glutamine-arginine-phenylalinine-ornithine-tryptophan-ornithine-phenylalinine-glutamate-glutamine-glutamine-NH_2 (QQRFOWOFEQQ) (Fig. 2.6) (Carrick et al., 2007; Maude et al., 2011) and is able to self-assemble due to the exposure of the charged sidechains of arginine (R), ornithine (O) and glutamate (E) on one side of the peptide, and non-polar aromatic phenylalanine (F) and tryptophan (W) on the opposite face (Maude et al., 2011).

The self-assembly mechanism is driven by a change in free energy; monomers in isolation have low free energy and must convert to a higher energy rod-like state to self-assemble (Aggeli et al., 2001). This trigger can be concentration, temperature or ionic strength of the solution and initiates formation of more complex structures; from beta-tapes to ribbons to fibrils to fibres (Aggeli et al., 2001; Carrick et al., 2007). The helical hierarchical self-assembly of peptides was believed to influence fibre morphology at much higher scales following electrospinning, with twisting of submicron fibres observed as well (Gharaei et al., 2016).

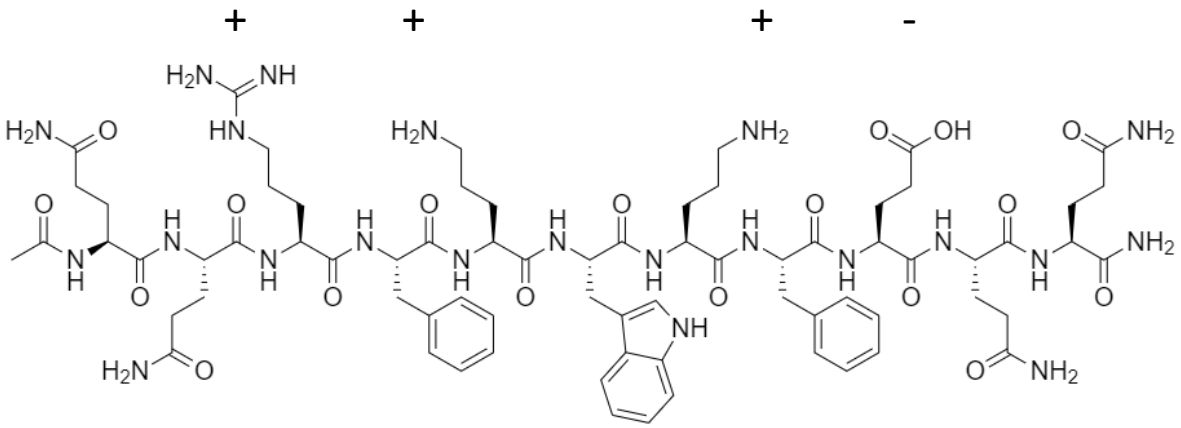

Figure 2.6 Chemical structure of P_{11}-8. P_{11}-8 has the amino acid sequence CH_3CO-glutamine-glutamine-arginine-phenylalinine-ornithine-tryptophan-ornithine-phenylalinine-glutamate-glutamine-glutamine-NH_2 (QQRFOWOFEQQ).The SAP is able to self-assemble due to the position of the charged sidechains of arginine (R), ornithine (O) and glutamate (E) on one side, and non-polar aromatic phenylalanine (F) and tryptophan (W) on the opposite side.

Owing to the unique bimodal distribution of fibre diameters produced from PCL/P_{11}-8 electrospinning, the web physically mimics structures found in the ECM, such as collagen fibrils and fibres (Kadler et al., 1996). Spread across two orders of magnitude, the fibre diameters also mimic the physical hierarchy seen in the ECM of all tissues, such as breast (Fabris et al., 2018), lung (Jorba et al., 2017), cardiovascular (Graham et al., 2010), and spinal cord (Guo et al., 2010; Xing et al., 2019).

Of note, P_{11}-8 was chosen alongside another P_{11}-*X* peptide, P_{11}-4, for incorporation into electrospun fibre webs for hard tissue repair owing to their previous evaluation as a hydrogel for hard tissue regeneration (Burke, 2011). However, only P_{11}-4 appeared to augment mineral nucleation and actively promote bone regeneration in a rabbit calvaria model, with P_{11}-8 performing similar to controls (Burke, 2011). Whilst some hydroxyapatite crystal growth was observed for PCL/P_{11}-8 electrospun fibre webs after 4 weeks *in vitro*, this was incomparable to the growth observed on PCL/P_{11}-4 fibre webs (Gharaei, 2017; Gharaei et al., 2020). This is somewhat reinforced by a more recent study showing the promotion of bone tissue regeneration by P_{11}-4 hydrogel in a rat calvaria model, although P_{11}-8 was not investigated alongside (Saha et al., 2019).

As such, this indicated P_{11}-8 lacked a propensity for mineralised tissue regeneration and, on top of the indication P_{11}-8 promoted nanoscale network formation better than P_{11}-4 (Gharaei, 2017; Gharaei et al., 2020), could be a strong candidate for investigating electrospun PCL/P_{11}-*X* nonwovens for soft tissue applications.

Taken together, incorporating P_{11}-8 into electrospun fibre webs successfully transferred their utility as biomimicking molecules to materials with more clinical practicality. However, for spinal cord tissue regeneration alignment of fibres in the electrospun webs is required to promote aligned cell growth and tissue regeneration similar to native spinal cord tissue, and the ability to align PCL/P_{11}-8 is not yet known.

Collagen-GMA

Collagen is a natural polymer that is the most abundant protein in the body (Tortora and Derrickson, 2014). As such, its use as a biomaterial for spinal cord tissue regeneration is of interest.

The basic structure of the collagen molecule is preserved across all types of collagen and consists of a right-handed triple helix of three left-handed polypeptide chains (Ricard-Blum, 2011; Sorushanova et al., 2019). The polypeptide chains vary in their composition, which are also combined in different configurations to give the twenty-nine known types of collagens, but are made up of the repeating amino acid units Gly-*X*-*Y*, where Gly refers to glycine, and X and Y are frequently proline and 4-hydroxyproline, but can be other amino acids (Ricard-Blum, 2011; Sorushanova et al., 2019).

Collagen type-I is specifically made up of two identical α1(I)-chains and one α2(I)-chain which bundle together to form higher order collagen structures, such as fibrils, fibres and fascicles (Ricard-Blum, 2011). This self-aggregation into fibrils is called fibrillogenesis and is stabilised by covalent crosslinks between collagen chains, giving collagen its structural and mechanical properties (Ricard-Blum, 2011; Sorushanova et al., 2019).

However, when collagen is extracted from natural sources for use as a biomaterial, these crosslinks are broken down and with it the stabilisation between chains (Sorushanova et al., 2019). These cannot simply be recapitulated *in vitro* during and following fibrillogenesis, and therefore exogenous means of crosslinking processed collagen have been developed (Sorushanova et al., 2019).

Recently, collagen type I has been functionalised with vinyl-bearing moieties through a nucleophilic substitution or nucleophilic addition reaction, owing to the availability of the amine group in the lysine side chain (Fig. 2.7) (Tronci et al., 2013; Tronci et al., 2015; Tronci, Yin, et al., 2016; Tronci, Grant, et al., 2016; Liang et al., 2018a; Liang et al., 2018b). These vinyl moieties react with each other in the presence of a

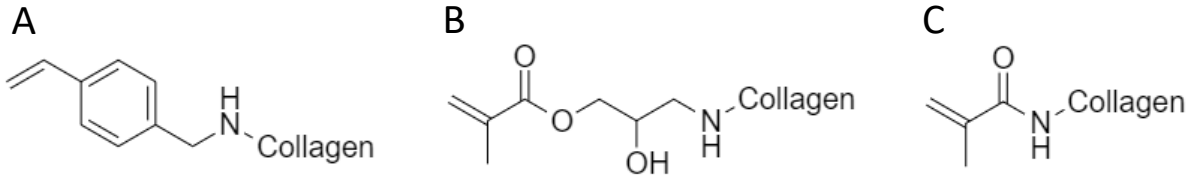

Figure 2.7 Collagen functionalised with the vinyl-bearing moieties. (A) 4-vinyl benzyl chloride (4VBC), (B) glycidyl methacrylate (GMA), and (C) methacrylic anhydride (MA).

photoinitiator under UV light to form covalent crosslinks at the molecular level that translates into a hydrogel at the macroscale. Control of the crosslinking using this system is possible at multiple levels; such as the type of linker moiety, the number of moieties attached and the number of crosslinks these form, as well as the amount of functionalised collagen in the hydrogel (Tronci et al., 2013). This indicates the system has wide optionality for tailoring mechanical properties, but this has not been fully investigated yet.

For the purposes of spinal cord tissue regeneration, low modulus hydrogels that are favoured by neural cells were desired, as covered in Chapter 2.6.2. As some mechanical characterisation of this system had taken place already, this indicated glycidyl methacrylate (GMA) may be an appropriate linker moiety of choice to achieve low modulus hydrogels (Tronci et al., 2013; Tronci et al., 2015; Tronci, Grant, et al., 2016; Liang et al., 2018b), with the other factors affecting hydrogel stiffness to be optimised as part of the work herein.

Further, a dual-phase hydrogel consisting of collagen-GMA and hyaluronic acid functionalised with methacrylic anhydride has been more recently investigated for bone tissue regeneration (Zhang et al., 2019). Whilst a storage modulus value of around 350 Pa was recorded and three-dimensional cell encapsulation of bone marrow-derived mesenchymal stem cells was displayed, no control sample of collagen-GMA hydrogel on its own was included. As such, the utility of a single-phase collagen-hydrogel for tissue regeneration and its characterisation remained unexplored.

2.4.1.1 Scaffold Structure

The structure of the scaffold is also an important consideration, as cells, deposited ECM and the regenerating tissue can be influenced by the surrounding structures. There are general principles for scaffold structuring that apply to most tissue regenerative applications and more specific ones that should form part of a design strategy for spinal cord tissue regeneration.

From a regenerative standpoint, the scaffold should allow for three-dimensional cell culture as this promotes native cell morphology; spatio-temporal interactions with other cells, materials and moieties; as well as promote similar internal responses to these stresses that would be observed *in vivo* (Jensen and Teng, 2020). Further, the

scaffold should allow cell binding and ECM deposition; be porous to allow for nutrient transport and waste removal, but likewise connected to allow for cell migration; and space-fill at the macroscale (Kárová et al., 2020).

Regarding scaffold-mediated spinal cord repair specifically, the scaffold should support recapitulation of the native tissue structure in three-dimensions. For spinal cord white matter, this is highly aligned tracts of neuronal axons, supporting neuroglia and ECM components that are destroyed following SCI (Chandar and Freeman, 2014; Haggerty et al., 2017; Bradbury and Burnside, 2019). This also applies to propriospinal interneurons of the grey matter that connect different spinal segments (Zavvarian et al., 2020).

The combination of electrospun nonwovens and hydrogels into biocomposite structures has gained traction as a tissue regenerative solution that together meets many of the above requirements over hydrogels and electrospun fibres in respective isolation (Shapiro and Oyen, 2013). The following section gives an overview of electrospinning aligned fibre nonwovens, with the subsequent section covering electrospun, hydrogel and composite nonwoven-hydrogel scaffolds for spinal cord tissue regeneration.

2.4.2 Electrospinning

Electrospinning is a well-established method for producing structures that meet many of the requirements for general regenerative medicine applications and can be further optimised for spinal cord tissue regeneration. Electrospinning is a solution-based fibre production technique that was invented more than a century ago (Boys, 1887; Cooley, 1899; Morton, 1900), whereby polymer is dissolved in a solvent and voltage applied, in contrast to melt-based spinning where polymer is simply melted and extruded (Russell, 2006).

However, it is only in the last 25 years, that its ability to produce fibres in the nanometre to micrometre scale has begun to be exploited, partly owing to advances and increased accessibility to electron microscopes (Xue et al., 2019). Today, wide-ranging applications include environmental filtration; catalysis, energy and electrical systems; and diverse biomedical applications, including regenerative medicine (Haider et al., 2015; Xue et al., 2019).

2.4.2.1 Principles of Electrospinning

The basic electrospinning setup includes a high voltage power supply, syringe pump, syringe with a blunt-tip conductive needle and a conductive collector (Haider et al., 2015; Xue et al., 2019). The power supply is connected to the conductive needle and positioned opposite the collector, which is grounded (Fig. 2.8). Upon electrification of the conductive needle, charge is transferred to the polymer solution being pumped from the syringe, which accumulates until it overcomes surface tension forming a characteristic cone at the needle tip and expelling a jet of charge solution towards the grounded collector. The cone is referred to as a Taylor cone after extensive characterisation by Gregory Taylor in the 1960s (Taylor, 1964; Taylor, 1966; Taylor, 1969).

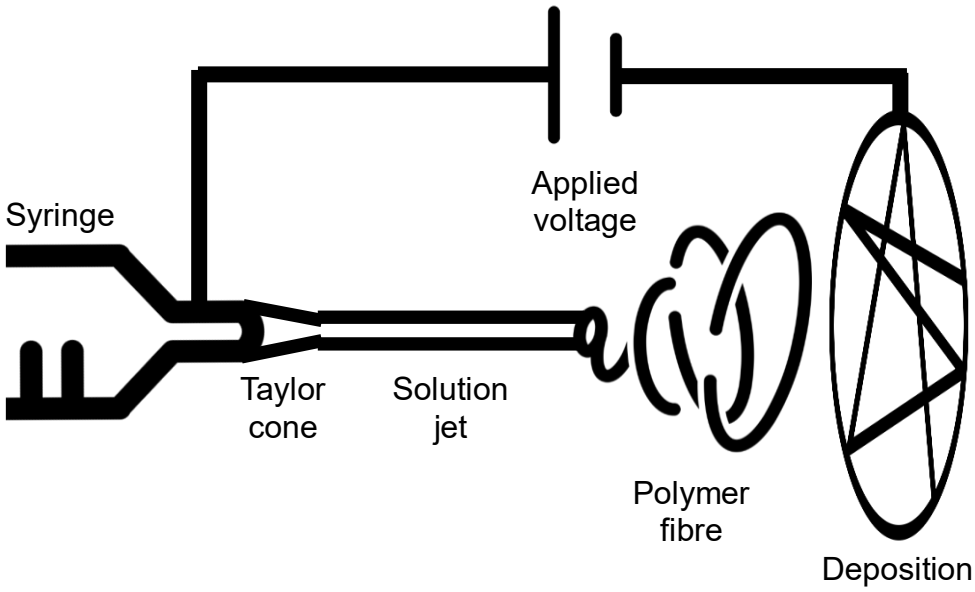

Figure 2.8 Diagram of the electrospinning process. To electrospin, a polymer solution was loaded into a syringe with a metal needle and ejected towards a metal collector, with a voltage applied between the needle and collector. As the jet of polymer solution is expelled from the needle, with a characteristic cone observed at the needle tip (known as a Taylor cone), solvent evaporation sees the jet of polymer solution form a dry polymer fibre. As the fibre forms and begins to whip through the air, charge held in the jet of solution is transferred to the surface of the dry fibre, which further promotes whipping due to charge repulsion, and thus further promotes solvent evaporation. The charged fibre is neutralised upon deposition on the grounded collector, forming a random web of mechanically entangled fibres (nonwoven).

During mid-air, evaporation of the solvent promotes solidification of the jet into dry fibres composed of intertwined polymer chains, with charge transferred from the solution to the surface of the fibre. This promotes whipping of the fibre from irregular charge distribution known as bending instabilities, which further promotes evaporation and thinning of the fibres, before deposition and charge dissipation on the grounded collector. Owing to the whipping motion, stationary collectors with flat surfaces produce randomly oriented, mechanically intertwined fibres (nonwoven). A detailed description of these steps has been compiled by Xue et al. (2019).

Of note, needleless electrospinning setups do exist. These include those fitted with annular (ring-shaped) spinnerets (Wei et al., 2019); rotating cylinder electrodes immersed in baths of polymer solution (Jirsak et al., 2009); and wire electrodes continuously fed with polymer solution (Sabantina et al., 2018), the latter two having been commercialised by Elmarco s.r.o. (Liberec, Czech Republic) (Elmarco, 2021).

However, as needle systems still dominate the research literature; are utilised in commercial manufacturing settings, such as those at The Electrospinning Company, UK (The Electrospinning Company, 2021); and the fact needleless systems have not been broadly utilised for producing aligned fibre webs, they have not been focused on herein. For a recent review of needleless electrospinning for biomedical applications, see Partheniadis et al., (2020).

2.4.2.2 Parameters of Electrospinning

There are many factors that affect the electrospinning process. These are referred to as parameters, which can be classified as electrospinning, solution or environmental (Haider et al., 2015).

Electrospinning

Applied Voltage

The voltage must be high enough to reach the critical voltage necessary to overcome surface tension and instigate electrospinning (Haider et al., 2015). Further increases in applied voltage affect fibre diameter in a system-dependent manner, with examples of increasing fibre diameter, decreasing fibre diameter, and no effect observed (Li and Wang, 2013). However, if voltage is too high the solution will be atomised.

Needle-to-Collector Distance

The collector must be sufficiently close that the expelling jet-fibre can interact with the collector surface or collector electric field (Haider et al., 2015). Too close and the solvent will not have sufficient time to evaporate from the whipping fibre, but too far away and beaded fibres can be formed (Li and Wang, 2013). Within this range, moving the collector further away can decrease fibre diameter, owing to increased whipping (Haider et al., 2015).

Flow Rate

Flow rate must be high enough to feed the expelled jet at the needle tip with fresh solution otherwise continuous fibre production is not achieved (Haider et al., 2015). Increasing flow rate can increase fibre diameter, but can also result in bead formation or dripping at the needle tip, owing to replacement of solution too quickly before it has been electrically expelled (Li and Wang, 2013; Haider et al., 2015).

Solution

Solvent

Solvent must be able to fully dissolve the polymer of choice and evaporate fast enough to promote fibre formation from the polymer jet during spinning (Haider et al., 2015). If the solvent is not volatile enough, fibre formation may not occur, but too high and the solvent will evaporate too quickly, leading to solidification of bulk polymer (Haider et al., 2015). Different solvents can also contribute different surface tensions, with reducing surface tension promoting bead-free fibre formation (Li and Wang, 2013).

Viscosity

Viscosity is mainly affected by polymer concentration or molecular weight (Li and Wang, 2013). Polymer concentration must be high enough that entanglement of the chains can take place to result in continuous fibres (Li and Wang, 2013; Haider et al., 2015). Above this critical value, increasing concentration can lead to beaded fibres, before forming uniform bead-free fibres (Li and Wang, 2013). Further increases generally lead to an increase in fibre diameter, as more polymer is available, but can result in helix-shaped micro-ribbons forming (Li and Wang, 2013). However, too high and the solution becomes too viscous or dries too quickly (Haider et al., 2015). Similar to concentration, polymer molecular weight must be high enough so that

chains can entangle and form fibres, but too high and helical micro-ribbons can be seen (Li and Wang, 2013).

Conductivity

Conductivity must be high enough to allow charge to increase above a critical threshold and overcome surface tension (Haider et al., 2015). Increasing conductivity usually decreases fibre diameter as higher charge promotes fibre whipping, which can be done through addition of ionic salts into the spinning solution (Li and Wang, 2013; Haider et al., 2015). However, too high and the ability to form a stable Taylor cone can be impeded, along with subsequent spinning of continuous fibres (Haider et al., 2015).

Environmental

Humidity

Humidity can affect solvent evaporation and therefore fibre formation and fibre diameter. However, both increases in fibre diameter (Li and Wang, 2013) and decreases in fibre diameter (Haider et al., 2015) have been reported when humidity has been increased, and thus the effects are likely system-dependent.

Temperature

On the other hand, elevated temperature tends to decrease fibre diameter by promoting evaporation of solvent (Haider et al., 2015) and decreasing the viscosity of the polymer solution (Li and Wang, 2013; Haider et al., 2015).

Whilst all of the above parameters can affect the diameter of fibres in the resulting web, many of the parameters are tuned towards an optimum to produce smooth, uniform, bead-free fibres first. Following this, individual parameters can be altered to observe changes in fibre characteristics. Of note, polymer concentration in solution is usually the parameter altered in practice to significantly modulate fibre diameter. Further, individual setups usually require optimisation independent of one another owing to inherent differences in apparatus, material source and the shape of generated electric fields. Further still, it should be noted this is not an exhaustive list of electrospinning parameters, with effects on spinnability and fibre morphology also altering further with polymer choice and collector type.

2.4.2.3 Aligned Electrospun Fibre Webs

Whilst all of the above electrospinning parameters affect spinnability and fibre morphology to some degree, they do not affect the alignment of fibres. When deposited on a stationary collector with a flat surface, electrospun fibres mechanically entangle and form a randomly orientated web. However, aligned electrospun fibre webs are required for SCI repair. In order to form aligned electrospun fibres, there are three main research strategies; mechanical force, electric field manipulation and hybrid systems.

Mechanical Force

Electrospinning on to a rotating collector can mechanically align fibres. Drums (also referred to as shafts in the literature) (Li et al., 2007; Wee-Eong Teo, 2014), belts (Wee-Eong Teo, 2014), discs (Krishnamoorthy et al., 2011), bowls (Tomaszewski et al., 2012) and an inverse setup using rotating needles (referred to as centrifugal electrospinning, electrocentrifugal spinning and centrifugal force spinning in the literature) (Dabirian et al., 2011) have all been attempted. The most common methods are drums and discs. Both are generally easy to set up, incur a reasonable cost and tend to produce thicker webs than other techniques (Wee-Eong Teo, 2013).

The alignment produced by discs is generally better, but as deposition only occurs on the edge of the disc, drums are able to produce much larger webs (Wee-Eong Teo, 2013). Improved alignment with drums is possible with high rotation speeds (Li et al., 2007), but this can increase set up costs and time as stricter safety controls may be necessary. High speeds can also create turbulence that blows fibres away from the collector, but this can be limited using windshields (Krishnamoorthy et al., 2011).

Electric Field Manipulation

Creating an air gap between two grounded collectors can also align fibres as well. Fibres bridge the gap between them due to the spatiotemporal change in charge as the fibre is deposited (Canejo and Godinho, 2013). Distances from a few hundred microns (Li et al., 2003) to 0.5 m (Beachley and Wen, 2009) have been recorded using this method. It is widely used and popular due to its cheap and easy setup and high alignment (Wee-Eong Teo, 2013). It is ideal for producing thinner webs (Wee-Eong Teo, 2013), but can suffer from undesirable spacing between fibres as charge

is retained on the fibre following deposition, repelling incoming fibres (Liu and Dzenis, 2008). Modified setups using an inclined gap have reportedly shown higher alignment due to spatiotemporal changes in the electric field, but still produce a limited monolayer of material (Park and Yang, 2010; Park et al., 2011).

Hybrid Systems

In an attempt to combine the benefits of both methods, hybrid systems involving mechanical alignment and electrodes to control the electric field have emerged. Alignment is generally better than drum setups, on a par with disc setups, but not as good as electrodes (Wee-Eong Teo, 2013).

Combining different aspects of methods can also combine problems as well as benefits, with turbulence from drums and discs moving at high velocity and unwanted deposition on exposed metal surfaces being common. Designs to simultaneously deflect turbulence and mask charged areas have been created with some success (Nguyen et al., 2016).

However, there is contradictory evidence to whether rotation speed has little effect on alignment in these setups (Afifi et al., 2009) or does affect them (Nguyen et al., 2016) and they are anecdotally harder to setup. This correlates with higher setup costs, whilst size and thickness of webs is difficult to predict as it varies between designs (Wee-Eong Teo, 2013). Increased efforts to refine this combination are needed to fully realise the benefits and reduce the challenges.

With any of the above systems, finding the most appropriate solution, processing and ambient parameters to obtain the desired fibre morphology is a key part of refining the experimental process. Whilst all the above methods would be applicable for spinal cord tissue regeneration in terms of producing highly aligned fibre webs, mechanical force is able to produce dense fibre webs quickly and with no further setup requirements compared to electrode or hybrid systems. This makes them the most obvious solution for manufacture of PCL/P_{11}-8 fibre webs with the potential for production scalability, and thus have been used herein.

2.5 Scaffold-Mediated Spinal Cord Repair

2.5.1 Electrospun Nonwoven Scaffolds

Electrospun nonwovens have been used to promote aligned cell morphology and extension of neurites for the purpose of spinal cord tissue regeneration for over a decade. These publications have used different materials for producing electrospun scaffolds, with different physical web features; different biological models for evaluating performance, some with *in vitro* and *in vivo* results; and in some cases, included growth factors, drugs and other materials to augment various features of SCI or regeneration. Despite this variation, there are similarities in results that could be taken as basic requirements and potential necessities for future electrospun scaffold design.

2.5.1.1 Fibre Alignment

The overriding trend is that alignment of fibres can and should be utilised to promote aligned cell and tissue morphology and direct migration. This has been observed for synthetic materials (Chow et al., 2007; Corey et al., 2007; Horne et al., 2010; Hurtado et al., 2011; Weightman, Pickard, et al., 2014; Zuidema et al., 2014; Zamani et al., 2014; Xinghan Li et al., 2015; Zuidema et al., 2015; Kabiri et al., 2015; Colello et al., 2016; Xia et al., 2016; Roman et al., 2016; Johnson et al., 2018; Xia and Xia, 2018; Gottipati et al., 2020), natural materials (T. Liu et al., 2012; Fan et al., 2013; Menezes et al., 2019), and combinations of both (Xiaoran Li et al., 2016).

Further, alignment has also been observed over a range of fibre diameters, from 200-400 nm (T. Liu et al., 2012; Fan et al., 2013), 400-600 nm (Corey et al., 2007; Horne et al., 2010; Weightman, Pickard, et al., 2014; Kabiri et al., 2015; Xia et al., 2016; Xia and Xia, 2018), 600-800 nm (Zamani et al., 2014), 800-1000 nm (Menezes et al., 2019), 1-2 µm (Hurtado et al., 2011; Xinghan Li et al., 2015; Roman et al., 2016; Gottipati et al., 2020), 2-3 µm (Chow et al., 2007; Zuidema et al., 2014; Johnson et al., 2018), and larger than 3 µm (Zuidema et al., 2015; Colello et al., 2016; Xiaoran Li et al., 2016).

Further still, alignment has also been observed using a range of biological models, such as cell lines (Corey et al., 2007; Gottipati et al., 2020), primary animal cells (Chow et al., 2007; Corey et al., 2007; Horne et al., 2010; Hurtado et al., 2011; T. Liu

et al., 2012; Fan et al., 2013; Zuidema et al., 2014; Zuidema et al., 2015; Kabiri et al., 2015; Colello et al., 2016; Xia et al., 2016; Roman et al., 2016; Johnson et al., 2018; Xia and Xia, 2018; Menezes et al., 2019; Gottipati et al., 2020), primary human cells (Xinghan Li et al., 2015), *in vitro* animal organotypic tissue slice models (Weightman, Pickard, et al., 2014) and *in vivo* animal models (Hurtado et al., 2011; W. Liu et al., 2012; Zamani et al., 2014; Xinghan Li et al., 2015; Colello et al., 2016).

Taken together, aligned electrospun nonwovens – irrespective of the fibre material, the fibre diameter from the submicron to the micron, and the biological model – have promoted aligned cell morphologies, directed cell process outgrowth and guided migration in a direct manner.

2.5.1.2 Fibre Diameter

Whilst alignment of cells and tissue has been observed irrespective of fibre diameter, some studies have suggested fibre diameter can be optimised to promote neurite extension. Yang et al. (2005) investigated the response of neural stem cell (NSCs) grown on aligned PLLA fibres, and after 2 days neurite outgrowth on 300 nm fibres was 100 µm, versus 78 µm on 1500 nm diameter fibres. Further, DRG neurites seeded on to PLLA with 290, 760 and 1330 nm diameter fibres promoted neurite extension 1000, 1500 and 1400 µm after 5 days (Wang et al., 2010). In both these cases a preference for submicron fibres was observed for neurite extension.

Further still, even when all fibre diameters are submicron, there appears to be a preferential size. Whilst aligned PLLA fibres of 300, 500, 700 and 900 nm diameter all promoted aligned morphologies and neurite extension for neonatal mouse cerebellum C17.2 stem cells, it was the 500 nm fibres that appeared to promote neurite outgrowth furthest and induce the strongest differentiation (He et al., 2010).

A similar result has been observed with silk fibroin. Subventricular zone rat neurons grown on aligned silk fibroin fibres of 400, 800 and 1200 nm diameter had primary dendrite lengths of 28 µm, 25 µm and 24 µm after 6 days, respectively, indicating a submicron preference (Qu et al., 2013). Again, when both fibre diameters are submicron a preference is also observed. Human embryonic stem cells cultured on aligned silk fibroin fibres of 400 and 800 nm diameter had average neurite length at 7 days of 495 µm versus 249 µm, respectively (Wang et al., 2012).

However, it should be noted that this may be cell-type dependent. Daud et al. (2012) showed rat DRG had a preference for smaller diameter fibres, with neurite extension of 2.5, 2.2 and 1.6 mm after 10 days on PCL fibres of 1, 5 and 8 µm diameter, respectively, but NG108-15 neuronal cells preferred larger fibres, with neurite outgrowth 62, 94, and 142 µm after 4 days, respectively. Of note, this altered again when NG108-15 neuronal cells were co-cultured with Schwann cells, with neurite outgrowth of 120, 140 and 134 µm, respectively. Whilst none of the fibres investigated had submicron diameters, this does illustrate how cells can respond differently and that more complex biological environments may need to be evaluated distinctly as well.

Further, some studies have presented contrary results to those above. Yao et al. (2009) observed PC12 cells on PCLEEP fibres of 800, 3700, 5900 and 8800 nm diameters extending neurites 160, 187, 192 and 175 µm, respectively. A statistically significant result was observed for 3700 and 5900 nm diameter fibres over the randomly orientated control and was deemed preferential over the submicron diameter fibre web. However, it should be noted the random control achieved neurite extension of over 150 µm itself and thus was not much different to the aligned fibre matrices. It should also be noted the 800 nm fibres had a standard deviation of 700 nm, indicating fibre diameters for this group had a broad spread, which questions the accuracy of the conclusions. Of note, the standard deviations for the other groups did not exceed 16%, versus the 88% for this group.

Further still, Binder et al. (2013) seeded ND7/23 neuron-like cells on PLGA fibres of 750 and 5750 nm diameters, with neurite outgrowth of around 100 versus 150 µm, respectively, and stronger alignment observed for the larger diameter fibres. However, it should be noted fibres were sparse monolayers, in some cases with cells not in contact with any fibres, which likely skewed results. Further, in terms of migration, whilst larger fibres appeared to perform better after 1 and 4 days, by 7 days no difference was observed. A similar result was seen for the speed of migration, where submicron fibres appeared preferential after 1 and 4 days, but diminished after 7 days.

As such, based on the above, there is an indication that submicron fibres may preferentially promote and direct neural regeneration over larger diameter fibres *in*

vitro to date. Further, within the submicron diameter range, there is an indication that a window around 300-750 nm diameter may be optimal. However, as discussed above, this may be cell-type dependent and subject to change in more complex multicellular environments.

Despite this optimisation, the thin sheets or sparse monolayers created by electrospinning do not adequately form three-dimensional matrices into the macroscale capable of space-filling and recapitulating tissue defects. This remains a caveat of electrospun nonwoven scaffolds on their own.

2.5.2 Hydrogel Scaffolds

In contrast, hydrogels have been used as three-dimensional cell culture environments and space-filling scaffolds. Further, characteristics that allow stiffness to be varied have elucidated preferential environments for promoting cell survival and behaviour, including those for cells of the spinal cord and other cell types with clinical potential for SCI.

2.5.2.1 Shear Modulus

Balgude et al. (2001) encapsulated chick DRG cells in agarose gel at varying weight percent to control the stiffness of the hydrogel. Gel stiffness negatively correlated with elongation rate of chick DRG neurites, with the hydrogels of 4 Pa shear modulus performing better than any stiffer hydrogels. Yu and Bellamkonda (2001) also encapsulated chick DRG in an agarose layer, with a layer above consisting of a different concentration. They observed that around 75% of neurites crossed the interface for hydrogels with a shear modulus of 13, 70 and 130 Pa, but dropped to 50% for 200 Pa hydrogels.

Banerjee et al. (2009) encapsulated adult rat neural stem cells (NSCs) in alginate hydrogels at varying $CaCl_2$ concentration, to control cross-linking, or weight percent and observed that cell number and β-tubulin III expression negatively correlated with hydrogel modulus. Cell number was highest for 200 Pa shear modulus hydrogels, and decreased for 1000, 2000 and 20,000 Pa hydrogels.

Stabenfeldt and LaPlaca (2011) encapsulated E18 rat cortical neurons in methylcellulose-laminin hydrogels at varying weight percent, and observed neurite

extension for cells in 565 Pa shear modulus hydrogels, but not for 174 or 53 Pa hydrogels.

Whilst Brännvall et al. (2007) did not investigate hydrogels at differing shear modulus values, collagen type I-hyaluronan hydrogels of 250 Pa supported growth and differentiation of neural stem/progenitor cells (NS/PCs).

Together, these results indicate that hydrogels with a shear modulus of a few hundred Pascals are supportive of three-dimensional neural cell culture, irrespective of hydrogel material. Whilst it is less clear if lower modulus hydrogels below 200 Pa are more supportive, with evidence for (Balgude et al., 2001; Yu and Bellamkonda, 2001) and against (Stabenfeldt and LaPlaca, 2011) – which may be partially cell-type dependent – evidence that higher shear modulus hydrogels are inhibitory is stronger (Balgude et al., 2001; Banerjee et al., 2009).

Of note, whilst Hynes et al. (2009) encapsulated mouse NSCs in PEG-PLL hydrogel at varying macromer weight and PEG:PLL ratio, the group only looked at hydrogels between 3,500 and 20,000 Pa shear modulus and only characterised migration on the surface despite cells growing into hydrogels. Whilst hydrogels of 3,500-5,500 Pa shear modulus appeared to promote migration and differentiation better than higher modulus hydrogels, the evaluation as a three-dimensional cell culture environment was limited, and it is not clear if even better results would have been seen with lower modulus gels.

Similarly, whilst Kuntz Willits and Skornia (2004) encapsulated E9 chick DRG in rat tail collagen type-I hydrogel at varying concentration, a range of only 2-17 Pa shear modulus values was investigated. Whilst the data suggested there was some neurite outgrowth benefit to the lower modulus hydrogels, the small stiffness range made comparison difficult, and indicated that cell-material interactions are an important influence that need consideration.

Further, Sundararaghavan et al. (2009) encapsulated E8 chick DRG in collagen crosslinked with varying concentration of genipin, to observe the effect of stiffness gradient on neurite extension. Again, whilst considerable differences in modulus values were not used, with 160-432 Pa shear storage modulus values all supporting growth, there is an indication for neurite extension down stiffness gradients rather than up.

2.5.2.2 Compressive Modulus

Comparing compressive modulus values is more difficult, as when hydrogels are compressed they usually display a J-shaped stress-strain curve. Unless the specific region in which the modulus value has been determined is published, it is inaccurate to compare compressive modulus values, but general trends can still be observed.

Seidlits et al. (2010) encapsulated mouse ventral midbrain NPCs and neonatal astrocytes in methacrylated hyaluronic acid hydrogels. NPCs expressed higher levels of β-tubulin III and extended processes further and branched more in 3 kPa modulus hydrogels versus 4 or 5 kPa modulus hydrogels. Further, glial fibrillary acidic protein (GFAP) expression increased and an astrocytic morphology was observed for NPCs in 5 kPa hydrogels. Astrocytes also appeared more spread in 5 kPa hydrogels, but notably produced lower levels of GFAP.

Lampe et al. (2010) encapsulated rat embryo neurons and neural precursor cells in PEG hydrogels, altering stiffness by macromer weight. Metabolic activity negatively correlated with modulus, whilst apoptotic activity positively correlated. Whilst the lowest modulus hydrogel investigated was around 3.8 kPa, proliferation, GFAP expression, glial-scar associated protein expression, and process length were all low. However, this may have been due to the small pore size of the material, being only 5-15 nm, as reasoned by the authors.

Man et al. (2011) encapsulated mouse neonatal DRG in fibrin hydrogels, at various concentrations of fibrinogen and thrombin to control stiffness. The lowest stiffness hydrogels investigated – 2.5 kPa compressive modulus – promoted neurite outgrowth the furthest, which negatively correlated with stiffness. However, similar to Lampe et al. (2010), they note the effect of pore size cannot be ignored, which reduces with increased fibrin concentration and may be partially responsible for the results observed.

Lampe et al. (2013) also encapsulated chick DRG in crosslinked elastin-like protein hydrogels. Hydrogels of 500 Pa compressive modulus promoted neurite outgrowth more favourably that 1500 or 2000 Pa hydrogels.

In summary, hydrogels provide hydrated, three-dimensional environments for cell culture and tissue regeneration. The work above illustrates how the stiffness of this surrounding environment can affect cell viability and function, with some similarities

and differences depending on cell type. Overall, it appears a hydrogel with weak mechanical properties benefits neural cells in general. However, the ideal hydrogel system would have the ability to alter the stiffness to fine tune this environment for specific cell types. Despite this beneficial environment, the homogeneity and lack of directional cues within hydrogels prevents them being fully suited on their own for guiding aligned axon growth and regenerating anisotropic spinal cord tissue.

2.5.3 Composite Nonwoven-Hydrogel Scaffolds

To address the shortcomings of electrospun nonwoven scaffolds and hydrogel scaffolds individually, composite nonwoven-hydrogel scaffolds have emerged as a scaffold design strategy for SCI repair. The following summarises the literature and groups them by distinguishing scaffold features, such as layering of successive nonwoven and hydrogel; mixing long fibres within the hydrogel; cutting fibres short and dispersing them throughout the hydrogel; using a single material for both the nonwoven and the hydrogel; and any other forms that fall outside of these groupings.

2.5.3.1 Layered Composite Structures

A number of publications have combined nonwoven and hydrogel for SCI repair by layering one on top of the other. Wang et al. (2018) utilised a shape memory polymer, poly(D,L-lactic acid-co-trimethylene carbonate), coated in a thin layer of hydrogel composed of gelatin, poly(ethylene glycol) diacrylate (PEGDA) and acrylated β-cyclodextrin (β-CD) to recapitulate alignment of fibres post-injection through a catheter. The shape memory functionality is triggered in response to body temperature.

The aligned scaffold promoted aligned neurite extension from motor neurons *in vitro*. When investigated in a mouse model of SCI, composite nonwoven-hydrogel scaffolds in general, whether containing randomly orientated or aligned fibres, appeared to reduce scarring and oedema at the injury site and integrated better with the native tissue versus hydrogel-only and cell-only controls. However, augmentation in terms of cell density, differentiation and aligned tissue integration was observed with the aligned scaffold only. It was also noted reduced inflammation at the site may have been due to the hindered migration of inflammatory cells into the scaffold. Overall, this translated to improved *in vivo* functional recovery, as speed of hind limb

and Basso-Mouse Scale (BMS) scores were higher for aligned scaffolds at 7, 14 and 28 days post implantation.

Hyysalo et al. (2017) also took a layered approach to combining nonwoven and hydrogel for SCI repair, mainly to interrogate the spatial effects of fibre alignment. PuraMatrix™ SAP-based hydrogel was cast on top of PCL fibres coated with laminin. When human embryonic stem cell (hESC)-derived neurons were cultured less than 10 µm from fibres, either on top of the hydrogel or encapsulated within, processes aligned in the direction of underlying fibres, which was not seen further away. Of note, neurons and astrocytes appeared to require laminin coating on PCL fibres for improved viability and migration, which was not required in the same way for OPCs, and possibly indicates the differing requirements from the ECM for cell types.

Similarly, Weightman, Jenkins, et al. (2014) also combined a sparse monolayer with hydrogel for SCI repair, using aligned electrospun poly-L,D-lactic acid and collagen hydrogel. A multi-layer scaffold was produced by alternating between aligned fibre layers and hydrogel layers. Astrocytes were shown to elongate along fibres in single culture, but OPCs remained spherical and appeared dead. However, when OPCs were added to pre-elongated astrocytes, cell survival improved and differentiation into myelin-producing oligodendrocytes was observed. Further, when a sequential seeding-stacking method was used and layers were aligned perpendicular to each other, multiple layers of perpendicular cell alignment were produced.

Y.S. Lee et al. (2017) investigated an electrospun piezoelectric polyvinylidene fluoride-trifluoroethylene (PVDF-TrFE) fibre web rolled into a conduit and filled with Schwann cell (SC)-laden Matrigel for SCI repair. SCs aligned along aligned Matrigel-coated and uncoated fibres *in vitro*, but with higher ATP levels recorded for Matrigel-coated samples. When a 5 mm long conduit was wrapped around a rat T8 2.5 mm complete transection model, transplanted SCs appeared aligned at the rostral stump, caudal stump, and in the centre for aligned conduits versus no obvious alignment for random samples, with higher cell number also visible in the aligned group after 3 weeks. Venule and arteriole blood vessels were observed in the centre of both random and aligned groups after 3 weeks, but the number and length of SC and neuronal processes was greater for aligned scaffolds than random. The same group

has also more recently shown Matrigel promotes SC proliferation, aligned myelination and DRG neurite outgrowth *in vitro*, with Matrigel and SC inclusion appearing to have a synergistic effect on neurite extension when DRG was co-cultured with SCs (Wu et al., 2018).

Ahi et al. (2020) created a bilayered scaffold for spinal cord injury repair, by directly electrospinning aligned collagen-PLGA-laminin fibres on to collagen hydrogel, incorporated with the growth factor NT-3 and enzyme chondroitinase ABC (ChABC). DRG neurons extended neurites in the direction of fibres in the fibre layer, with the collagen-only layer showing no alignment irrespective of collagen to PLGA content. ASCs showed similar behaviour but a collagen to PLGA ratio of 70:30 appeared to improve proliferation. Of note, by altering the ratio of PLGA to collagen in the nonwoven, mechanical properties could be augmented, with Young's modulus increasing up to 20-fold in wet conditions between 50:50 and 80:20 for collagen to PLGA ratios, respectively. Further, NT-3 augmented DRG outgrowth and ASC cell density. Whilst ChABC was also added into the hydrogel, its presence and activity was not confirmed, but could likely act as a useful biomolecule following implantation to breakdown the overexpressed CSPG environment following SCI.

Whilst not specifically for SCI, layering has also been investigated for neural tissue regeneration in general. McMurtrey (2014) combined a sparse monolayer of electrospun PCL, PCL-gelatin and laminin-coated PCL surrounded by a cell-laden hyaluronic acid (HA) hydrogel. SH-SY5Y cells, a human neuroblastoma cell line, were observed extending neurites along fibres with angle distribution tightest in composite nonwoven-hydrogel scaffold versus fibre-only, and laminin coating augmented the degree of contact between cells and fibres and the length of neurites. Interestingly, when the HA hydrogel was replaced with Engelbreth-Holm-Swarm (EHS) extracellular matrix, which is rich in cell attachment points, the improved alignment was inhibited. This possibly indicates the competing features within a combined scaffold and that a relatively inert hydrogel with more bioactive fibres may provide a better environment for controlling neurite length and promoting extension.

Similarly, layering has also been investigated specifically for peripheral nerve regeneration. Shelke et al. (2016) formed a thin coating of hydrogel over nonwoven, using aligned electrospun PCL and alginate hydrogel. The composite led to

increased mechanical properties, including suture pull-out, over PCL alone, and improved cell attachment, proliferation and neural marker expression of iPSCs and hMSCs. Of note, low molecular weight sodium alginate appeared to augment cell properties over high molecular weight sodium alginate, and was possibly down to the more uniform matrix coating.

Further still, the benefits of layering have been investigated for cancer treatment as well. Huang et al. (2016) looked at composite nonwoven-hydrogel scaffolds for treating glioma; a type of cancer tumour that starts in the glial cells of the CNS and, whilst rare, can itself cause non-traumatic spinal cord injury (New et al., 2014). To do so, a multi-layered scaffold was produced consisting of random nerve growth factor (NGF)-coated PCL, alginate hydrogel and random PCL containing temozolomide (TMZ). TMZ is an oral chemotherapeutic medicine for glioma, but has low efficacy due to low local bioavailability caused by the blood-CNS barrier and drug resistance from prolonged use. As such, it was reasoned a scaffold introducing TMZ locally would be efficacious whilst avoiding systemic side-effects. A fairly linear release of TMZ was observed over 30 days and affected C6 proliferation, whilst PC12 neurite extension was promoted by the NGF-PCL layer when tested on its own. However, the combined scaffold was not tested on PC12 cells owing to the cytotoxicity of TMZ, but does indicate a scaffold with inhibitory and promotional factors could be viable if release was controlled temporally.

2.5.3.2 Mixed Long Fibre-Hydrogel Scaffolds

In contrast to layering, where the nonwoven fibres and hydrogel appear in differing planes, long fibres have been mixed with hydrogel, or placed into the centre of a conduit and filled with hydrogel, to try and recapitulate the shape of the spinal cord and the aligned white matter tracts.

Baklaushev et al. (2019) recently implanted a composite nonwoven-hydrogel scaffold into the spinal cord of *Rhesus macaque* monkeys. The scaffold was made up of a nonwoven of aligned PCL and recombinant analogues of spider dragline silk proteins, and a hydrogel of platelet-rich plasma (PRP), implanted with directly reprogrammed Neural Precursor Cells (drNPCs). The addition of the PRP-based hydrogel promoted neuronal differentiation, as indicated by long βIII-tubulin and Microtubule Associated Protein 2 (MAP2) processes oriented in the direction of fibre

alignment. After 12 weeks, following insertion of the scaffold at T8, limited immune response and scarring was observed and the scaffold appeared integrated with the tissue. ECM and cells surrounding the scaffold appeared of normal structure and density, and drNPCS survived transplantation and differentiated down a neuronal pathway. In some rare cases, dual staining of h-Mito and β-III tubulin indicated some of the transplanted cells even differentiated into neurons and migrated into the spinal cord from the scaffold.

Milbreta et al. (2016) produced a composite nonwoven-hydrogel scaffold of electrospun poly(ε-caprolactone-co-ethyl ethylene phosphate) (PCLEEP) placed in the core of a cylindrical mould and surrounded by collagen hydrogel. Scaffolds 1 mm in length were implanted into a hemi-section rat model. Whilst similar astrocytic, microglial and macrophage reactions were observed for all experimental groups, indicating the scaffold had limited effect on modulating neuroinflammation and scarring, cell penetration was improved and cavity formation reduced compared to hydrogel-only and injury-only controls. Further, neurite length, laminin alignment and early blood vessel formation appeared to align with the direction of fibre alignment in the scaffold, and functional recovery was improved for the aligned scaffold versus other groups, and augmented by inclusion of the growth factor neurotrophin-3.

The same group also investigated the PCLEEP-collagen composite nonwoven-hydrogel scaffold as a non-viral delivery vehicle for proteins and nucleic acid therapeutics for enhanced regeneration following SCI, on top of the aligned contact guidance fibre cues (Nguyen et al., 2017). NT-3 was incorporated into the hydrogel to promote neuronal cell survival and neurite outgrowth, as well as OPC proliferation and differentiation. The microRNA miR-222 was also incorporated into both the fibres and hydrogel by complexing with polymer-based micellar nanoparticles and added during electrospinning and hydrogel production. MiRNA-222 expression usually drops after SCI, but is utilised in normal and injured axons for local protein synthesis and has been shown to enhance regrowth of injured neurons *in vitro*. Following implantation into a rat C5 hemisection model, NF+ neurofilaments were observed throughout the scaffold after 1 and 2 weeks, with MAG+ remyelination also observed after 4 weeks. MiR-222 appeared to promote neurofilament regeneration, whilst microglia (Ox-42) and astrocyte (GFAP) activation were comparable to controls. Of note, a burst release of NT-3 from the hydrogel was observed *in vitro*,

with around 88% released within 1 day and reaching around 98% by 60 days, whilst miRNA release was around 25% after 25 days and 30% after 90 days.

The same group has recently investigated the PCLEEP-collagen composite nonwoven-hydrogel scaffold as a non-viral delivery mechanism for promoting re-myelination following SCI (Milbreta et al., 2019). MicroRNA-219 (miR-219) and microRNA-338 (miR-338), which promote OPC differentiation into oligodendrocytes were added into the hydrogel along with NT-3. OPCs seeded on to the scaffold differentiated into myelin-producing oligodendrocytes and ensheathed surrounding fibres regardless of miRNA inclusion, though the extent was augmented by their presence. However, miRNA appeared to have a greater long-term effect *in vivo* when inserted into a rat hemisection model, with the number of oligodendroglial cells in general, as measured by Olig2, greater at 2 and 4 weeks versus scaffolds without miRNA. Further, the number of mature oligodendrocytes, as measured by the marker CC-1, increased in the miRNA group whilst the number of OPCs, as measured by PDGFRa, reduced. Further still, the higher expression of MBP and 2',3'-Cyclic-nucleotide 3'-phosphodiesterase (CNPase) measured in the miRNA group compared to the group without indicated enhanced myelination of regenerating fibres within the scaffold, with tubular structures surrounding axons at 4 weeks. Of note, release kinetics of both miRNA and NT-3 was similar, with around 70% released in the first 20 hours, and around 80% released after 70 hours.

The same group has more recently investigated the PCLEEP-collagen composite nonwoven-hydrogel scaffold for the effects of fibre density on cell growth (Cnops et al., 2020). By altering the spinning time, a high and low density fibre bundle was produced, with an average gap between bundles of 0.6 and 0.8 µm, respectively. The scaffolds were placed into a rat T9-10 2 mm complete transection model for 2 weeks. Axonal ingrowth as measured by staining of NF appeared to be around 2.5 fold higher for the higher density fibre scaffolds, but the number of blood vessels appeared to reduce. Although it should be noted that neither of these results was significant. Whilst also not significant, slightly reduced cavitation and fibrotic scarring was noted in the higher density group, but a reduction in scarring was significant rostral to the injury site. The authors stated the findings surprising as they would expect larger gaps to allow improved ingrowth. Whilst the results indicate greater contact of fibrous scaffold components with spinal cord tissue may promote

regeneration, and at least indicate fibre density is not a significant feature when fibres are at the minimum density created here, it may have been that the difference between the two scaffolds was not great enough to observe significant differences.

Johnson et al. (2019) used superparamagnetic iron oxide nanoparticles (SPIONs) incorporated in to PLLA to produce aligned electrospun fibres that could be incorporated into a hydrogel and realigned in situ using an external magnetic field. Fibres were 3-5 mm in length and mixed with collagen or fibrin hydrogel. Magnetisation, the speed of realignment and the speed with respect to viscosity of the environment could be modulated through SPION concentration. Primary rat neurons extended neurites in the direction of fibre alignment on fibre-only samples, which was also observed for neurites extending from DRG when fibres were incorporated into collagen and fibrin hydrogels. Further, SPION incorporation appeared to promote neurite length. Of note, fibres were coated in laminin to promote cell adherence, and Matrigel added into hydrogel solutions for cell survival and attachment due to its laminin, fibronectin and additional factors.

Whilst not specifically for SCI, Vashisth et al. (2020) produced an electrospun aligned poly(vinyl alcohol) (PVA)-gellan-gelatin web, rolled up and soaked in gellan-gelatin hydrogel for neural tissue regeneration. SH-SY5Y cells aligned in the direction of fibre alignment versus a round morphology in the hydrogel-only group. Of note, degradation *in vitro* showed almost 90% of scaffold mass was lost within 4 weeks in a linear manner. Quercetin was also incorporated into the fibres as a model drug and shown to release in a characteristic curve, with almost 70% released within 24 hours and 95% within 180 hours. Compression of the scaffold indicated the composite nonwoven-hydrogel had augmented mechanical properties over the hydrogel on its own, with maximum stress increasing 2.5-fold to 2.21 MPa from 0.88 MPa, whilst maximum strain was largely unaffected, to 67% from 64%, respectively.

Further, Quigley et al. (2013) used melt-extruded fibres as part of a composite nonwoven-hydrogel scaffold for peripheral nerve repair. A core of aligned melt-extruded PLGA fibres was placed into a knitted tube of the same material and filled with alginate hydrogel. Of note, the fibres had a diameter of 30 microns, around one to two orders of magnitude larger than typical electrospun fibres. However, neurites still extended from DRG in the direction of fibre alignment and Schwann cells were

also able to migrate along the fibres. Further, when placed into a rat sciatic nerve model, myelinated axons were observed growing into the conduit in the direction of the distal stump, with some reduction in animal distress recorded, possibly due to reduced pain from regeneration.

Further still, Lee et al. (2016) manufactured a composite nonwoven-hydrogel for CNS applications following stroke. Core-shell PCL-polystyrene fibres were created and then polystyrene selectively leached to produce a sponge-like, voluminous nonwoven instead of a sheet-like, flat web. Long fibres were then mixed with methacrylated hyaluronic acid hydrogel. The combined composite nonwoven-hydrogel appeared to be injectable along a catheter, whilst the hydrogel-only and nonwoven-only controls were not. In fact, despite the fibres being randomly orientated, fibres aligned with the direction of shear flow through the catheter. When seeded with human neural stem cells (hNSCs) and injected in a rat stroke model, NSCs remained viable after 4 weeks and prevented early migration of microglia in the acute stages of a stroke.

2.5.3.3 Mixed Short Fibre-Hydrogel Scaffolds

In contrast, short-cut fibres have also been mixed with hydrogel to form composite nonwoven-hydrogel scaffolds for SCI repair. Omidinia-Anarkoli et al. (2017) utilised SPIONs in electrospun aligned PLGA to align fibres post-injection. Fibres 60 µm in length were mixed with the hydrogel in low volume and then exposed to an electric field to align before hydrogel curing. Aligned fibres promoted aligned growth of fibroblasts and aligned extension of neurites from DRG, versus random growth from composite nonwoven-hydrogels with random fibres and hydrogel-only controls. Alignment also augmented neurite length compared with non-aligned experimental groups, and propagation of calcium signals from neurons was observed along neurites in the direction of fibre alignment.

Of note, whilst not a composite nonwoven-hydrogel scaffold, the same group has also incorporated SPIONs into a photo-curable PEG-based hydrogel fabricated into short rod-like “microgels”, themselves dispersed in a weaker fibrin hydrogel for alignment post-injection for SCI repair (Rose et al., 2017). Hydrogel rods could be made as small as 1 × 1 × 10 μm^3 using soft lithography, with chick DRG and individual neurons extending neurites in the direction of fibre alignment, which could

be modulated with the amount of aligned microgels. Recent optimisation of parameters indicated longer, thinner microgels of just a few microns in diameter promote neurite length, neurite alignment and aligned fibrin ECM deposition from chick DRG over larger diameter and shorter (less than 50 μm) microgels (Rose et al., 2020).

Similarly, another composite nonwoven-hydrogel composition for SCI repair using fibres dispersed in a hydrogel was created by Hsieh et al. (2010), using genipin-crosslinked collagen or poly(3-caprolactone-co-D,L-lactide) (P(CL:DLLA) in a hyaluronan-methylcellulose (HAMC) hydrogel. Whilst fibre alignment was not addressed, and although details such as fibre length, method of cutting and method of combination were not included, composite nonwoven-hydrogels retained individual benefits of nonwoven and hydrogel, such as promoting process formation and neurosphere distribution of neural stem progenitor cells, respectively. Interestingly, the minimal swelling of this particular hydrogel was noted as a potential benefit for avoiding pressure build-up in the cavity following implantation.

Whilst not specifically for SCI repair, Bruggeman et al. (2017) also introduced short cut fibres into a hydrogel, but as a slow-release drug delivery system for promoting neural regeneration rather than a mechanism for alignment. Fibres of PLA 100-2000 nm in length were dispersed into a SAP hydrogel of fluorenylmethyloxycarbonyl (Fmoc)-capped aspartic acid-isoleucine-lysine-valine-alanine-valine (DIKVAV). Glial cell line-derived neurotrophic factor (GDNF) showed a burst release over 12 hours when mixed into the hydrogel alone and a similar release over 24 hours from electrospun fibres when mixed with PLA during electrospinning.

However, when the hydrogel and fibres were combined, with GDNF in both the hydrogel and PLA fibres dispersed within, a burst release was observed over 12 hours followed by a second peak at 7 days with a stable plateau of 10-20% release sustained over 3-4 days. This promoted metabolic activity in mouse cortical neurons *in vitro*. This was attributed to the growth factor having to diffuse first into the hydrogel and then out, acting as a reservoir. This release profile was beneficial for viability of primary cortical mouse neurons.

Of note, an earlier paper by the same group showed a similar GDNF-releasing composite nonwoven-hydrogel scaffold with short cut fibres for treating Parkinson’s

disease (Wang et al., 2016), this time using PLLA fibres dispersed in a xyloglucan-Poly-D-Lysine (PDL) hydrogel, but with GDNF immobilised on the surface of polymer fibres. Implantation into the brain of a mouse Parkinson's model showed greatest improvement in cell viability and area re-innervated when using hydrogel containing GDNF and GDNF-immobilised fibres, over hydrogel containing GDNF without fibres and hydrogel without GDNF but containing GDNF-immobilised fibres. From this work, there is an indication it may be possible to create a temporal delivery schedule spanning minutes to months depending on whether growth factor is in hydrogel, mixed in the polymer or immobilised on the fibre surface.

2.5.3.4 Homogeneous Single Polymer Fibrous Hydrogel Scaffolds

A number of publications have also investigated fibrous hydrogels for SCI repair, utilising both the fibre and hydrogel properties from a single material rather than combining separate nonwoven and hydrogel materials.

Recently, Chen et al. (2019) electrospun photo-crosslinked methacrylated gelatin (GelMA) or pure gelatin to produce aligned nanofibrous composite nonwoven-hydrogel scaffolds of a single material. *In vitro* evaluation showed bone mesenchymal stem cells were viable and aligned in the direction of fibre alignment on both materials, as well as promoting neurite extension of hippocampal neuronal cells. However, cells were able to infiltrate deeper into the GelMA scaffold, possibly due to the weaker mechanical properties. Following implantation into a rat T9 3 mm hemisection model, Tuj-1 and nestin staining was observed for both materials, but augmented for GelMA, with significantly greater BBB score for the GelMA group at 12 weeks. Further, implantation of gelatin and GelMA scaffolds appeared to reduce astrocytic reactivity, as measured by GFAP and CSPG, and promote vascularisation, as measured by CD31 and synaptophysin. However, in all cases, GelMA performed better than gelatin.

Miller et al. (2018) used interfacial polyelectrolyte complexation (IPC) to produce a scaffold of chitosan fibres surrounded by chitosan hydrogel for SCI repair. IPC uses solutions of oppositely charged ions to form fibres at the interface which are then drawn. Whilst the chitosan scaffold on its own had aligned fibres encased in a hydrogel, and this promoted alignment of neurites from rat cortical neurons, the scaffold was also placed over aligned electrospun PLLA fibres. This layering also

influenced neurite extension, especially when the underlying electrospun fibres were perpendicular to the aligned chitosan hydrogel bundle, promoting extension in different directions depending on the focal plane.

Yao et al. (2016) also focused on a single material that formed aligned fibres as well as the hydrogel for SCI repair, by electrospinning fibrin. By using fibrin as the base material, manufacturing fibres using electrospinning and then coiling and bundling together produced a scaffold with alignment from the nanoscale to the macroscale. The scaffold promoted alignment and neural differentiation of human umbilical mesenchymal stem cells (hUMSCs) in the absence of growth factors and aligned extension of neurites from DRG *in vitro*. Aligned ECM and neural tissue regeneration was further observed *in vivo* in a rat hemi-section model. Of note, the same author also combined the scaffold with drug-encapsulated microspheres, and showed cell elongation behaviour of hUMSCs was not hindered, whilst microspheres were held by fibre layers and drug elution profile was augmented versus microspheres on their own (Yao et al., 2017).

The same author also added a second hydrogel component to the electrospun fibrin composite nonwoven-hydrogel scaffold, by wrapping it up into a semi-cylindrical bundle and then dip-coating the dorsal portion in alginate hydrogel (Yao et al., 2018). This was to selectively prevent connective tissue ingrowth following implantation into a rat hemi-section model, owing to the poor cell adhesion properties of alginate. Whilst further comment on the effectiveness of alginate for preventing fibrous tissue ingrowth was not given, improved cell infiltration, vascularisation, and aligned tissue regeneration was observed with the aligned scaffold at early time points, versus the scaffold with random fibres. As regeneration progressed, higher neuron-specific markers, aligned neuron growth and length was also observed for the aligned scaffold. In later time points, higher myelination density and anisotropy of regenerated tissue was observed for the aligned scaffold, along with improved functional recovery.

More recently, the same author has also evaluated the same aligned electrospun fibrin composite nonwoven-hydrogel scaffold seeded with mesenchymal stem cells (MSCs) for SCI repair (Yao et al., 2020). The scaffold was implanted in a 4 mm rat T9 complete transection model versus cell-only and injury-only controls. MSCs

aligned in the direction of fibre alignment *in vitro*, which was also observed in the lesion site *in vivo* after 1 week. Regardless of scaffold implantation, cells appeared to survive in the SCI environment, but the scaffold promoted neural regeneration, as measured by β-tubulin expression. Nerve fibre density after 8 weeks, as measured by NF200 expression for nerve fibres and Growth Associated Protein 43 (GAP-43) for growth cone, was augmented by the presence of MSCs over the injury-only control, augmented further by the presence of a scaffold instead, and augmented further still when MSCs were transplanted with the scaffold. Regeneration was observed all the way through the scaffold, though it should be noted some cavitation was observed in all groups. Extensive serotonergic nerve fibres were also observed in the cell-scaffold group. Functional and electrophysiological recovery was observed, with cell-only and scaffold-only groups performing similarly and better than the injury-only control, but the cell-scaffold group performing best after 12 weeks.

Further, the same group also investigated the aligned fibrin composite nonwoven-hydrogel for peripheral nerve repair, encasing it in a hollow chitosan tube (Du et al., 2017). The scaffold appeared to expedite ingrowth and bridging of a gap defect in a rat model. However, the autograft gold-standard control performed better in terms of degree of muscle atrophy, motor function amplitude and, at the tissue level, myelination thickness. Despite this, the aligned fibrin scaffold was comparable at the functional level in degree of morbidity, gait analysis and motor function latency, and at the tissue level in nerve fibre thickness and innervating muscle fibre features. The authors believe this was potentially due to providing the early stages of regeneration artificially as a design feature, as fibrin cables would occur spontaneously at the injury site to direct migration and proliferation of Schwann cells and axonal regrowth naturally.

2.5.3.5 Other Composite Fibre-Hydrogel Scaffolds

Other methods for combining nonwoven and hydrogel distinct from those above have also been investigated and the findings from which are worth noting herein.

Lee et al. (2017) combined nonwoven and hydrogel using 3D printing for neural tissue regeneration, electrospinning PCL and PCL-gelatin before printing polyethylene (glycol) (PEG) and polyethylene (glycol) diacrylate (PEG-DA) in a grid-like pattern onto the sheets of aligned nonwoven. In doing so, some areas of the

scaffold were fibre-only, creating micro-wells surrounded by walls of printed hydrogel. Improved cell adhesion was observed with NSCs on composite nonwoven-hydrogel scaffolds versus hydrogel-only, but reduced differentiation marker Tuj-1 expression was also observed. The authors reasoned this was possibly due to the influence of fibres on cell growth, indicating that alignment may not actually be beneficial for neural stem cells. In contrast, primary neurons showed aligned growth on aligned scaffolds and appeared to grow into the hydrogel from seeding on to the fibres, but it was unclear how deep hydrogel penetration was and whether cells grew underneath instead. Of note, the inclusion of gelatin into the nonwoven reduced contact angle and led to increased neurite length versus PCL alone.

Stankus et al. (2006) looked at combining nonwoven and hydrogel for a more general tissue regenerative approach, rather than spinal cord specific, by concurrent electrospinning of elastomeric poly(ester urethane)urea (PEUU) and electrospraying of smooth muscle cell-laden bovine gelatin hydrogel. Cell viability did not appear diminished through electrospraying of cells, remaining above 95%, and aligned in the direction of fibre alignment. However, for thicker scaffolds of 300-500 µm, cell migration into scaffolds and subsequent proliferation was greatly improved using a transmural perfusion bioreactor as opposed to static culture.

2.6 Summary

In summary, spinal cord tissue is anisotropic at both the macroscale and microscale, which supports its primary function of information transmission between the CNS and periphery. During SCI, this structure is lost from both the impact of initial injury, but also the secondary biological response to the injury. This remains a chemically inhibitory environment and prevents native SCI repair.

However, implantation of regenerative scaffolds represents an emerging, potential treatment for tissue regeneration and functional recovery. The research literature reports multiple ways of combining nonwoven and hydrogel materials for this purpose, and similar results can be achieved regardless of method, as follows.

Aligned neurite extension and elongated cell morphologies were observed *in vitro* as long as aligned fibres were present in the scaffold; when layering in composite

structures (Weightman, Jenkins, et al., 2014; McMurtrey, 2014; Shelke et al., 2016; Hyysalo et al., 2017; Wang et al., 2018); when including long fibres and mixing with the hydrogel (Quigley et al., 2013); when cutting fibres short and aligning throughout the hydrogel (Omidinia-Anarkoli et al., 2017); when using an aligned single material as both the nonwoven and hydrogel component (Yao et al., 2016; Yao et al., 2017; Du et al., 2017; Miller et al., 2018); when 3D printing hydrogel onto aligned fibres (S.J. Lee et al., 2017); and concurrently electrospinning and electrospraying on to a rotating collector (Stankus et al., 2006).

Whilst only a few of these approaches have been experimentally investigated as scaffolds *in vivo*, fibre alignment within the scaffold appears necessary to recapitulate alignment of regenerated tissue (Quigley et al., 2013; Milbreta et al., 2016; Yao et al., 2016; Du et al., 2017; Yao et al., 2018; Wang et al., 2018) and this appears to translate into improved functional recovery as well (Quigley et al., 2013; Yao et al., 2018; Wang et al., 2018). As such, some degree of alignment is likely necessary for SCI repair.

Further, there is some evidence to suggest the presence of a composite nonwoven-hydrogel scaffold can reduce inflammation and formation of the spinal injury scar, compared with hydrogel-only, cell-only and injury-only controls (Milbreta et al., 2016; S. Lee et al., 2016; Wang et al., 2018), and this is actually regardless of whether fibres are aligned or not. As such, the pairing of fibres and hydrogel appears to space-fill the cavity in a way that reduces the body's perception of the injury, or at least does not appear to augment the inflammatory response.

Together, these findings indicate aligned composite nonwoven-hydrogel scaffolds are potentially superior in terms of promoting regeneration versus electrospun nonwovens or hydrogels on their own, and provides clear rational for the pairing of aligned electrospun PCL/P_{11}-8 nonwoven and collagen-GMA hydrogel intended herein. Further, the preferential fibre diameter and alignment characteristics of electrospun nonwovens investigated for spinal cord and neural tissue regeneration outlined in Chapter 2.5.1 will inform the production of the nonwoven herein. Similarly, the mechanical properties of three-dimensional hydrogels investigated in isolation for spinal cord and neural tissue regeneration outlined in Chapter 2.5.2 will inform the production of the hydrogel.

Chapter 3

Materials and Methods

This chapter reports the chemicals, consumables and equipment used to conduct the experimental research study presented herein, as well as experimental setups, methodologies and characterisation techniques used throughout.

3.1 Materials and Equipment

The equipment listed below relates to the electrospinning rigs for manufacturing fibrous scaffolds, and for the preparation, testing and analysis of polymer materials before and after processing.

3.1.1 Equipment

Table 3.1 Equipment used herein, including supplier information.

Equipment and model	**Supplier**
Blunt needle, 18 gauge	Kaisertech, UK
Power supply, Constant Voltage Current	Glassman High Voltage, USA
Syringe pump, Model 200 Series	KD Scientific, USA
Rotating drum collector, custom-built (300 (w) × 200 (⌀) mm)	The Electrospinning Company, UK
Phenom Desktop SEM	Lambda Photometrics, UK
Digital Tachometer, DT-2234C+	HDE, UK
Scanning Electron Microscope (SEM), SU8230	Hitachi, JP
Sputter coater, Agar Auto Sputter Coater	Agar Scientific, USA
Image analysis software, ImageJ	NIH, USA
Dionex HPLC with a P680 pump, ASI-100 Automated Sample Injector, PDA-100 Photodiode Array Detector (deuterium lamp) and C18 column	Thermo Fisher Scientific, USA
Mass spectrometer, Xevo QTof G2-XS coupled to an Acquity M-Class UPLC	Waters, USA
Freeze dryer, Alpha 1-2 Ldplus	Martin Christ, DE
Confocal Laser Scanning Microscope, SP8	Leica, DE
Uniaxial tensile testing machine, ElectroPuls E3000	Instron, USA

Table 3.1 Continued from previous page.

Equipment and model	Supplier
Digital micrometre	Mitutoyo, JP
Contact angle goniometer, FTA 4000	First Ten Angstroms, UK
Ultracentrifuge, Avanti J26XP	Beckman Coulter, USA
UV lamp and viewing cabinet, Spectroline E-Series	Spectroline, USA
Modular Compact Rotational Rheometer, MCR302	Anton Paar, AU
ElectroForce® 3200 Mechanical Test Instrument	Bose, USA
FB1800 Laser Cutting and Engraving Machine	CadCam Technology, UK
Minusheet® tissue carrier	Minucells, DE
Jenway 6300 Spectrophotometer	Cole-Parmer, UK
HI-2210-02 pH meter	Hanna Instruments, UK

3.1.2 Chemicals

The chemicals listed below relates to those required to form the fibrous scaffolds, as well as those required for their preparation, testing and analysis before and after processing.

Table 3.2 Chemicals and reagents used herein, including supplier information.

Chemicals and reagents	Supplier
Poly(ε-caprolactone) (PCL); 80,000 Mw	Sigma Aldrich, UK
1,1,1,3,3,3-hexafluoro-2-propanol (HFIP); purity≥ 99.0%	Sigma Aldrich, UK
P_{11}-8 (CH_3CO-Gln-Gln-Arg-Phe-Orn-Trp-Orn-Phe-Glu-Gln-Gln-NH_2); SAP content 75%, HPLC purity of 96%	C.S. Bio Co., USA
Acetonitrile, HPLC-grade	Sigma Aldrich, UK
Water, HPLC-grade	Sigma Aldrich, UK
Poly-D-lysine (PDL)	Sigma Aldrich, UK
RPMI 1640	Lonza, UK
Horse serum, heat-deactivated	Sigma Aldrich, UK
Foetal bovine serum (FBS)	Sigma Aldrich, UK
L-Glutamine, 200 mM	Sigma Aldrich, UK
Penicillin-streptomycin, 5000 U ml^{-1}	Sigma Aldrich, UK
Recombinant Human β-NGF	Bio-Legend, USA
Neutral buffered formalin, 10%	Sigma Aldrich, UK
DAPI (4,6-diamidino-2-phenylindole)	Sigma Aldrich, UK
Triton X-100	Sigma Aldrich, UK
Phosphate buffered saline (PBS)	Sigma Aldrich, UK
Glacial acetic acid (CH_3COOH)	Sigma Aldrich, UK
Sodium hydroxide (NaOH)	Sigma Aldrich, UK
Glycidyl methacrylate	Sigma Aldrich, UK

Table 3.2 Continued from previous page.

Chemicals and reagents	Supplier
Triethylamine	Sigma Aldrich, UK
Tween-20	Sigma Aldrich, UK
Ethanol	Sigma Aldrich, UK
2-Hydroxy-1-[4-(2-hydroxyethoxy)phenyl]-2-methylpropan-1-one (I2959)	Fluorochem, UK
Sodium hydrogen carbonate ($NaHCO_3$)	Sigma Aldrich, UK
2,4,6-trinitrobenzene sulfonic acid (TNBS)	Sigma Aldrich, UK
Hydrochloric acid (HCl), 6N	Sigma Aldrich, UK
Diethyl ether	Fisher Scientific, USA
Dimethyl sulfoxide (DMSO)	Fisher Scientific, USA
Dulbecco's modified Eagle's medium (DMEM), High Glucose	Lonza, UK
Distilled water	Distilled in-house
Rat tail collagen type-I	Extracted in-house

3.1.3 Consumables

The consumables listed below relates to those required to manufacture fibrous scaffolds, as well as prepare them for testing and analysis.

Table 3.3 Consumables used herein, including supplier information.

Consumables	Supplier
Syringe, 10 ml	Sigma Aldrich, UK
Circular punches, diameter 5-25 mm	ToolZone, UK
Steri-Strip™	3M, USA
Silicone sheet, 200 (l) x 200 (w) x 1.5 (h) mm	Camthorne Ind. Supplies, UK
Glass slides	Fisher Scientific, UK
LIVE/DEAD™ Viability/Cytotoxicity Kit	Invitrogen, USA
Mouse-on-Mouse (M.O.M.) Immunodetection Kit, BMK-2202	Vector Labs, UK

3.1.4 Cells

All cell lines were supplied by the European Collection of Authenticated Cell Cultures (ECACC). The rat PC12 ECACC 92090409 neuronal cell line was used for cell viability and neurite extension studies herein. Mouse L929 ECACC 85103115 cell line was used for cell permeability testing.

3.1.5 Antibodies

The antibodies listed below relates to those required to identify PC12 cells when used on their own, as well as when investigated alongside L929 cells in a co-culture.

Table 3.4 Antibodies used herein, including supplier information.

Antibody	Supplier
Mouse Anti-Neuron-specific β-III Tubulin Monoclonal Antibody (clone TuJ-1), MAB1195	Bio-Techne, USA
Polyclonal Rabbit Anti-Mouse Immunoglobulins/Fluorescein isothiocyanate (FITC), F0232	Dako, DK
Goat Anti-Mouse IgG/Alexa Fluor Plus 488, A32723	Thermo Fisher Scientific, USA
Rabbit Anti-CD31 Polyclonal Antibody, PA5-16301	Thermo Fisher Scientific, USA
Donkey Anti-Rabbit IgG/Alexa Fluor Plus 555, A32794	Thermo Fisher Scientific, USA

3.2 Experimental Methods

3.2.1 Manufacture of Electrospun Nonwoven Scaffolds

Aligned electrospun nonwoven scaffolds were manufactured to serve as a directional guide for neurite extension. Aligned in this context relates to the preferential fibre orientation in the scaffold relative to the machine direction. Poly(ε-caprolactone) (PCL), average M_n 80 kDa (Sigma-Aldrich, UK) was dissolved in 1,1,1,3,3,3-hexafluoro-2-propanol (HFIP) (Sigma-Aldrich, UK) overnight by stirring, to form a 6% w/w spinning solution and SAP P_{11}-8 (CH_3CO-Gln-Gln-Arg-Phe-Orn-Trp-Orn-Phe-Glu-Gln-Gln-NH_2) (SAP content 75%, HPLC purity of 96%) (C.S. Bio Co., USA) was directly blended into the spinning solution at 10, 20 or 40 mg ml^{-1} and stirred for a further 24 h before use, in accordance with previous work (Gharaei et al., 2016; Gharaei, 2017; Gharaei et al., 2020). The spinning solution was loaded in to a 10 ml syringe (Sigma-Aldrich, UK) fitted with an 18 gauge blunt needle and connected to a Model 200 Series syringe pump (KD Scientific, USA). To electrospin, the loaded syringe was connected to a power supply (Glassman High Voltage, USA) and placed opposite a grounded collector with the following spinning parameters; flow rate, 1 ml h^{-1}; needle-to-collector distance, 110 mm; applied voltage, 25 V.

As electrospinning has many parameters that have to be balanced to establish a stable setup where uniform fibres can be continuously produced, certain parameters were set and then others optimised. An 18 gauge blunt needle was readily available and provided adequate resistance to control ejection from the syringe using a syringe pump. Likewise, a flow rate of 1 ml h^{-1} appeared to match the volume of spinning solution and collector dimensions to result in a web of adequate proportions, as well as being frequently used in the literature. From these set parameters, preliminary experiments identified a needle-to-collector distance of 110 mm and an applied voltage of 25 V as optimal to create a stable Taylor cone at the needle tip and result in uniform electrospun fibres.

To control the degree of fibre alignment, a stationary collector was employed for collection of randomly orientated control samples (Fig. 3.1A) and a rotating drum spinning at up to 30 m s^{-1} was used to collect aligned electrospun webs (Fig. 3.1B). This was the maximum velocity of the equipment and only worked up to after establishing no adverse effects to the stability of the electrospinning setup or fibre uniformity. The material was collected for 2 h, which produced a web-like sheet of nonwoven thick enough to handle, and retrieved by cutting the web across the width

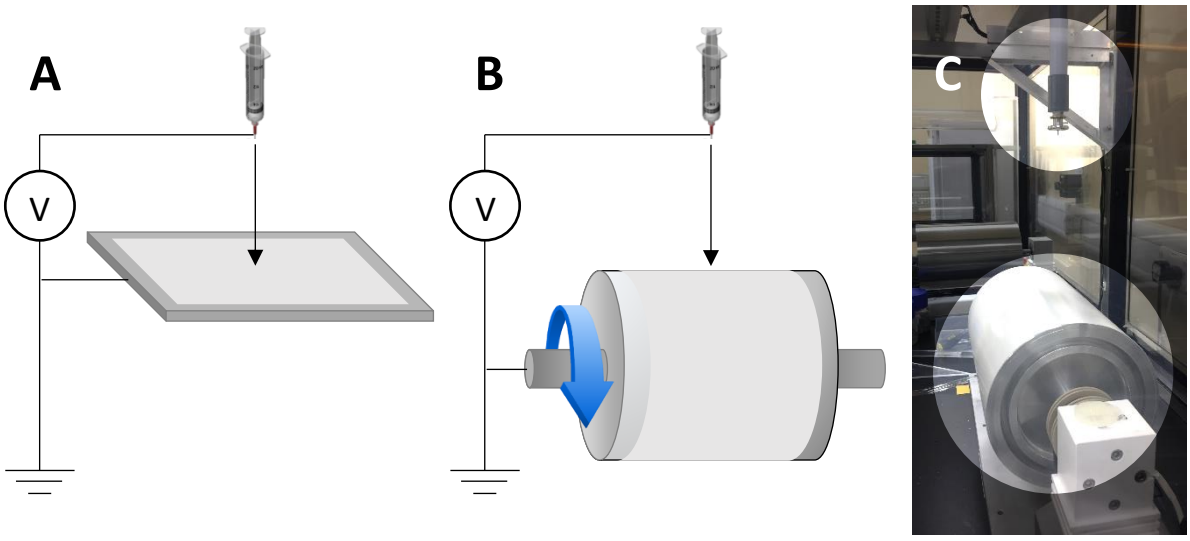

Figure 3.1 Electrospinning setup used to produce nonwoven fibre webs of PCL and PCL/P_{11}-8. (A) To obtain random nonwoven fibre webs a stationary flat metal plate was used as a collector. (B) To obtain aligned nonwoven fibres a rotating metal drum spinning at up to 30 m s^{-1} was used as a collector. (C) An image of the actual electrospinning setup used, with the needle highlighted at the top and the rotating metal drum highlighted at the bottom.

of the collector to deliver 600 × 200 mm long samples for further evaluation and measurement. Mean sample thickness was 62 ± 6 µm (SD), as measured using a desktop SEM by imaging a cross section of the fibre web on its edge to ensure similar thickness between samples (defined as less than 10% SD) and no obvious difference in alignment on the front and back. Further, as access to the equipment was limited due to its location at The Electrospinning Company (Didcot, UK), this time frame allowed two to three samples to be produced per day.

To ascertain linear drum velocity, a DT-2234C+ digital tachometer (HDE, UK) was focused on a reflective strip positioned at the edge of the drum and velocity in revolutions per minute (RPM) ascertained. RPM was then converted to angular velocity (rad s^{-1}) using the formula:

$$\omega = \frac{rpm\ 2\pi}{60}$$

Where, ω is angular velocity (rad s^{-1}), rpm is revolutions per minute of the drum (rpm), 2π is a revolution expressed in terms of radians (rad) and 60 is the number of seconds in a minute (s). Next, angular velocity was converted to linear velocity using the formula:

$$v = r\ x\ \omega$$

Where, v is linear velocity (m s^{-1}), r is radius of the drum (m) and ω is angular velocity (rad s^{-1}).

Of note, the SAP dry weight reflected 25% non-SAP content, ascribed to residual amount of water and trifluoroacetic acid counterions bound to positively charged groups.

3.2.2 Manufacture of Collagen-GMA Hydrogel

Collagen-GMA hydrogels were manufactured to serve as a space-filling component of the composite nonwoven-hydrogel scaffold and allow three-dimensional encapsulation of cells. Manufacture of collagen-GMA hydrogels required extraction of collagen, functionalisation with GMA and photo-activation as detailed in Chapter 3.2.1.1, 3.2.1.2 and 3.2.1.3, respectively, and was adapted from Tronci et al. (2013).

3.2.2.1 Collagen Extraction

Collagen type-I was isolated in-house from rat tail tendons (Fig. 3.2A) as a readily available and inexpensive source of collagen (Bell et al., 1979). Frozen rat tails were obtained from Central Biological Services at the University of Leeds, thawed in distilled water, skin discarded and tendons removed. Tendons were placed in 17.4 mM acetic acid (Sigma-Aldrich, UK) and stirred for 72 h at 4°C to dissolve the collagen type-I. Solution was centrifuged at 38,500 x *g* for 60 min, pellet discarded and supernatant lyophilised for 5 days to obtain collagen type-I. Lyophilised collagen type-I was stored at 4°C for up to 3 months.

3.2.2.2 Collagen Functionalisation

Collagen was functionalised with GMA to enable controlled cross-linking between collagen chains (Fig. 3.2B). Lyophilised rat tail collagen type-I was solubilised in 17.4 mM acetic acid (0.25 weight percent (wt%), 100 g solution) for 24 h at room temperature. Solution was neutralised dropwise to pH 7.4 using 1 M and 10 mM NaOH (Sigma-Aldrich, UK) at room temperature to enhance the reactivity of primary amino groups of collagen lysines. GMA (Sigma-Aldrich, UK) was added at a 25 molar excess with respect to collagen lysine content, as per previous work indicating further excess did not translate into increased functionalisation (Tronci et al., 2015). This was followed by an equimolar amount of triethylamine (Sigma-Aldrich, UK) as a reaction catalyst and 1 wt% Tween-20 (Sigma-Aldrich, UK) with respect to initial solution mass as a surfactant to improve GMA miscibility, which have shown together to improve reaction yield (Tronci et al., 2013). After 24 h at room temperature, the solution was precipitated in a ten-fold volume excess of ethanol (Sigma-Aldrich, UK) and stirred for a further 24 h to remove unreacted species (Tronci et al., 2013). Solution was centrifuged at 26,500 x g for 40 min, supernatant discarded and collagen-GMA lyophilised for 24 h. Lyophilised collagen-GMA was used immediately.

3.2.2.3 Collagen-GMA Photo-Activation

Photo-activation and the resulting cross-linking between collagen-GMA chains was achieved using UV light and I2959 photo-initiator (Fig. 3.2C), as the absorption of a photon cleaves I2959 into substituent radicals (Fig. 3.2D). PBS was used as the solvent to mimic physiological conditions (Tronci et al., 2013; Tronci et al., 2015) and could allow three-dimensional cell encapsulation. I2959 was dissolved in PBS prior

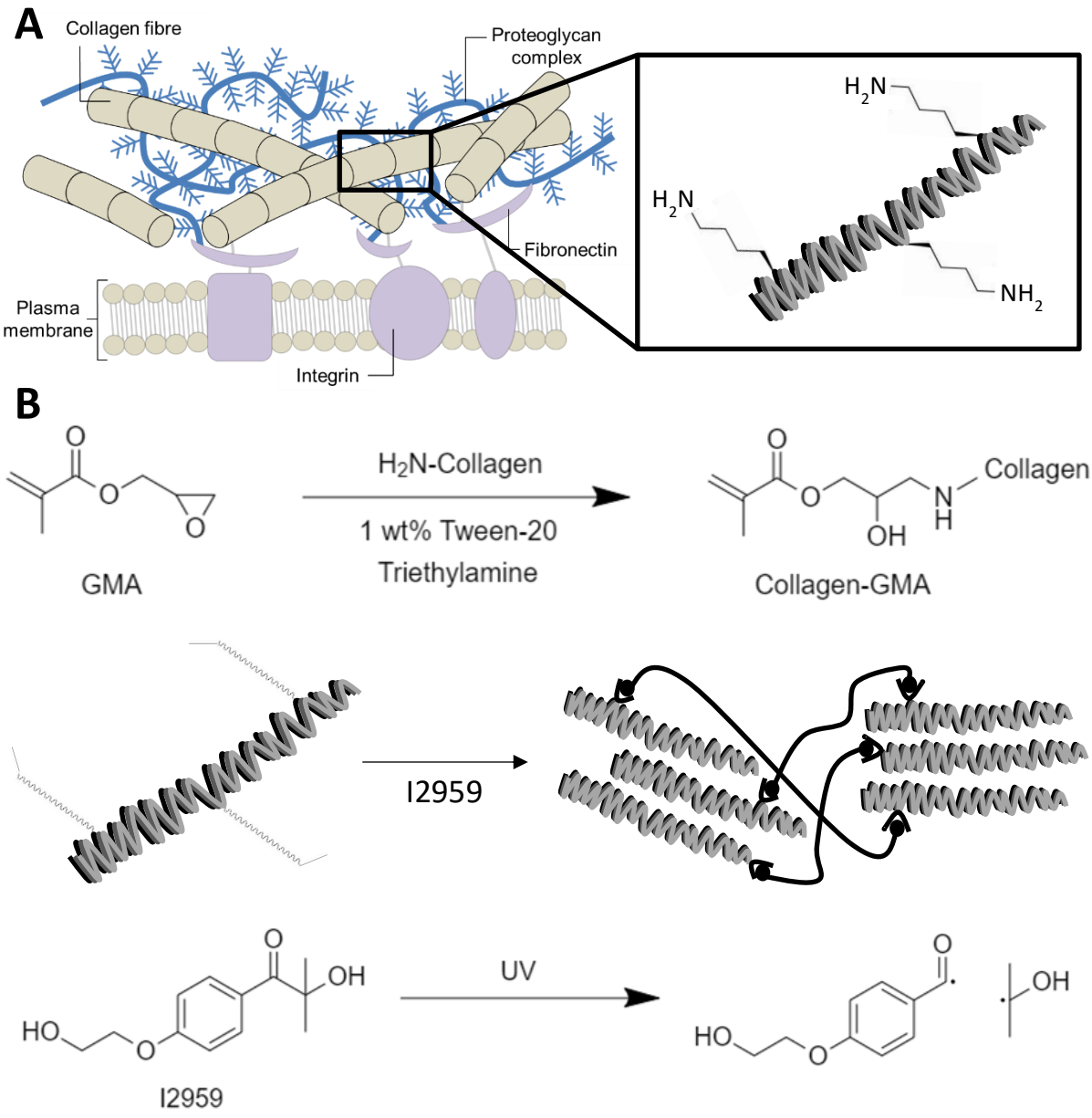

Figure 3.2 Diagram of collagen extraction, functionalisation with GMA and photo-activation to form collagen-GMA. (A) Collagen type-I was extracted from rat tail tendons. Whilst the majority of collagen is made up of the repeating unit glycine-proline-hydroxyproline, the occasional appearance of lysine residues presents amine groups available for modification. (B) GMA is able to undergo a nucleophilic addition reaction with the available amine group of lysine sidechains from collagen, producing collagen-GMA. Triethylamine is added to act as a catalyst and Tween-20 to improve miscibility, with both improving reaction yield (Tronci et al., 2013). (C) The vinyl groups now available in collagen-GMA react with each other in the presence of I2959 photoinitiator and UV light to crosslink between different collagen-GMA chains, mimicking covalent crosslinks found in native tissue that stabilises higher order collagen structures. (D) The photo-activation reaction is possible due to I2959 cleavage into substituent radicals due to photon absorption.

to collagen-GMA addition as this required heating to 60°C in a water bath and stirring for 3 h to fully dissolve. Once cooled to room temperature, lyophilised collagen-GMA (0.8-1.6 wt%) was solubilised in I2959-PBS (Lonza, UK) (1.0 wt%) for 24 h at room temperature. Collagen-GMA hydrogel-forming solution was used to fill silicone moulds sandwiched between glass slides and UV-irradiated (Spectroline, 365 nm, 9 mW cm^{-2}) for 10-60 min. Resulting hydrogels were washed with distilled water.

Chapter 4

Manufacture and Structure of Aligned Fibre Scaffolds

4.1 Introduction

This chapter reports the feasibility of manufacturing an aligned PCL/P_{11}-8 nonwoven scaffold using electrospinning, to form part of a composite nonwoven-hydrogel scaffold to support spinal cord tissue regeneration. Previously, it has been demonstrated that P_{11}-8 self-assembling peptide (SAP) can be dissolved with poly(ε-caprolactone) (PCL) in 1,1,1,3,3,3-hexafluoro-2-propanol (HFIP) to prevent hydrogen bonding and hydrophobic interactions (Aggeli et al., 2003) and make a spinning solution capable of producing random fibre networks via electrospinning (Gharaei et al., 2016; Gharaei, 2017; Gharaei et al., 2020). The augmented wetting profile, lack of cytotoxicity and bimodal distribution of fibre diameters of the resulting electrospun nonwoven (Gharaei et al., 2016) potentially make this an appropriate structure for spinal cord tissue regeneration. However, the feasibility of producing aligned fibre networks using such spinning solutions, desired due to the anisotropy of spinal cord tissue, has not been demonstrated yet. Accordingly, the purpose of this chapter was to determine the extent to which manufacturing was feasible and to characterise the structure of resulting aligned fibre scaffolds.

4.2 Materials and Methods

4.2.1 Manufacture of Electrospun Nonwoven Scaffolds

Aligned electrospun nonwoven was manufactured to serve as a directional guide for neurite extension within the composite nonwoven-hydrogel spinal cord tissue scaffold. Electrospun nonwoven was prepared as previously described in Chapter 3.2.1. Briefly, PCL and P_{11}-8 SAP at 40, 20 and 10 mg ml^{-1} were dissolved in HFIP, loaded into a 10 ml syringe with an 18 gauge blunt needle and electrospun on to a

rotating drum spinning at up to 30 m s^{-1}, with the following set parameters; flow rate, 1 ml h^{-1}; needle-to-collector distance, 110 mm; applied voltage, 25 V; spin time, 2 h. Alternatively, a flat, stationary collector was used to produce randomly orientated control samples. A desktop SEM was used to ensure samples were of similar thickness and there was no obvious differences in sample alignment on the front and back.

4.2.2 Fibre Characterisation

Scanning electron microscopy using a Hitachi SU8230 was employed to study the fibre morphology, diameter and fibre alignment in PCL and PCL/P_{11}-8 nonwovens. Nonwoven samples were sputter-coated with iridium using an Agar Auto Sputter Coater (Agar Scientific, USA) and imaged randomly on the nonwoven surface to reduce sampling error. Fibre diameter data was obtained by averaging individual fibre measurements to determine the mean, standard error of the mean and associated frequency distributions. Fibres were only counted if both edges were visible to reduce sampling error. To characterise the degree of fibre alignment in the nonwoven, data was obtained by taking care to image the sample in the direction of rotation of the collector for aligned samples, further referred to as the machine direction (MD), and measuring the projected angle of individual fibres with respect to the MD. For random controls collected on stationary targets imaging and measuring was done as-collected. ImageJ software (http://imagej.nih.gov/ij/) was used for all measurements. At least 100 fibres per sample were used to determine measurements, with three replicates per sample.

4.2.3 High Performance Liquid Chromatography

High performance liquid chromatography (HPLC) was used to detect P_{11}-8 in the electrospun nonwoven post-spinning and quantify the amount of SAP per square centimetre of the web.

HPLC works by mixing the redissolved samples in a solvent (the mobile phase) and injecting this through a column (the stationary phase) (Fig. 4.1). The column is filled with silica that has carbon chains attached to it to promote interaction with nonpolar components. As the mobile phase is made increasingly non-polar, by increasing the ratio of nonpolar solvent (acetonitrile) to polar solvent (water), polar components in

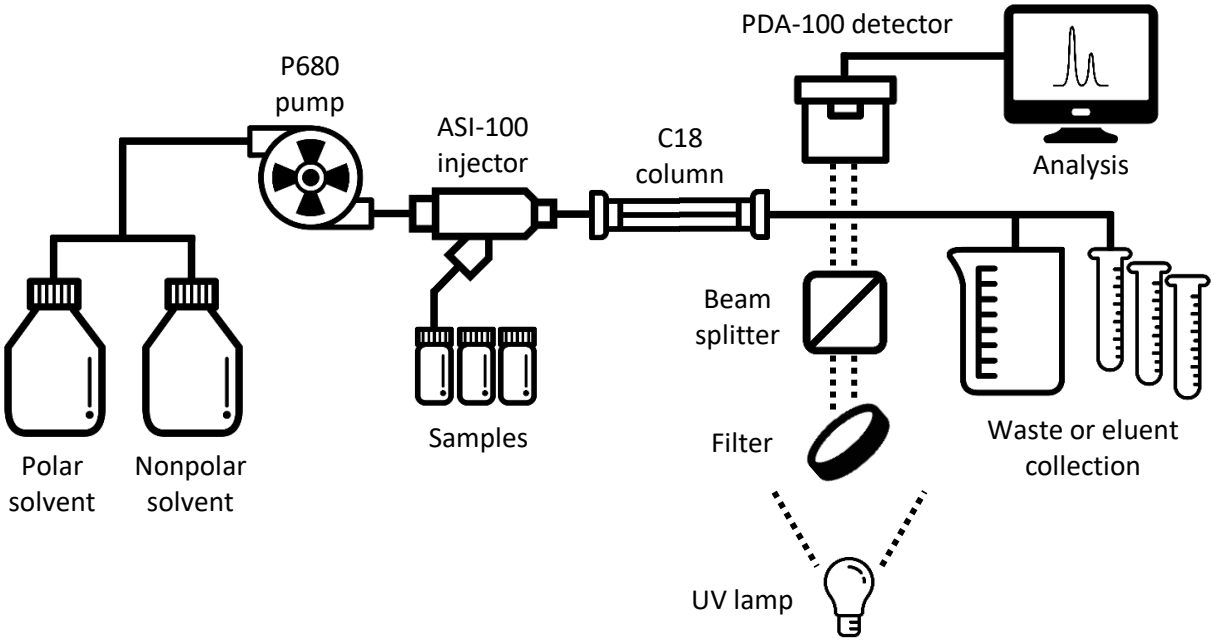

Figure 4.1 Diagram of the HPLC system used to detect and quantitate P_{11}-8. HPLC was used to separate the components of the redissolved electrospun nonwoven samples to detect and quantify P_{11}-8. The system works by mixing the redissolved samples in a solvent (the mobile phase) and injecting this through a column (the stationary phase), with components interacting differently with the stationary phase and mobile phase as the polarity of the mobile phase is altered with time. Detection of P_{11}-8 was then performed at 280 nm wavelength, and quantified by comparing the degree of absorption to a calibration curve of known concentrations.

the sample are washed through quickly and nonpolar components are retained on the column for longer. This allows for separation of individual components in the redissolved samples.

To detect the tryptophan residue in P_{11}-8, UV light was passed through a filter to direct light at wavelengths between 220-330 nm, and then passed through a beam splitter to provide both a reference value and direct light through the sample to the detector. Using an expression of the Beer-Lambert law, the degree of absorption of a sample (A) can be calculated as a product of the absorption coefficient of the material (ε), the path length the light travels through (l) and concentration of the material (c):

$$A = \varepsilon l c$$

This results in a chromatogram showing changes in the degree of absorption with time, with peaks on the spectrum representing different components. As the path

length is always fixed in the system and the absorption coefficient is a material property, changes in concentration of a material are directly proportional to changes in the degree of absorption, or the area under each specific peak.

To obtain quantitative concentration values of the unknown samples, a calibration curve of peak area against concentration was built by running sequences of known concentrations and then plotting peak areas of the unknown samples.

A Dionex HPLC system with a P680 pump, ASI-100 Automated Sample Injector and PDA-100 Photodiode Array Detector (deuterium lamp) was fitted with a C18 column (C18 refers to the average carbon chain length attached to the silica) (Thermo Fisher Scientific, USA) as the stationary phase to adequately promote interaction with nonpolar components of the sample. A polar to non-polar progressing gradient of water to acetonitrile was used as the mobile phase to separate the different components of the sample by altering the polarity over time.

Samples 1 cm^2 of PCL-only and PCL/P_{11}-8 at 10, 20 and 40 mg ml^{-1} were dissolved in 1 ml HFIP on a roller for 72 h to ensure full dissolution. Of these samples, 100 µl was placed into the HPLC vials, and of this, 10 µl was injected into the column, which was enough sample to obtain a reliable reading. A concentration gradient of P_{11}-8 in HFIP was run at 400, 200, 100, 50, 20, 10 and 2 µg ml^{-1} to produce a calibration curve broad enough to capture potential results for quantifying SAP in the above unknown samples. All samples were run in triplicate.

4.2.4 Mass Spectrometry

Mass spectrometry was used to further identify P_{11}-8 in the separated HPLC sample. A Xevo QTof G2-XS Mass Spectrometer coupled to an Acquity M-Class UPLC (Waters, USA) was used to confirm the mass of unknown sample and compare to known values of P_{11}-8. PCL/P_{11}-8 40 mg ml^{-1} was chosen as the sample to be analysed as this gave the highest recorded SAP content, as per the HPLC results (Fig. 4.2). The same sequences were run and fractions were collected every 1 min. However, injection volume was increased from 10 µl to 50 µl, three repeats for the sample were used and any fractions that covered the peak around 15 min retention time were pooled to ensure enough material was available or identification. The

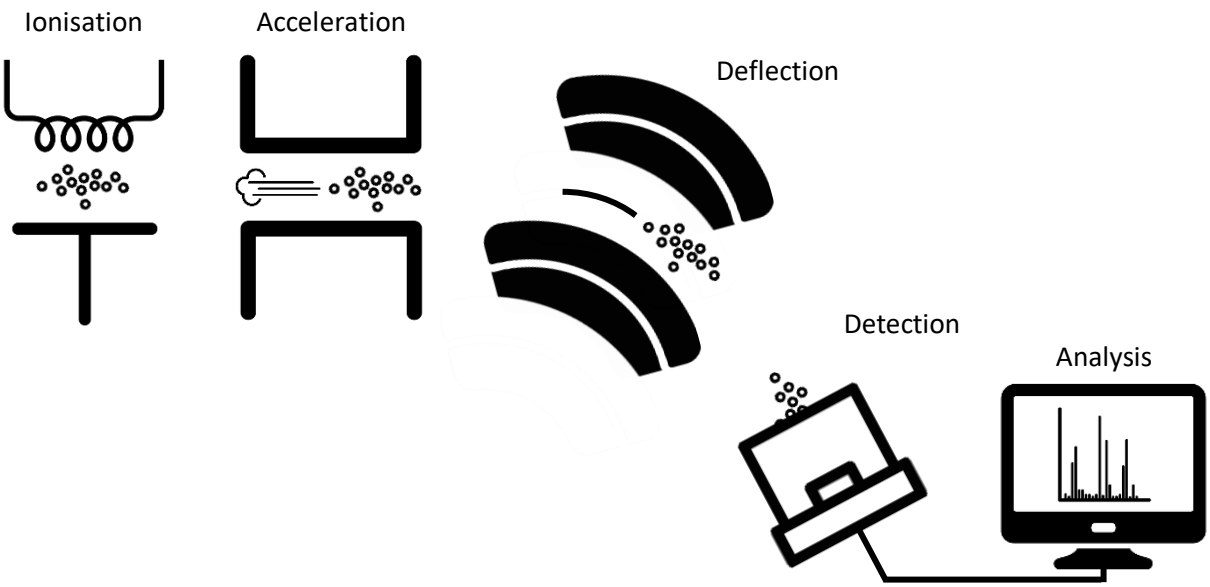

Figure 4.2 Diagram of the mass spectrometer used to identify P_{11}-8. Mass spectrometry was used to confirm the identity of P_{11}-8 in the electrospun nonwoven post-electrospinning. Fractions eluted from the HPLC around the retention time of the peak thought to correspond to P_{11}-8 were collected, pooled and lyophilised. Mass spectrometry works by (1) ionising the substance by knocking off an electron, (2) accelerating the positively-charged ions, (3) deflecting these ions using a magnetic field, and (4) detecting the ions. Mass/charge ratio is recorded against abundance giving peaks on the mass spectrum.

collected sample was lyophilised overnight and resuspended in 100 mM ammonium acetate by agitating on ice for 3 h, with a final volume of 25 µl.

4.3 Results and Discussion

Nonwoven samples consisting of PCL/P_{11}-8 with SAP at 10, 20 and 40 mg ml^{-1} were successfully electrospun and characterisation was conducted to determine fibre diameter, alignment and SAP distribution. Before spinning the P_{11}-8 SAP with the PCL polymer, spinning parameters were first optimised for the polymer alone.

4.3.1 Electrospinning of Aligned PCL Fibre Nonwovens and the Effect of Collector Surface Velocity on Fibre Diameter

To achieve an effective supporting fibrous scaffold for neurite extension, high preferential MD fibre alignment and a mean fibre diameter in the submicron range

were targeted in accordance with recommendations from previous research, as detailed in Chapters 2.5.1.1 and 2.5.1.2. In the present study, fibre alignment was controlled by adjusting the surface velocity of the rotating collector during electrospinning, relative to the polymer feed rate from the syringe. Fibre diameter was controlled by modulating the concentration (weight percent), and therefore viscosity, of the spinning solution.

A spinning solution of 6% w/w PCL to HFIP was selected as a starting point reflecting previously reported work on PCL with P_{11}-8 (Gharaei et al., 2016) and the effect of collector surface velocity on fibre alignment and fibre diameter were initially studied with 100% PCL without SAP. SEM images of the nonwoven show how fibre diameter decreased as velocity of the collector increased (Fig. 4.3A-D). Mean fibre diameter at 0 m s^{-1}, with the collector held stationary, was 1366 ± 29 nm (standard error, SE) (Fig. 4.3E). As collector velocity was increased to 10, 20, and 30 m s^{-1}, mean fibre diameter decreased to 1035 ± 26 nm, 741 ± 37 nm and 600 ± 40 nm, respectively (Fig. 4.3F-H).

Whilst 6% w/w PCL in HFIP created a nonwoven with a mean fibre diameter of more than a micron when the collector was stationary, with increasing collector velocity mean fibre diameter decreased into the desired submicron range as alignment increased. This can be attributed to the deposition velocity ratio (V_{in}:V_{out}) (Russell, 2006) and the resulting tensile force applied to the fibres during deposition, which has been observed on a range of synthetic materials such as PLGA (Bashur et al., 2006; Lee et al., 2010), poly(esterurethane urea) (PEUUR) (Bashur et al., 2009) and PCL (Thomas et al., 2006), as well as natural materials such as collagen (Zhong et al., 2006). This can result in a 28-36% reduction in fibre diameter when comparing static collection to fibres collected at velocities between 4.6-15.0 m s^{-1} (Thomas et al., 2006; Bashur et al., 2006; Zhong et al., 2006; Bashur et al., 2009; Lee et al., 2010).

A similar pattern of results was observed herein, where the 10 m s^{-1} sample reduced mean fibre diameter by 24%, from 1366 ± 29 nm (SE) to 1035 ± 26 nm compared to the stationary control. As collector velocity increased further to 20 and 30 m s^{-1}, mean fibre diameter reduced further by 46% and 56%, to 741 ± 37 nm and 600 ± 40 nm, respectively.

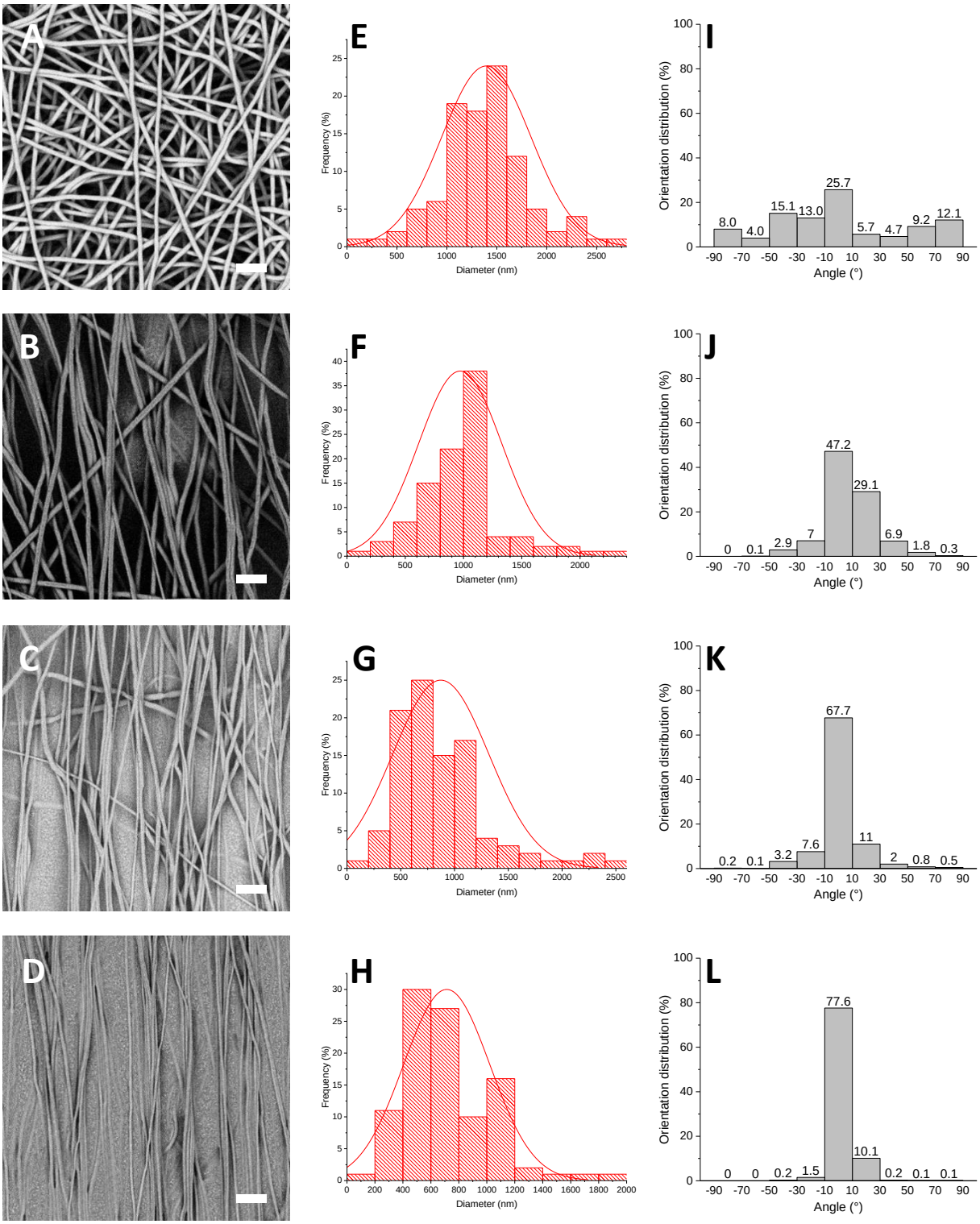

Figure 4.3 Aligned electrospinning of PCL. (A-D) SEM images showing the effect of collector velocity on fibre diameter and alignment of PCL. Graphs showing mean fibre diameter at (E) 0 m s^{-1} was 1366 ± 29 nm (SE), reducing to (F) 1035 ± 26 nm, (G) 741 ± 37 nm and (H) 600 ± 40 nm, as velocity increased to 10, 20, and 30 m s^{-1}, respectively. The percentage of fibres ± 10° of 0° increased from (I) 26% at 0 m s^{-1} to (J) 47%, (K) 68% and (L) 78% at 10, 20 and 30 m s^{-1}, respectively. Further, the percentage of fibres ± 30° of 0° also increased from (I) 44% at 0 m s^{-1} to (J) 83%, (K) 86%, and (L) 89% at 10, 20, and 30 m s^{-1}, respectively. Scale bar is 10 µm.

Of note, some evidence supporting the opposite, with fibre diameter increasing with increasing collector velocity, has been published. PCL increased in mean fibre diameter by 18% at a collector velocity of 9.3 m s^{-1} (Li et al., 2007). However, high standard deviations and a similar range between the stationary sample (438 ± 156 nm; min: 256, max: 821) and the 9.3 m s^{-1} sample (519 ± 127 nm; min: 287, max: 748), with no information on the number of data points, suggests these could be similar results.

Further, PCL has also been observed increasing in mean fibre diameter by around 15% up to collector velocities of around 2 m s^{-1}, before reducing from this peak by 65% at 7 m s^{-1} (Edwards et al., 2010). Whilst standard deviation or standard error of the mean values aren't given for this data and no statistics are provided on the significant differences between sample groups, diameter distributions indicate large overlaps in groups up to 2 m s^{-1}, before distributions become tighter and decrease as collector velocity increases. As such, whilst an initial increase is observed in the mean fibre diameter, this could be explained by the velocity of the collector not being high enough to cause enough tensile stress to initiate a reduction in fibre diameter.

However, the results seen herein, where fibre diameter decreases with increasing collector velocity, are in keeping with the consensus in the literature for collector velocities up to 15 m s^{-1}, but provide further evidence this phenomenon extends for collector velocities up to 30 m s^{-1}.

4.3.2 Electrospinning Collector Surface Velocity and the Effect on Fibre Alignment

As fibre diameter decreased with increasing collector surface velocity, SEM images also show how alignment of the fibres increased as collector surface velocity increased relative to feed velocity (Fig. 4.3A-D). The percentage of fibres ± 10° of 0° increased from 26% at 0 m s^{-1} to 47%, 68% and 78% at 10, 20 and 30 m s^{-1}, respectively (Fig. 4.3I-L). When this range was increased to include fibres ± 30° of 0°, the percentage increased from 44% at 0 m s^{-1} to 83%, 86%, and 89% at 10, 20, and 30 m s^{-1}, respectively. Whilst "high alignment" can be a subjective term, these figures and accompanying SEM images clearly indicate increasing anisotropy in terms of fibre alignment as the collector surface speed increased, compared to when the collector was stationary.

As the fibre is deposited on the collector due to electrostatic forces, high surface velocity of the rotating collector continuously draws the fibre in the machine direction. As such, there are three velocity-dependent outcomes; either the collector velocity is too slow to promote alignment and randomly orientated fibres are deposited; collector velocity is high enough to promote a degree of alignment and positively correlates up to a threshold; or collector velocity is above a threshold that impairs alignment due to excessive tensile stress causing fibre fracture (Edwards et al., 2010). It is also possible necking of fibres can occur, if collector velocity is much higher than that of fibres forming from the jet and excess tension is experienced (Zussman et al., 2003; W. Liu et al., 2012; Sun et al., 2012), or excessive turbulence prevents deposition (Yuan et al., 2017).

Whilst fracture and impairment to fibre alignment has been seen at collector velocities much lower than the 30 m s^{-1} used herein, the velocity at which each outcome starts and the threshold at which alignment is impaired is dependent on a multitude of factors, from the spinning material to collector set-up (Beachley et al., 2012). With the set-up used herein and the experimental conditions chosen, it was ascertained that a collector velocity of 10 m s^{-1} was high enough to initiate alignment of the electrospun web and a velocity of 30 m s^{-1} but not high enough to cause fracture or necking of fibres or affect alignment due to excessive turbulence.

Further, whilst the threshold velocity was not reached and therefore the optimal velocity for fibre alignment herein could be higher than 30 m s^{-1}, the degree of alignment relative to the fibre morphology implies this threshold velocity is close. Also, any further alignment could result in a lack of adequate fibre entangling, so further alignment is likely undesirable.

As such, with high alignment, a mean submicron fibre diameter and an absence of fracture or necking observed in the PCL-only fibres created at 30 m s^{-1}, this velocity was chosen for spinning aligned PCL/P_{11}-8 for the first time.

4.3.3 Electrospinning of Aligned PCL/P_{11}-8 Fibre Nonwovens and the Effect of SAP on Fibre Diameter

For the first time, aligned PCL/P_{11}-8 fibres were made by incorporating P_{11}-8 SAP into the spinning solution and spinning on to the rotating collector set-up (Fig. 3.1B,

C) at 30 m s^{-1}. Interestingly, despite the high surface velocity of the collector, a secondary nanoscale network of fibres was also observed alongside a primary submicron fibre network, giving a bimodal distribution of fibre diameters. For the purpose of the work herein, submicron diameter is defined as fibres of diameter between 100-1000 nm, while nanoscale are defined as being between 1-100 nm. This has been previously observed using a static collector, but prior to the present experiment, it was not known whether PCL/P_{11}-8 nanofibres would be present on a collector spinning with a surface velocity of 30 m s^{-1}, or whether such a high surface velocity would impede nanofibre formation, for example by fracture due to excessive tensile forces or prevent deposition due to excessive turbulence.

However, whilst the submicron fibre network aligned in the machine direction, similar to the PCL-only control, the secondary nanoscale network did not, with large dense areas appearing randomly orientated and with no preferential alignment with respect to the machine direction, but also aligned orthogonal to adjacent submicron fibres. Thus, the physical forces responsible for alignment of the submicron fibre network during electrospinning did not appear to influence the alignment of secondary nanoscale network, nor its structural integrity.

As shown in the SEM images, electrospinning of PCL led to uniform submicron fibres (Fig. 4.4A). Whilst this was similar to part of the web observed for PCL/P_{11}-8, which also featured uniform submicron fibres, a secondary nanoscale network was observed throughout the web (Fig. 4.4B). Plotting the fibre diameters showed that

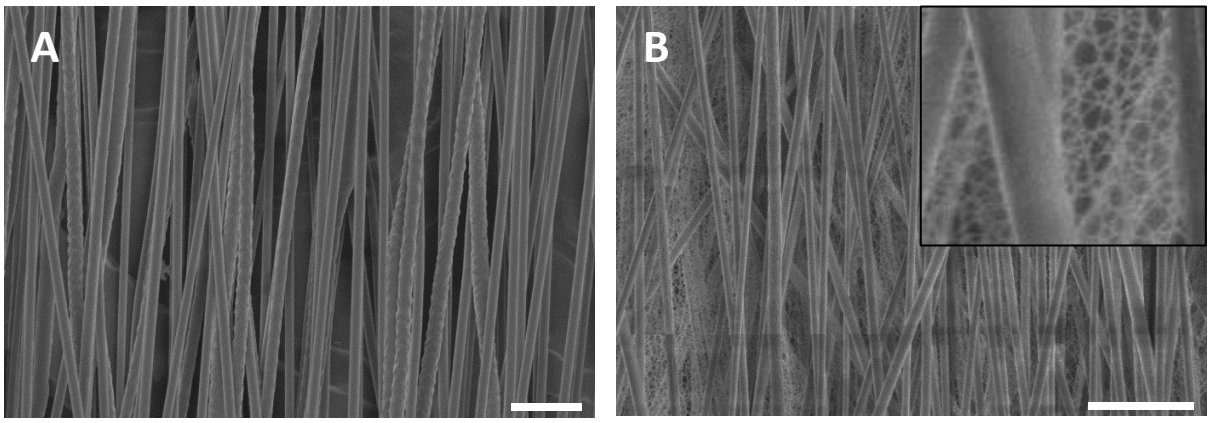

Figure 4.4 SEM images of electrospun PCL and PCL/P_{11}-8 nonwovens. High alignment of the submicron fibre network in the machine direction can be seen in both (A) PCL and (B) PCL/P_{11}-8 40 mg ml^{-1}. The appearance of a secondary nanoscale network can be seen throughout the PCL/P_{11}-8 web, which is dense and fractal (inset). Scale bar is 5 μm.

distribution for PCL was unimodal, giving a normal distribution around a single mean value (Fig. 4.5A). This was in contrast to the bimodal distribution for all PCL/P_{11}-8 groups (Fig. 4.5B-D), due to the formation of the secondary nanoscale network, and was similar to the results for PCL/P_{11}-8 randomly orientated webs previously published (Gharaei et al., 2016; Gharaei, 2017).

Focusing on the submicron fibre network, mean fibre diameter (± SD) reduced from 743 ± 139 nm in the PCL-only control to 398 ± 76 nm, 415 ± 81 nm and 418 ± 95 nm for PCL/P_{11}-8 with a SAP concentration of 10, 20 and 40 mg ml^{-1}, respectively (Fig. 4.5E).

Negligible changes and even slight increases in submicron fibre diameter have been observed when spinning other polymer-SAP mixes. Electrospinning of PLGA and RADA16-I-BMHP1 created a network of 300-500 nm diameter fibres versus 200-400 nm for PLGA-only. Whilst the authors recognised the increase in fibre diameter due to SAP, they did not give an explanation for the increase. The SAP, having the sequence RADARADARADARADAG-GPFSSTKT, would have had a +1 net charge and thus may not have conveyed a high enough charge density to promote jet repulsion. Further, the mean or range was not given and it is also not clear how many fibres were used for the measurement. As such, it is hard to tell the accuracy of the data and therefore the strength of any conclusions (Nune et al., 2017). Furthermore, in a more recent paper by the same group, similar drawbacks for the information reported on fibre diameter are seen but diameters are given as 200-300 nm for both the PLGA and PLGA-SAP samples, with exactly the same electrospinning parameters (Nune et al., 2019).

However, the reduction in fibre diameter has been explained previously due to the higher charge density of the electrospinning solution as P_{11}-8 has a +2 net charge (Gharaei et al., 2016; Gharaei, 2017). This results in more repulsive charge promoting elongation of the jet and higher tension in the drying fibre reducing fibre diameter (Zong et al., 2002; Beachley and Wen, 2009). Similar results have also been observed when electrospinning aligned fibre webs of polyethylene oxide (PEO) with increasing salt content to increase conductivity (Sun et al., 2012). With regards to the nanoscale fibre network, mean fibre diameter (± SD) was 38 ± 15 nm, 24 ± 10 nm and 22 ± 8 nm for 10, 20 and 40 mg ml^{-1} concentrations, respectively (Fig. 4.5F). This is similar to those reported previously when electrospinning random PCL/P_{11}-8

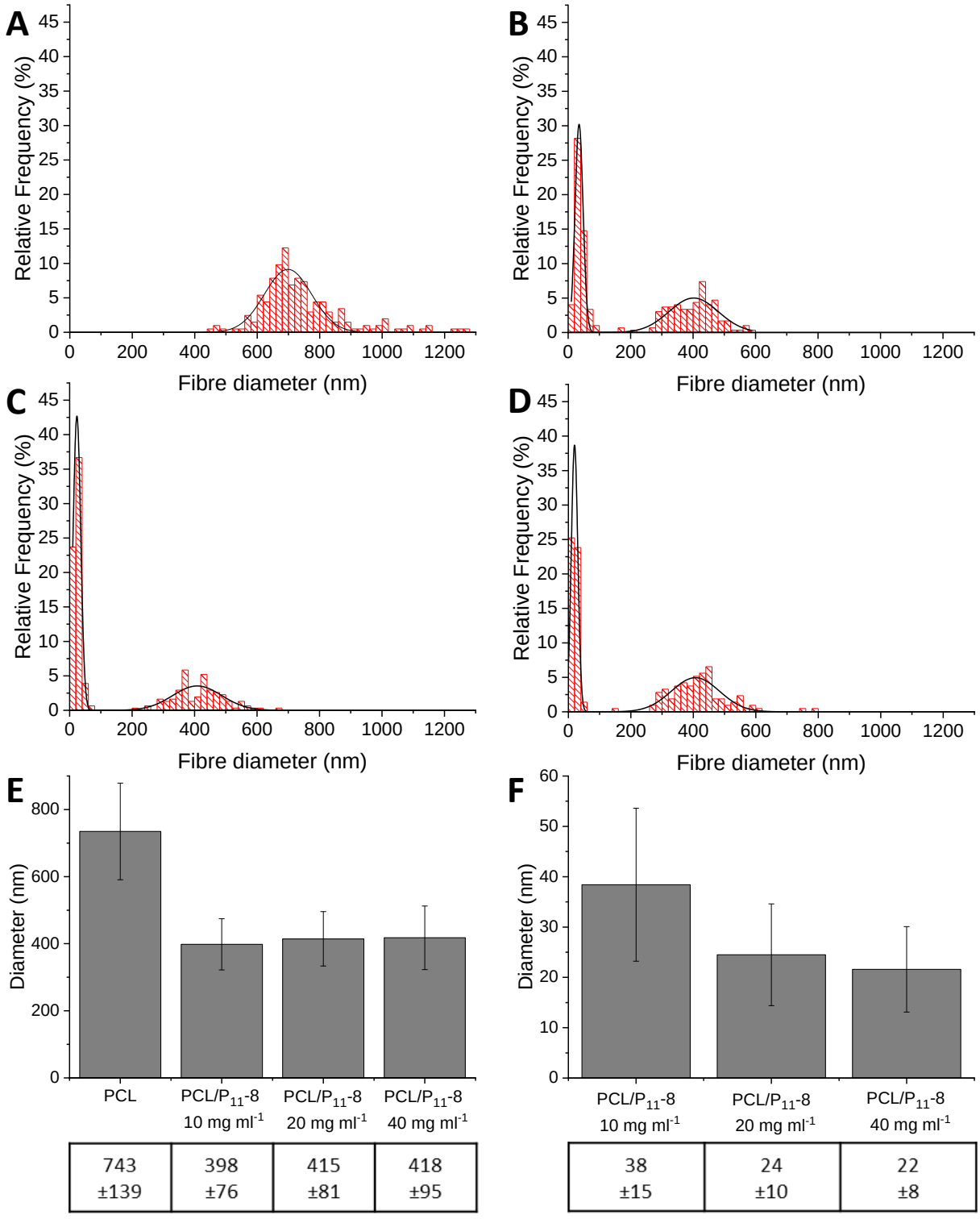

Figure 4.5 Fibre diameter distribution of PCL-only and PCL/P_{11}-8 nonwoven webs. (A) PCL has a unimodal distribution of fibre diameters versus a bimodal distribution of fibre diameters for PCL/P_{11}-8 webs at (B) 10 mg ml^{-1}, (C) 20 mg ml^{-1} and (D) 40 mg ml^{-1}. Separating the two distinct peaks shows the mean fibre diameter (± SD) for the (E) submicron network and (F) nanoscale network. *n* = 100.

nonwoven (Gharaei, 2017) and similar to the 20-30 nm diameter fibres observed for P_{11}-8 SAP hydrogel (Carrick et al., 2007).

4.3.4 Electrospinning of Aligned PCL/P_{11}-8 Fibre Nonwovens and the Effect of SAP on Fibre Alignment

Whilst mean fibre diameter for the submicron network decreased but remained in the desired submicron range following SAP addition, alignment of the PCL/P_{11}-8 submicron network was remarkably similar to the alignment of the PCL-only control (Fig. 4.6A-B). The percentage of fibres ± 30° of 0° was 83% and 86% for PCL and PCL/P_{11}-8, respectively. However, a degree of fibre alignment was affected by SAP with regards to those fibres most highly aligned, as the percentage of fibres ± 10° of 0° fell from 75% to 65% for PCL and PCL/P_{11}-8, respectively. The slight reduction in fibre alignment may be explained by the higher charge density as a result of the SAP, as salt addition into the spinning solution has been shown to reduce alignment when spinning on to a fibre drum rotating at 8 m s^{-1}, due to the promoted whipping of the drying fibre (Sun et al., 2012).

However, the similarity in percentage of fibres ± 30° of 0° for PCL and PCL/P_{11}-8, despite the increased charge density of the latter, may be due to the much higher collector velocity used here. Any increased whipping due to higher charge density of the SAP-containing solution seems to have been largely nullified by the effect of the surface velocity of the collector. In contrast, whilst a random orientation was observed for the nanoscale network in high density throughout the web, nanoscale fibres were also observed between adjacent submicron fibres, producing regions with fibres in the cross direction. Nanoscale fibres can be seen between the highly aligned submicron fibres (Fig. 4.6C-E), versus the random orientation of the nanoscale network when the submicron network is also random (Fig. 4.6F). This is presented in the bar graphs of fibre alignment, where the webs with highly aligned submicron fibres have a V-shaped graph (Fig. 4.6G-I), as fibres are orientated towards ± 90° of the machine direction, versus a relatively flat graph for webs with randomly orientated submicron fibres (Fig. 4.6J).

If high density regions and low density regions had been observed separately throughout the web, this may have been an indication that the SAP had not been well distributed within the spinning solution or had potentially aggregated in response

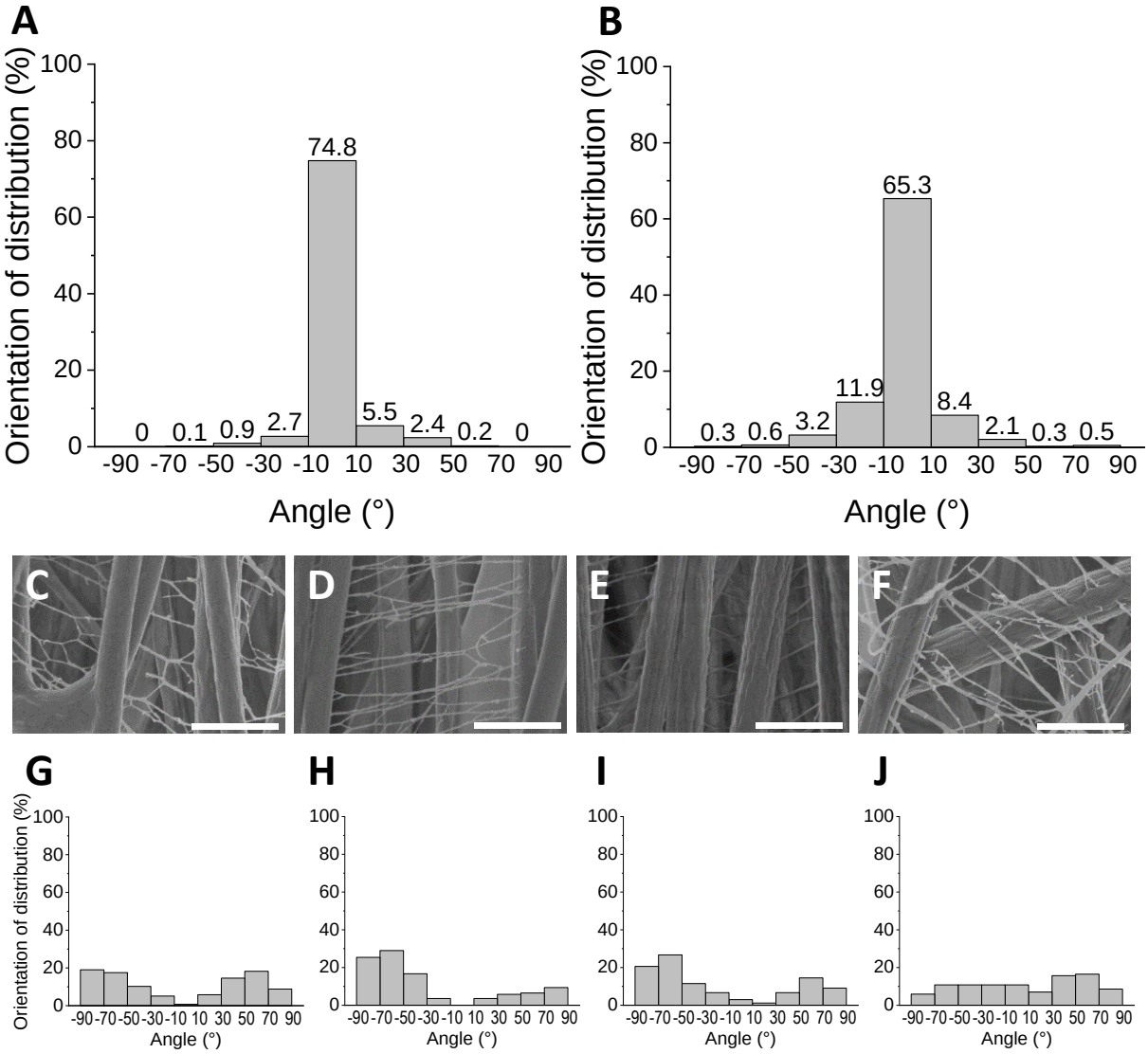

Figure 4.6 SEM images and graphs showing alignment of the submicron and nanoscale networks. Alignment of the submicron fibre network for (A) PCL and (B) PCL/P_{11}-8 40 mg ml^{-1} was 75% and 65% ± 10° of 0°, and 83% and 86% ± 30° of 0°, respectively. Focusing on the nanoscale network, SEM images show aligned PCL/P_{11}-8 webs at (C) 10 mg ml^{-1}, (D) 20 mg ml^{-1} and (E), 40 mg ml^{-1}, and (F) a randomly orientated sample of PCL/P_{11}-8 40 mg ml^{-1}. (G-I) V-shaped graphs can be seen for the aligned webs, due to the formation of fibres between highly aligned submicron fibres, versus (J) a relatively even distribution of fibre orientations for the randomly orientated web. *n* = 100. Scale bar is 1 µm.

to a physical parameter, such as pH. However, the nanoscale network was observed in abundance throughout the web, alongside regions where nanoscale fibres appeared in the cross direction, between adjacent submicron fibres. Whilst it is not clear at what point during the electrospinning process the secondary nanoscale network is forming, its structural integrity and lack of broken ends potentially indicates that at least part of the nanoscale network is forming after fibres have been

aligned; post-deposition. This could be possible as EDX has previously shown that both submicron and nanoscale fibres contain SAP (Gharaei et al., 2016) and it is well known that residual solvent can continue to evaporate after electrospinning. It is therefore feasible that SAP monomer still in solution on the surface of drying aligned submicron fibres could self-assemble as solvent evaporated, and form nanoscale fibres along the shortest distance between the already aligned submicron fibres.

This hypothesis of late-stage secondary network formation is built on elements of models previously suggested, such as fibre formation from the requirement to maintain ionic balance as solvent evaporates (Barakat et al., 2009); fibre formation following relaxation of the electrical stress in the electrical double layer on the surface of drying fibres (Nirmala et al., 2010); and fibre formation from phase separation and spinodal decomposition of residual solution in the web (Ding et al., 2006).

As such, a PCL/P_{11}-8 nonwoven with an aligned submicron fibre diameter network and random nanoscale network, which showed some alignment in the cross direction, was created. The similarity of the submicron fibre diameter network in alignment ± 30° of 0° to the PCL-only control made this a strong sample for further comparison.

4.3.5 Detection of SAP in the Nonwoven Web Post-Electrospinning

As shown so far, the amount of SAP in the nonwoven affects the abundance of the nanoscale network and, in turn, the mechanical properties of the fibre web. However, whilst the amount of SAP going into the spinning solution was known, the amount of SAP in the dry nonwoven product also needed to be ascertained. As such, a methodology for detecting and quantifying SAP post-electrospinning was developed.

In order to detect and quantify the SAP content in the electrospun fibres, the unique absorption properties of the tryptophan functional group found in P_{11}-8 was exploited. From the rational design of the SAP, tryptophan was included at position six to promote self-assembly (Aggeli et al., 1997; Aggeli et al., 2001; Davies et al., 2006) but this was the first time the absorption properties of the double-ring sidechain had been suggested as a method for identifying and even quantifying mass of the SAP in the product.

Prior to detection and subsequent quantification, the SAP was separated from the polymer using high performance liquid chromatography (HPLC). HPLC is an analytical chemistry technique used routinely in the lab and industry to separate, identify, collect and quantify components of a mixture. During the HPLC run, an increasing concentration of acetonitrile versus water in the eluent reduces polarity of the mobile phase. As such, more polar components of the sample should wash through faster, whilst less polar components are retained on the stationary phase for longer.

In the resulting chromatograms, the peak profiles for HFIP, PCL, and PCL/P_{11}-8 at 10, 20 and 40 mg ml^{-1} can be seen (Fig. 4.7A-E). A unique peak at a retention time of around 15 min was visible in all three PCL/P_{11}-8 samples but not visible in the HFIP and PCL controls. The HFIP profile serves as the background reading which was mimicked by the PCL sample due to the lack of entities in PCL that absorb light at a wavelength of 280 nm. However, due to the double ring structure of the tryptophan residue in P_{11}-8, the SAP absorbs at 280 nm and an additional peak was observed in the chromatogram. Furthermore, a positive concentration-dependent result was observed, with area under the peak at 15 minutes increasing as P_{11}-8 concentration increased.

For confirmation the peak at 15 min retention time was P_{11}-8, the sample was collected and run on a mass spectrometer. P_{11}-8 has a theoretical molecular weight of 1565.70 Da. This was calculated by the sum of the amino acids in the QQRFOWOFEQQ sequence (1704.7 Da), minus the ten H_2O molecules from peptide bond formation (-180 Da), correcting the N-terminal by subtracting the -OH (-17 Da) and adding the $-NH_2$ (+16 Da), and correcting the C-terminal by subtracting the hydrogen from the $-NH_2$ (-1 Da) and adding the $-COCH_2$ (+43 Da). The fraction representing the peak at around 15 minutes was collected and confirmed to have a molecular weight of 1565.25 ± 0.28 Da (Fig. 4.8). This not only closely matched the theoretical mass above, but also closely matched the original mass spectrum result of 1565.41 Da in the quality control record from the SAP manufacturer (Fig. 4.9) and strongly indicated the material in the fraction eluted at around 15 minutes was P_{11}-8.

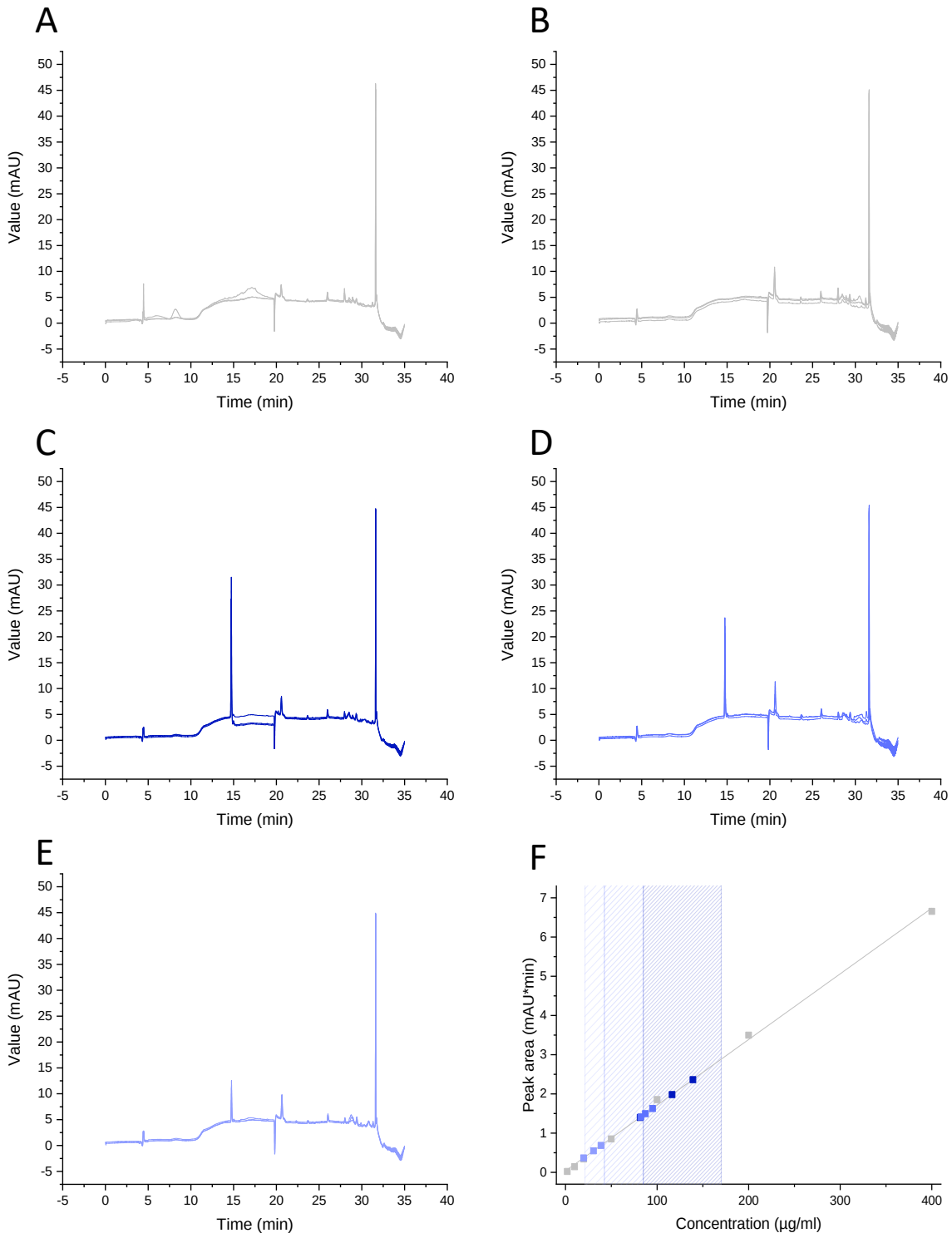

Figure 4.7 Detection and quantitation of P_{11}-8 in PCL/P_{11}-8 nonwoven. HPLC chromatograms of (A) HFIP (solvent-only), (B) PCL, (C) PCL/P_{11}-8 40 mg ml^{-1}, (D) PCL/P_{11}-8 20 mg ml^{-1}, and (E) PCL/P_{11}-8 10 mg ml^{-1}. (F) Quantitation of samples was done using a calibration curve of known concentrations against measured peak area. Shaded sections show estimated range of peptide concentration in nonwoven prior to HPLC. *n* = 3.

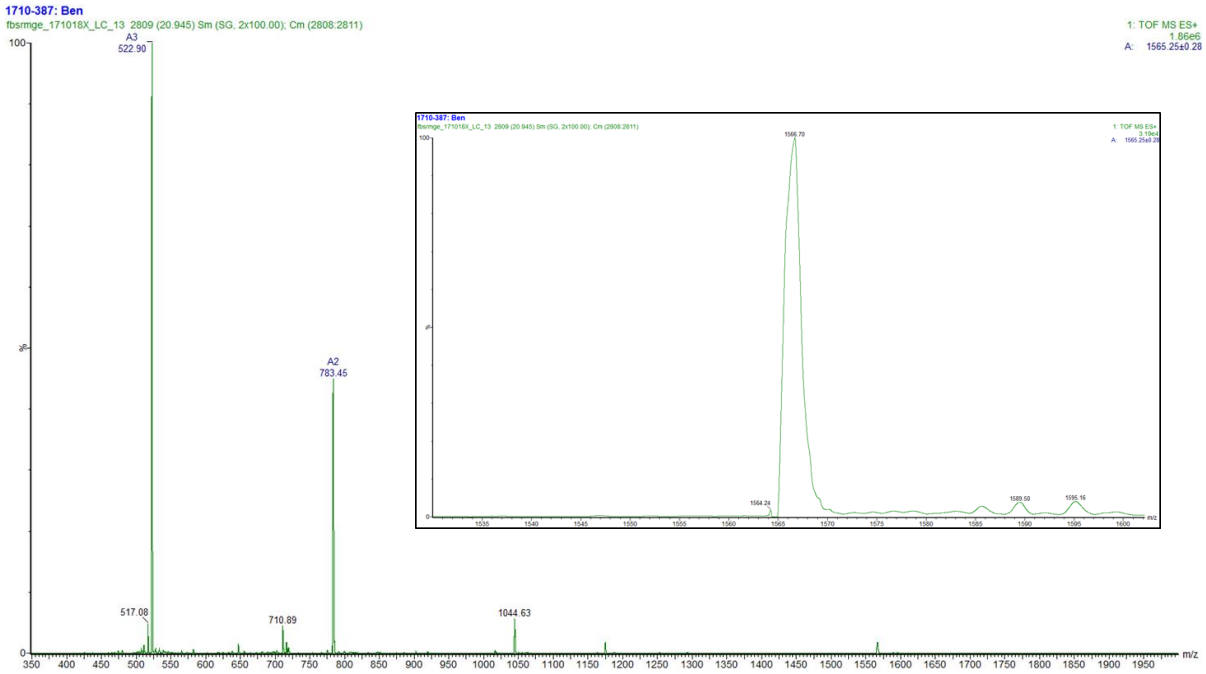

Figure 4.8 Mass spectrum of the HPLC peak at 15 minutes retention time. A molecular ion peak is visible between 1550-600 m/z. The inset spectrum shows this region enlarged, giving the unknown sample a mass of 1565.25 ± 0.28 Da. This closely matches the original mass spectrum results of 1565.41 Da on the quality control record from the manufacturer and the 1565.70 Da of the theoretical calculated mass of the peptide.

4.3.6 Quantification of SAP Post-Electrospinning

Following confirmation of P_{11}-8 detection, quantification of SAP in each of the three sample concentrations was achieved by building a calibration curve of known P_{11}-8 concentrations and plotting the unknown sample concentrations (Fig. 4.7F). As a representation of the precision of HPLC, an adjusted R^2 of 0.99842 was achieved for the calibration curve over two orders magnitude, from 2 µg ml^{-1} to 400 µg ml^{-1}. Further, mass of SAP per square centimetre was predicted to fall between 21.3-42.5, 42.5-85.0 and 85.0-170.0 µg cm^{-2} for the 10, 20 and 40 mg ml^{-1} samples. These boundaries were calculated by multiplying the concentration of the spinning solution by the volume used during spinning to give the mass of SAP used. This was then divided by the area of the nonwoven web, with the lower boundary considering the full length of the 200 mm sample and the upper boundary considering the usable nonwoven area to be the central 100 mm of the web, due to poorer deposition at the edges.

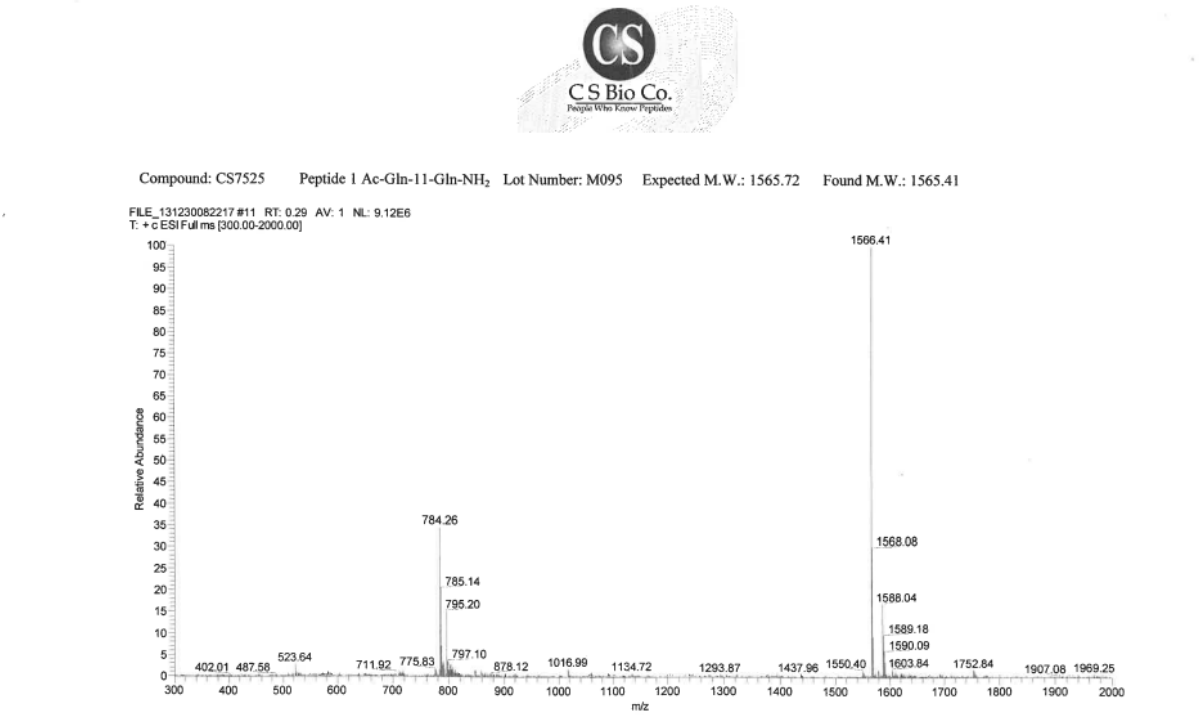

Figure 4.9 Mass spectrum of P_{11}-8 from C.S. Bio, the peptide manufacturer. A molecular ion peak can be seen at 1566.41 Da, giving a molecular weight of 1565.41 Da. This closely matches the 1565.70 Da of the theoretical calculated mass of the peptide, and the subsequent mass spectrum results of 1565.25 ± 0.28 Da on the mass spectrum following HPLC of the PCL/P_{11}-8 samples.

Actual values calculated by HPLC were 29.7 ± 5.5 (SE), 88.2 ± 3.7 and 112.4 ± 16.8 µg cm^{-2} for the 10, 20 and 40 mg ml^{-1} samples respectively, falling in the middle of the boundaries for the 10 and 40 mg ml^{-1} samples and just outside the upper boundary for the 20 mg ml^{-1} sample. As such, the ability of HPLC for quantifying SAP mass per square centimetre of nonwoven had been demonstrated and would represent a feasible quality control technique to use during PCL/P_{11}-8 nonwoven web manufacture. Of note, the HPLC result for the 20 mg ml^{-1} sample falling just outside the calculated boundaries could be explained by human error during sample preparation or may be further reduced by increasing the sample size, as only three were used, but its closeness to the upper boundary indicates this is still a robust technique.

A similar method was used to detect and quantify the short antimicrobial peptide derived from bovine lactoferricin when electrospun with the polymer pullulan (Román et al., 2019). As done here, the electrospun web was redissolved and passed

through an HPLC column. Whilst the UV detector could have been used at 280 nm wavelength as the peptide had the sequence RWQWRWQWR, containing four tryptophan residues, a 210 nm wavelength was used to detect the peptide bonds instead. Similar to what was observed here, a peak (this time at a retention time of 5.9 min) is observed in the redissolved polymer-peptide web and the peptide solution control, but not in the redissolved polymer-only sample. Of note, detecting at this wavelength would also allow peptides that do not contain tryptophan residues to be detected and quantified.

However, a “peptide incorporation efficiency” value was given as 31%, but it was not clear what this refers to or how this value was calculated. The work done herein using PCL and P_{11}-8 is thus the only example where peptide amount (SAP, in this case) has been determined per square centimetre of sample using HPLC, giving a relevant measure of peptide for the dry electrospun nonwoven.

Further, it should be noted that other techniques have been used to confirm SAP incorporation in electrospun nonwovens. EDX has been used through the detection of nitrogen in the sample (Nune et al., 2015; Gharaei et al., 2016; Nune et al., 2016) and other methods that indirectly confirmed SAP incorporation in PCL/P_{11}-8 webs has included circular dichroism, Fourier transform infrared spectroscopy (FTIR), attenuated total reflection (ATR)-FTIR and confocal microscopy of a fluorescein-conjugated P_{11}-4 (Gharaei et al., 2016). Elsewhere, carbon-hydrogen-nitrogen (CHN) analysis, X-ray photoelectron spectroscopy (XPS) analysis, thermogravimetry–differential thermal analysis (TG-DTA), differential scanning calorimetry (DSC) and confocal microscopy of dansylated primary amines has also been used to identify RADA16-I-BMHP1 SAPs when electrospun with PLGA (Nune et al., 2015; Nune et al., 2016). However, all of the above serve as qualitative measures of SAP inclusion rather than providing a quantitative measure per square centimetre of material. Further, SEM-EDX was unable to detect presence of nitrogen in the PCL/P_{11}-8 10 mg ml^{-1} sample (Gharaei et al., 2016) evidencing the applicability and precision of HPLC for detecting and quantifying the SAP.

HPLC was employed herein to accurately separate the polymer and peptide components before measuring absorbance of the relevant fraction believed to be P_{11}-8, which was then confirmed using mass spectrometry. It may be possible to use a much simpler methodology and much cheaper equipment than that attempted

above to detect and quantify SAP or peptide in these samples, which could constitute a more accessible quality control process for a manufacturing setting. Use of a bench-top UV/Vis spectrophotometer would allow measurement of P_{11}-8 absorbance at 280 nm, following dissolution of a sample in a solvent as done herein, and should be able to detect in the concentration ranges required here depending on the instrument (Thermo Fisher Scientific, 2017).

However, PCL does absorb to some degree at a 280 nm wavelength, due to the absorption of the carbonyl (C=O) group (Martins-Franchetti et al., 2008; Abdelrazek et al., 2016), and use of absorbance at 280 nm wavelength for protein concentration determination is recommended in pure samples to avoid skewing results. Further, simply using a blank PCL control would not be accurate as the concentration of a polymer-only sample would not be equivalent to a polymer-peptide sample.

To overcome the above limitations, use of colourimetric assays would allow measurement of peptide at a different wavelength away from 280 nm. The Pierce 660 nm, Bicinchoninic acid (BCA) assay and Bradford assay would allow measurement of peptide concentration at wavelengths above 280 nm (660, 562 and 595 nm, respectively) at the concentration ranges here (Thermo Fisher Scientific, 2017), where PCL is unlikely to have an effect (Abdelrazek et al., 2016). Whilst the author could not find examples relating to electrospun nonwoven with SAP or peptide incorporation, Bagher et al. (2016) used the Bradford assay to quantify concentration of immobilised collagen on the surface of electrospun PCL fibres at 15 µg cm^{-2}. Similarly, Patel et al. (2020) determined total protein content in the range 66-79 µg cm^{-2} for an electrospun PCL-poliglecaprone scaffold coated with HuBiogel™ human ECM-derived material.

Similarly, bench-top fluorometers would also avoid issues of measurement around 280 nm by binding of specific fluorescent dyes and measuring away from 280 nm and would also detect at the concentration ranges here (Thermo Fisher Scientific, 2015), but could also allow detection of much lower concentrations. These would both represent a cost effective measurement methodology, as the equipment and reagents are relatively inexpensive.

Based on the above, HPLC could be used to quality control PCL/P_{11}-8 electrospun webs. This can be broadened to any web containing a peptide, not just SAP, spun

with a polymer that would not interfere with absorbency around 210 nm wavelength to detect the peptide bonds, or 280 nm if the peptide contained a tryptophan residue. Whilst this is a destructive technique, it is feasible that samples could be taken post-production, redissolved and analysed to calculate the amount of peptide in the web. This not only provides more accurate data than the qualitative methods outlined above but also a more precise method, as smaller amounts can be detected than, for example, with EDX. To avoid the setup and maintenance cost of an HPLC setup in a manufacturing quality control setting, use of a colourimetric assay for measuring peptide concentration with a spectrophotometer or fluorometric assay with a fluorometer could be feasible for avoiding interference by PCL, rather than attempting to separate the components before quantifying. Once a manufacturing methodology has been established, these methods could be used to ensure peptide amount falls within desired ranges; peptide was evenly distributed within the web; identify the amount of usable material from production by excluding areas below a threshold (such as those towards the edge of webs); and could be optimised to a much shorter time frame than that done here, potentially within hours of production.

4.4 Summary

The purpose of this chapter was to determine whether an aligned fibrous electrospun PCL/P_{11}-8 nonwoven could be produced and to characterise the structure of the resulting aligned fibre scaffold. Subsequently, electrospinning of PCL with P_{11}-8 on to a rotating collector was able to produce a fibre web with a bimodal distribution of fibre diameters, consisting of a submicron fibre network co-existing with a nanoscale fibre network. The high surface velocity of the collector was predicted to promote alignment of the fibre web, but only did so for the submicron fibre network that aligned to a similar degree to the PCL-only controls. In contrast, a secondary nanoscale fibre network was also present, and appeared to retain a random and semi-orthogonal nanofibre orientation, with network abundance positively correlating with the concentration of SAP in the spinning solution. Despite the high surface velocity of the collector, nanofibres appeared able to form undisturbed without breakage.

Further, and also despite the high surface velocity of the collector, alignment of the secondary nanofibre network appeared unaffected in relation to the machine direction. Normally, collector surface velocity affects alignment of fibres in electrospun webs, as evidenced by the PCL-only controls spun prior to SAP inclusion and the effect on the PCL/P_{11}-8 submicron fibre network. However, the results herein indicate collector surface velocity does not affect the alignment of the PCL/P_{11}-8 nanoscale fibre network in the same way it affects the submicron fibre network, and potentially indicates some nanofibres are forming post-deposition.

Lastly, a reliable methodology for detecting and quantifying SAP per square centimetre was suggested for the first time using HPLC and mass spectrometry. A second methodology is also suggested using UV/Vis spectrophotometry, colourimetric assays or fluorometric assays, which may present a more cost-effective methodology for uptake in a less well-equipped laboratory, such as in a manufacturing setting.

Chapter 5

Physical Characterisation and *in vitro* Neurite Extension of Aligned Fibre Scaffolds

5.1 Introduction

This chapter explores the ability of the aligned electrospun PCL/P_{11}-8 nonwoven scaffolds produced herein to modulate neurite extension *in vitro* as a proxy for aligned tissue regeneration, along with the physical characterisation of the scaffold.

In the previous chapter, the feasibility of manufacturing aligned electrospun PCL/P_{11}-8 webs was detailed for the first time, including characterisation of the fibre web, and detection and quantification of the SAP post-spinning. As seen previously, a bimodal distribution of fibre diameters was observed in the resulting fibre web (Gharaei et al., 2016). However, herein it was further discovered that the use of a rotating drum as a collector during electrospinning only promoted alignment of submicron diameter fibres in the machine direction, but did not affect the alignment of the nanoscale fibre network. This nanoscale network was distributed throughout the web in dense, randomly orientated regions with no discernible alignment in the MD, as well as aligned orthogonal between adjacent aligned submicron fibres. As such, whilst part of the fibre web was directionally aligned in the MD as desired for spinal cord tissue regeneration, the effect on neurite extension by the aligned submicron diameter fibres co-existing with randomly orientated and orthogonally-aligned nanoscale fibres remained unknown, as well as the effect on other properties important for evaluating the scaffold with respect to spinal cord tissue regeneration.

Accordingly, the purpose of this chapter was to determine the neurite extension, tensile and wetting properties of the aligned fibre scaffolds with and without the presence of SAP and the resulting secondary randomly oriented fibrous network.

5.2 Materials and Methods

5.2.1 Manufacture of Electrospun Nonwoven Scaffolds

Aligned electrospun nonwoven sample were manufactured to serve as a directional guide for neurite extension. Samples were prepared as previously described in Chapter 4.2.1. Briefly, PCL average M_n 80 kDa (Sigma-Aldrich, UK) was dissolved in HFIP (Sigma-Aldrich, UK) overnight by stirring, to form a 6% w/w spinning solution. SAP P_{11}-8, (CH_3CO-Gln-Gln-Arg-Phe-Orn-Trp-Orn-Phe-Glu-Gln-Gln-NH_2) (SAP content 75%, HPLC purity of 96%) (C.S. Bio Co., USA) was added into the spinning solution at 10, 20 or 40 mg ml^{-1} and stirred for a further 24 h before use. The spinning solution was loaded in to a 10 ml syringe (Sigma-Aldrich, UK) fitted with an 18 gauge blunt needle. To electrospin, the loaded syringe was connected to a power supply and placed opposite a grounded collector (Fig. 3.1A) with the following spinning parameters; flow rate, 1 ml h^{-1}; needle-to-collector distance, 110 mm; applied voltage, 25 V; spin time, 2 h. A stationary collector was employed for collection of randomly orientated control samples (Fig. 3.1B) and a rotating drum spinning at up to 30 m s^{-1} was used to collect aligned electrospun webs (Fig. 3.1C).

5.2.2 Neurite Extension

Neurite alignment was studied to determine the ability of the aligned electrospun nonwoven to promote aligned neurite extension. The direct result of SCI is the inability of neuronal cells to send impulses along cell processes in the damaged area. As an emerging treatment for SCI is resection of the damaged area and potential repopulation of the gap between the proximal and distal stumps, effective alignment of cell processes could translate into functional regeneration. Samples of nonwoven were cut out using a 10 mm circular punch and attached to ethanol-sterilised glass cover slips using 3M™ Steri-Strip™. Samples were secured down to glass coverslips to prevent movement during seeding and media changes, and to allow easy removal from well plates for staining and imaging. All samples were coated with poly-D-lysine (PDL) to promote cell adhesion by electrostatic interactions.

Due to the direct result of SCI being the inability of neuronal cells to send impulses along cell processes, a neuron-like *in vitro* cell model was desired for investigating neurite extension. PC12 neuron-like cells (ATCC CRL 1721) were chosen due to their ability to sprout neurites in response to nerve growth factor (NGF), which can be easily incorporated into cell culture media. The choice to use PC12 cells as an initial model was reinforced by the local knowledge for optimal growth within the Institute for Medical and Biological Engineering at the University of Leeds and their relative inexpensiveness compared to primary cells. PC12 cells were grown in RPMI 1640 (Lonza, UK) media supplemented with 10% heat-deactivated horse serum (Sigma-Aldrich, UK), 5% foetal bovine serum (FBS) (Sigma-Aldrich, UK), 1% L-Glutamine (Sigma-Aldrich, UK) and 1% penicillin/streptomycin (Sigma-Aldrich, UK). Nonwoven was seeded with 1 x 10^5 cells, and after 24 h to allow for cell adhesion, media switched to include 100 ng ml^{-1} recombinant human β-NGF (BioLegend, USA). Media was changed every 2-3 days.

After 14 days, samples were fixed by immersing in 10% neutral buffered formalin (Sigma-Aldrich, UK) for 15 min, and permeabilised by immersing in 0.2% Triton X-100 (Sigma-Aldrich, UK) for 20 min. Samples were stained using Mouse Anti-Neuron-specific β-III Tubulin Monoclonal Antibody (clone TuJ-1) (MAB1195, Bio-Techne, USA) for 1 h at room temperature, followed by Polyclonal Rabbit Anti-Mouse Immunoglobulins/FITC (F0232, Dako, Denmark) for 1 h at room temperature in the dark. Samples were washed using phosphate buffered saline (PBS) (Sigma-Aldrich, UK) between each step and imaged using a Leica SP8 Confocal Laser Scanning Microscope. Neurite alignment was obtained using ImageJ. At least 100 neurites were used to determine measurements, with three replicates per sample.

5.2.3 Tensile Testing

Uniaxial tensile testing was employed to determine the tensile properties of samples and therefore their ease of handling for future clinical manipulation and manufacture. Where possible, steps advised by ISO 9073-3 (1989) (Test methods for nonwovens – Part 3: Determination of tensile strength and elongation) were adhered to; specifically, force was applied longitudinally to a test piece of a specified length and width at a constant rate of extension for determination of tensile properties using the cut strip method. Values for ultimate tensile strength (UTS) have been provided.

However, due to material size constraints, samples could not be taken 100 mm from the material edge, nor at the recommended dimension of 50 mm ± 0.5 mm. Whilst a 200 mm jaw separation on the uniaxial testing apparatus and constant rate of 100 mm min^{-1} is recommended, it is stated that if deviations from this are used then they are clearly noted, as has been done herein. For clarity, a shorter gauge length (jaw separation) was used herein due to apparatus constraints, and a slower strain rate (constant rate) was utilised for relevance to strain rates likely experienced by spinal cord tissue natively.

An ElectroPuls E3000 (Instron, USA) running associated WaveMatrix software was fitted with a 250 N load cell. Nonwoven samples were cut into 20 x 5 mm strips in the machine direction (MD) and cross direction (CD) and fixed across a paper window with a 10 mm gauge length using double-sided tape. Sample thickness was determined prior to use using a micrometer (Mitutoyo, Japan). Samples were loaded to failure at a rate of 1 mm min^{-1}. Stress-strain curves were derived from load-displacement data and tensile modulus defined as the slope of the linear portion of the stress-strain curve for the 5% of the graph following the identified toe region.

Mean Young's modulus values were compared to determine statistically significant difference between aligned PCL and aligned PCL/P_{11}-8 at 40, 20 and 10 mg ml^{-1}. As there were more than two independent variables, a one-way analysis of variants (ANOVA) was used. Data was initially checked for normality using a Shapiro-Wilk test and homogeneity of variance (HOV) using Levene's test (required assumptions of ANOVA). For MD values, data was normal and homogeneous. Statistical significance was concluded if *p*-value was less than 0.05. A Tukey Honestly Significant Difference (HSD) post-hoc test was used to determine differences between individual groups due to the HOV being met. For CD values, data was normal but not homogeneous. However, this violation was considered permissible due to equal sample sizes between groups. Statistical significance was concluded if *p*-value was less than 0.05. A Games-Howell post-hoc test was used to determine differences between individual groups due to the HOV violation.

Mean Young's modulus values were also compared between random PCL in both the MD and CD. A two-sample T-test was used as groups were from two separate populations and was two-tailed as the concern was only for difference in general rather than in a specific direction. Data was normal and homogeneous. Statistical

significance was concluded if p-value was less than 0.05. All statistics were done using OriginPro software (OriginLab Corporation, USA).

5.2.4 Wettability

Wettability was studied to determine the behaviour of the electrospun nonwoven in a highly hydrated environment, such as the spinal cord, as well as related properties such as cell adhesion and degradation. Wettability was conducted using contact angle goniometry (Fig. 5.1). Samples of nonwoven were cut out using a 10 mm circular punch and attached to glass slides using double-sided tape to ensure samples were as flat as possible. Using an FTA 4000 contact angle goniometer (First Ten Angstroms, UK), a droplet of ultrapure water (Sigma-Aldrich, UK) was placed on the surface of the sample. The inside angle of the droplet was measured over 15 s using the associated software to give a dynamic assessment of wettability, with three replicates per sample.

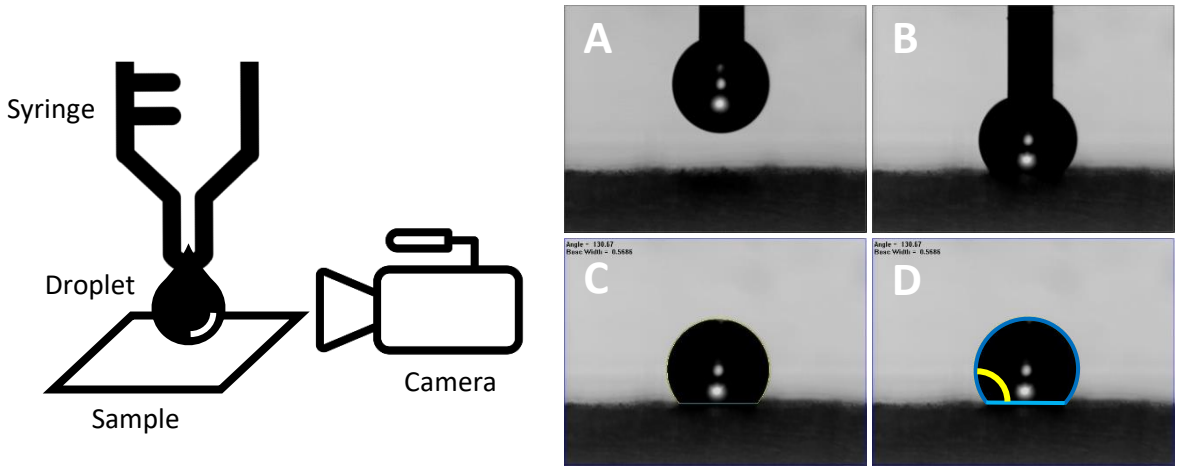

Figure 5.1 Diagram of the wettability test method. Contact angle goniometry was used to determine the angle of a droplet of water on the surface of the electrospun nonwoven webs, as a measurement of wettability. To do so, (A) a droplet of water at the end of a blunt needle is (B) brought down into contact with the sample and (C) retracted, before recording the action of the droplet over time. (D) Subsequently, the video is analysed and the internal angle of the droplet measured. This is done by manually setting the base of the droplet (light blue) and the rounded part of the droplet (dark blue), with the software computing the internal angle of the droplet (yellow) for each frame.

5.3 Results and Discussion

5.3.1 Neurite Extension and the Importance of an Aligned Submicron Fibre Network

The primary interest when studying the PCL/P_{11}-8 webs was to determine the effect of the random and semi-orthogonal nanoscale network on the desired neurite alignment. Interestingly, despite the lack of fibre alignment in the machine direction of the secondary nanoscale network, neurite extension appeared unaffected. This is evidenced by the confocal images, where neurite extension is random on the random webs (Fig. 5.2A-B) and unidirectional on the aligned webs (Fig. 5.2C-D), irrespective of SAP inclusion. In fact, neurite extension mirrored the alignment of the underlying submicron network, as shown by the similarity of the black and grey columns in the bar graphs (Fig. 5.2E-H), but not by the secondary nanoscale network. This finding is reinforced by the fact this was observed even for the nonwoven with the highest SAP concentration of 40 mg ml^{-1}, with the highest abundance of nanoscale network. Thus, it was observed that the alignment of the larger diameter submicron fibres in the web was found to be most important for ensuring neurite extension, rather than the smaller nanoscale network.

In relation to the polymer-SAP nonwoven literature, an aligned PLGA/RADA-16-I-BMPH1 nonwoven scaffold has been shown to promote elongation of Schwann cells (Nune et al., 2017; Nune et al., 2019) and the work here shows a similar polymer-SAP nonwoven can also support neurite extension from PC12 neuron-like cells. The PLGA/RADA-16-I-BMPH1 scaffold also showed aligned tissue regeneration *in vivo* that was improved compared to the polymer-only control (Nune et al., 2017). Whilst beyond the scope of this work, unless the *in vivo* result is solely a response to the cell binding sequence of RADA-16-I-BMPH1, a similar result may be possible using P_{11}-8 based on the early results seen here.

This latter point, on the regenerative effect of SAPs without cell binding sequences, is also supported by the significantly higher GAP-43+ neurons, indicating higher axon sprouting, and significantly improved Basso-Beattie-Bresnahan (BBB) score for a rat contusion model injected with an LDLK12 SAP hydrogel (Gelain et al., 2012). An FAQRVPP cell-binding sequence has been subsequently added (with the SAP

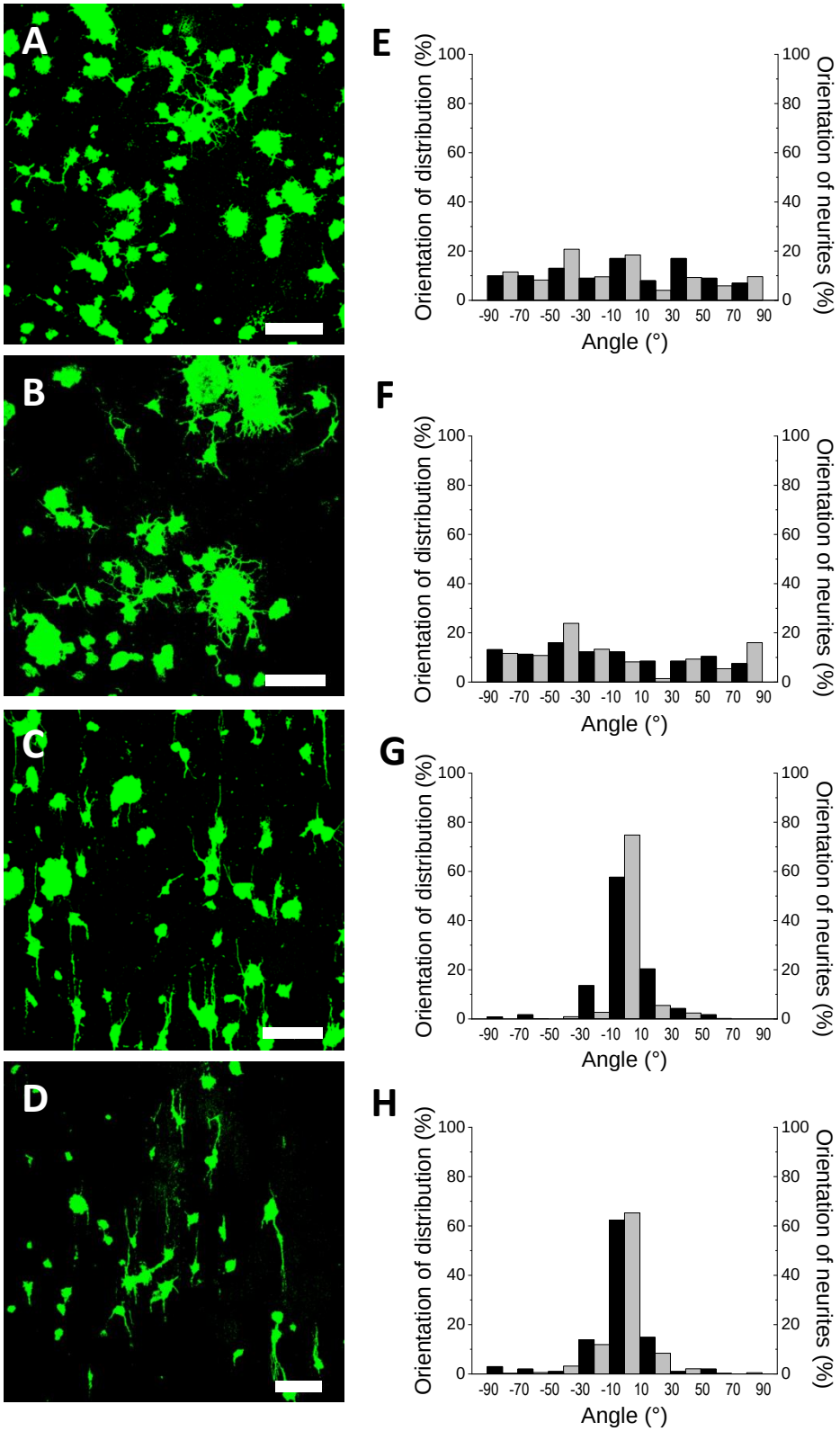

Figure 5.2 Confocal images and graphs showing neurite extension of PC12 cells after 14 days compared to alignment of the underlying nonwoven fibre web. (A) Random PCL, (B) random PCL/P_{11}-8 40 mg ml^{-1}, (C) aligned PCL, and (D) aligned PCL/P_{11}-8 40 mg ml^{-1}. Scale bar is 200 µm. (E-H) Graphs show the directionality of the neurites (grey) and the underlying submicron network (black). *n* = 100. Scale bar is 200 µm.

renamed Ac-FAQ) and the combined PCL-PLGA/Ac-FAQ nonwoven implanted into a rat spinal cord injury model, showing SMI31+ neurofilaments indicating axonal regeneration, reduced immune response compared to sham, and comparable effect on neuroglial viability and differentiation compared to Cultrex® commercial ECM hydrogel (Raspa et al., 2016). Whilst this effect could be solely down to the cell-binding sequence, the earlier work presenting the positive effect of the SAP as a hydrogel indicates regeneration may occur from the SAP itself.

Of note, a PLLA/RADA16-IKVAV polymer-SAP nonwoven scaffold also had a positive effect *in vitro* on neurite outgrowth of mouse NSCs and was the only other polymer-SAP web identified in the literature as having a nanoscale and submicron network similar to the PCL/P_{11}-8 web here (Zhao et al., 2018). However, the promotion of the neural pathway over glial differentiation may have been solely down to the laminin-derived IKVAV sequence, but as no SAP without a binding sequence was included this is difficult to ascertain. Further, the limited nanoscale network compared to that generated here, and the fact this was a random nonwoven, also limits comparison. Further still, for both the PLLA/RADA16-IKVAV nonwoven and PCL-PLGA/Ac-FAQ nonwoven, contact angle remained high at 92° and 135°, respectively, indicating different SAPs can impart different wettability to polymer nonwovens, which may also affect cell response.

Whilst PLLA/RADA16-IKVAV nonwovens have shown a degree of nanoscale network alongside the submicron network, the abundance of the nanofibres was very low (Zhao et al., 2018). In comparison, there are a number of publications that have reported similar nanoscale and submicron networks with other materials, but none of these papers included any cell work, and all networks were randomly orientated anyway (Ding et al., 2006; Kimmer et al., 2009; Parajuli et al., 2009; Barakat et al., 2009; Nirmala et al., 2010; Pant, Bajgai, Nam, et al., 2010; Pant, Bajgai, Yi, et al., 2010; Pant et al., 2011; Wang et al., 2011; Oh et al., 2012). Of note, one publication, which did have a bimodal distribution of fibre diameters, but submicron to micron rather than nanoscale to submicron, indicated epithelial CHO-K1 cells preferentially bound and extended along submicron fibres over the micron-sized fibres (Gentsch et al., 2010). This preference for submicron sized fibres seems to appear throughout the literature, as detailed in Chapter 2.5.1.2.

Whilst there is an indication submicron sized fibres can be favoured over micron sized fibres when occupying the same space (Gentsch et al., 2010), the work presented herein indicates submicron fibres can be preferable to nanofibres; at least for neurite outgrowth and cell alignment from PC12 cells. Whilst these affects may be cell-type dependent, this builds on a body of literature that has previously indicated a preference for submicron fibres over nanofibres when nonwovens with different mean fibre diameters have been evaluated separately (Yang et al., 2005; Wang et al., 2010; He et al., 2010; Wang et al., 2012; Daud et al., 2012; Qu et al., 2013).

To reinforce this point, the effect of submicron being preferable over nanoscale has also been observed for structures other than fibres. Grooves of 100 nm width created by nanoimprint lithography on PMMA were poorer at promoting axonal guidance than larger submicron grooves, and this was augmented as axon diameter increased (Johansson et al., 2006). Further, DRG grown directly on polystyrene with unidirectional heat-moulded surface roughness, showed poor alignment when root-mean-square values were below 100 nm and increasing alignment as they became submicron (Walsh et al., 2005). Similar results were observed for astrocytes (Biran et al., 2003), adult meningeal cultures and postnatal day 1 meningeal cultures (Manwaring et al., 2004), with the relative alignment of the glial cells also influencing the degree of alignment of DRGs grown on top (Biran et al., 2003; Walsh et al., 2005).

Despite the apparent role of submicron fibre alignment in promoting neurite alignment discovered by the present research, previous researchers have highlighted the importance of nanoscale structures in promoting alignment. SAP-only materials that assemble into fibres of similar size to that of the nanoscale fibres observed here have been tested and there is evidence aligned nanoscale fibres made solely of SAP can influence cell alignment. Aligned hydrogels made of SAP amphiphiles that self-assemble into fibre bundles of 30 nm diameter promoted aligned outgrowth of hMSCs (Mata et al., 2009; Zhang et al., 2010). Whilst not aligned, other SAPs of 10-40 nm fibre diameter have been shown to support neurite outgrowth of PC12 cells and mouse neurons (Holmes et al., 2000), NSC attachment and differentiation (Gelain et al., 2006), neural cell division and migration from an *ex vivo* rat brain organotypic model (Semino et al., 2004), and regeneration of optic tract

in hamsters (Ellis-Behnke et al., 2006). Neurite outgrowth from NPCs has also been observed, and whilst the publication stated fibre diameter was 5-8 nm, SEM images seemed to indicate this was really in the region 20-40 nm (Silva et al., 2004). Together, this shows that fibre diameters below 100 nm can support neural and precursor cells and promote alignment, but these publications only show the effect when these are the only fibre diameters present.

As such, this work further reinforces the preference of cells to align along submicron fibres, but provides evidence this occurs even when a nanoscale network is also present that is not aligned in the same direction.

5.3.2 Nanoscale Fibres and their Impact on Macroscale Scaffold Stiffness

Whilst the nanoscale network appeared to have no effect on the alignment of extending neurites, it was hypothesized the random and semi-orthogonal network may lead to a measurable increase in stiffness of the web in the cross direction. Typically, aligned nonwovens are anisotropic; having augmented mechanical properties in the machine direction but poor mechanical properties in the cross direction. This can lead to difficulty in handling and even damage to the web during manufacture, and would possibly be a concern during clinical implantation as well. The improved mechanical properties were already noticeable in terms of handling the material post-production, but was subsequently confirmed by tensile testing in both the machine direction and cross direction.

Mean UTS values (± SD) in the MD were recorded as 49.2 ± 12.9, 4.4 ± 0.4, 42,4 ± 7.2, 58.4 ± 4.0 and 52.3 ± 14.9 MPa for aligned PCL, random PCL, and PCL/P_{11}-8 at 40, 20 and 10 mg ml^{-1}, respectively, and in the CD values were 0.7 ± 0.1, 4.1 ± 0.1, 4.0 ± 0.6, 60 ± 0.5 and 4.2 ± 0.4, respectively (Table 5.1).

However, owing to the nature of elastic polymers, the UTS occurs following plastic deformation and is of less importance for the case of a spinal cord regenerative scaffold. Of greater significance is the Young's modulus, which is the ability of a material to withstand changes in length when under uniaxial tension, and represents the stiffness of a material. Young's modulus is defined by the equation:

UTS ± SD (MPa)	PCL		PCL/P_{11}-8		
	Aligned	Random	40 mg ml^{-1}	20 mg ml^{-1}	10 mg ml^{-1}
MD	49.2 ±12.9	4.4 ±0.4	42.4 ±7.2	58.4 ±4.0	52.3 ±14.9
CD	0.7 ±0.1	4.1 ±0.1	4.0 ±0.6	6.0 ±0.5	4.2 ±0.4

Table 5.1 Table showing the ultimate tensile strength (UTS) values for PCL and PCL/P_{11}-8 at 40, 20 and 10 mg ml^{-1} in both the MD and CD.

$$E = \frac{\sigma}{\varepsilon}$$

Where, *E* is Young's modulus (Pa), σ is stress (Pa) and ε is strain, and is taken from the linear elastic region of the stress-strain curve.

In the MD, all align ed PCL and PCL/P_{11}-8 samples had a mean Young's modulus (± SD) above 100 MPa, and as high as 160 ± 22 MPa for aligned PCL-only (Fig. 5.3A). This is higher than aligned PCL-only webs in the literature, which have recorded Young's modulus values in the range 9.3 – 70 MPa with strain rates ranging from 1.8 – 60 mm min^{-1} (Li et al., 2007; Baker et al., 2008; Gaumer et al., 2009; McClure et al., 2009; Wang et al., 2009; Ionescu et al., 2010; Tseng et al., 2014; Thayer et al., 2016; Walser et al., 2016), but similar to the 120 ± 30 MPa recorded for a single PCL fibre (Tan and Lim, 2006). The increase observed herein may be due to the augmentation from the inclusion of SAP in the PCL-P_{11}-8 samples, but also due to the high alignment of the fibres and experimental setup used here; which may also explain the high result from the PCL-only sample.

However, whilst the high alignment in the machine direction lead to a high Young's modulus in the machine direction, stiffness in the cross direction for aligned PCL was as low as 0.19 ± 0.15 MPa (Fig. 5.3B). In contrast, a statistically significant increase in the Young's modulus was seen at all PCL/P_{11}-8 concentrations of 10, 20 and 40 mg ml^{-1} with values of 1.34 ± 0.11 MPa, 2.22 ± 0.16 MPa and 4.32 ± 0.69 MPa, respectively (Fig.5.3B). This concentration-dependent result, where increasing SAP in the nonwoven lead to an increase in Young's modulus in the cross direction, reflected the increase in abundance of the network observed in the SEM images herein and previously (Gharaei et al., 2016; Gharaei, 2017; Gharaei et al., 2020). Further, this is compared to the random PCL control, where no statistical significance

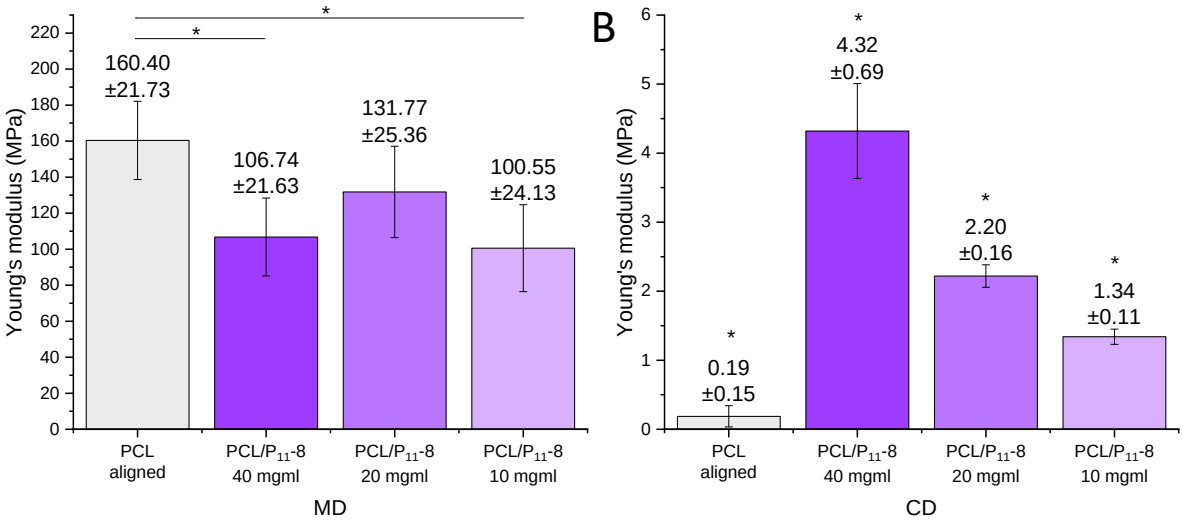

Figure 5.3 Graphs showing the Young's modulus of aligned PCL and aligned PCL/P_{11}-8 at 10, 20 and 40 mg ml^{-1}. (A) Machine direction (MD) and (B) cross direction (CD). Random PCL had similar modulus values in both MD and CD, with no significant difference (not shown). All aligned samples, whether PCL or PCL/P_{11}-8, had mean modulus values above 100 MPa in MD. In CD, aligned PCL had significantly lower modulus values than PCL/P_{11}-8, with modulus increasing with peptide concentration. *$p \leq 0.05$. Data is shown as mean ± SD. $n = 8$.

was seen in the Young's modulus in both the machine direction and cross direction, with values of 17.39 ± 2.02 MPa and 16.98 ± 1.24 MPa, respectively (data not shown).

Whilst it is well documented, even with just PCL and PCL-polymer blends, that higher alignment leads to higher Young's modulus values when mechanically loaded parallel to the machine direction (Li et al., 2007; Gaumer et al., 2009; McClure et al., 2009; Wang et al., 2009; Ahvaz et al., 2013; Tseng et al., 2014; Walser et al., 2016; Gao et al., 2017; Sheng et al., 2019), in only a small number of cases the dramatically reduced modulus in the cross direction has also been analysed (Li et al., 2007; Baker et al., 2008; McClure et al., 2009; Tseng et al., 2014).

Increases by almost two orders of magnitude for PCL-only samples have been seen prior, from 0.3 to 11.6 MPa (Li et al., 2007), 0.6 to 42.7 MPa (McClure et al., 2009) and 0.5 to 17.5 MPa (Tseng et al., 2014), but not by the three orders of magnitude seen here. The discrepancies between the above may be down to both features of the webs and experimental design, similar to those stated for the difference in Young's modulus values above. Whilst a similar degree of alignment with similar fibre diameters of 400-500 nm was observed for Li et al. (2007), a slower strain rate

of 0.1% s^{-1} and a preconditioning cycle prior to testing may explain the differences observed. Further, McClure et al. (2009) and Tseng et al. (2014) had larger fibres of 600-700 nm and 600-800 nm diameter, respectively, and both appeared to have a lower degree of alignment, with the former having a slower strain rate of 0.02% s^{-1}, and samples tested in wet conditions, and the latter at a faster strain rate of 10% s^{-1}. Further still, a difference of around one order of magnitude was observed for Baker et al. (2008), possibly down to the reduced degree of alignment with respect to the webs tested herein, the preload and preconditioning cycles used during testing, and the slower strain rate of 0.1% s^{-1}. Whilst images indicated fibre diameter was possibly submicron, this was not recorded and adds to the discrepancies.

Elsewhere, polymer-SAP webs have been mechanically characterised. Whilst not featuring aligned electrospun nonwovens and no visible additional nanoscale network, the SAPs EAK, RGD-EAK and EAbuK, as well as the non-SAP GE3M, have been electrospun with PCL and tensile tested (Dettin et al., 2015). Addition of RGD-EAK into these randomly orientated webs produced a linear increase in Young's modulus with increasing concentration, from 1.0 ± 0.1 to 9.6 ± 0.7 MPa, and higher than the 6.3 ± 0.5 MPa for PCL-only. However, enrichment with EAbuK saw erratic changes in Young's modulus as concentration increased, from 2.7 ± 0.2 to 4.8 ± 0.5 to 7.8 ± 0.8 to 2.8 ± 0.3 MPa, which was similar to that of EAK from 4.1±0.5 to 1.4 ± 0.2 to 6.3 ± 0.5 to 1.0 ± 0.1 MPa. Further, addition of the non-SAP GE3M into these randomly orientated webs produced a linear increase in Young's modulus with increasing concentration, from 1.2 ± 0.1 to 5.4 ± 0.4 MPa, despite the inability to self-assemble. As such, there is evidence SAP-polymer nonwovens can increase modulus values over polymer-only nonwovens. However, as not all SAP appears able to produce the same physical fibre structures when electrospun, not all are able to produce direct concentration-dependent changes in tensile mechanical properties to the degree seen by P_{11}-8 herein.

Whilst not all SAP-polymer electrospinning produces nanofibres, similar structures described as "spider-net" and "web-like" appearing alongside a submicron network have been seen when electrospinning other polymers, such as nylon with and without additional materials (Ding et al., 2006; Parajuli et al., 2009; Barakat et al., 2009; Nirmala et al., 2010; Pant, Bajgai, Nam, et al., 2010; Pant, Bajgai, Yi, et al., 2010; Pant et al., 2011), poly(acrylic acid) (Ding et al., 2006), poly(vinyl alcohol) with

added salts (Barakat et al., 2009), polyurethane with added salts (Barakat et al., 2009), polyurethane with MWCNTs (Kimmer et al., 2009), meta-aramid (Oh et al., 2012), PCL with PLGA (Gentsch et al., 2010), peptide-conjugated PLLA with PLGA (Gentsch et al., 2011), and gelatin (Wang et al., 2011).

For five of these publications, tensile mechanical properties were evaluated for randomly orientated webs (Barakat et al., 2009; Pant, Bajgai, Nam, et al., 2010; Pant, Bajgai, Yi, et al., 2010; Pant et al., 2011; Oh et al., 2012). Nylon spun at different applied voltages was also able to produce nanofibres, with no fibres at 12 V, the most abundance at 22 V and a lower abundance at 32 V (Pant, Bajgai, Yi, et al., 2010). This was reflected in the improvement in UTS, with 22 V highest, followed by 32 V, followed by 12 V. Similar results were seen when spinning nylon with MPEG (Pant, Bajgai, Nam, et al., 2010) and nylon with TiO_2 (Pant et al., 2011), where the most nanofibre was seen at 1%, which translated into the highest UTS for both. Whilst Young's modulus values were not given in these publications, the stress-strain curves indicated Young's modulus also scaled with nanoscale network abundance. Meta-aramid spun at different concentrations also produced spider-net nanofibres, but only when the by-product $CaCl_2$ from production was left in (Oh et al., 2012). UTS increased with increasing concentration from 12% to 14% to 16%, which mirrored the increasing abundance and diameter of the nanofibres. Again, whilst Young's modulus was not given, stress-strain curves indicated the same increase with nanofibre abundance. Of note, once $CaCl_2$ was removed from the 14% sample, a dramatic increase in UTS, strain at break and Young's modulus was seen, and put down to the salt ions no longer interfering with hydrogen bonding of meta-aramid.

Lastly, it should be noted that the opposite has also been observed. Addition of 1.5% NaCl or $CaCl_2$ induced nanofibre formation when spun with nylon-6, improving strain at break and UTS (Barakat et al., 2009). Whilst Young's modulus values were again not provided, the stress-strain curves indicated lower modulus values with appearance of nanoscale network.

However, in short, in webs where nanofibres were most abundant, tensile mechanical properties were generally greatest (Barakat et al., 2009; Pant, Bajgai, Nam, et al., 2010; Pant, Bajgai, Yi, et al., 2010; Pant et al., 2011), and an augmentation of this effect was also observed when increasing concentration further

maintained abundance, but led to thicker fibres in both the nanoscale and submicron networks (Oh et al., 2012).

In summary, an electrospun PCL/P_{11}-8 web was created that showed a change in the abundance of a nanoscale network with SAP concentration, and this augmented tensile mechanical properties, particularly in the cross direction, that was measurable at the macroscale. Further, when nanofibres have been observed alongside submicron networks in randomly orientated webs, nanofibre abundance has reflected an increase in tensile mechanical properties, reinforcing the observations seen here in aligned webs.

5.3.3 The Effect of SAP on the Wettability of PCL/P_{11}-8 Electrospun Fibre Webs

As shown so far, addition of SAP into the spinning solution promoted nanoscale fibre production and bimodal fibre diameter distribution within the web, with abundance of the nanoscale network affecting the stiffness of the material. Beyond mechanical properties, wettability is a relevant material property for an implantable nonwoven medical device, considering the affect this could have on cell-binding and degradation. Therefore, the surface contact angle with respect to time was investigated.

The surface contact angle of water on the PCL/P_{11}-8 nonwoven was greatly reduced compared with the PCL-only control. An initial contact angle at t_0 of 131.0° was recorded for aligned PCL, but following SAP inclusion this reduced to 42.4°, 37.2° and 23.8° for the 10, 20 and 40 mg ml^{-1} samples, respectively (Fig. 5.4A). Images have been inset to show the dramatic change in wettability for the initial contact angle (Fig. 5.4B-C). Further, contact angle with respect to time was investigated by measuring the droplet per second, with all aligned PCL/P_{11}-8 samples reaching 0° within 2 s versus a sustained contact angle for the PCL-only control (Fig. 5.4A). This result is similar to that reported previously for random PCL/P_{11}-8 nonwovens (Gharaei et al., 2016; Gharaei, 2017), with respect to the 20 and 40 mg ml^{-1} samples. However, for the random 10 mg ml^{-1} sample a reduction of only around 10°

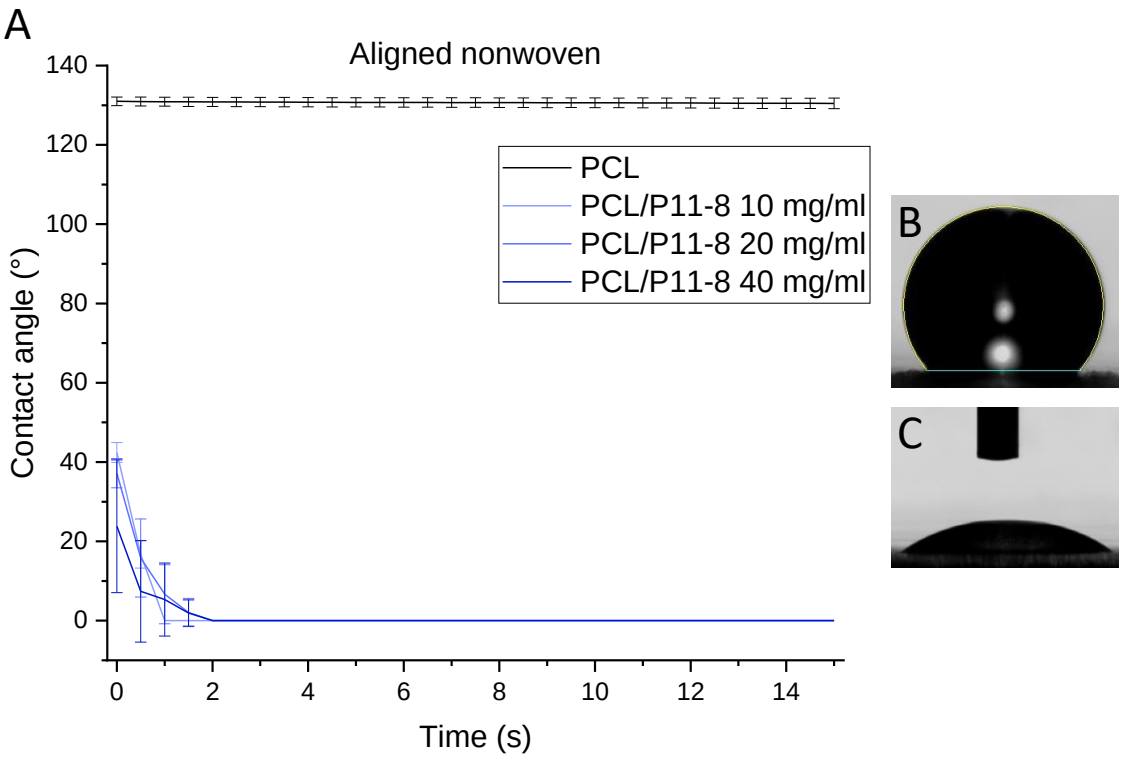

Figure 5.4 Wettability of PCL/P_{11}-8 aligned nonwoven. Dynamic wettability was investigated by placing a droplet of water on the material surface and measuring the internal contact angle over time. (A) PCL gave a high contact angle above 131.0° sustained for 15 seconds. Contact angle was reduced at t_0 for all PCL/P_{11}-8 webs, with initial contact angles of 42.4°, 37.2° and 23.8° for 10, 20 and 40 mg ml^{-1}, respectively, and all reduced to 0° within 2 seconds. Inset are images of the initial contact angle for (B) PCL and (C) PCL/P_{11}-8 40 mg ml^{-1}.

over 15 s from a t_0 of 79° was observed, versus a reduction to 0° also within 2 s for the aligned 10 mg ml^{-1} sample herein.

This complete reversal in wetting performance between the PCL-only and SAP-containing nonwovens can be explained in terms of the chemical structure of the respective materials. PCL is hydrophobic due to the five-carbon-long hydrocarbon repeating unit (Kwansa and Freeman, 2015). Addition of P_{11}-8 SAP introduces arginine, ornithine and glutamate charged amino acid sidechains, along with the polar uncharged side chain of glutamine. Theoretically, the hydrophobic faces of the SAP molecules will adhere to one another and the hydrophilic faces will be displayed on the outside of the higher self-assembled structures (Davies et al., 2006). This enables hydrogen bonding with water molecules and therefore improves hydrophilicity. Further, for hydrophilic materials, higher surface area promotes hydrophilicity further as the formation of an interface is energetically favourable

(Valipour M. et al., 2014). Thus, the appearance of nanofibres likely further drives hydrophilicity of the newly hydrophilic PCL-P_{11}-8 nonwoven.

Further still, the availability of directional capillary action within the small wetting radius between adjacent fibres is likely to explain the difference in the rate of wetting observed between the previously evaluated randomly orientated 10 mg ml^{-1} sample (Gharaei et al., 2016) and aligned 10 mg ml^{-1} sample herein. In the aligned nonwoven, the water droplet is actively drawn away from the initial contact point in the shortest distance. This is particularly apparent when considering the aligned PCL control, where improved capillary action is available, but not utilisable, due to the hydrophobicity of the material.

Poor cell adhesion to PCL-only nonwovens is known (Schnell et al., 2007; Swindle-Reilly et al., 2014), and whilst not investigated here, other publications have indicated the affect improved wettability has on cell-binding and growth. SAPs EAK, RGD-EAK and EAbuK, as well as the non-SAP GE3M, reduced contact angle with increasing concentration when combined with PCL and all promoted cell growth over PCL-only controls (Dettin et al., 2015), with similar results seen elsewhere for EAK and EAbuK (Danesin et al., 2012) and with PEO instead of PCL (Brun et al., 2011). Whilst the result with RGD-EAK could be explained by the cell-binding motif, the results with the other SAPs and non-SAP that lack this feature indicate cell attachment can be enhanced possibly through wetting performance alone with a SAP or peptide.

Further, similar results have been observed when contact angle has been reduced for PCL using other methods. Growth of human placental endothelial cells (HPECs) on PCL/PVA blended webs improved versus PCL-only samples when contact angle reduced to 0° (Kim et al., 2006), as seen here. Plasma treatment of aligned PCL fibres also reduced contact angle, from 77° to 63°, and increased fibroblast proliferation more than four-fold (Arabi et al., 2014). Whilst subsequent sodium hydroxide treatment was used to increase surface roughness, the authors believed the similar improvement in fibroblast proliferation was down to the improved wettability of 39°.

Further still, all cell experiments herein were conducted by coating PCL and PCL/P_{11}-8 nonwoven samples in PDL first, to provide a positively charged surface for

electrostatic interactions with negatively charged cell membranes (Karmiol et al., 2008). This material is widely used and commercially available for the same purpose and there is no reason why PDL or other materials, such as collagen (Schnell et al., 2007) or elastin (Swindle-Reilly et al., 2014), which have been shown to aid cell attachment with PCL, could not be used to coat as long as this does not disturb the cell guidance functionality. Poor binding of such adhesion-mediating molecules themselves, leading to poor cell adhesion and even spontaneous detachment of cell sheets, has been reported for some highly hydrophilic polymers (Bacakova et al., 2011). However, it should be noted this was for polymer films rather than electrospun nonwovens, of which fibre morphology may aid cell adhesion, and the authors also noted the mobility of PEO chains in the films augmented poor cell adhesion. With regards to the composite nonwoven-hydrogel scaffold herein, the fact a collagen hydrogel is planned to make up part of the device may overcome any cell attachment issues faced by the PCL-only or PCL/P_{11}-8 fibres anyway.

Again, whilst degradation has not been investigated directly herein, resorption of the implanted tissue regenerative scaffold can be affected by wetting performance, and this is noteworthy as the ideal outcome is concurrent tissue regeneration.

PCL is well-known for its slow degradation time compared with other synthetic polymers used as biomaterials. It has been shown PCL bioresorption initially starts with a reduction in molecular weight, followed by break-up of the material and mass loss when molecular weight reaches around 5000, followed by phagocytic ingestion and digestion (Pitt and Schindler, 1984; Woodward et al., 1985), with no accumulation within body tissue when tested *in vivo* (Pitt et al., 1981; Sun et al., 2006). The high hydrophobicity of PCL affects the rate of hydrolysis, which is the initial degradation reaction prior to the loss of monomeric and oligomeric material from the bulk polymer mass, known as erosion (Davison et al., 2014).

However, as described in the results above, SAP inclusion into the web reverses the wetting performance of PCL and likely increases the rate of hydrolysis and subsequent degradation. As the anisotropy of the web is not envisioned to affect degradation and the degree of wetting of the material is no different between the random samples tested previously (Gharaei et al., 2016; Gharaei, 2017) and the aligned samples created herein, it can be inferred a similar degradation profile may

be expected. From previous experiments, it is known that addition of P_{11}-8 into the nonwoven and incubation in deionised water at pH 7.5 prompted a mass loss of around 5% after 1 h, increasing to 13.1% after 7 days (Gharaei, 2017; Gharaei et al., 2020). It was suggested this represented around 55% of the SAP put in at the start, considering the PCL-only control did not change in mass throughout the 7 days and thermogravimetric analysis results reinforced the notion mass loss was solely from the SAP component.

Whilst this suggests a large percentage of the initial SAP is no longer available after 7 days, SEM images of the nonwoven show the bimodal distribution of fibre diameters remains intact. This further indicates both submicron and nanoscale networks are composite fibres of PCL and P_{11}-8 and suggests fibres of PCL/P_{11}-8 may be available for cell-guiding and tissue-structuring functions weeks after implantation. Further, whilst mechanical performance reduces with time (Bölgen et al., 2005), this is of less importance in a non-weight bearing tissue such as the spinal cord; as long as fibre structure remains intact long enough to adequately guide tissue regeneration. This is of further regard to the nonwoven created herein, as the larger fibres that provide the cell-guiding function are expected to remain intact for longer, due to the reduced degradation rate from the higher surface area to volume ratio (Bölgen et al., 2005).

However, it should be noted that degradation is likely enhanced *in vivo* due to the availability of the foreign body response, autocatalysis, radical interactions and enzymatic catalysis (Pitt and Schindler, 1984; Woodward et al., 1985; Bölgen et al., 2005; Sun et al., 2006; Bartnikowski et al., 2019). Further, medical grade PCL has not been used herein and there is evidence to suggest this material may degrade at a different rate (Lam et al., 2009; Seyednejad et al., 2012). As such, these points would need to be considered for any clinical translation.

In summary, electrospun webs showed a complete reversal in wetting performance following SAP introduction, with a contact angle of 0° for PCL/P_{11}-8 versus 131° for PCL-only webs. A reduction in initial contact angle with increasing SAP concentration was observed, but this was largely irrelevant as within 2 s contact angles reduced to 0°. This was similar to the results obtained previously for random PCL/P_{11}-8 webs (Gharaei et al., 2016; Gharaei, 2017), but likely augmented by the

availability of capillary action from the highly aligned submicron network. Whilst there is evidence to suggest a reduction in contact angle can both improve and weaken cell attachment, when considering this material is planned as part of a composite nonwoven-hydrogel scaffold this may be less of an issue. Further, based on the wetting performance seen here, a similar degradation profile to that observed previously for random PCL/P_{11}-8 may be expected (Gharaei, 2017; Gharaei et al., 2020).

5.4 Summary

The purpose of this chapter was to determine whether an aligned PCL/P_{11}-8 nonwoven could promote *in vitro* neurite extension, as a proxy for aligned tissue regeneration, and also to investigate the tensile and wetting properties of the electrospun nonwoven fibre web. Despite the nanoscale network not exhibiting the desired alignment in the MD, neurite alignment was still clearly observed in the MD, modulated primarily by the high degree of fibre alignment in the underlying submicron network. Interestingly therefore, neurite extension was largely unaffected by the lack of nanoscale alignment present within the PCL webs containing SAP. Furthermore, it was discovered that the nanoscale network increased the stiffness of the web in the cross-direction, improving the manual handling of the webs useful for manufacturing and clinical purposes, and notably to a scaffold considered as highly aligned to cells. Further, peptide inclusion dramatically altered the wettability profile from highly hydrophobic PCL to highly hydrophilic PCL/P_{11}-8, which may have cell binding, tissue integration and degradation benefits as a tissue regenerative scaffold.

Chapter 6

Manufacture and Optimisation of Hydrogel Properties

6.1 Introduction

This chapter reports the manufacture and characterisation of collagen-glycidyl methacrylate (GMA) hydrogel for the composite nonwoven-hydrogel spinal cord scaffold. Optimisation of hydrogel properties prior to combining with the nonwoven was desired to ensure three-dimensional cell encapsulation was possible and demonstrate the versatility of the collagen-GMA hydrogel system.

As shown in Chapter 4, highly aligned nonwovens of PCL and PCL/P_{11}-8 were electrospun using a drum rotating at 30 m s^{-1}. Further, as shown in Chapter 5, SAP addition promoted nanofibre assembly in the web that imparted mechanical reinforcement in the CD, useful for manual handling of the webs during manufacturing and clinical use, and reversed the wetting properties of the web. Most importantly, SAP addition did not affect the desirable aligned neurite extension behaviour promoted by aligned submicron fibres.

However, despite the favourable properties imparted by the SAP and the favourable alignment using the setup herein, neurite extension occurs in two dimensions at the cellular level on a nonwoven and therefore lacks the ability to space-fill a cavity. Thus, the addition of a hydrogel to form a composite nonwoven-hydrogel scaffold was theorised to maintain the favourable properties imparted by the nonwoven above, as well as adding space-filling capability and providing a three-dimensional, hydrated and mechanically-optimised environment for regeneration.

Collagen functionalised with GMA was believed to be a strong candidate for the hydrogel component of the scaffold due to the biocompatibility of collagen and its abundance, both globally and locally, as a source material.

Further, some mechanical characterisation of this hydrogel system had already been investigated, giving some relevant data to compare to, as well as extensive chemical characterisation, indicating the robustness and flexibility of the system had not yet been fully explored (Tronci et al., 2013; Tronci et al., 2015). This was reinforced by the local knowledge for producing and using this hydrogel system within the research group. Whilst this hydrogel system had been broadly investigated as a wound dressing and regenerative scaffold, and investigated as part of a dual-phase hydrogel with hyaluronic acid functionalised with methacrylic anhydride for bone tissue regeneration by a separate group (Zhang et al., 2019), successful three-dimensional encapsulation of cells in a single-phase collagen-GMA hydrogel had not yet been achieved, as well as specific characterisation for spinal cord tissue regeneration.

Accordingly, the purpose of this chapter was to investigate collagen-GMA hydrogel properties, including suitability for three-dimensional cell encapsulation, resulting cell viability and mechanical properties as a spinal cord scaffold.

6.2 Materials and Methods

6.2.1 Manufacture of Collagen-GMA Hydrogel

Collagen-GMA hydrogels were manufactured to serve as a space-filling component of the composite nonwoven-hydrogel spinal cord tissue regenerative scaffold and allow three-dimensional encapsulation of cells. Manufacture of collagen-GMA hydrogels required extraction of collagen, functionalisation with GMA and photo-activation as detailed in 3.2.2.1, 3.2.2.2 and 3.2.2.3, respectively, and was adapted from Tronci et al. (2013).

Briefly, collagen type-I was isolated in-house from rat tail tendons by acid dissolution, functionalised with GMA, and photo-activated in the presence of I2959 photo-initiator under UV light. Resulting hydrogels were washed and allowed to fully hydrate in distilled water for 24 h and either air-dried in a fume-hood overnight or frozen at -80°C for 24 h and lyophilised for a further 24 h to investigate methods of dehydrating collagen-GMA. SEM imaging using a Hitachi SU8230 was employed to study pore

architecture. Rehydration was conducted by immersing hydrogels in deionised water for 24 h.

6.2.2 Degree of Functionalisation of Collagen-GMA

The degree of functionalisation of collagen-GMA was determined to ensure consistency between batches as this would affect the resulting mechanical properties. Degree of functionalisation was determined using a 2,4,6-trinitrobenzene sulfonic acid (TNBS) assay (Bubnis and Ofner, 1992).

TNBS reacts with primary amines and has a specificity for ε-amino groups at alkaline pH, as can be found in lysine. The reaction product is a trinitrophenol (TNP) derivative that is highly chromogenic and can be measured using a spectrophotometer. Whilst α-amino groups are also susceptible, trinitrophenol (TNP)-α-amino groups can be removed by extraction with ether at an acid pH as the groups are un-ionised.

Briefly, 11 mg of lyophilised collagen-GMA was placed in 1 ml 4% $NaHCO_3$ and 1 ml 0.5% TNBS and stirred at 40°C for 4 h. Following addition of 3 ml 6N HCl, samples were heated to 60°C for 1 h. Samples were cooled to room temperature, diluted in water and unreacted TNBS extracted using diethyl ether. Excess ether was evaporated from the aqueous phase, diluted in water again and absorbance measured at 365 nm wavelength. For blank samples, the same protocol was followed except 1 ml $NaHCO_3$ and 3 ml HCl was added to 11 mg before stirring at 40°C for 4 h, and 1 ml TNBS was then added before heating to 60°C for 1 h.

The following equations were then used to derive the degree of functionalisation:

$$Lys_{FC} = \frac{2 \times A_{365} \times V}{\varepsilon \times b \times x}$$

Where Lys_{FC} is the content of free amino groups per gram in the functionalised collagen product (mol g^{-1}), A_{365} is the absorbance at 365 nm, V is the sample volume of 0.02 L, ε is the molar absorption coefficient for 2,4,6-trinitrophenol lysine of 1.46×10^4 M cm^{-1}, b is the cell path length of 1 cm, and x is the sample weight of 0.011 g.

$$F = 100 - \frac{100 \times Lys_{FC}}{Lys_C}$$

Where *F* is the degree of functionalisation (%), Lys_{FC} is the content of free amino groups per gram in the functionalised collagen product (mol g^{-1}), and Lys_C is the content of free amino groups in native collagen of 3.3×10^{-4} mol g^{-1} (Tronci et al., 2013).

6.2.3 Rheology of Collagen-GMA Hydrogel

Rheology of collagen-GMA hydrogels was studied to identify the relationship between weight percent of collagen-GMA in hydrogels and the resulting shear modulus, as well as the most appropriate weight percent for a spinal cord tissue scaffold. Hydrogels were created by UV-curing as above in silicone moulds sandwiched between glass slides to create shallow cylinders that were loaded in to an MCR302 Modular Compact Rotational Rheometer (Anton Paar, Austria). Fully hydrated hydrogels were trimmed to 25 mm diameter to match the dimensions of the 25 mm diameter parallel measuring plate. Sample height was approximately 1.5 mm and compressed by 10% to ensure satisfactory grip between the plate and sample. Amplitude sweeps were run at 10 rad s^{-1} across 0.01-10% strain to identify the critical strain and preceding linear viscoelastic region (TA Instruments, 2013). Frequency sweeps were subsequently run at an amplitude within the identified linear viscoelastic region across 0.1-100 rad s^{-1} to obtain storage (G') and loss (G'') modulus values, as within the linear viscoelastic region the storage modulus is largely independent of frequency (TA Instruments, 2013). Complex shear modulus values were calculated using the following formula:

$$G^* = \sqrt{G' \ + \ G''}$$

Where G^* is the complex shear modulus, G' is the storage modulus and G'' is the loss modulus. All samples were run at 37°C and a solvent trap was filled with distilled water to prevent dehydration.

6.2.4 Compression of Collagen-GMA Hydrogel

Compression of collagen-GMA hydrogels was studied to identify the relationship between weight percent of collagen-GMA in hydrogels and the stress-strain behaviour, including the stress-strain profile, strain at break and maximum stress. Discs of hydrogel were created by UV-curing as above in silicone moulds

sandwiched between glass slides. Fully hydrated hydrogels were trimmed to 5 mm diameter and compressed between two parallel plates using a Bose ElectroForce® 3200, fitted with a 10 N load cell. Sample height was approximately 1.5 mm. Strain rate was 1% s^{-1}. All samples were compressed to failure.

6.2.5 Cell Viability of PC12 Cells in Collagen-GMA Hydrogel

Cell viability was studied to determine whether three-dimensional cell encapsulation was possible with the collagen-GMA hydrogel system. PC12 cells were expanded in RPMI 1640 media (Lonza, UK) supplemented with 10% heat-deactivated horse serum (Sigma-Aldrich, UK), 5% FBS (Sigma-Aldrich, UK), 1% L-Glutamine (Sigma-Aldrich, UK) and 1% penicillin/streptomycin (Sigma-Aldrich, UK). Cells were either seeded on top of pre-cured 0.8 wt% collagen-GMA hydrogel or mixed with collagen-GMA hydrogel-forming solution at 3 x 10^6 cells ml^{-1}. Collagen-GMA hydrogel-forming solution at 0.8 wt% would normally contain 0.8 wt% lyophilised collagen-GMA, 1.0 wt% I2959 and 98.2% PBS. To ensure no extra volume of liquid was added when cells were mixed with collagen-GMA hydrogel-forming solution, 88.2 wt% of PBS was added during hydrogel production and 10.0% of cell-laden media was loaded into the collagen-GMA hydrogel-forming solution and triturated thoroughly to ensure even distribution, whilst avoiding production of air bubbles. Positive controls, where a cytotoxic response was expected, were prepared as above but with 50% (v/v) DMSO in the cell culture media. PC12 cells grown on tissue culture polystyrene coated in PDL to aid adherence were used as negative controls, with high viability expected.

Cell-laden collagen-GMA hydrogel-forming solution was used to fill silicone moulds sandwiched between glass slides and UV-irradiated as above for 10 min. Cell-laden hydrogels were allowed to fully hydrate in pre-warmed media and transferred to an incubator at 37°C/5% CO_2. Cells were allowed to grow for 48 h with one 50% media change after 24 h. A LIVE/DEAD™ Viability/Cytotoxicity Kit for mammalian cells (Invitrogen™, USA) was used to stain live cells green using calcein-AM and dead cells red with ethidium homodimer-1. Cells were imaged using a Leica SP8 Confocal Laser Scanning Microscope. ImageJ (http://imagej.nih.gov/ij/) was used to count the number of cells and given as a percentage of total cell number.

6.2.6 Neurite Extension of PC12 Cells in Collagen-GMA Hydrogel

Neurite extension was studied as an *in vitro* proxy to determine whether collagen-GMA hydrogel could support spinal cord tissue regeneration. PC12 cells and collagen-GMA hydrogels were prepared as detailed in Chapter 6.2.5. Cell-laden gels were incubated in the presence of recombinant human β-NGF (BioLegend, USA), added to the media at 100 ng ml^{-1}. Media was changed every 2-3 days. After 7 days, cells were fixed by immersing in 10% neutral buffered formalin (Sigma-Aldrich, UK) for 15 min, and permeabilised by immersing in 0.2% Triton X-100 (Sigma-Aldrich, UK) for 20 min. Samples were stained using Mouse Anti-Neuron-specific β-III Tubulin Monoclonal Antibody (clone TuJ-1) (MAB1195, Bio-Techne, USA) for 1 h at room temperature, followed by Polyclonal Rabbit Anti-Mouse Immunoglobulins/FITC (F0232, Dako, Denmark) for 1 h at room temperature in the dark. Cells were imaged using a Leica SP8 Confocal Laser Scanning Microscope.

6.3 Results and Discussion

Collagen-GMA hydrogels at different weight percent were evaluated to determine the most appropriate weight percent to use in a composite nonwoven-hydrogel scaffold for spinal cord tissue regeneration. Characterisation included three-dimensional cell encapsulation, cell viability, neurite extension, mechanical investigation in shear and compression, as well as the effect of UV-irradiation time.

6.3.1 Achieving Three-Dimensional Cell Encapsulation by Prioritising Cell Viability

For the first time, cells were successfully encapsulated in a single-phase collagen-GMA hydrogel. PC12 cells were expanded and seeded at 3 x 10^6 cells ml^{-1} of collagen-GMA hydrogel-forming solution (0.8 wt%, $F \pm SD = 49.0 \pm 2.4\%$), UV-irradiated for 10 min, immediately transferred to well-plates containing pre-warmed cell culture media and placed in an incubator at 37°C. Cells were observed throughout the collagen-GMA hydrogel immediately after incubation (Fig. 6.1A), and after 7 days could be seen extending neurites into the hydrogel (Fig. 6.1B). Some neurites were over 250 µm in length (Fig. 6.1C) and were observed extending in multiple planes (Fig. 6.1D).

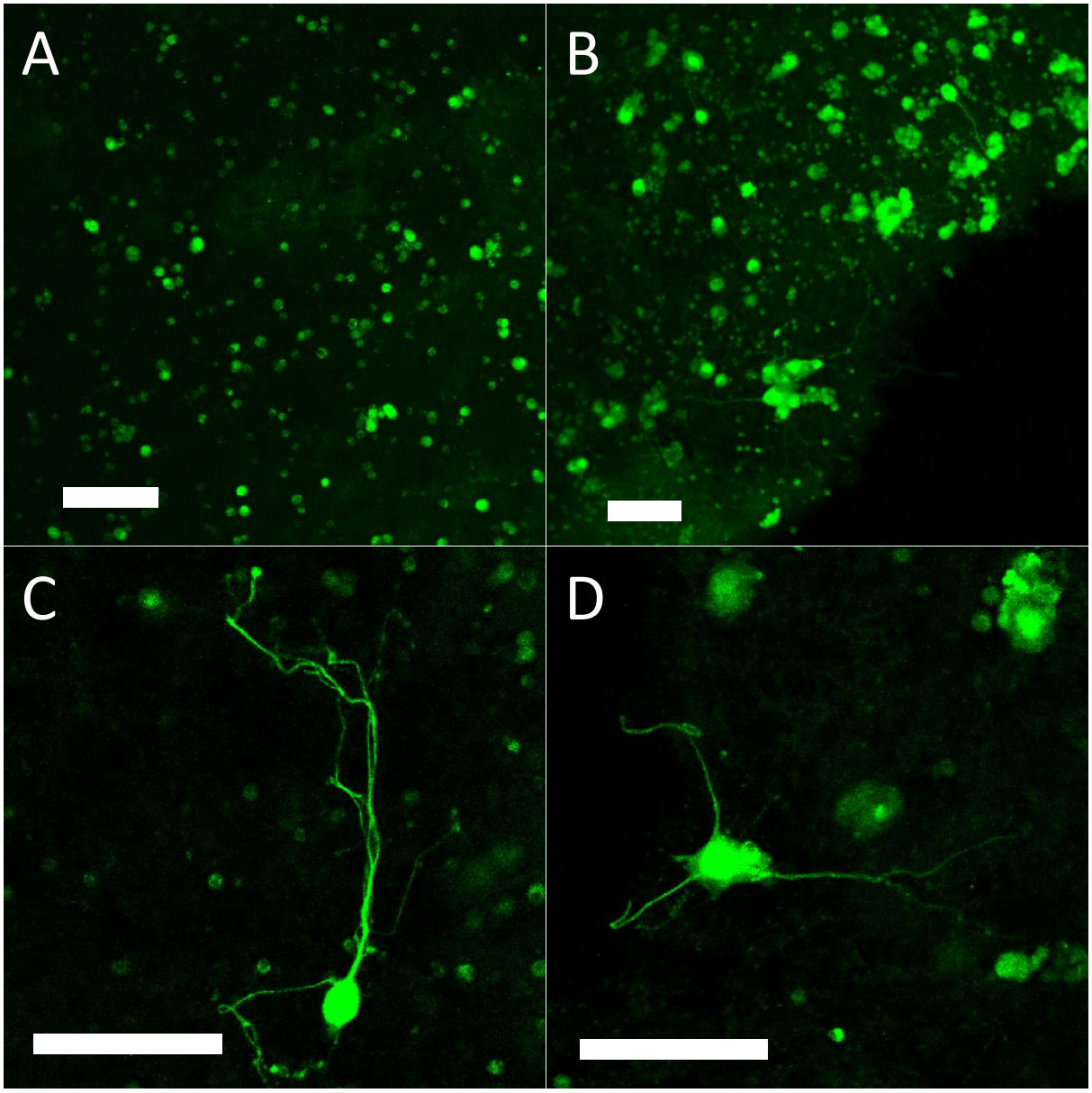

Figure 6.1 Neurite extension of PC12 cells in collagen-GMA hydrogel. PC12 cells were mixed with collagen-GMA hydrogel-forming solution, UV-irradiated for 10 min and placed into an incubator at 37°C/5% CO_2 for 7 days. (A) Immediately after incubation cells were observed throughout the collagen-GMA hydrogel. (B) Following 7 days of NGF exposure, PC12 cells were observed extending neurites throughout the collagen-GMA hydrogel, (C) with some neurites observed over 250 µm in length and (D) extending in multiple planes. Scale bar is 100 µm.

Further, after 48 hours and one 50% media change, high mean cell viability (± SD) of 84 ± 2% was observed as seen in the exemplary confocal images (Fig. 6.2A), and above the 70% recommended to indicate a non-cytotoxic effect (ISO, 2009). This was reinforced by the complete cell death observed in the positive control, where 50% of the media was substituted for DMSO (Fig. 6.2B), and the complete cell

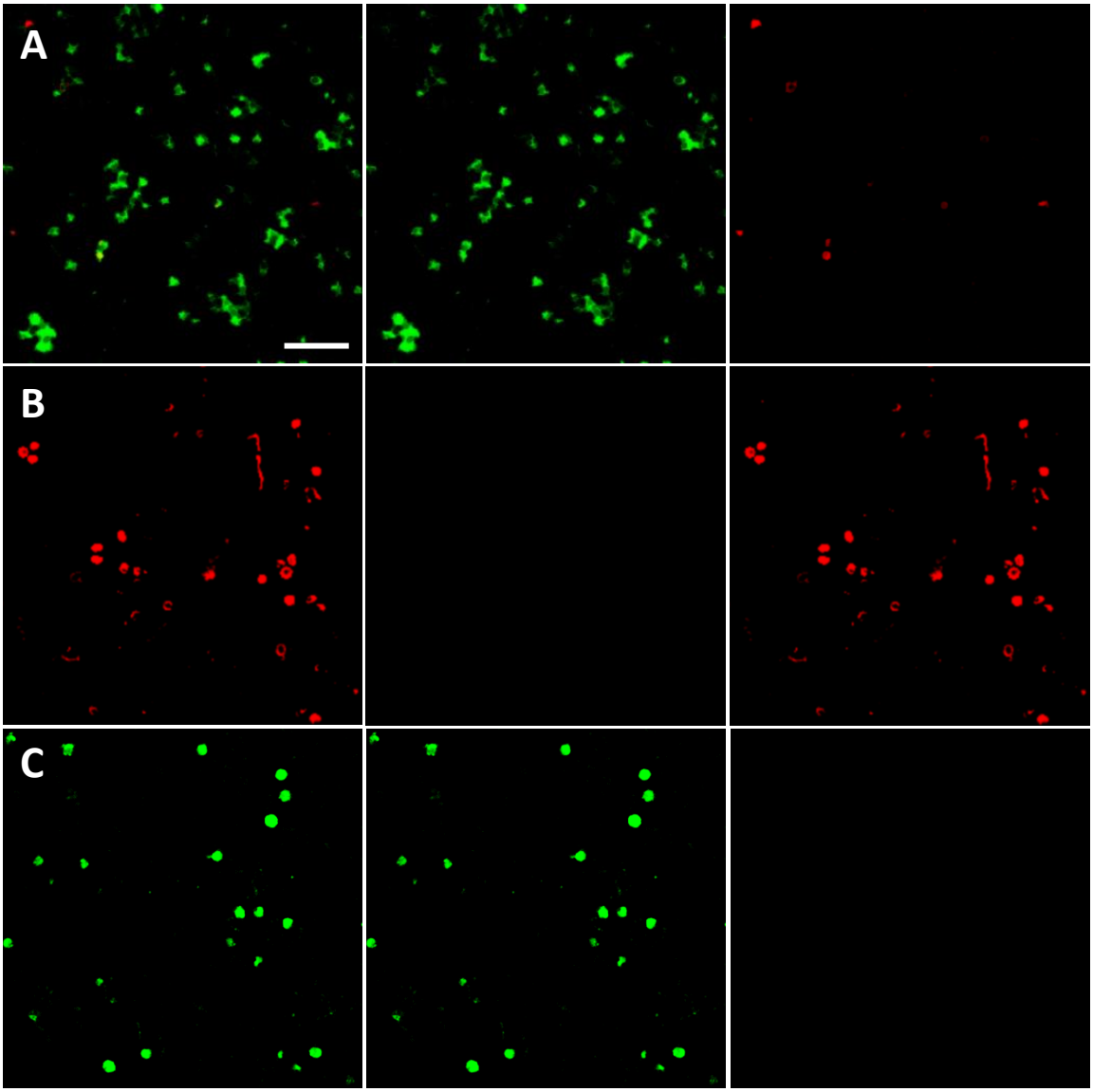

Figure 6.2 Cell viability of PC12 cells encapsulated in collagen-GMA hydrogel. (A) Exemplary confocal images show live (green) and dead (red) PC12 cells 48 hours after encapsulation in 0.8 wt% collagen-GMA hydrogel. (B) PC12 cells 48 hours after encapsulation in 0.8 wt% collagen-GMA hydrogel with DMSO added to cell culture media at 50% (v/v). (C) PC12 cells grown on glass coverslips coated in PDL as the negative control. Combined channels (left), as well as separate green (middle) and red (right) channels are shown for each image. Cell viability was calculated at 84 ± 2% (± SD) for the collagen-GMA hydrogel. Scale bar is 50 µm. *n* = 3.

survival in the negative control, where PC12 cells were grown on tissue culture polystyrene coated with PDL (Fig. 6.2C).

Further still, live cells were visibly evenly distributed in the hydrogel (Fig. 6.3A), and throughout a 160 µm Z-stack (Fig. 6.3B). This was similar to cells seeded on top of pre-cured hydrogel, which were also evenly distributed (Fig. 6.3C), but only infiltrated

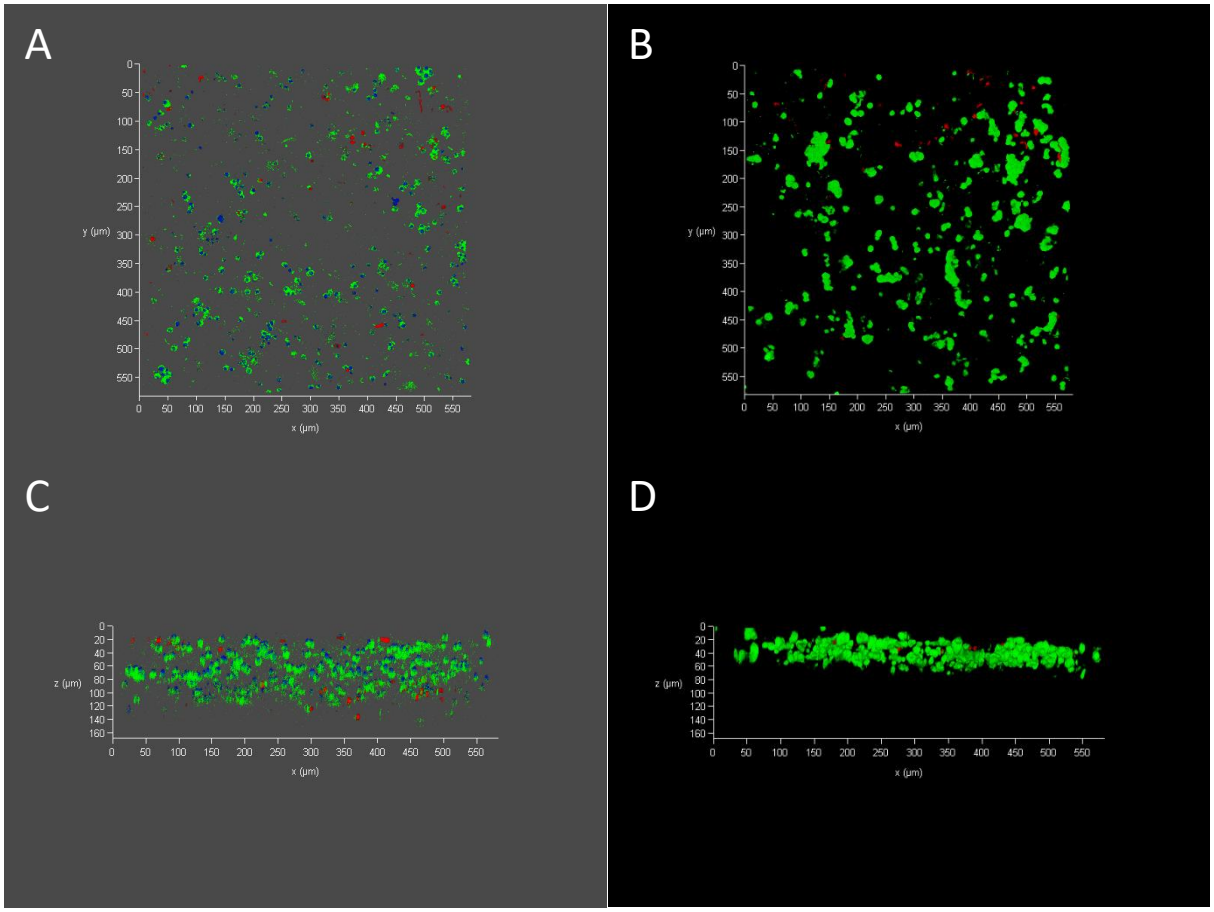

Figure 6.3 PC12 cell distribution in collagen-GMA hydrogel. Exemplary confocal images show live (green) and dead (red) PC12 cells 48 hours after cell seeding in or on 0.8 wt% collagen-GMA hydrogel. Viable cells can be seen evenly distributed in the 600 x 600 µm section when cells were either (A) mixed with collagen-GMA hydrogel-forming solution prior to UV-irradiation or (B) seeded on top of post UV-irradiated collagen-GMA hydrogel. Z-stack sections show (C) PC12 cells throughout the 160 µm section of the mixed group, but (D) only in the top 50 µm of the group with cells seeded post-curing. Note: Cell nuclei are visible for A and C (blue).

into the hydrogel to around 50 µm (Fig. 6.3D). Together, these results indicated for the first time that the collagen-GMA hydrogels were capable of supporting neural cell viability as a three-dimensional cell culture system.

The collagen-GMA hydrogel system used herein had been previously investigated for a similar purpose, as an *in vitro* spinal cord injury model (Kirk, 2018). Target criteria for the hydrogel system was (1) to be affordable, (2) to be capable of achieving at least three stiffness variations, (3) allowed three-dimensional cell seeding, (4) could support neural cell viability and attachment, and (5) could be visualised using microscopy. Unfortunately, whilst the collagen-GMA hydrogels were able to meet the affordability and variable stiffness criteria, it was concluded that

three-dimensional cell seeding was not possible due to certain steps in the hydrogel production protocol, and therefore the rest of the criteria could also not be met. The production protocol used for the collagen-GMA hydrogels was adapted from an earlier protocol by Tronci et al. (2013) (Table 6.1).

In both protocols the I2959 photo-initiator was dissolved in PBS prior to lyophilised collagen-GMA addition. This is due to the difficulty in solubilising I2959 in which the elevated temperature noted by Kirk (2018) aids dissolution. In the original protocol by Tronci et al. (2013), a lowered temperature of 4°C was used for lyophilised collagen-GMA solubilisation. This was possibly due to the improved solubility of collagen away from body temperature, as body temperature promotes aggregation of molecules into fibrils (Bronzino and Peterson, 2015), and possibly to prevent bacterial contamination as well. In the adapted protocol by Kirk (2018), lyophilised collagen-GMA was solubilised at 60°C instead. No rationale was given for this change, but it may have been an attempt to improve solubility and reduce the time required to solubilise.

Following lyophilised collagen-GMA solubilisation, vacuum desiccation was used to remove air bubbles after casting in moulds prior to UV-irradiation. No rationale was provided as to the length of time for UV-irradiation in either protocol – 30 min either side, for a total of 60 min, in Tronci et al. (2013) and 30 min in Kirk (2018) with no

Table 6.1 Collagen-GMA hydrogel production protocol as detailed in Kirk (2018) and Tronci et al. (2013).

	Kirk (2018)	Tronci et al. (2013)
1.	I2959 was dissolved in PBS at 40°C until solubilised.	I2959 was dissolved in PBS.
2.	Collagen-GMA was added and stirred at 60°C for 60 min.	Collagen-GMA was added and stirred at 4°C.
3.	Cast into moulds and vacuum desiccated.	Cast into moulds and vacuum desiccated.
4.	UV-irradiated at 365 nm for 30 min.	UV-irradiated at 365 nm for 30 min either side.
5.	Washed overnight in distilled water.	Washed overnight in distilled water.
6.	Washed in an ascending series of ethanol.	Washed in an ascending series of ethanol.
7.	Air-dried.	Air-dried.

mention of time per side – but was presumably deemed long enough in both cases to reach full cross-linking. Following UV-irradiation and cross-linking, both protocols washed hydrogels in distilled water overnight to remove unreacted photo-initiator, washed in an ascending series of ethanol to dehydrate and sterilise, and air-dried to store.

Whilst cells need to be introduced prior to the UV-irradiation step to encapsulate, as once cross-linking between collagen-GMA chains takes place cell infiltration is difficult, as shown in Fig. 6.3D, cells do not need to be introduced until just prior to UV-irradiation. As such, in the above protocol by Tronci et al. (2013) the vacuum desiccation; 60 minute UV-irradiation; overnight swelling in water; and dehydration and sterilisation in ethanol steps were noted as preventing introduction of cells during manufacture and resulting three-dimensional encapsulation. Indeed, this was the assessment following evaluation as an *in vitro* spinal cord injury model (Kirk, 2018).

However, whilst adaptations to the protocol were made by Kirk (2018), these did not address the shortcomings with respect to prioritising cell viability. Despite, an apparent reduction in UV-irradiation time to 30 min from a total of 60 min (30 min per side), it is likely this would still be too long to achieve adequate cell viability (Vile et al., 1995; Ruiz-Cantu et al., 2020). Further, whilst not necessarily a problem for subsequent cell encapsulation, if cooled to a lower temperature, dissolution of collagen-GMA at 60°C could cause denaturation (Tronci et al., 2013).

In either case, both protocols were not optimised to prioritise cell viability and three-dimensional cell encapsulation was not possible. Thus it was concluded by Kirk (2018) the system would only allow for two-dimensional culture of cells on top of the preformed hydrogels and collagen-GMA was abandoned as an option for an *in vitro* spinal cord injury model.

However, to overcome the above issues preventing introduction of cells during the hydrogel production process and achieve three-dimensional cell culture, the above protocol was examined, altered and tested (Table 6.2).

As in Tronci et al. (2013), I2959 was dissolved in PBS to be more physiologically relevant and provide a pH suitable for three-dimensional cell encapsulation. Further, the reduced temperature of 4°C used in Tronci et al. (2013) was maintained to

Table 6.2 The altered Collagen-GMA hydrogel production protocol used in herein.

	Step
1.	I2959 was dissolved in PBS at 40°C until solubilised (around 3 h).
2.	Collagen-GMA (0.8 wt%) was added and stirred at 4°C until solubilised (48 h).
3.	Cast into moulds.
4.	UV-irradiated at 365 nm for 10 min.
5.	Hydrogels were placed straight into pre-warmed media and incubated at 37°C. A 50% media change after 24 h was performed.

improve solubility of collagen (Bronzino and Peterson, 2015) and the elevated temperature of 60°C used in Kirk (2018) was avoided to prevent potential denaturation of collagen-GMA (Tronci et al., 2013). Collagen-GMA hydrogel-forming solution at 0.8 wt% was chosen after undertaking a rheological study to identify the percentage weight that resulted in the desired hydrogel stiffness (Chapter 6.3.2). After carefully casting in moulds to ensure no air bubbles were introduced, collagen-GMA hydrogel-forming solution was UV-irradiated at 365 nm for 10 min. This was also following a rheological study to optimise UV-irradiation time and minimise exposure for cells (Chapter 6.3.3). Lastly, by providing a large volume of media and performing a media change after 24 h, washes in distilled water were avoided and likely still allowed for unreacted photo-initiator to be removed. As hydrogels were used straight away, dehydration and drying for storage was not required. Whilst no sterilisation step was conducted, all steps were performed in an aseptic manner in a hood and no evidence of contamination was observed.

These results are further supported by the encapsulation of bone marrow-derived mesenchymal stem cells (BMSCs) in a dual phase collagen-GMA/HA-MA hydrogel (Zhang et al., 2019). Encapsulation was performed just prior to UV-irradiation of 5 min at a similar intensity (7 mW cm^{-2}), with high levels of cell survival and good distribution of cells. Further, promotion of osteogenic differentiation over the HA-MA control hydrogel was recorded, as measured by the biomarkers Runx2, ALP, OC, as well as upregulation of Col-I and OPN, BSP and OSX proteins relevant to osteogenic differentiation.

In summary, by avoiding the need to use vacuum desiccation; reducing UV-irradiation time to 10 min; replacing water washes with an excess of pre-warmed media; performing all steps in an aseptic environment; and using hydrogels straight away, cell viability was prioritised at every step of the protocol. As such, whilst BMSCs had been encapsulated and differentiated in a dual phase collagen-GMA/HA-MA hydrogel (Zhang et al., 2019), and L929 cells had previously shown high viability after growing on top of ethanol-treated single-phase collagen-GMA hydrogels (Tronci et al., 2015) and normal morphology following extract cytotoxicity testing (Tronci et al., 2013; Tronci et al., 2015), by following the above protocol instead of Tronci et al. (2013) or Kirk (2018), cells were successfully encapsulated in a single-phase collagen-GMA hydrogel for the first time, as shown in Fig. 6.1.

6.3.2 Hydrogel Stiffness and the Effect of Collagen-GMA Weight Percent

Prior to three-dimensional cell encapsulation, rheology was used to observe the effect of weight percent of the collagen-GMA hydrogel-forming solution on hydrogel stiffness. A range of 0.8-1.6 wt% was studied, as below 0.8 wt% gelation into stable hydrogels that could be supported under their own weight was not achieved, and above 1.6 wt% full dissolution was not observed.

Following identification of the linear viscoelastic region, frequency sweeps – where the sample was sheared over a range of frequencies at a shear strain within the linear viscoelastic region – indicated all concentrations of the collagen-GMA hydrogel-forming solution were behaving as viscoelastic solids (Fig. 6.4A-F). This was evidenced by the higher storage modulus values in relation to the loss modulus values for all concentrations, indicating a dominance of elastic strength over viscous strength. Further, the relatively flat storage modulus lines indicated the frequency-independence of the results, as would be expected for solids whose mechanical properties are strain-rate independent. Most importantly, increasing storage and loss modulus values with increasing weight percent of the collagen-GMA hydrogel-forming solution was observed.

Whilst the position of the relatively flat storage and loss modulus lines can be compared between frequency sweep rheograms, the increase in values with increasing weight percent of the collagen-GMA hydrogel-forming solution was more easily observed if values at a specified frequency were plotted. For example, at an

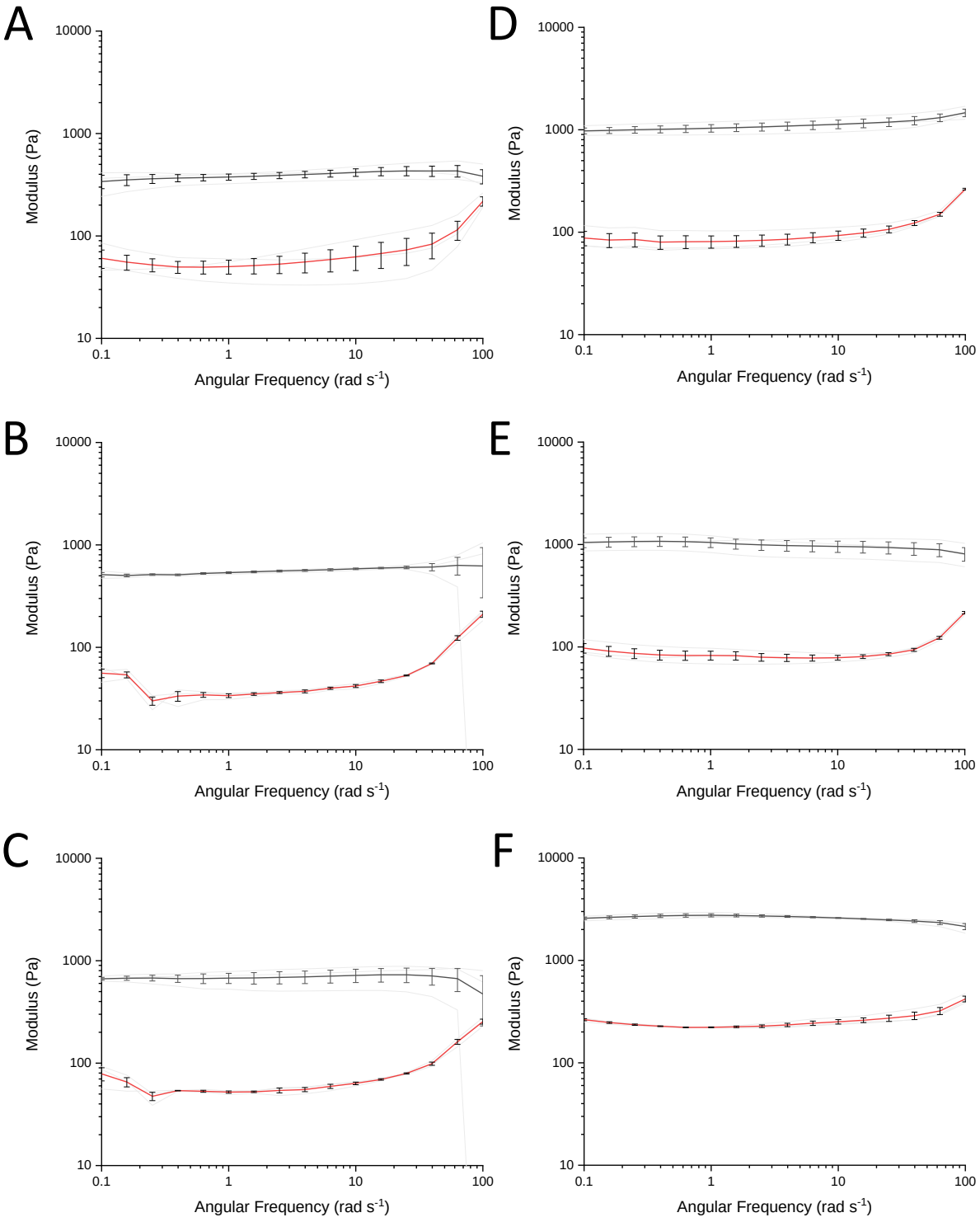

Figure 6.4 Mechanical properties in shear of collagen-GMA hydrogel at varying weight percent (wt%). Frequency sweeps show collagen-GMA hydrogel at (A) 0.8, (B) 0.9, (C) 1.0, (D) 1.1, (E) 1.2 and (F) 1.6 wt%. The black and red lines show the mean storage and loss modulus for each experimental group (±SE), respectively. Grey lines depict actual measurements. All samples had a higher storage modulus compared to loss modulus, indicating hydrogels were behaving as viscoelastic solids. As weight percent of collagen-GMA hydrogels increased, storage modulus also increased. *n* = 3.

angular frequency of 0.1 rad s^{-1}, collagen-GMA hydrogel-forming solution at 0.8, 0.9, 1.0, 1.1, 1.2 and 1.6 wt% resulted in hydrogels with storage modulus values of 340 ± 51, 512 ± 25, 667 ± 21, 976 ± 64, 1047 ± 116 and 2574 ± 79 Pa, and loss modulus values of 61 ± 12, 56 ± 5, 79 ± 11, 88 ± 14, 97 ± 10 and 264 ± 6 Pa, respectively (Fig. 6.5A, Table 6.3). As such, a positive linear relationship was observed, as increasing weight percent resulted in increased modulus values, the strength of which was evidenced by the 0.94 and 0.95 adjusted R^2 values for the storage and loss modulus trends, respectively (Fig. 6.5A).

Further, this trend was maintained when storage and loss modulus values were combined to give a complex shear modulus value that fully described the viscoelastic properties of each collagen-GMA hydrogel concentration. Complex shear modulus values were 345, 515, 672, 980, 1050 and 2588 Pa, respectively, with an adjusted R^2 value of 0.95 (Fig. 6.5B, Table 6.3). Importantly, as all weight percent solutions were evaluated using the same batch of lyophilised collagen-GMA, degree of functionalisation was kept constant within each replication study.

The above study indicated that collagen-GMA hydrogels at lower concentrations were likely more favourable for three-dimensional neural cell encapsulation in terms of shear stiffness. Guidance on ideal shear stiffness for cell encapsulation was taken from the literature for a number of reasons, including the volume of work on this topic that appeared to give a consensus on a favourable stiffness range for three-dimensional neural cell encapsulation; the aims of this work herein that did permit adequate time and resource to meaningfully add to the literature; and the variability in stiffness that can be achieved using this hydrogel system, as detailed herein, making it modifiable if further optimisation was required due to new evidence or for a specific cell type. With respect to a consensus in the literature, a shear modulus around a few hundred Pascals is believed to be optimal for neural cell viability and growth for three-dimensional cell culture, as detailed in Chapter 2.5.2.1. As such, further mechanical testing focused on collagen-GMA hydrogels at 0.8-1.1 wt%.

Further, these results also evidenced the specificity and control in modulus values achievable when altering the amount of collagen-GMA in the hydrogel solution. Control of hydrogel stiffness using this system is possible by varying the network architecture in a number of ways; through the type of linker applied to the collagen

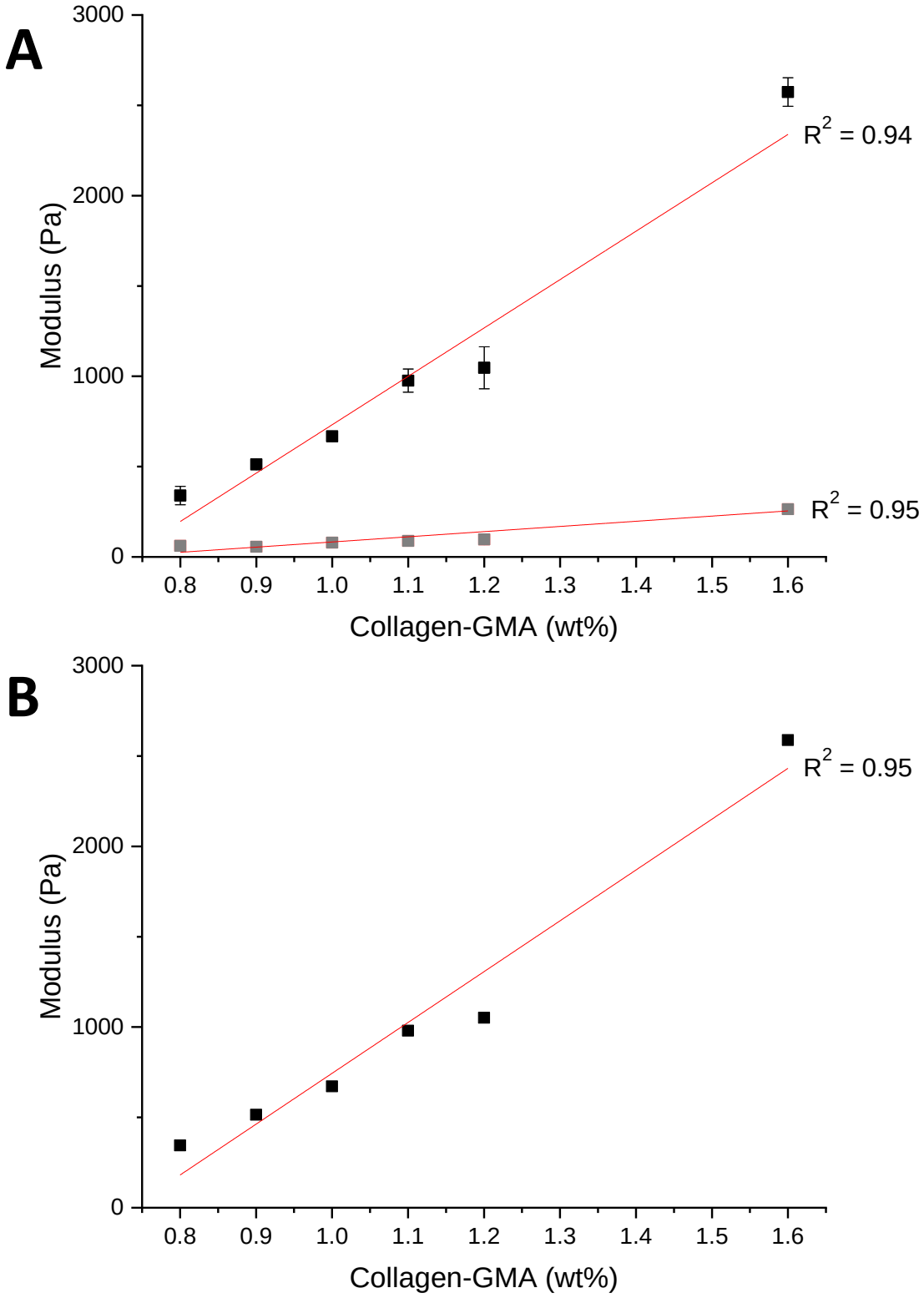

Figure 6.5 Shear modulus values of collagen-GMA hydrogel at varying weight percent (wt%). (A) Storage (black) and loss (grey) modulus values (±SE) of collagen-GMA hydrogel at 0.8, 0.9, 1.0, 1.1, 1.2 and 1.6 wt%. Linear regression gave an adjusted R^2 of 0.94 and 0.95 for the storage and loss modulus trends, respectively. (B) Complex modulus values of collagen-GMA hydrogel at 0.8, 0.9, 1.0, 1.1, 1.2 and 1.6 wt%. Linear regression gave an adjusted R^2 of 0.95. All values as at 0.1 rad s^{-1}. *n* = 3.

Table 6.3 Table of storage, loss and complex shear modulus values of collagen-GMA hydrogel at varying weight percent (wt%). All values as at 0.1 rad s^{-1}. *n* = 3.

Collagen-GMA (wt%)	0.8	0.9	1.0	1.1	1.2	1.6
Storage modulus ± SE	340 ±51	512 ±25	667 ±21	976 ±64	1047 ±116	2574 ±79
Loss modulus ± SE	61 ±12	56 ±5	79 ±11	88 ±14	97 ±10	264 ±6
Complex modulus	345	515	672	980	1051	2588

backbone that forms the cross-link; the number of linkers attached to the backbone and the number of cross-links they can make (the degree of functionalisation); and the amount of functionalised collagen in the hydrogel (Tronci et al., 2013), as done herein. This presents a variety of levels at which stiffness can be manipulated (Tronci et al., 2013; Tronci et al., 2015; Tronci, Grant, et al., 2016; Liang et al., 2018b).

For the purposes of spinal cord tissue regeneration and neural cell encapsulation, GMA was chosen as the linker moiety over other previously investigated moieties, such as 4-vinylbenzyl chloride (4VBC) and methacrylic anhydride (MA) (Tronci et al., 2013; Tronci et al., 2015; Tronci, Grant, et al., 2016; Liang et al., 2018b), due to its greater elasticity and resulting hydrogels of greater compressibility and reduced compressive modulus (Tronci et al., 2013; Tronci et al., 2015). As such, it was rationalised GMA would produce hydrogels closer to the desired shear modulus.

Further, whilst the degree of functionalisation can be controlled by varying the excess of linker used in the reaction with respect to collagen lysine content (Tronci et al., 2013; Tronci et al., 2015; Liang et al., 2018b), it was rationalised that it would be better to reach a plateau with respect to the concentration-functionalisation relationship, as this would ensure a similar degree of functionalisation was achieved when batch producing lyophilised collagen-GMA. Indeed, it had already been shown an excess of GMA above 25 molar with respect to collagen lysine content did not result in considerable further functionalisation (Tronci et al., 2013; Tronci et al., 2015), and thus a 25 molar excess was used herein.

As such, with the linker moiety and molar excess taken as set parameters, this left the amount of collagen-GMA used in the hydrogel solution as the most reliable, and

therefore the most appropriate, method of altering hydrogel stiffness. This was observed herein by the positive linear relationship observed between weight percent and shear modulus values.

In summary, by choosing a more flexible linker moiety in GMA, reaching a plateau with respect to the relationship between linker excess in the reaction and degree of functionalisation, and therefore using collagen-GMA hydrogel concentration as the parameter for varying the network architecture, hydrogel stiffness was controlled in a step-wise manner. Taken together, shear modulus values within a few hundred Pascals were achieved as a desirable stiffness for three-dimensional neural cell encapsulation. However, it should also be noted that if further optimisation is required then the method herein would allow straightforward control for varying hydrogel stiffness, and stiffness values below and above those seen here may be possible by further exploring the interplay between the network architecture parameters.

6.3.3 Hydrogel Stiffness, Cell Viability and the Effect of UV-Irradiation Time

Whilst collagen-GMA hydrogel may be capable of achieving shear stiffness values of a few hundred Pascals, and thus be within a range favourable for three-dimensional neural cell encapsulation, the system still requires UV-irradiation for radical-induced photo-crosslinking with cells *in situ*. Indeed, a common and persisting criticism of photo-curable hydrogel systems is their radical-induced toxicity (Nguyen and West, 2002; Nicodemus and Bryant, 2008; Slaughter et al., 2009; Hasturk and Kaplan, 2019; Tomal and Ortyl, 2020). As such, minimising radical-induced toxicity was considered critical to achieving viable three-dimensional cell culture using this hydrogel system, via optimising UV-irradiation time with respect to shear properties. To do so, collagen-GMA hydrogels at 0.8 wt% were UV-irradiated for 5, 10, 20, 40 and 60 min and shear properties used as a proxy to indicate formation of photo-crosslinks.

Collagen-GMA hydrogel-forming solution UV-irradiated for 5 min did not produce stable hydrogels that could be supported under their own weight, but all other irradiation time periods did and thus were studied using rheology. Resulting

rheograms show the similarity in storage and loss modulus for the 10, 20, 40 and 60 min UV-irradiated samples (Fig. 6.6). This indicated a plateau had been reached with respect to the photo-induced crosslinking and, as the degree of crosslinking is proportional to mechanical stiffness, it can be inferred that 10 min was long enough to efficiently crosslink the hydrogel.

Of note, whilst similar storage modulus values were obtained between 0.1-30 rad s^{-1}, some loss of correlation was seen at angular frequencies above 30 rad s^{-1}. This may be explained by the high water content of the hydrogel influencing the frequency-dependence of the results (TA Instruments, 2013). Further, the slightly lower storage and loss modulus values observed here for the 0.8 wt% collagen-GMA hydrogel, compared to those recorded during the shear stiffness investigation (Chapter 6.3.2), were likely due to a lower degree of mean functionalisation (± SD) of 38 ± 1.9% for this batch of collagen.

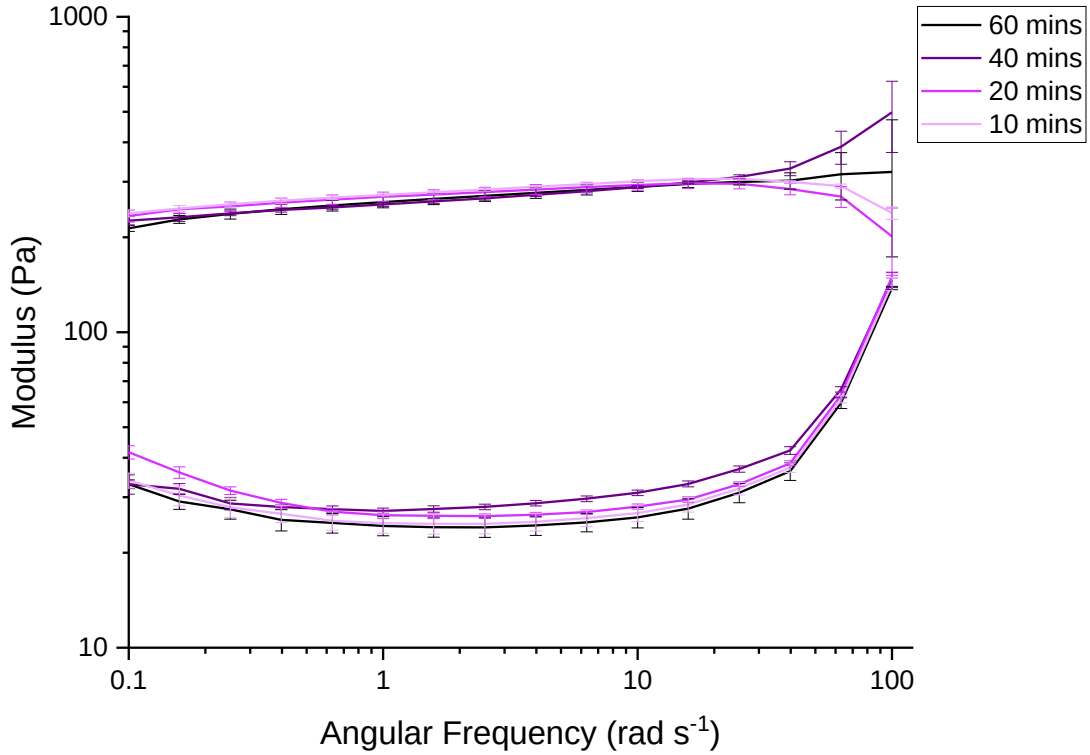

Figure 6.6 Mechanical properties in shear of collagen-GMA hydrogel at varying UV-irradiation time. Frequency sweeps show 0.8 wt% collagen-GMA UV-irradiated for 60, 40, 20 and 10 min (mean±SE). The similarity of the experimental groups indicated complete photo-crosslinking had taken place. *n* = 3.

Using this knowledge, 10 min UV-irradiation time was used to photo-crosslink PC12-containing collagen-GMA hydrogel-forming solution and resulted in viable cells and successful three-dimensional encapsulation (Chapter 6.3.1).Whilst UV-irradiation time was the independent factor used in the study herein, it should be kept in mind this was (a) to reduce the overall dose of UV received by cells, and (b) to limit the radical-induced toxicity, with this latter point linked to the former. Regarding dose, this is calculated using the following formula:

$$D = I \times t$$

Where *D* is UV dosage in J cm^{-2}, *I* is UV intensity in W cm^{-2} and *t* is time in seconds. Using this formula, PC12 cells encapsulated in collagen-GMA hydrogels subjected to 9 mW cm^{-2} of UV for 10 min herein received a UV dose of 5.4 J cm^{-2}. This is at the lower end of the 5-10 J cm^{-2} doses typically used in cell-based photochemistry applications (Wong et al., 2015).

In comparison, both the original photo-activation protocol (Tronci et al., 2013; Tronci et al., 2015) and previously altered protocol for evaluation as an *in vitro* spinal cord injury model (Kirk, 2018) used prolonged UV-irradiation time of 60 and 30 min, respectively. Converted to UV dose, these would amount to 32.4 J cm^{-2} and 16.2 J cm^{-2}, respectively. Whilst cell viability was not evaluated for these time periods herein, there is strong evidence to suggest these doses would have been severely cytotoxic (Vile et al., 1995; Ruiz-Cantu et al., 2020). As such, the optimisation performed herein showed for the first time that a single-phase collagen-GMA hydrogel-forming solution could be photo-crosslinked at lower UV doses, even at the lower end of the window typically used in cell-based photochemistry applications, and thus likely the reason cell viability was high.

As suggested, these results were similar to other studies using similar materials and conditions; such as BMSCs in a dual-phase hydrogel of collagen-GMA and hyaluronic acid-MA (7 mW cm^{-2}, 5 min, 2.1 J cm^{-2}, I2959) (Zhang et al., 2019); chondrocytes in glycidyl acrylate functionalised poly(vinyl) alcohol (8 mW cm^{-2}, 10 min, 4.8 J cm^{-2}, I2959) (Bryant et al., 2000); smooth muscle cells in PEGylated fibrinogen hydrogels (5-20 mW cm^{-2}, 5 min, up to 1.5-6 J cm^{-2}, I2959) (Mironi-Harpaz et al., 2012); and chondrocytes in gelatin-MA (31 mW cm^{-2}, up to 12 min, up to 22.3 J cm^{-2}, I2959) (Ruiz-Cantu et al., 2020). As such, the study herein reinforces the

understanding that cells are able to sustain some UV exposure when used as a reaction tool and cell viability can still be kept high.

Beyond cell viability though, UV-irradiation is known to induce DNA damage (Sinha and Häder, 2002), and therefore whilst a cytotoxic dose may not have been received, genotypic changes could still have occurred that promote latent cell death, affect genetic stability or even initiate morbidity. Recently, however, it has been shown that a UV dose at the lower end of the window used for cell-based photochemistry applications likely does not induce changes in gene expression itself, but rather it is the radical generation that results in gene expression changes, including those related to signalling, DNA damage and cell cycle (Wong et al., 2015).

This point has been exemplified recently in a study looking at cartilage regeneration using 3D printed gelatin-MA (Ruiz-Cantu et al., 2020). Cell viability remained high up to a dose of 5.58 J cm^{-2} (31 mW cm^{-2}, 3 min), but after 4.65 J cm^{-2} (31 mW cm^{-2}, 2.5 min) 50% of cells were DNA-damaged, as per detection of the DNA damage marker γ-H2αX. DNA damage is measured using γ-H2αX, as this is the phosphorylated version of the H2A histone protein found in chromatin, which occurs as a result of double stranded breaks in DNA. Whilst the latter genotoxic study was performed on monolayers of cells and the former cytotoxic study on encapsulated cells, and therefore a direct comparison should be made cautiously, there is an indication cell viability can look high whilst also masking high levels of genotoxicity. Thus, whilst cell viability remained high after a UV dose of 5.4 J cm^{-2} for PC12 cells encapsulated in collagen-GMA hydrogel herein, DNA damage may well have occurred.

However, similar to the fact some UV exposure is tolerable to cells before becoming cytotoxic, there is an indication cells can be subjected to some level of UV dose without any measurable DNA damage as well. For example, after a UV dose of 1.86 J cm^{-2} none of the DNA damage marker γ-H2αX was measured in chondrocytes, and this could well be higher as the next experimental group measured was not until a UV dose of 4.65 J cm^{-2} (Ruiz-Cantu et al., 2020). In relation to the collagen-GMA hydrogels herein, this indicates further optimisation between 5-10 min UV-irradiation time that was not investigated could still result in fully cross-linked hydrogels, whilst minimising any genotoxicity.

Further, this is without even considering other factors that could influence toxicity; such as reducing the amount of photoinitiator (Bryant et al., 2000; Williams et al., 2005); the fact different cell types respond differently to radical-induced toxicity (Williams et al., 2005); that depending on scaffold dimensions and manufacturing method prolonged UV exposure may be required (Ruiz-Cantu et al., 2020) or that other photoinitiator systems also exist (Tomal and Ortyl, 2020). Indeed, the photoinitiator lithium phenyl-2,4,6-trimethylbenzoylphosphinate (LAP), has been shown to photo-crosslink diacrylated poly(ethylene glycol) hydrogels faster at a similar UV wavelength (365 nm) and also phot-crosslink within the visible spectrum (405 nm), further reducing the likelihood of toxicity (Fairbanks et al., 2009). However, it should be noted that LAP at the time of writing is around 20 times the cost of I2959, and may be an influencing factor on photo-initiator system choice.

In summary, UV-irradiation time as short as 10 min appeared to create collagen-GMA hydrogels as stiff as those UV-irradiated for 60 min and it was therefore inferred complete photo-crosslinking had taken place. Further, a 10 min UV exposure brought the overall UV dose into the window used typically in cell-based photochemistry applications and thus was likely the reason three-dimensional cell encapsulation was possible for the first time and cell viability was high, similar to other studies. Further still, whilst genotoxic effects cannot be ruled out, further optimisation with respect to UV-irradiation time may be possible as well as potential use of other lower toxicity photoinitiator systems.

6.3.4 Hydrogel Compression and the Effect of Collagen-GMA Weight Percent

As well as mechanical characterisation in shear, collagen-GMA hydrogels were also compressed to observe the effect of weight percent on the stress-strain behaviour of the hydrogels, and to compare to both previous evaluation of this hydrogel system and the literature on spinal cord tissue. After the rheological testing implying the lower weight percent hydrogels may be more appropriate for three-dimensional neural cell encapsulation in a spinal cord tissue scaffold, collagen-GMA hydrogels of 0.8, 0.9, 1.0 and 1.1 weight percent were compressed to failure. J-shaped stress-strain curves were observed for all four weight percent groups (Fig. 6.7A-D). Strain at break was 68.3 ± 0.8, 74.6 ± 1.8, 71.0 ± 2.8 and 80.6 ± 0.7 % (± SE), respectively

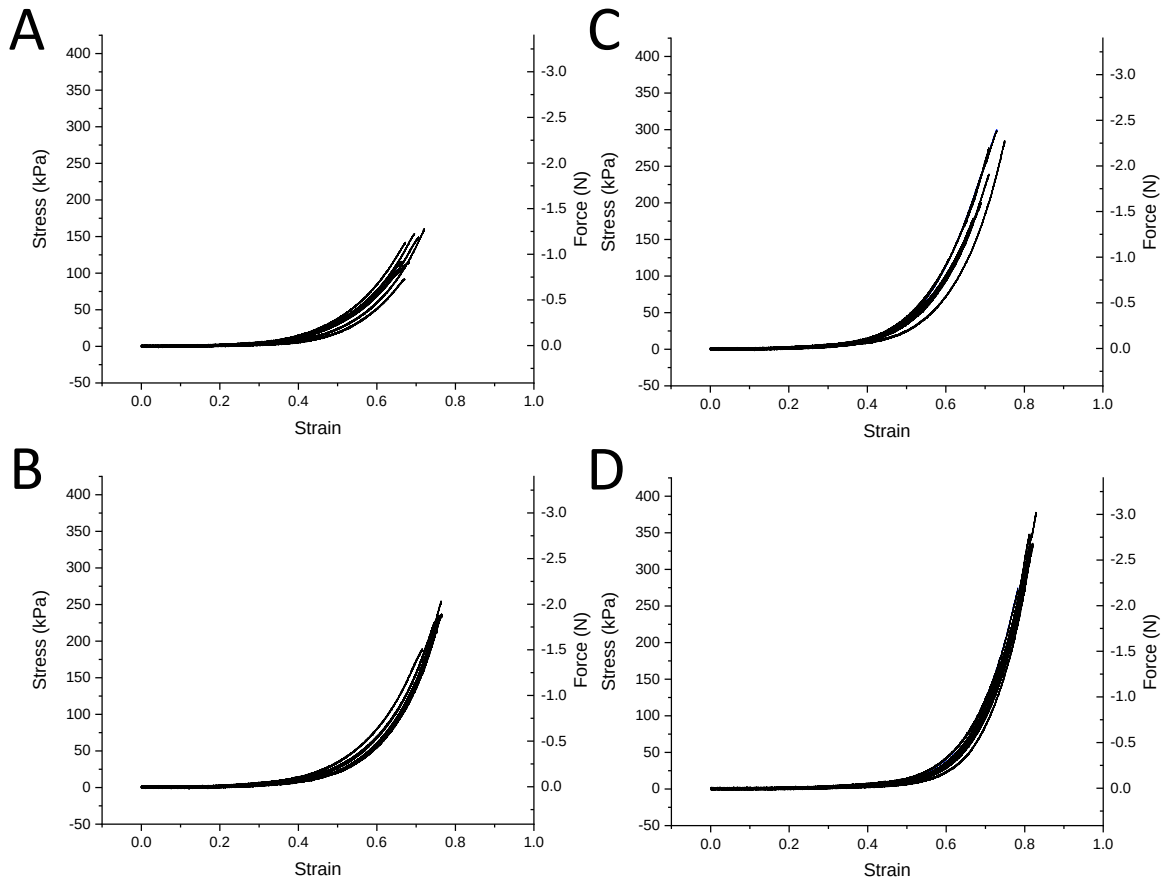

Figure 6.7 Mechanical properties in compression of collagen-GMA hydrogel at varying weight percent (wt%). Stress-strain graphs of collagen-GMA hydrogel at (A) 0.8, (B) 0.9, (C) 1.0 and (D) 1.1 wt%. Force has been added as a second Y-axis. *n* = 6-8.

(Fig. 6.8A). Maximum stress was 128.4 ± 9.1, 219.2 ± 8.0, 246.3 ± 20.0 and 311.2 ± 17.9 kPa (± SE), and maximum force was 1.0 ± 0.1, 1.7 ± 0.1, 2.0 ± 0.2 and 2.5 ± 0.1 N (± SE), respectively (Fig. 6.8B).

J-shaped stress-strain curves are typical of many biological tissues (Mitsuhashi et al., 2018), and though limited data exists, this includes spinal cord (Hung et al., 1982; Sparrey and Keaveny, 2011; Fradet et al., 2016; Karimi et al., 2017). Describing this stress-strain curve indicates that a large increase in strain is observed for a relatively short increase in stress at stresses far away from the failure point, but much larger stress is required for further increases in strain close to the failure point. The benefit of this stress-strain behaviour is highly deformable tissue during normal everyday stresses and protection against injury when stresses are extreme (Guimarães et al., 2020). It has recently been reiterated that J-shaped stress-strain behaviour should be mimicked by regenerative scaffolds to produce

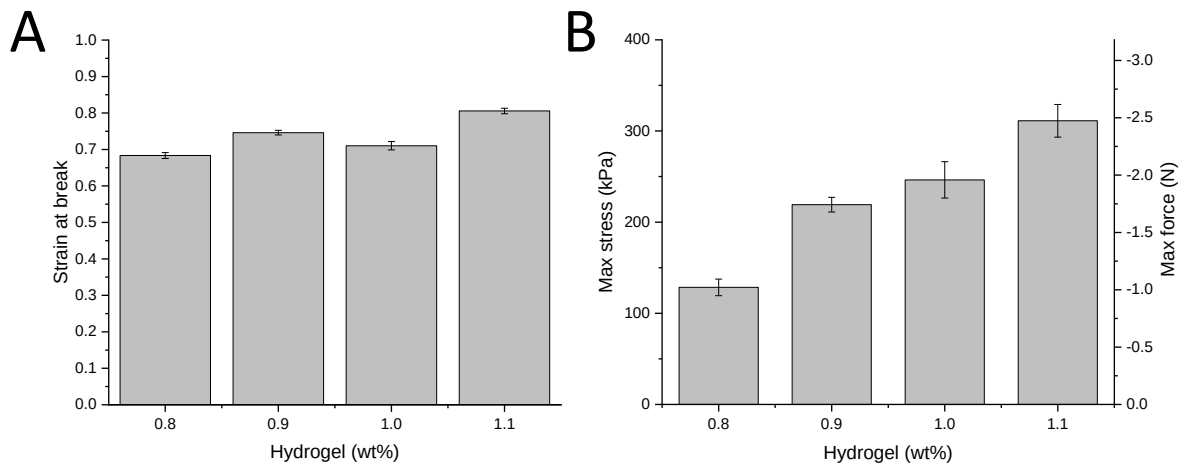

Figure 6.8 Key compression properties of collagen-GMA hydrogel at varying weight percent (wt%). (A) Strain at break was 68.3±0.8, 74.6±1.8, 71.0±2.8 and 80.6±0.7 % (±SE) with for 0.8, 0.9, 1.0 and 1.1 wt%, respectively. (B) Maximum stress was 128.4±9.1, 219.2±8.0, 246.3±20.0 and 311.2±17.9 kPa (±SE) and maximum force was 1.0±0.1, 1.7±0.1, 2.0±0.2 and 2.5±0.1 N (±SE) for 0.8, 0.9, 1.0 and 1.1 wt%, respectively. *n* = 6-8.

implants that match both the everyday movement and injury-prevention characteristics of these tissues (Guimarães et al., 2020).

Compression of the spinal cord where load-deformation or stress-strain data has been displayed can be found for animals such as cats (Hung et al., 1982) and pigs (Sparrey and Keaveny, 2011; Fradet et al., 2016), as well as more recently in human tissue (Karimi et al., 2017).

Cat spinal cords were not simply compressed to failure as done to hydrogels herein, but rather compression was performed at a constant rate to a defined deformation posterior to anterior, followed by decompression at the same rate (Hung et al., 1982). However, during one experiment the cord was deformed to approximately 3, 4, 4.5 and 4.75 mm in 4 different cats, with a cord diameter of approximately 5 mm. For the cord loaded to 4.75 mm, a “sudden decrease in the slope of the curve (or in the rigidity of the spinal cord)” is observed at approximately 4.25 mm, at a force of approximately 290,000 dynes.

Whilst not explicitly stated in the publication, this sudden decrease looks a lot like the failure point of the tissue. If we take this as the failure point and convert deformation to strain and force in dynes to Newtons, this occurs at approximately 85% strain and at a force of approximately 2.9 N. Going further, we can approximate a stress value

at failure of around 150 kPa, as the area of the indenter is given as 19.6 mm^2 (Hung et al., 1982). This is remarkably similar to the hydrogels described herein, especially the 0.8 wt% collagen-GMA hydrogel.

Whilst this was a single anima l cord, two of the other animals loaded to 4 and 4.5 mm experienced a slight plateau before decompression which may have been an indication of failure as well, and also occurred at similar strain values, approximately 80 and 85%, and stress values, approximately 130 and 180 kPa (force approximately 2.6 and 3.6 N, respectively). Further, it should also be noted that very little force is recorded until a deformation of 2-2.5 mm, or 40-50% strain. Again, this is remarkably similar to the collagen-GMA hydrogels described herein, which also see little force measured until 35-45% strain. As such, the hydrogels described herein appear to closely mimic the compressive mechanical properties of spinal cord in the transverse plane.

Further still, more recently the load-deformation data in Hung et al., (1982) for cat spinal cord has been replotted as stress-strain data and a modulus of 5 kPa given for a linear region up to 10% strain (Cheng et al., 2008). A similar value of 4.5 kPa up to 15% strain was calculated elsewhere, dropping to 2 kPa with the dura mater removed (Kroeker et al., 2009). Whilst a linear region up to 10% or 15% strain was not clearly discernible from the compression of collagen-GMA hydrogel, there is clear similarity in the tissue compression data up to 40% strain replotted in Cheng et al., (2008) and the hydrogel data herein (Fig. 6.9). Whilst the specific strain rate used in this experiment was not given, it should be noted that strain rates used throughout Hung et al., (1982) were very slow (<0.0084 s^{-1}), which was similar to the 1% s^{-1} used to test collagen-GMA hydrogels herein. This further indicates that collagen-GMA hydrogels adequately mimic the mechanical properties of spinal cord tissue at low strains, and weight percent of the hydrogel could even be used to finely tune modulus to reflect presence or absence of the dura mater.

Similar J-shaped stress strain curves have also been observed when compressing porcine spinal cord in the same transverse plane (Fradet et al., 2016). Strain at break values appeared similar to those for collagen-GMA hydrogels, occurring at a lowest of 61.0 ± 4.6% up to 74.7 ± 7.1% depending on vertebral level and strain rate. Similar maximum stress values were also recorded, ranging from approximately 150-

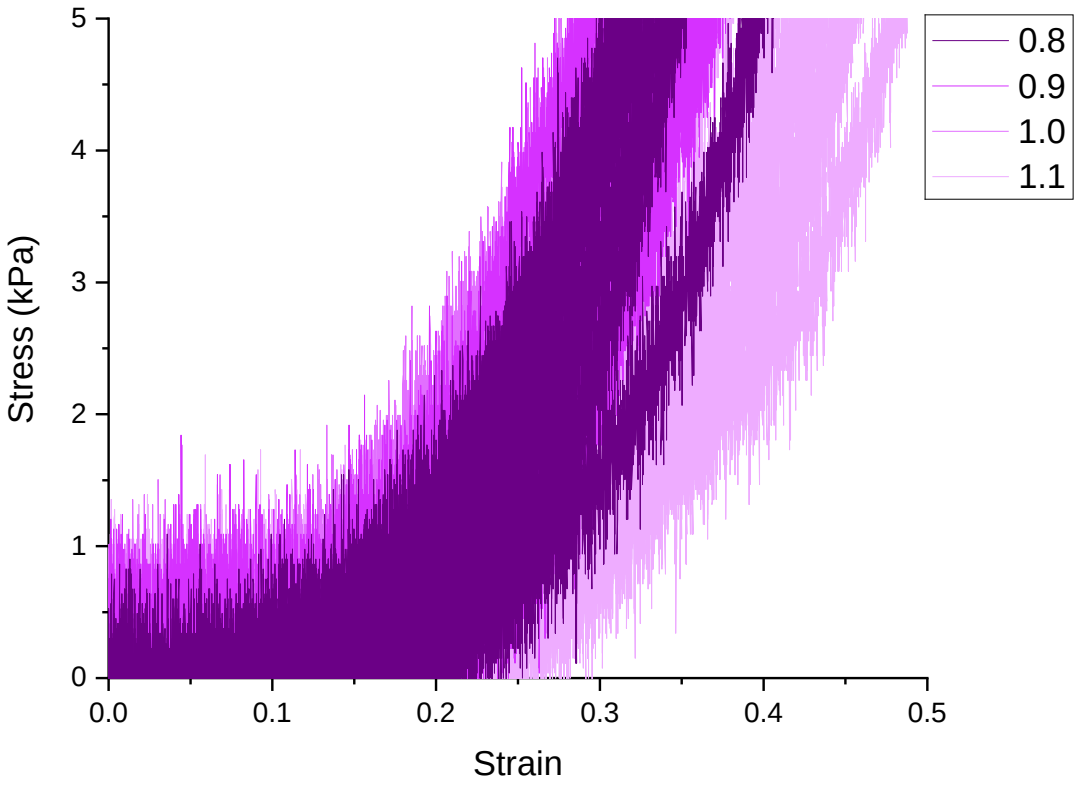

Figure 6.9 Mechanical properties in compression of collagen-GMA hydrogel at varying weight percent (wt%) up to 0.5 strain. Similarities to the replotted spinal cord tissue data of Hung et al. (1982) in Cheng et al. (2008) can be seen up to 0.4 strain. *n* = 6-8.

500 kPa, depending on vertebral level and strain rate. The similarity of the values to those of cat recorded by Hung et al., (1982) indicate spinal cord mechanical properties may be well preserved across mammals.

However, it should be noted that strain rates used by Fradet et al., (2016) were 50% s^{-1} at the lowest, up to 500% and 5000%. As spinal cord is known to display viscoelastic properties in compression, with both rat (Sparrey et al., 2008) and porcine (Sparrey and Keaveny, 2011; Fradet et al., 2016) spinal cord becoming stiffer with increased strain rate, a direct comparison to the hydrogels tested at 1% s^{-1} herein should be made cautiously. Of note, a modulus value was also provided, but specific strain range across which the modulus was calculated was not provided. Instead, a linear region spanning around 40% strain in an example was suggested. However, as curves appeared to be nonlinear this value has not been included for comparison.

Similar J-shaped stress-strain curves have also been observed specifically for the white matter of porcine spinal cord (Sparrey and Keaveny, 2011). Whilst not explicitly stating the plane in which samples were tested, sample height in the transverse plane was given as approximately 1.5 mm with a sample diameter of 3 mm, and as such it has been assumed testing was done at 90° to the angle of axon alignment rather than dorsal-ventral as with Hung et al., (1982) and Fradet et al., (2016). Strain values of approximately 1, 2, 3 and 4 kPa up to 40% strain were recorded for strain rates of 0.5, 5, 50 and 500% s^{-1}. This again highlights the importance of recording strain rate and where appropriate comparisons can be made, but also highlights the similarity of collagen-GMA hydrogels to spinal cord at a similar strain rate, even when compressed in a different plane.

The J-shaped stress-strain curves observed for collagen-GMA hydrogels are also similar to those of human spinal cord (Karimi et al., 2017). However, human spinal cord is reported to have an ultimate compressive strength of around 62.26 ± 5.02 kPa and strain at break around 27% (Karimi et al., 2017). Whilst a strain rate was not given and cord diameters were also not provided to enable calculation, load was applied at 5 mm min^{-1} which is likely similar to the 1% s^{1} used herein, if samples had a similar diameter to that of human spinal cords recorded elsewhere (Bilston and Thibault, 1996). As such, the collagen-GMA hydrogels described herein display both a higher ultimate compressive strength and strain at break, indicating they can be deformed to a greater extent and experience greater stress than native human spinal cord tissue before failure.

However, no analysis was given, and thus it is not clear, why the values of human spinal cord reported by Karimi et al., (2017) appear so different to those reported for cat (Hung et al., 1982) and porcine (Sparrey and Keaveny, 2011; Fradet et al., 2016) spinal cord. Of note, whilst a compressive modulus value was stated for the human spinal cord tissue studied by Karimi et al., (2017), the author herein could not replicate the value from the stress-strain data provided. This was partly due to the omission of the specific portion of the curve from which the modulus value was derived – a common and critiqued inconsistency (Cheng et al., 2008) – and as such has not been used to compare to collagen-GMA hydrogels herein.

If required, tailoring of this hydrogel system to match closer to human spinal cord tissue closer may be possible by altering the linker moiety to 4-vinylbenzyl chloride (4VBC), which has been reported to display a maximum stress around 25-35 kPa and strain at break around 35-40% (Tronci et al., 2013; Tronci et al., 2015). Whilst the maximum stress is around half that desired, the strain at break value more closely matches that of spinal cord. Further, if a similar relationship between weight percent and ultimate compressive strength exists for 4VBC functionalised hydrogels as displayed with GMA functionalised hydrogels herein, a higher ultimate compressive strength for relatively little change in strain at break may be observed.

However, whilst it may be possible to create a hydrogel which mimics these macroscale mechanical properties more closely, it is not yet clear whether this is necessary or desirable for a regenerative spinal cord tissue scaffold. For example, matching shear modulus for optimised cellular activity may be more important than matching macroscale stress-strain behaviour for a spinal cord tissue regenerative scaffold, especially if this is to be remodelled into regenerated tissue in an ideal scenario, which itself should match native mechanical properties. In this way, the scaffold could be thought of as a pre-tissue environment that should be geared towards tissue regeneration and not simply mimicking tissue properties.

Similarly, other factors may become important, such as ensuring a regenerative scaffold is not damaged during implantation. A recent study by Sugiyama et al. (2018) fitted strain gauge force sensors to surgical forceps and measured intra-operative forces on patients during neurosurgery, with forces then coupled to the surgical task being performed. For example, a maximum grip (closing) force of 1.71 N was recorded when placing cotton patties, which could be regarded as a similar task to placement of a regenerative scaffold. Whilst this would fall above the maximum force recorded for the 0.8 and 0.9 wt% collagen-GMA hydrogels, and could indicate weaker hydrogels may be damaged during implantation, this knowledge means factors such as this can be considered when designing regenerative scaffolds and their surgical implantation.

In summary, collagen-GMA hydrogels had J-shaped stress-strain curves that mimicked those seen for spinal cord tissue. Collagen-GMA hydrogels appeared to mimic curves and key values, such as strain at break and maximum stress, recorded

for animal spinal cord tissue. This was both in the transverse plane and perpendicular to it, of which the 0.8 wt% hydrogel appeared most close to spinal cord tissue values, and therefore could mimic bulk mechanical properties from a tissue regeneration requirement. Whilst these values weren't necessarily similar to those recorded for human spinal cord tissue, these findings have not been adequately discussed with respect to the animal tissue values making it hard to compare and understand these findings. As such, the rationale for progressing these hydrogels with respect to the values from animal tissue stands, as well as the appropriateness of the shear modulus of these hydrogels for promoting cellular activity.

Further, the ability to tailor the maximum stress, as described herein by altering the concentration of cross-linked collagen, and the ability to tailor the strain at break by altering the linker moiety, as described previously in the literature (Tronci et al., 2013; Tronci et al., 2015), suggests this is a hydrogel system with high controllability, but further experimentation is required to fully evaluate this claim. This could extend tailoring of the system to more closely match those values recorded for human spinal cord tissue or for specific patient requirements, as tissue mechanical properties appear different with respect to vertebral level (Fradet et al., 2016) and with age (Sparrey et al., 2009).

Further still, whilst not a focus of the work herein, collagen-GMA hydrogels are also likely a better spinal cord surrogate than other materials evaluated in the literature (Kroeker et al., 2009) and could be a suitable *in vitro* model for spinal cord despite previous evaluation (Kirk, 2018), especially as collagen is a component of spinal cord ECM (Haggerty et al., 2017). The J-shaped stress-strain behaviour of collagen-GMA hydrogels would also likely make them appropriate tissue regenerative scaffolds for other biological tissues, such as skin, muscles and arteries (Mitsuhashi et al., 2018).

6.4 Summary

The purpose of this chapter was to investigate collagen-GMA hydrogel properties for three-dimensional cell encapsulation, and evaluate mechanical properties with respect to prioritising cell viability and mimicking spinal cord tissue. Despite a previous investigation ruling out the collagen-GMA hydrogel system as capable of

supporting three-dimensional cell encapsulation (Kirk, 2018), for the first time PC12 cells were shown to be viable after 48 h encapsulation by removing or substituting steps in the hydrogel production protocol that were detrimental for cell survival. One of the main steps was to reduce UV-irradiation time to 10 min, and whilst this was considerably less than that previously reported (Tronci et al., 2013; Tronci et al., 2015; Kirk, 2018), appeared to still result in stable network formation as per rheological evaluation.

Further, a linear relationship was observed between collagen-GMA weight percent in the hydrogel and shear modulus, with modulus values close to those suggested in the literature as being favourable for three-dimensional neural cell encapsulation, particularly the 0.8 wt% hydrogel. Compression of collagen-GMA hydrogels resulted in J-shaped stress-strain curves similar to human spinal cord tissue, with a similar linear relationship observed between collagen-GMA weight percent and maximum stress. Further, maximum stress and strain at break values were close to experimental values in animal tissue, again, particularly the 0.8 wt% hydrogel.

Taken together, the results herein indicate the ability of the collagen-GMA hydrogel system to support three-dimensional neural cell encapsulation and have appropriate mechanical stiffness values for supporting cellular activity and mimicking bulk tissue properties.

Chapter 7

Manufacture and Characterisation of a Composite Nonwoven-Hydrogel Spinal Cord Scaffold

7.1 Introduction

This chapter reports the manufacture and characterisation of a composite nonwoven-hydrogel scaffold for spinal cord injury repair. A combined composite nonwoven-hydrogel scaffold was hypothesized to retain the benefits of the individual nonwoven and hydrogel components, overcome the shortcomings of them in isolation and together provide an environment optimised for spinal cord tissue regeneration.

As determined in Chapter 5, a nonwoven containing a network of highly aligned submicron diameter fibres could promote neurite extension in the direction of fibre alignment. However, the two-dimensional nature of the growth on the surface of the nonwoven fibre web was recognised as an incomplete system for three-dimensional tissue regeneration. Further, in Chapter 6, a single-phase collagen-GMA hydrogel system was shown for the first time to be capable of supporting three-dimensional neural cell encapsulation, and had mechanical properties both suited for neural cell survival and mimicking spinal cord tissue, but was deficient itself in directional cues relevant to support neurite extension. As such, space-filling and cell distribution within the combined composite nonwoven-hydrogel scaffold, as well as neurite alignment, were evaluated to ensure the capabilities of the hydrogel and nonwoven were retained, respectively.

However, whilst numerous methods exist for combining nonwoven and hydrogel, layering was evaluated as likely the simplest method, but one which has drawn a number of critiques that were investigated and challenged using the materials herein. These included the limitation of directional cues to surface effects (Meco and Lampe,

2018) and the limited cell infiltration into and past the electrospun nonwoven. Similarly, whilst numerous methods exist for modulating cell infiltration, laser ablation was evaluated based on the merits of technique in the literature (Sakaguchi et al., 2014; Jun, Kim, et al., 2018; Xue et al., 2019; Ameer et al., 2019; Kowalczyk, 2020), but the lack of evidence nanoscale features might be retained following its use.

Further, the appropriateness of such a scaffold for manufacturability and *in vivo* implantation was also considered and taken as major design constraints. This was addressed by identifying an embodiment of the combined composite nonwoven-hydrogel scaffold that met the ideals of an off-the-shelf product with little preparation required in the clinic, and addressed the potential complication of non-native cell infiltration and connective tissue in-growth in the CNS ECM following implantation.

Accordingly, the purpose of this chapter was to investigate a method of combining electrospun PCL/P_{11}-8 nonwoven and collagen-GMA hydrogel for the first time, as well as characterising the combined composite nonwoven-hydrogel scaffold in terms of cell guidance, infiltration and addressing key challenges as a proposed spinal cord injury repair scaffold.

7.2 Materials and Methods

7.2.1 Manufacture of Dry Collagen-GMA Hydrogel

Collagen-GMA hydrogels were manufactured to serve as a space-filling component of the composite nonwoven-hydrogel spinal cord tissue scaffold and allow three-dimensional encapsulation of cells. Manufacture of collagen-GMA hydrogels required extraction of collagen, functionalisation with GMA and photo-activation as detailed in 3.2.2.1, 3.2.2.2 and 3.2.2.3, respectively, and was adapted from Tronci et al. (2013).

Briefly, collagen type-I was isolated in-house from rat tail tendons by acid dissolution, functionalised with GMA, and photo-activated in PBS in the presence of I2959 photo-initiator under UV light. Resulting hydrogels were washed and allowed to fully hydrate in distilled water for 24 h. To investigate the most suitable drying method enabling minimal microstructure alteration, hydrogel samples were air-dried in a fume-hood overnight or frozen at -80°C for 24 h prior to lyophilisation. SEM imaging

using a Hitachi SU8230 was employed to study pore architecture. Rehydration was conducted by immersing hydrogels in deionised water for 24 h.

7.2.2 Manufacture of the Composite Nonwoven-Hydrogel Scaffold

Aligned electrospun nonwoven was manufactured to serve as a directional guide for neurite extension within the composite nonwoven-hydrogel spinal cord tissue composite scaffold. Electrospun nonwoven was prepared as previously described in Chapter 3.2.1. Briefly, PCL and P_{11}-8 SAP at 40 mg ml^{-1} were dissolved in HFIP, loaded into a 10 ml syringe with an 18 gauge blunt needle and electrospun on to a rotating drum spinning at 30 m s^{-1}, with the following set parameters; flow rate, 1 ml h^{-1}; needle-to-collector distance, 110 mm; applied voltage, 25 V; spin time, 2 h.

Samples of nonwoven were cut out using a 10 mm circular punch and sandwiched between silicone moulds sandwiched between glass slides. Collagen-GMA hydrogel-forming solution prepared as detailed in Chapter 3.2.2 was then mixed with PC12 cells as detailed in Chapter 6.2.5 and UV-irradiated (Spectroline, 365 nm, 9 mW cm^{-2}) for 10 min, placed in pre-warmed media and incubated at 37°C/5% CO_2.

For lyophilised samples, nonwoven was cut out using a 10 mm circular punch and sandwiched between silicone moulds sandwiched between glass slides to produce composite bi-layered (nonwoven-hydrogel) and tri-layered (hydrogel-nonwoven-hydrogel or nonwoven-hydrogel-nonwoven) scaffolds (Fig. 7.1). Silicone moulds sandwiched between glass slides were alternately filled with collagen-GMA hydrogel-

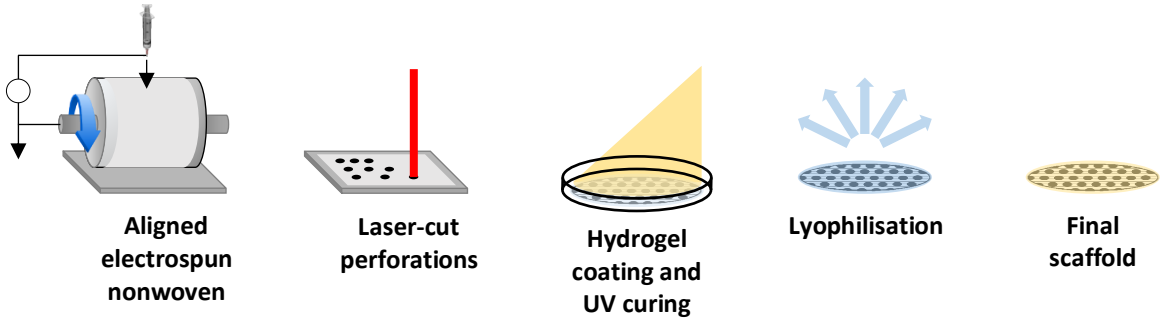

Figure 7.1 Diagram showing the scaffold manufacturing process. Nonwoven is electrospun on to a rotating drum to highly align fibres. The sheet of highly aligned nonwoven is then perforated using laser-ablation. The laser-ablated nonwoven is coated in hydrogel using silicone moulds sandwiched between glass slides and UV cured. Successive layers of hydrogel and nonwoven can be added, including non-ablated nonwoven. Lastly, the scaffold is lyophilised.

forming solution prepared as detailed in Chapter 6.2.1 and UV-irradiated (Spectroline, 365 nm, 9 mW cm^{-2}) for 10 min on either side. Samples were washed and allowed to full hydrate in distilled water for 24 h, frozen at -80°C for 24 h and lyophilised for a further 24 h. SEM imaging using a Hitachi SU8230 was employed to study integration of the nonwoven and hydrogel components.

7.2.3 Cell Viability of PC12 Cells in Lyophilised Collagen-GMA Hydrogel

Cell viability was studied to determine whether high cell viability could also be achieved in dry collagen-GMA hydrogel. PC12 cells were expanded as detailed in Chapter 6.2.5, but directly seeded onto lyophilised collagen-GMA hydrogel at 3 x 10^6 cells ml^{-1}. After 60 min, cell-laden lyophilised collagen-GMA hydrogels were immersed in pre-warmed media and transferred to an incubator at 37°C. Positive controls, where a cytotoxic response was expected, were prepared as above but with 50% (v/v) DMSO in the cell culture media. PC12 cells grown on tissue culture plastic coated in PDL to aid adherence were used as negative controls, with high viability expected.

Cells were allowed to grow for 48 h with one 50% media change after 24 h. A LIVE/DEAD™ Viability/Cytotoxicity Kit for mammalian cells (Invitrogen™, USA) was used to stain live cells green using calcein-AM and dead cells red with ethidium homodimer-1. Cells were imaged using a Leica SP8 Confocal Laser Scanning Microscope. ImageJ (http://imagej.nih.gov/ij/) was used to count the number of cells and given as a percentage of total cell number.

7.2.4 Neurite Extension of PC12 Cells in Composite Nonwoven-Hydrogel Scaffolds

Neurite extension was studied to determine the directional cues in the combined composite nonwoven-hydrogel scaffold. Bi-layered composite nonwoven-hydrogel scaffolds were constructed as detailed in Chapter 7.2.2. PC12 cells were expanded as detailed in Chapter 6.2.5 and seeded to form pre-hydrated composite nonwoven-hydrogel scaffolds or on to lyophilised composite nonwoven-hydrogel scaffold at 3 x 10^6 cells ml^{-1}. Cell-laden scaffolds were kept in an incubator at 37°C, media changed every 2-3 days and supplemented with recombinant human β-NGF (BioLegend, USA) at 100 ng ml^{-1}. After 7 days, composite nonwoven-hydrogel scaffolds were

fixed, stained and imaged as detailed in Chapter 5.2.2. Briefly, cells were fixed in neutral buffered formalin, permeabilised in Triton X-100 and stained using Mouse Anti-Neuron-specific β-III Tubulin Monoclonal Antibody, followed by Polyclonal Rabbit Anti-Mouse Immunoglobulins/FITC. Samples were washed using PBS between each step and imaged using a Leica SP8 Confocal Laser Scanning Microscope.

7.2.5 Liquid Wicking Rate of Collagen-GMA Hydrogel-Forming Solution into Electrospun PCL and PCL/P_{11}-8

To investigate the effect of SAP on liquid wicking rate of collagen-GMA hydrogel-forming solution into electrospun PCL and PCL/P_{11}-8, the wicking strip test was adapted to suit the materials herein. Due to the lightness of samples and their tendency to curl from static build-up, samples were secured at both ends and a 50 µl droplet of collagen-GMA hydrogel-forming solution pipetted at the base of the sample.

Electrospun nonwoven as prepared in Chapter 4.2.1 was cut into strips 30 x 5 mm (L x W) in the machine direction due to the smaller quantities of the material available and fixed across a paper window with a 20 mm gauge length using double-sided tape. Due to the lightness of samples and their tendency to curl from static build-up, samples were secured at both ends and a 50 µl droplet of collagen-GMA hydrogel-forming solution pipetted at the base of the sample, rather than immersing into a reservoir of solution. Samples were secured at the top end in jaw clamps attached to a Bose ElectroForce® 3200 fitted with a 10 N load cell, and at the bottom to a flat plate using double-sided tape, using the setup to ensure the sample was tort but not placed under excess tension (under 1 N). Samples were filmed for 300 s, backlight to aid visualisation, and secured next to a ruler to accurately measure the advancing liquid front. The height of the liquid front was measured at 0, 10, 30, 60 and 300 s. n = 8.

7.2.6 Dry Mass of Composite Nonwoven-Hydrogel Scaffolds

Total dry mass of composite nonwoven-hydrogel scaffolds was investigated to understand the effect of SAP on collagen-GMA hydrogel-forming solution absorption. Samples of nonwoven were cut out using a 10 mm circular punch, weighed, and laid

face down for 60 s on a reservoir of collagen-GMA hydrogel-forming solution prepared as detailed in 6.2.1, before turning on to the opposite side for a further 60 s. Samples were UV-irradiated (Spectroline, 365 nm, 9 mW cm^{-2}) for 10 min on either side. Coating and UV-curing was repeated for second-coat samples. Samples were washed and allowed to full hydrate in distilled water for 24 h, frozen at -80°C for 24 h and lyophilised for a further 24 h. Mass was re-recorded and compared to the nonwoven without hydrogel.

7.2.7 Laser Ablation of PCL/P_{11}-8 Nonwoven

Laser ablation was used to introduce pores into the nonwoven to promote cell infiltration. An FB1800 Laser Cutting and Engraving Machine fitted with a 100 W CO_2 laser and running ApS-Ethos software (CadCam Technology Ltd, UK) was used to introduce porosity into PCL/P_{11}-8 electrospun nonwoven. Pores were created in the nonwoven by programming single points for the laser and setting axial speed at 600 mm s^{-1}. Power setting was altered between 5-100% and inter-pore distance between 0.5-10 mm. SEM imaging using a Hitachi SU8230 was employed to study size and the effect on the fibre surface from laser exposure. ImageJ (http://imagej.nih.gov/ij/) was used to measure inter-pore distance, pore area and compare to the total area available for cell infiltration.

7.2.8 PC12 Cell Infiltration Assay of Laser-Ablated Composite Nonwoven-Hydrogel Scaffold

To evaluate the effects of laser ablation on cell infiltration, bi-layered composite nonwoven-hydrogel scaffolds were prepared as detailed in Chapter 7.2.2 and placed in a Minusheet tissue carrier (https://minucells.com/). PC12 cells were expanded as detailed in Chapter 6.2.5 and seeded at 1 x 10^5 cells ml^{-1}. Electrospun PCL/P_{11}-8 nonwoven with laser-ablated pores set at an inter-pore distance of 1.0, 1.5 and 2.0 mm gave porosities of 23.9, 12.5 and 5.5%, respectively. PCL/P_{11}-8 without laser-ablated pores and collagen-GMA hydrogel on its own were used as 0% and 100% controls, respectively.

After 24 hours in an incubator at 37°C/5% CO_2 cells were fixed, stained and imaged as detailed in Chapter 5.2.2. Briefly, cells were fixed in neutral buffered formalin, permeabilised in Triton X-100 and stained using Mouse Anti-Neuron-specific β-III

Tubulin Monoclonal Antibody, followed by Polyclonal Rabbit Anti-Mouse Immunoglobulins/FITC. Samples were washed using PBS between each step and imaged using a Leica SP8 Confocal Laser Scanning Microscope.

Mean cell count values were compared to determine statistically significant difference between porosity groups. As there were more than two independent variables, a one-way ANOVA was used. Data was initially checked for normality using a Shapiro-Wilk test and homogeneity of variance (HOV) using Levene's test (required assumptions of ANOVA). Data was normal but not homogeneous. However, this violation was considered permissible due to equal sample sizes between groups. Statistical significance was concluded if *p*-value was less than 0.05. A Games-Howell post-hoc test was used to determine differences between individual groups due to the HOV violation. All statistics were done using OriginPro software (OriginLab Corporation, USA).

7.2.9 L929 Cell Exclusion Assay of Non-Ablated PCL/P_{11}-8

Cell-impermeability of non-ablated electrospun PCL/P_{11}-8 nonwoven was evaluated for its potential use as an outer layer for preventing non-native cell infiltration. A tri-layer composite nonwoven-hydrogel scaffold consisting of a first laser-ablated PCL/P_{11}-8 web (1.0 mm inter-pore distance), a second lyophilised collagen-GMA hydrogel, and a third non-ablated PCL/P_{11}-8 web was prepared as detailed in Chapter 7.2.2. The scaffold was placed into a Minusheet tissue carrier (https://minucells.com/) to provide a reservoir on both sides of the scaffold and incubated at 37°C. PC12 cells were expanded as detailed in Chapter 6.2.5 and seeded at 1 x 10^6 cells ml^{-1} on the first collagen-GMA hydrogel side. Recombinant human β-NGF (BioLegend, USA) was included in the media at 100 ng ml^{-1}.

After 5 days with one 50% media change after 3 days, scaffolds were turned over and L929 fibroblasts seeded on to the non-ablated PCL/P_{11}-8 layer. L929 cells were expanded and grown in High Glucose DMEM (Lonza, UK) media supplemented with 10% heat-deactivated horse serum (Sigma-Aldrich, UK), 5% foetal bovine serum (FBS) (Sigma-Aldrich, UK), 1% L-Glutamine (Sigma-Aldrich, UK) and 1% penicillin/streptomycin (Sigma-Aldrich, UK). After 24 hours, scaffolds were fixed as in Chapter 5.2.2, stained and imaged using a Leica SP8 Confocal Laser Scanning Microscope.

PC12 cells were stained using Mouse Anti-Neuron-specific β-III Tubulin Monoclonal Antibody (MAB1195, Bio-Techne, USA) followed by Goat Anti-Mouse IgG/Alexa Fluor Plus 488 (A32723, ThermoFisher Scientific, USA). L929 cells were stained using Rabbit Anti-CD31 Polyclonal Antibody (PA5-16301, ThermoFisher Scientific, USA) followed by Donkey Anti-Rabbit IgG/Alexa Fluor Plus 555 (A32794, ThermoFisher Scientific, USA). A Mouse-on-Mouse (M.O.M.) Immunodetection Kit (BMK-2202, Vector Labs, UK) was used to prevent non-specific binding of the Goat Anti-Mouse secondary antibody to L929 cells. M.O.M. Mouse IgG Blocking Reagent was used to block following primary antibody incubation for 1 h before addition of secondary antibodies for 1 h in the dark, diluted in M.O.M. Diluent as per the manufacturer's protocol.

7.3 Results and Discussion

A composite nonwoven-hydrogel scaffold of electrospun PCL/P_{11}-8 and collagen-GMA hydrogel was combined for the first time and evaluated as a spinal cord tissue scaffold. Characterisation of the composite scaffold included confirmation of the integration between the two materials, effect of SAP in the nonwoven, cell infiltration into the scaffold and neurite alignment.

7.3.1 Neurite Extension in the Composite Nonwoven-Hydrogel Scaffold and the Effect of Surrounding Material on the Alignment of Neurites

For the first time, electrospun PCL/P_{11}-8 nonwoven and collagen-GMA hydrogel were combined to form a composite nonwoven-hydrogel scaffold that supported directional neurite extension. PC12 cells were mixed with collagen-GMA hydrogel-forming solution, pipetted on top of electrospun PCL/P_{11}-8 nonwoven, UV-irradiated and immediately placed in an incubator. Cells were observed both on the nonwoven surface (Fig. 7.2A) and away from the nonwoven surface surrounded by hydrogel (Fig. 7.2B). After 7 days of NGF exposure, cells in contact with the nonwoven surface were visualised extending neurites in the direction of fibre alignment (Fig. 7.2C), whilst cells away from the nonwoven surface were observed extending neurites in a random orientation in the hydrogel (Fig. 7.2D).

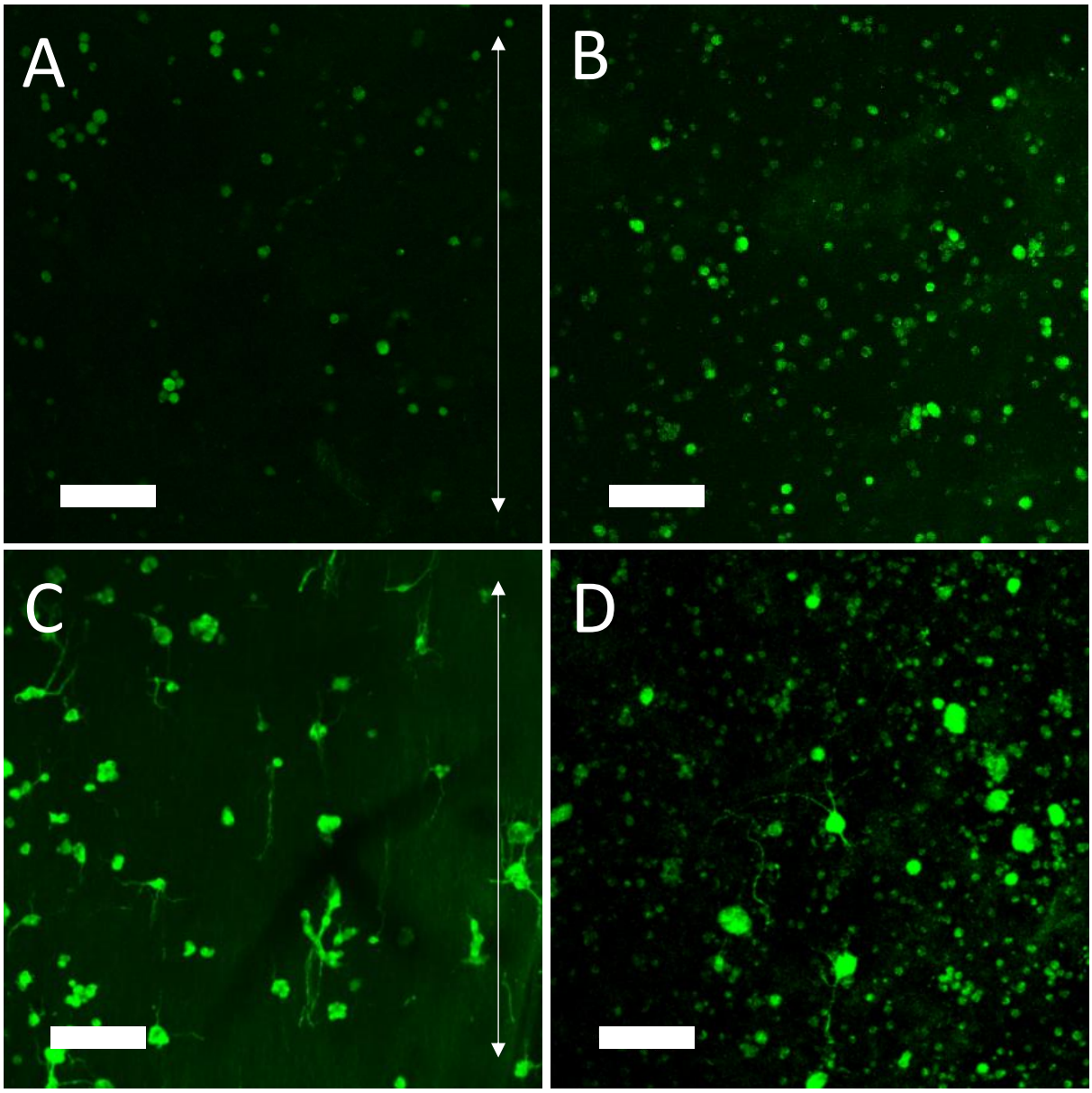

Figure 7.2 Neurite extension of PC12 cells in the composite nonwoven-hydrogel scaffold. PC12 cells were mixed with collagen-GMA hydrogel-forming solution, pipetted on top of electrospun PCL/P_{11}-8 nonwoven, UV-irradiated for 10 min and placed into an incubator at 37°C/5% CO_2 for 7 days. Immediately after incubation cells were observed on both the (A) surface of electrospun PCL/P_{11}-8 and (B) at least 50 µm away from the nonwoven surrounded by collagen-GMA hydrogel. Following 7 days of NGF exposure, (C) PC12 cells in contact with the nonwoven surface were observed extending neurite in the direction of fibre alignment, whilst (D) away from the nonwoven surface, cells were observed extending neurites in a random orientation. Arrows show direction of alignment. Scale bar is 100 µm.

This spatial effect of layering hydrogel and nonwoven on manipulating neurite extension agrees with the results observed elsewhere. Neurite alignment from SH-SY5Y neuron-like cells was influenced greater in a scaffold of electrospun PCL and

hyaluronic acid hydrogel when cells were in close contact with fibres, and augmented when fibres were coated in laminin (McMurtrey, 2014). Similarly, neurite elongation from rat cortical neurons was observed in a composite scaffold of aligned chitosan hydrogel layered over aligned electrospun PLLA, the effects of layering most notable when each material was layered perpendicular to each other and neurites were observed extending in the direction of alignment relative to the focal plane (Miller et al., 2018). This effect has also been observed with glial cells, where rat astrocytes aligned relative to the direction of aligned fibres in a stacked composite scaffold of electrospun poly-L,D-lactic acid and collagen hydrogel, and complex process-bearing oligodendrocytes were also observed contacting aligned fibres and astrocytes (Weightman, Jenkins, et al., 2014).

Whilst the effects were not quantified herein, there was an indication that cells did not have to be in direct contact with fibres to be directionally influenced. This has been somewhat quantified in a different study, where a composite scaffold of aligned PCL fibres with a PuraMatrix™ SAP-based hydrogel layered on top observed human embryonic stem cell (hESC)-derived neurons aligning processes with the direction of the underlying fibres when up to 10 µm away but no further (Hyysalo et al., 2017).

However, despite the affects observed herein, the clinical applicability of manufacturing the scaffold in this way was questioned. The main issue was the requirement to combine a pre-cell-mixed and pre-hydrated collagen-GMA hydrogel with electrospun PCL/P_{11}-8 nonwoven and how realistic this would be as an off-the-shelf product. Firstly, the requirement to mix cells with collagen-GMA hydrogel-forming solution to ensure cell distribution throughout hydrogel would either require cells to be available at the point of scaffold production or require scaffold production to occur in the clinic. In both cases, this would negate the product as being off-the-shelf and present difficulties in maintaining sterility.

Further, limited cell infiltration of 50 µm in 48 hours was observed if cells were seeded post UV-irradiation, as shown in Chapter 6.3.1, and whilst it may be possible to improve this by using means such as a perfusion pump or incubating for longer period of time, this would still involve combining a water-filled hydrogel with a water-soluble polymer-peptide nonwoven and would compromise any shelf life for the product.

As such, whilst directed neurite extension had been observed in a composite scaffold of electrospun PCL/P_{11}-8 and pre-hydrated collagen-GMA hydrogel, the commercial potential of this embodiment was not deemed feasible. To address this, a method of dehydrating the scaffold was investigated to see if similar results could be obtained, but in an embodiment that would not compromise shelf-life. Whilst discussed further in Chapter 7.3.5, lyophilisation was found to retain pore structure, volume and cell viability, and so was chosen for further investigation.

Of greatest importance, directed neurite outgrowth was still observed following lyophilisation of the scaffold and hydration only at the point of PC12-cell seeding. Following seeding, cells were observed on the surface of PCL/P_{11}-8 nonwoven (Fig. 7.3A), and on the surface of aligned PCL (Fig. 7.3B) and random PCL (Fig. 7.3C) control groups, as well as away from the nonwoven surface in lyophilised collagen-GMA hydrogel for all groups (Fig. 7.3D, E, F). After 7 days exposure to NGF, PC12 cells were observed extending neurites in all experimental groups and when seeded on both lyophilised collagen-GMA hydrogel and electrospun nonwoven. However, as seen previously herein, neurites from cells in contact with electrospun nonwoven aligned with the direction of the underlying fibres, with both aligned PCL/P_{11}-8 (Fig. 7.3G) and aligned PCL (Fig. 7.3H) promoting unidirectional neurite outgrowth and random PCL (Fig. 7.3I) promoting random outgrowth. Similarly, cells found in lyophilised collagen-GMA hydrogel promoted random neurite outgrowth irrespective of the experimental group (Fig. 7.3J, K, L).

As such, the results herein show a lyophilised composite nonwoven-hydrogel scaffold of electrospun PCL/P_{11}-8 fibres and collagen-GMA hydrogel are still able to support directed neurite outgrowth, as seen when pre-hydrated collagen-GMA hydrogel is used, but address the temporal issue of having water and cells mixed with nonwoven during scaffold production and provide an embodiment suitable as an off-the-shelf product.

However, whilst either embodiment show layering can produce a composite nonwoven-hydrogel scaffold capable of influencing cell morphology and process alignment, it should be highlighted these effects are regionally defined. Indeed, this has been labelled as a critique of layering as an approach for combining nonwoven and hydrogel, as materials are still limited to surface or near-surface effects rather

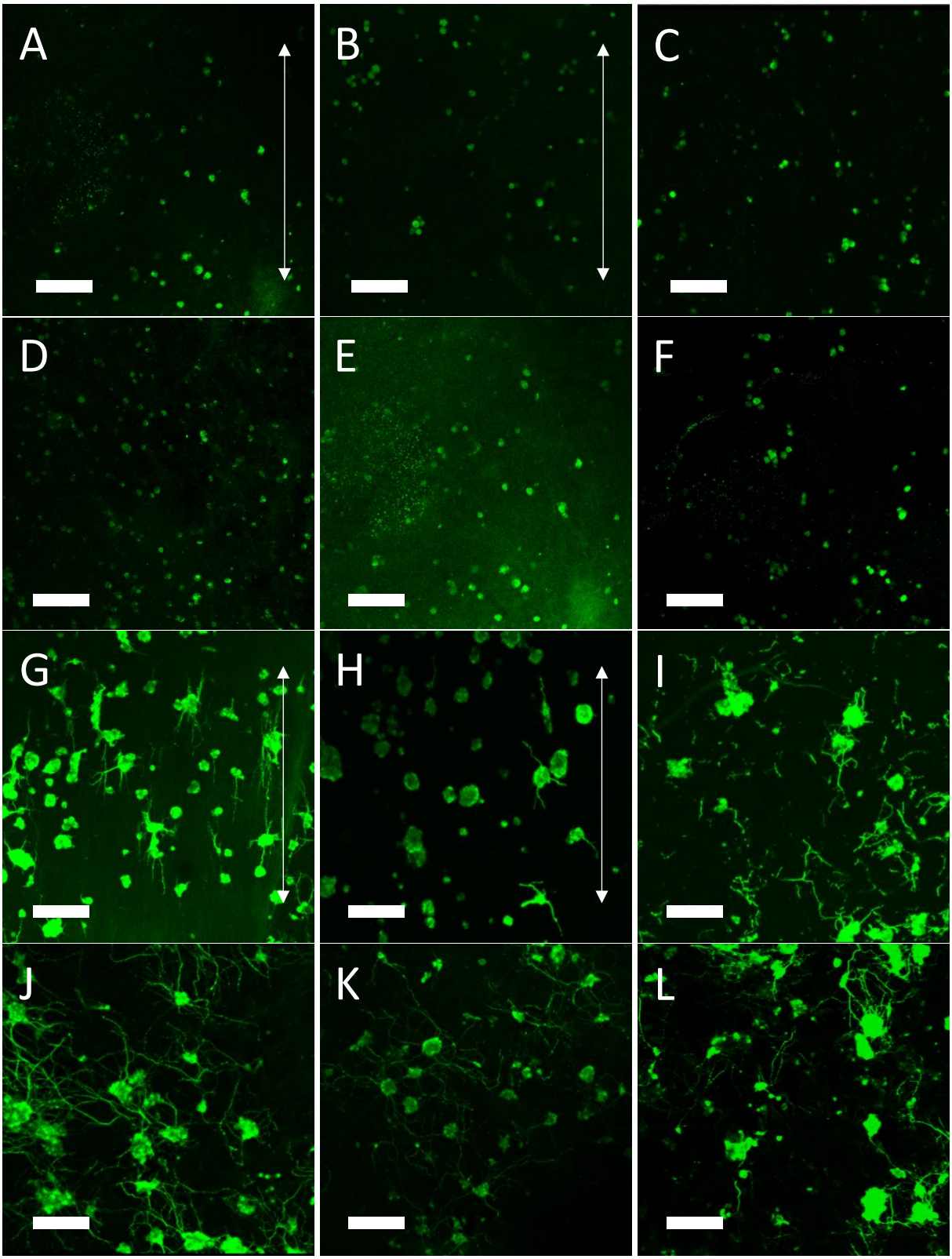

Figure 7.3 Neurite extension of PC12 cells in lyophilised composite nonwoven-hydrogel scaffold. After seeding, cells were observed on the nonwoven surface of (A) aligned PCL/P_{11}-8, (B) aligned PCL and (C) random PCL, as well as at least 50 μm away in the hydrogel (D, E, F). After 7 days, cells in contact with the nonwoven extended neurites in the direction of fibre alignment for (G) aligned PCL/P_{11}-8 and (H) aligned PCL, but random on (I) random PCL. (J, K, L) Away from the nonwoven neurites extended randomly for all groups. Arrows show direction of alignment. Scale bar is 100 μm.

than a more homogeneous three-dimensional environment at the cell scale (Meco and Lampe, 2018). This is observed physically to some extent in the results herein, where PC12 cells appear to retain a more rounded, spherical morphology in the collagen-GMA hydrogel region of the pre-hydrated composite nonwoven-hydrogel scaffolds (Fig. 7.2), but flatter and more spread when in contact with the lyophilised collagen-GMA hydrogel region of the lyophilised composite nonwoven-hydrogel scaffolds (Fig. 7.3). The results herein reinforce the understanding that layering, especially at the scale performed herein, can influence cell and process alignment, but does not provide a homogeneous environment in which all cells are exposed to directional cues.

However, the author challenges the notion this is a major drawback to layering as an approach for creating a combined composite nonwoven-hydrogel scaffold, especially for spinal cord injury repair. The spinal cord itself is made up of regions where promoting alignment would be beneficial for recapitulating the tissue structure, such as in the white matter, but also of regions where alignment is only partially required, such as in the grey matter. As such, defining regions within a scaffold where alignment would be necessary and beneficial, but also defining those regions where alignment would possibly promote abnormal tissue structuring compared to the native environment, seems just as important. As such, whilst not taken further in the work herein, the author would suggest that regional variation in a scaffold to promote spinal cord regeneration be looked at as an advantage for controlling tissue structuring, especially for tissues such as spinal cord, where heterogeneity is apparent and important for the structure-function relationship.

In summary, PC12 cells were visualised for the first time extending neurites in a layered composite nonwoven-hydrogel scaffold of aligned electrospun PCL/P_{11}-8 nonwoven and collagen-GMA hydrogel. Neurite extension was observed when the hydrogel was pre-hydrated and also following lyophilisation of the whole scaffold as an embodiment closer to an off-the-shelf product. Whilst the scaffold consisted of both nonwoven and hydrogel, the layering approach lead to heterogeneity with regards to the materials within the scaffold. This ultimately meant cells in contact directly with nonwoven had neurite alignment influenced by the underlying fibre alignment, but cells in contact with collagen-GMA hydrogel, whether pre-hydrated or lyophilised, extended neurites randomly.

As such, the layering approach herein does not overcome the main criticism to layering as an approach for combining nonwovens and hydrogels, namely that directional cues are still limited to surface effects, but rather provides further evidence this is the case. However, the main criticism itself is challenged with respect to the spinal cord tissue architecture, as spinal cord tissue contains regions in which tissue alignment is not required and should therefore not be sought.

7.3.2 Cell Infiltration in the Composite Nonwoven-Hydrogel Scaffold and the Effect of Laser Ablation on Nonwoven Porosity

Whilst lyophilisation was identified as an adequate means of dehydrating the scaffold to retain pore structure and volume of the hydrogel, which contributed to retaining cell infiltration and distribution throughout the scaffold, the issue of cell distribution past the nonwoven was still unaddressed. This is even more of an issue for a layered scaffold, especially if multiple nonwoven and hydrogel layers are desired, as cells would not be able to infiltrate consecutive layers.

Indeed, despite high percentage porosity, it is well known the small pore size typical of electrospun nonwovens inhibits cell infiltration, and thus numerous techniques have been developed to increase pore size and porosity, including optimisation of the conventional electrospinning parameters for pore size augmentation (Sakaguchi et al., 2014; Ameer et al., 2019); methods of concurrent or sequential electrospinning of different polymers or polymer concentrations (Ameer et al., 2019); concurrent electrospraying of cells, media or hydrogel (Sakaguchi et al., 2014); and introduction of sacrificial elements (Sakaguchi et al., 2014; Ameer et al., 2019).

Whilst these mid-production techniques are able to achieve increased pore size and porosity, their reliance on custom apparatus has limited their widespread adoption, and has meant post-production techniques have emerged as more favourable methods for altering porosity for cell infiltration, as they require little change to the conventional electrospinning setup. These include, introducing leachable components (Sakaguchi et al., 2014; Kowalczyk, 2020), ultrasonication (Sakaguchi et al., 2014; Ameer et al., 2019; Kowalczyk, 2020), gas-foaming (Ameer et al., 2019) and laser ablation (Sakaguchi et al., 2014; Jun, Han, et al., 2018; Xue et al., 2019; Ameer et al., 2019; Kowalczyk, 2020).

Of these, the regularity, precision, reproducibility and speed of the porosity introduced using laser-ablation sets it apart from the other post-production techniques. However, whilst laser ablation of electrospun nonwoven for creating porosity for improved cell infiltration has been investigated extensively for bone tissue repair (Rodríguez et al., 2014; Kim et al., 2014; Aragon et al., 2017; Jahnavi et al., 2017; Ma et al., 2018; Datta and Dhara, 2019), and to some degree for dental (Ma et al., 2018), smooth muscle (Joshi et al., 2013; Walthers et al., 2014), ligament (Petrigliano et al., 2015) and more general regenerative medicine (McCullen et al., 2011; Lee et al., 2012; Fuller et al., 2019), its use in spinal cord regenerative scaffolds has not yet been investigated.

As such, to investigate the use of laser ablation for introducing porosity into the electrospun nonwoven and its effect on cell infiltration for spinal cord tissue repair, a cell infiltration assay was set up using lyophilised composite nonwoven-hydrogel scaffolds of electrospun PCL/P_{11}-8 nonwoven and collagen-GMA hydrogel, seeding PC12 cells on top and subsequently counting the number of cells in the collagen-GMA hydrogel. Further, scaffolds were encased in a Minusheet tissue carrier (https://minucells.com/) to prevent cells being lost from the scaffold into the media. In this study, the individual pore area was kept constant at around 0.329 mm^2 per pore (~250 µm pore diameter) (see Fig. 7.15B) but by altering the inter-pore distance, the laser-ablated porosity available to cells in the area within the Minusheet was altered (Fig. 7.4A). Inter-pore distances of 1.0, 1.5 and 2.0 mm introduced a porosity of 23.9, 12.5 and 5.5%, respectively, and these groups were taken forward for use in the cell infiltration assay, along with nonwoven without any laser ablated holes and collagen hydrogel on its own as 0% and 100% porosity controls, respectively. Mean cell count was 70 ± 7 (SE), 632 ± 36, 978 ± 61, 2362 ± 111 and 2117 ± 166 for the 0, 5.5, 12.5, 23.9 and 100% porosity groups, respectively (Fig. 7.4B).

From these results, there is an indication that by increasing the percentage porosity using pores of this size, increased cell infiltration across a cell-impermeable nonwoven and into the collagen-GMA hydrogel was achieved. However, this only appears to have occurred up to a porosity of 23.9%, with the 23.9% group and the 100% group (no nonwoven, just collagen-GMA hydrogel) showing similar cell counts and no statistical difference between them. As such, a linear relationship appears to exist up to a porosity of 23.9%, the strength of which is indicated by the R^2 value of

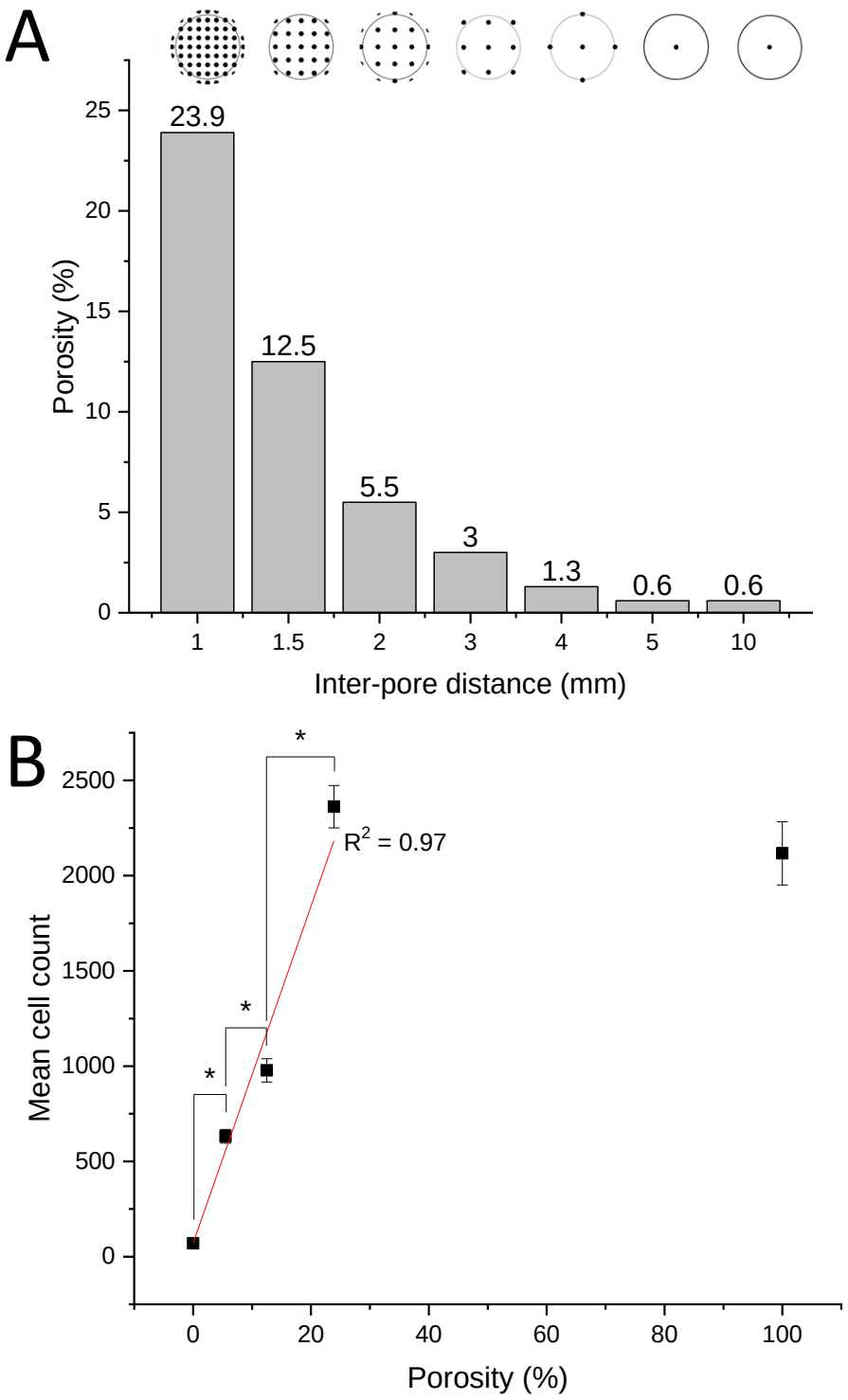

Figure 7.4 Porosity introduced into the electrospun nonwoven using laser ablation and its effect on cell infiltration into the underlying collagen-GMA hydrogel. (A) By altering the inter-pore distance, a matrix of laser-ablated pores was created that modulated the available porosity for cell infiltration within the Minuclip. Above each bar the pattern of laser-ablated dots can be seen within the circle depicting the area of the Minuclip. (B) Mean cell count was 70±7 (SE), 632±36, 978±61, 2362±111 and 2117±166 for the 0, 5.5, 12.5, 23.9 and 100% porosity groups, respectively. The available porosity from laser ablation positively correlated with the number of cells in the underlying collagen-GMA hydrogel up to 23.9%, with an adjusted R^2 of 0.97, with no significant difference to the number of cells in the hydrogel-only group. *$p \leq 0.05$. $n = 6$.

0.98, but potentially reaches a threshold here, beyond which further increases in porosity do not translate into increased cell infiltration.

Similarly, Walthers et al. (2014) kept pore size constant at 250 µm diameter and altered percentage porosity using inter-pore distance when investigating electrospun PCL with smooth muscle cells (SMCs). The electrospun scaffold was seeded with intestinal SMCs and wrapped around the omentum of Lewis rats. After 2 weeks, a similar result was observed where virtually no cells were able to penetrate past an intact electrospun nonwoven, but with increasing porosity from 15 to 20 to 25%, the number of surviving SMCs increased, as well as the quantification of von Willebrand Factor (vWF) as an indication of angiogenesis. Whilst the authors note in this case the 15 and 20% porosity groups had similar results, and a threshold seemed to occur between 20 and 25% porosity for significantly promoting SMC survival three-fold, the results herein still support a similar narrative; that increasing porosity at these pore sizes leads to increased cell infiltration both *in vitro* and *in vivo*.

The authors also state the dichotomy between promoting cell infiltration by removing material and leaving enough material for adequate cell attachment, and go on to muse whether 25% porosity is optimal or whether further increases would further promote infiltration and survival. Whilst the study performed by Walthers et al. (2014) and the study herein have stark differences, including the cell type, scaffold morphology and experimental environment, our results herein suggest a porosity of around 25% may be optimal, or at least a threshold may be reached where increasing porosity further does not result in higher cell infiltration. As such, it may be possible to maximise cell infiltration before a tipping-point is reached and cell attachment is significantly affected, though to understand this further studies focusing on optimisation would need to be completed on specific scaffolds.

Whilst it does not explicitly say, Walthers et al. (2014) may have reached a limit with respect to percentage porosity anyway, as SEM images indicate a smaller inter-pore distance may have caused melting between holes and prevented defined holes from being created. This was the case herein, as an inter-hole distance of 0.5 mm versus 1 mm meant defined holes in the nonwoven could not be made. Whilst laser technology does exist that could produce much smaller laser-ablated holes with minimal melting of polymer, such as that displayed for femtosecond lasers (Rebollar

et al., 2011; Lee et al., 2012; Kim et al., 2014; Adomavičiūtė et al., 2015), there is an indication that hole diameters of over 100 µm may required for adequately promoting cell infiltration.

For example, Joshi et al. (2013) in an earlier publication used the same laser-ablated electrospun PCL scaffold as Walthers et al. (2014) but kept percentage porosity constant at 15% and altered pore size from 80 to 160 to 300 µm diameter. Cell infiltration, collagen deposition and ECM deposition increased as pore size increased. However, anti-α-SMA antibody used to detect blood vessel formation and red blood cells themselves could only be seen in the 160 and 300 µm diameter groups. These results indicate that a threshold pore size may be required to achieve adequate cell infiltration and tissue regeneration, and whilst smaller pores spaced closer together could be used to increase the overall percentage porosity of a scaffold, this would not necessarily lead to increased cell infiltration.

Of note, Joshi et al. (2013) also investigated the effect of laser-ablated porosity on mechanical properties of the nonwoven. Maximal mechanical force reduced by around 40% from 10 N to 6 N in 15% porosity samples, regardless of pore size, but Young's modulus remained relatively unaffected. The authors explained this as the melted ring of polymer being a focus for stress and area of propagation for fractures between fibres, but with no inherent change to the chemical or crystal structure of PCL. Whilst this should be kept in mind, as the composite nonwoven-hydrogel scaffold herein does not have a load-bearing function and the mechanical properties of the hydrogel are more relevant for the spinal cord scaffold, the effect of laser-ablation on the mechanical properties of the electrospun nonwoven are of less importance. However, for load-bearing scaffolds or those where the mechanical properties of the nonwoven are essential, the effect of material removal should be considered.

In summary, to facilitate cell infiltration past the nonwoven and into the layered scaffold, porosity was introduced using laser ablation. By altering the inter-pore distance in a matrix of laser-ablated pores, the porosity available for cell infiltration could be altered. The degree of PC12 cell infiltration past the electrospun nonwoven and into the underlying lyophilised collagen-GMA hydrogel positively correlated with percentage porosity up to 23.9%, after which no statistical difference was observed

with the hydrogel-only group. This result reinforces complementary results observed from the literature that increasing percentage porosity leads to increased cell infiltration, but goes further to suggest that this only occurs up to a point, after which this relationship is no longer true. Again, from the results herein and complementary results from the literature, the author suggests that laser-ablated pore diameters of at least 150 µm in diameter and porosity of around 25% are potentially optimal for cell infiltration.

7.3.3 Proof of Principle for PCL/P_{11}-8 as a Cell-Impermeable Layer for Preventing Non-Native Cell Infiltration in a Composite Nonwoven-Hydrogel Scaffold

There is also a requirement for a spinal cord injury scaffold to prevent non-native cell infiltration. Normally, it is only in severe spinal cord injuries that stab lesions feature, where the meninges are disrupted and connective tissue ingrowth occurs on top of the secondary biological response to the injury itself (Silver and Miller, 2004). This is infiltration into the CNS of cell types that do not normally reside on this side of the blood-CNS barrier, such as fibroblasts, and deposition of additional connective tissue, such as collagen, into the CNS ECM.

Unfortunately, in order to implant scaffolds for spinal cord injury repair, the meninges will have to be disrupted, and thus lesions of this severity may be introduced surgically as part of the regenerative therapy. Indeed, examples of scaffold implantation, and the disruption of the meninges to do so, has already been documented in human patients for both chronic (Xiao et al., 2016; Zhao et al., 2017) and acute spinal cord injuries (Theodore et al., 2016; Layer et al., 2017; Chen et al., 2020; Deng et al., 2020; Kim et al., 2021); the latter even when the original injury does not disrupt the meninges itself. Thus, it is important to recognise that the injury may actually be made more severe in order to treat using a spinal cord injury scaffold, and therefore connective tissue ingrowth becomes a complication for all spinal cord injury scaffolds that must be addressed by rational design.

As determined above, layering is likely a strong methodology for defining regions within a scaffold and controlling functionality heterogeneously. Following this conclusion, and building on the result observed in the laser ablation nonwoven

control group, where almost no cells were able to cross the non-ablated electrospun nonwoven, the value of having a cell-impermeable layer was considered for non-native cell types, such as fibroblasts.

Thus, a proof of principle experiment for determining non-ablated PCL/P_{11}-8 as a cell-impermeable layer was conducted, where a composite nonwoven-hydrogel scaffold of three layers was assembled and exposed to a co-culture of a model native and non-native cell type. The scaffold consisted of a first laser-ablated PCL/P_{11}-8 electrospun nonwoven layer; a second lyophilised collagen-GMA hydrogel layer; and a third non-ablated PCL/P_{11}-8 layer. The scaffold was assembled in a Minusheet to provide a reservoir on both side of the scaffold and PC12 cells were seeded onto the laser-ablated nonwoven side, as the model native cell type, and allowed to populate the 'inside' of the scaffold. After 5 days of NGF exposure, the scaffold was turned over and L929 fibroblasts seeded on to the 'outer' side of the non-ablated PCL/P_{11}-8 nonwoven to simulate the non-native cell type, incubated for a further 24 hours, and then fixed and stained.

Confocal images of the disassembled scaffold showed PC12 cells in all layers, indicating cell infiltration had occurred past the laser-ablated PCL/P_{11}-8 nonwoven, and through the lyophilised collagen-GMA hydrogel, to populate the internal face of the non-ablated PCL/P_{11}-8 nonwoven (Fig. 7.5). Neurites were visible extending in all layers, with alignment observed for PC12 cells in contact with both the laser-ablated and non-ablated PCL/P_{11}-8. Further, and of most significance, L929 fibroblasts were observed in abundance only on the outer side of the non-ablated nonwoven, where they had been seeded, and were not found in any layers on the other side.

The benefits of promoting an optimal environment for regeneration are usually made with respect to promoting axonal regeneration, such as via drug elution (Yao et al., 2017) or temporally delivered growth factors (Wang et al., 2016; Bruggeman et al., 2017). However, reducing the spinal injury scar or preventing further connective tissue ingrowth has been discussed to a lesser extent. For the former, it is likely physical removal of the scar is required, as therapeutic means of reduction would likely have negative effects on all cells in the environment (Huang et al., 2016), and also allows insertion of a regenerative scaffold in its place, as has been attempted to date (Xiao et al., 2016; Theodore et al., 2016; Layer et al., 2017; Zhao et al., 2017;

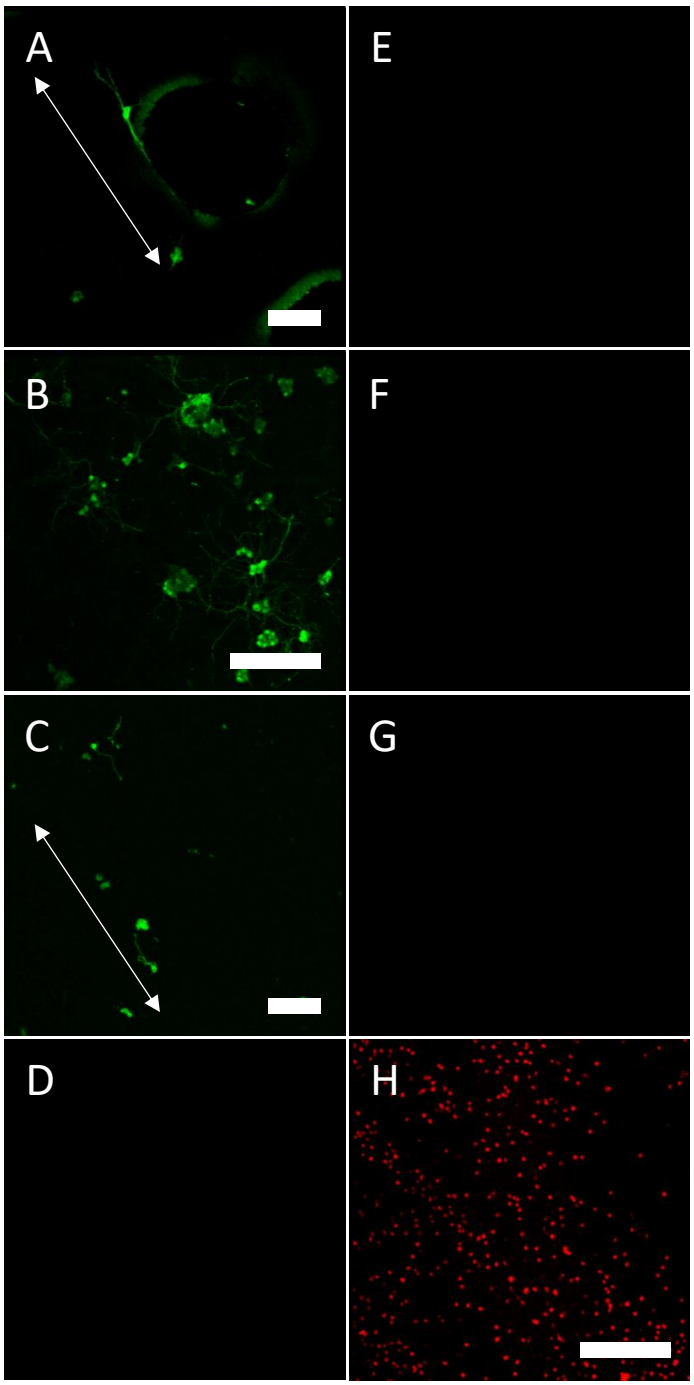

Figure 7.5 Neurite extension of PC12 cells and exclusion of L929 cells. A co-culture was set up to model connective tissue ingrowth *in vitro* and investigate non-ablated PCL/P_{11}-8 as a barrier layer for preventing non-native cell infiltration. A layered composite nonwoven-hydrogel scaffold consisting of laser-ablated electrospun PCL/P_{11}-8, lyophilised collagen-GMA hydrogel and non-ablated electrospun PCL/P_{11}-8 was seeded with PC12 cells on the laser-ablated side. After 5 days, the scaffold was seeded on the non-ablated side with L929 cells, and fixed after 24 hours. (A,B,C) PC12 cells were visible in contact with laser-ablated nonwoven, collagen-GMA and non-laser ablated nonwoven on the 'inside' of the scaffold. PC12 cells were observed extending neurites in the direction of fibre alignment on nonwoven, including around laser-ablated pores, and randomly in collagen-GMA. (D) No PC12 cells were visualised on the non-ablated PCL/P_{11}-8 'outer' side, where (E-H) L929 cells were only seen. Scale bar is 50 μm.

Xiao et al., 2018; Chen et al., 2020; Deng et al., 2020; Kim et al., 2021). Thus, the real remaining complication, especially from scaffold implantation, is potential connective tissue ingrowth.

Exclusion of non-native cell types from the regenerating environment in composite nonwoven-hydrogel scaffolds has been evaluated for peripheral nerve regeneration (Quigley et al., 2013). A complex scaffold consisting of a melt-extruded PLA knitted tube, filled with melt-extruded PLGA fibres and alginate hydrogel, had an electrospun PLA nonwoven with a pore diameter of less than 2 µm applied to the outside to allow permeability of trophic factors, but hinder cell infiltration. Whilst the benefit of the outer electrospun membrane was not evaluated in the publication, the premise of its benefits was taken from an earlier publication where connective tissue ingrowth was observed in a “macroporous” scaffold with pores in the range 10 – 230 µm but not in a “microporous” scaffold with pores in the range 1 – 10 µm for a rat sciatic nerve model (Vleggeert-Lankamp et al., 2007). The results herein reinforce this evidence, that cell-impermeable layers can be used to prevent non-native cell infiltration, and highlight its applicability for spinal cord regenerative scaffolds as well.

Of note, there is evidence hydrogel may also be able to limit non-native cell infiltration, not just nonwoven. Alginate hydrogel has been used to coat electrospun fibrin/poly(ethylene oxide) (PEO) nonwoven, and was applied only on the dorsal side to inhibit cell adhesion in a rat dorsal hemisection model (Yao et al., 2018).

In summary, a proof of principle experiment for evaluating PCL/P_{11}-8 as a cell-impermeable layer for preventing non-native cell infiltration was successful. PC12 cells populated throughout a multi-layered scaffold when seeded on to a cell-permeable face, but L929 cells were only found on the outside of the scaffold when seeded on to a cell-impermeable face. Thus, electrospun nonwoven of PCL/P_{11}-8 could serve as an outer layer in a composite nonwoven-hydrogel scaffold and gives further evidence layering can be used as a methodology for designing heterogeneous scaffolds for spinal cord injury repair.

7.3.4 Integration of Collagen-GMA Hydrogel with PCL and PCL/P_{11}-8 at the Fibre Level and the Effect of SAP on Hydrogel Absorption

For the first time, PCL and PCL/P_{11}-8 nonwoven was combined with collagen-GMA hydrogel to form a composite nonwoven-hydrogel scaffold. The main concern when bringing the two materials together was whether integration of the collagen-GMA hydrogel would occur with the nonwoven, especially with hydrophobic PCL; whether fibre alignment would be disturbed or remain intact; and what effect the SAP may have on hydrogel absorption.

SEM images of the lyophilised composite nonwoven-hydrogel scaffold when cross-sectioned in the direction of fibre alignment show a scaffold 300-350 µm in thickness, with pores of collagen-GMA hydrogel appearing connected to both sides of the nonwoven (Fig. 7.6A). Further, using higher magnification and focusing on the nonwoven, integration is confirmed as sheets of collagen-GMA hydrogel can be seen in between adjacent nonwoven fibres when cross-sectioned perpendicular to fibre alignment (Fig. 7.6B).

Whilst in both images fibres have become wavy, as tension has been lost after punching out the samples, alignment appears to remain intact. Importantly, other

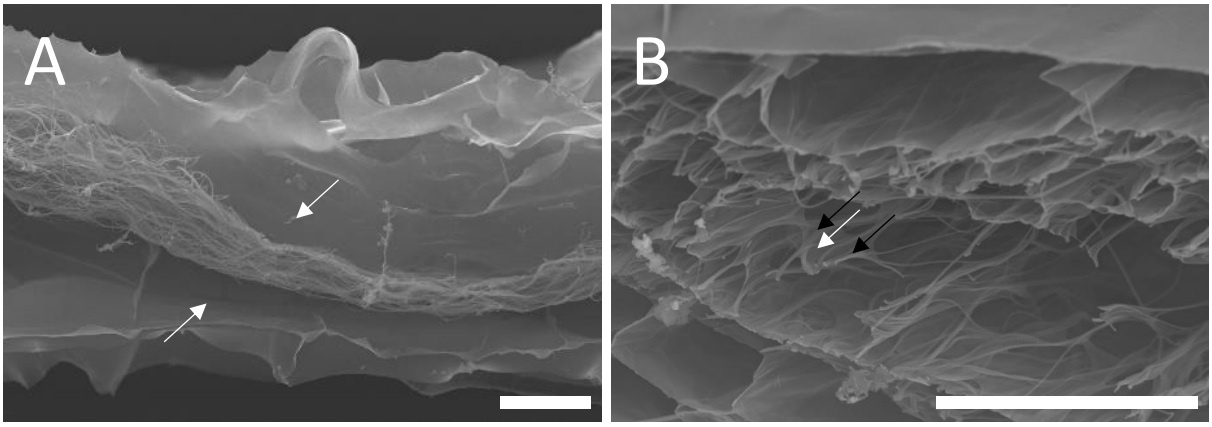

Figure 7.6 SEM images of composite nonwoven-hydrogel scaffolds. Composite nonwoven-hydrogel scaffolds were produced by sandwiching (A) PCL/P_{11}-8 or (B) PCL electrospun nonwoven between silicone moulds and glass slides, UV-curing collagen-GMA hydrogel on both sides and lyophilising the scaffold. (A) Pore structures of collagen-GMA could be seen on both sides of the scaffold (white arrows), whilst alignment of the nonwoven fibres was retained. (B) Higher magnification showed sheets of collagen-GMA (white arrow) between aligned nonwoven fibres (black arrows), indicating integration at the fibre level of both materials. Scale bar is 100 µm.

studies which used layering to combine nonwoven and hydrogel and saw some loss of tension, or the degree of alignment had been less stark than herein, did not appear to hinder process extension (McMurtrey, 2014; Hyysalo et al., 2017) and was similar to those studies where tension and alignment had been maintained better (Weightman, Jenkins, et al., 2014; Miller et al., 2018). As such, integration of collagen-GMA hydrogel with PCL and PCL/P_{11}-8 fibres was confirmed, even considering the hydrophobicity of PCL, and fibre alignment was not disturbed.

The other main interest when combining the nonwoven and hydrogel was the effect of SAP in the nonwoven on total hydrogel uptake. Electrospun PCL and PCL/P_{11}-8 were coated in collagen-GMA hydrogel-forming solution, UV-irradiated and lyophilised. Mean mass (± SE) was 0.63 ± 0.07 and 1.03 ± 0.03 mg, respectively, from a starting mass of 0.4 mg (Fig. 7.7). As such, whilst PCL was able to absorb 0.23 mg of collagen-GMA despite its high contact angle and perceived hydrophobicity, PCL/P_{11}-8 was able to absorb almost three times as much at 0.63 mg. This increased absorptive capacity is possibly due to the reduced contact angle from SAP inclusion, as ascertained in Chapter 5, but also the increased surface area from the nanoscale network.

Further, additional layers of collagen-GMA hydrogel could be built-up to increase the hydrogel to nonwoven ratio. When coated a second time and UV-irradiated again, no obvious delamination was observed between successive layers of collagen-GMA hydrogel, and composite nonwoven-hydrogel mean mass (± SE) increased to 0.9 ± 0.06 and 1.53 ± 0.03 mg for PCL and PCL/P_{11}-8, respectively. As such, a composite nonwoven-hydrogel of PCL and collagen-GMA produced scaffolds of roughly 1:0.5 and 1:1 by successively coating in collagen-GMA hydrogel-forming solution and UV-irradiating. However, PCL/P_{11}-8 produced scaffold of roughly 1:1.5 and 1:3 by successive coating in the same manner. Understanding this difference in absorption between the materials and the weight ratios when layering and coating are important design parameters when manufacturing such a device, and whilst not investigated herein, could play a role in defining how much SAP is put into the nonwoven.

Further still, the effect of SAP in the nonwoven could also be observed in the rate of hydrogel-forming solution uptake. All samples showed a characteristic rate curve, which saw the highest gradient at the initiation of the test and reduced thereafter to a

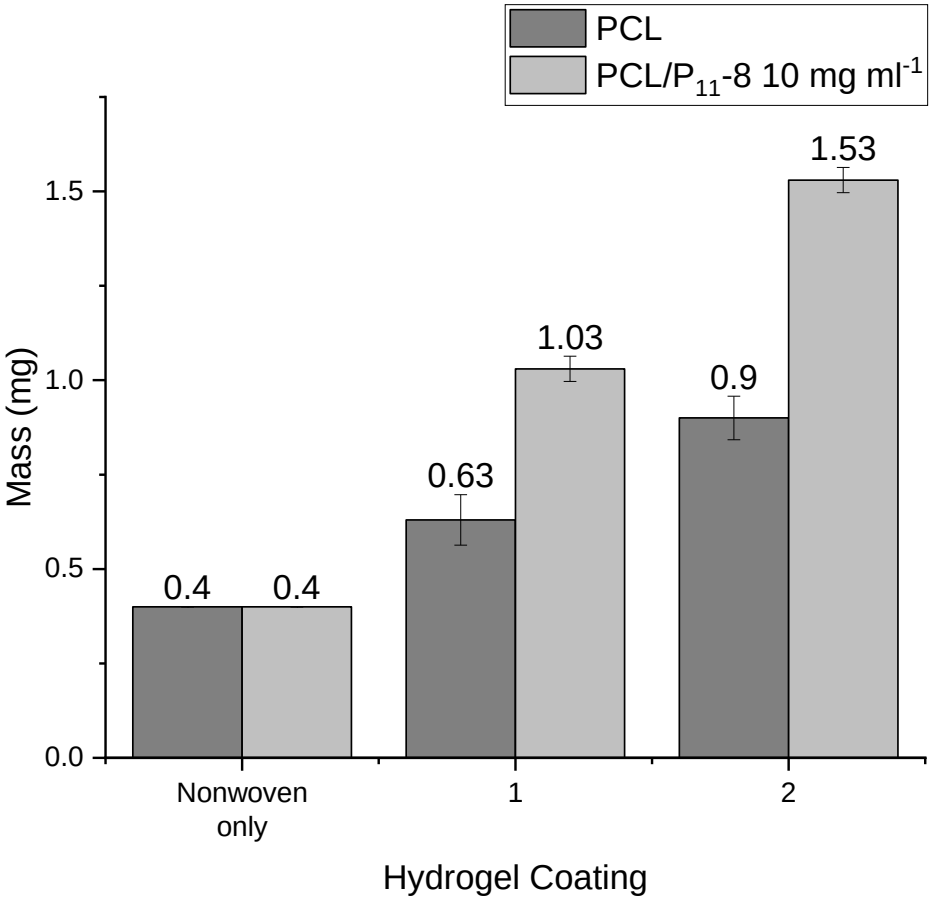

Figure 7.7 Total dry mass of composite nonwoven-hydrogel scaffolds. Total dry mass was measured to observe the effect of P_{11}-8 SAP on the amount of hydrogel solution uptake and the ability of successive hydrogel layering to alter nonwoven to hydrogel ratio. Electrospun nonwoven samples were allowed to absorb collagen-GMA hydrogel-forming solution for 1 min on either side before UV-curing, hydrating and lyophilising. Mean dry mass (± SE) of PCL-only, PCL with one coat of hydrogel, and two coats of hydrogel weighed 0.4, 0.63 ± 0.07 and 0.9 ± 0.06 mg, respectively. Dry mass of PCL/P_{11}-8-only, PCL/P_{11}-8 with one coat of hydrogel, and two coats of hydrogel weighed 0.4, 1.03 ± 0.03 and 1.53 ± 0.03 mg, respectively. *n* = 3.

plateau (Fig. 7.8A). However, stark differences were observed in the rate of absorption for all SAP-containing groups compared to PCL-only, with alignment also influencing the rate of uptake. After 300 s, hydrogel solution had travelled a distance (± SE) of 6.4 ± 0.3, 7.2 ± 0.7, 5.4 ± 0.2, 4.4 ± 0.2 and 3.3 ± 0.3 mm in PCL/P_{11}-8 at 40, 20 and 10 mg ml^{-1}, aligned and random PCL, respectively. Of note, whilst the average results for the 20 mg ml^{-1} group were higher than that of the 40 mg ml^{-1} group, the overlap in the standard error, differentiation with respect to the 10 mg ml^{-1} group, and the similar results seen with respect to contact angle in Chapter 5, indicate these may be similar results and not a true reflection of the effect of

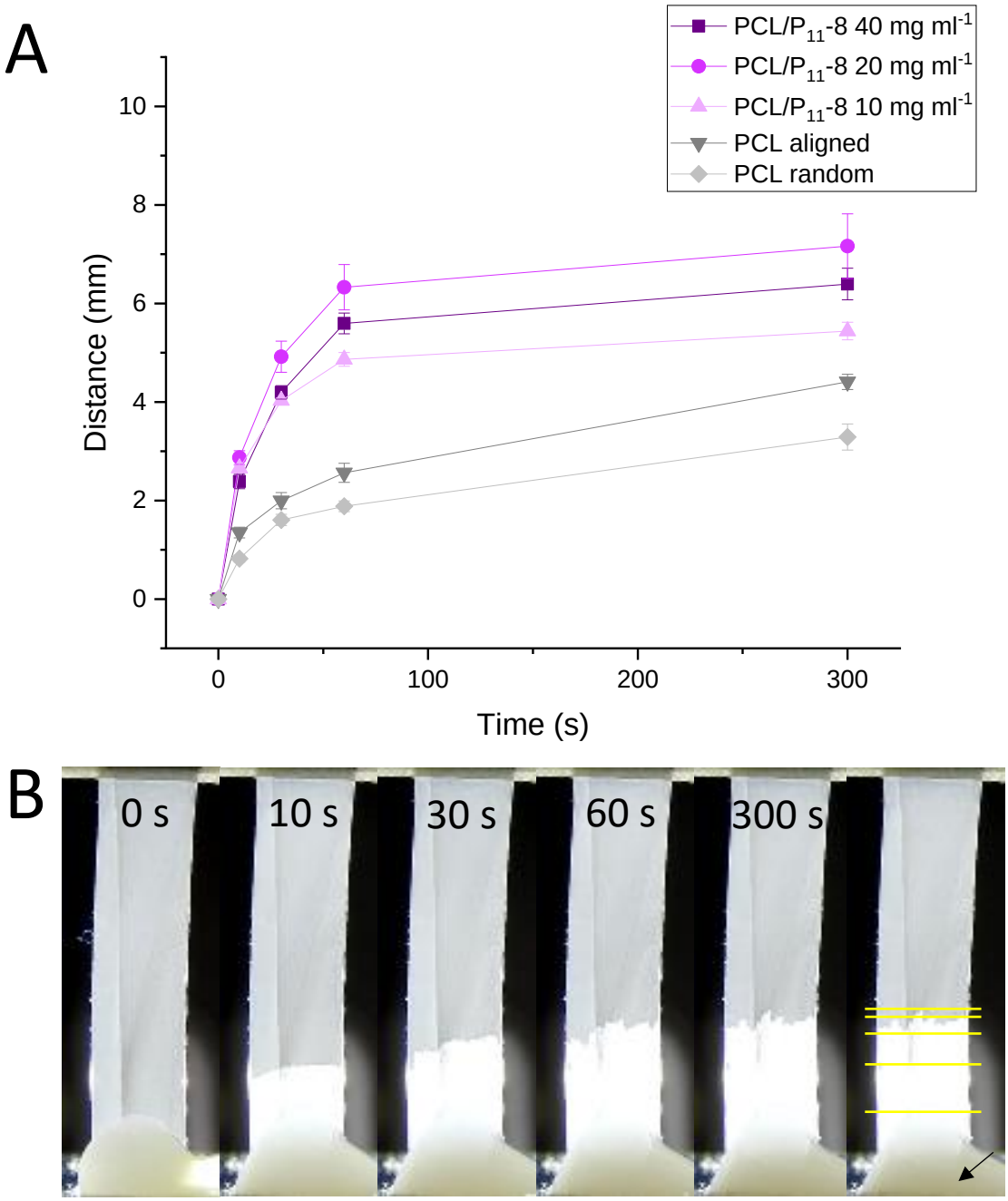

Figure 7.8 Liquid wicking rate of collagen-GMA hydrogel-forming solution into electrospun nonwoven. Liquid wicking rate was investigated to observe the effect of P_{11}-8 SAP on the rate of hydrogel solution uptake. (A) A characteristic rate curve was observed for all sample groups, which reduced in gradient with time and lead to a plateau. After 300 s, hydrogel solution had travelled a distance (± SE) of 6.4±0.3, 7.2±0.7, 5.4±0.2, 4.4±0.2 and 3.3±0.3 mm in PCL/P_{11}-8 at 40, 20 and 10 mg ml^{-1}, aligned and random PCL, respectively. (B) Images of the test strips and wicking of hydrogel-forming solution, with measurements of the liquid front over time (yellow lines). An adapted methodology for the wicking strip test was developed to suit the lightness, static-sensitive and limited amount of electrospun web. Samples with a gauge length of 20 x 5 mm (L x W) were secured at both ends a droplet of collagen-GMA hydrogel-forming solution (black arrow) placed at the base of the strip. Samples were filmed for 300 s, backlight to aid visualisation, and secured next to a ruler to accurately measure the advancing liquid front. *n* = 5.

concentration on rate, but further increases in SAP or refinement of the methodology would help determine this point.

Of note, liquid wicking rate is traditionally ascertained using the wicking strip test, where a strip of fabric is suspended at one end and immersed at the other end in a reservoir of solution, with the solution level in the nonwoven measured after a specific time frame (Russell, 2006). Whilst standard test methods exist, such as BS EN ISO 9073-6 (2003), the methodology used herein had to be adapted to suit the test material; with electrospun PCL and PCL/P_{11}-8 produced in too small quantities to be able to match the standard dimensions; the static build-up in the samples that promoted strips to roll-up and curve; and the lightness of the samples that meant immersing into a reservoir of hydrogel solution whilst under tension was not possible.

As such, an adapted method herein was used, where test samples were cut to dimensions of 20 x 5 mm (L x W), secured at both ends and a droplet of hydrogel-forming solution placed at the base of the strip. By videoing the experiment, the initial contact point between the solution and nonwoven was ascertained and the liquid front observed over time (Fig. 7.8B). Standards were kept to where possible, such as the 300 s time frame in BS EN ISO 9073-6 (2003) for fabrics that experience rapid wicking (Russell, 2006), but by ensuring samples were secured tightly at both ends but not under excess tension (measured herein using a 10 N load cell); using a set volume of solution that was placed in the same position at the base of the strip; and making use of a backlight to illuminate the liquid front, a reliable methodology for liquid wicking in lightweight electrospun nonwovens was realised and is recommended for use where parameters in standards also cannot be met.

In summary, combining collagen-GMA hydrogel with either electrospun PCL or PCL/P_{11}-8 lead to a composite nonwoven-hydrogel scaffold where the two materials appeared to integrate well at the fibre level and, whilst tension was lost in the fibres, alignment was not disturbed. Further, SAP inclusion in the nonwoven augmented the amount of collagen-GMA absorbed, and understanding the degree of absorption and the ratio of nonwoven to hydrogel this produces, is important for scaffold manufacture. This augmentation was also observed in the rate of absorption of the collagen-GMA hydrogel-forming solution and from this a new methodology for measuring wicking rate in electrospun nonwovens was developed.

7.3.5 Dehydration of Collagen-GMA and the Effect of Methodology on Retaining Pore Structure

In Chapter 6, it was ascertained that collagen-GMA hydrogel could act as a three-dimensional cell culture environment for PC12 cells. To ensure cells were evenly distributed throughout the hydrogel, cells were triturated in a pipette with hydrogel-forming solution and then UV-irradiated to encapsulate within the cured hydrogel. This process of mixing cells during the production process of the hydrogel itself is straightforward in the lab and potentially transferable to a clinical setting in some form. Whilst best clinical practice for such an intervention is yet to be determined and may differ depending on a multitude of factors, such as cell source, scaffold type, or whether the patient is acute or chronic, it is expected that if cells could be harvested or made available during an operation, they could be mixed with hydrogel solution in theatre and then cured *in situ*, or cured and then implanted.

However, cell infiltration and distribution within a combined composite nonwoven-hydrogel scaffold is more challenging, especially when considering clinical applicability. As mentioned in Chapter 7.3.1, composite nonwoven-hydrogel construction using the layered approach herein would require either cells to be available at the point of scaffold production or scaffold production to be done in the clinic, including layering with nonwoven. Whilst this may be possible, it is far removed from the 'ideal' intervention, where a scaffold is available off-the-shelf for implantation and no manufacture and limited preparation is required in the clinic.

Furthermore, it is unadvisable to have an off-the-shelf product that is pre-hydrated. Not only would a pre-hydrated hydrogel likely impede cell infiltration to some extent, as shown for the hydrogel herein (Fig. 6.3), but would begin the process of degradation for both the nonwoven and hydrogel that are bioresorbable.

As such, to enable adequate cell infiltration and distribution, and for the composite nonwoven-hydrogel scaffold to be close to the clinically idealised off-the-shelf form, the scaffold would need to be porous, premade and dry from the start. For these reasons a method of dehydrating the scaffold that maintained these properties was desired. Two methods were investigated as drying procedures for the hydrogel; air-drying and lyophilisation. Leaving the hydrogel to dry overnight in a fume hood lead to a flat, flexible but crisp sheet of collagen-GMA hydrogel being formed that was

tens of microns thick and had appeared to lose all pore structure (Fig. 7.9A), with tightly packed, randomly-orientated collagen fibres visible in higher magnification SEM images (Fig. 7.9B). Rehydration of the air-dried collagen-GMA hydrogel sheet did not lead to the reformation of pore structure.

In contrast, SEM images of lyophilised collagen-GMA hydrogel lead to a sponge-like scaffold being formed that was hundreds of microns thick, with pore structure maintained throughout (Fig. 7.9C). Pores around 100 µm in diameter were clearly visualised (Fig. 7.9D), and whilst this was slightly larger than the 35 ± 7 µm recorded previously for collagen-GMA hydrogel (Tronci et al., 2015), this is likely explained by the removal of the ethanol dehydration step during hydrogel manufacture herein, which can promote hydrogen bonding between collagen fibres and thus cause

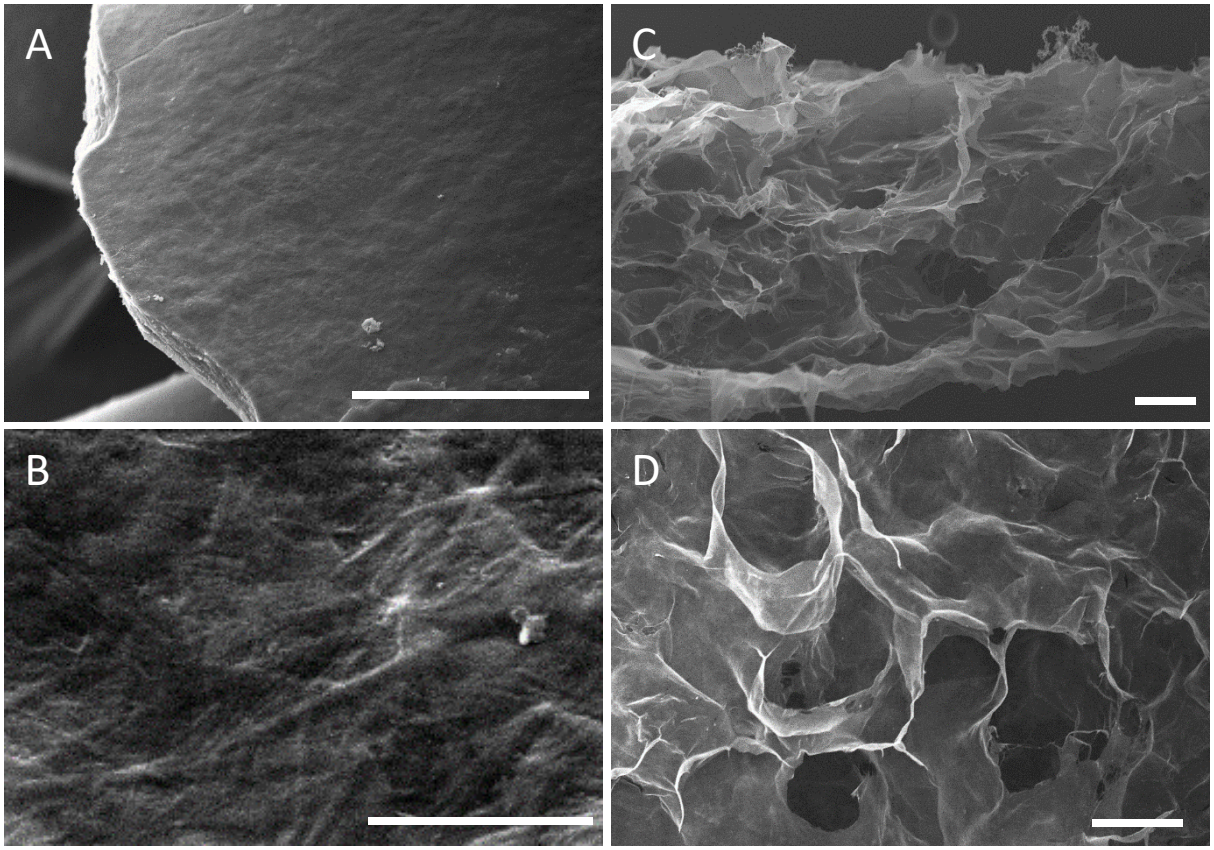

Figure 7.9 SEM images of dry collagen-GMA hydrogel. Methods of drying collagen-GMA were investigated to meet the criteria for an off-the-shelf composite nonwoven-hydrogel scaffold. (A) Air-drying formed a flat, flexible but crisp sheet of collagen-GMA that was tens of microns thick. (B) Higher magnification of air-dried collagen-GMA showed tightly-packed, randomly-orientated collagen-GMA fibres. (C) Lyophilisation formed a sponge-like collagen-GMA hydrogel that was hundreds of microns thick, with pore structure visible and around (D) 100 µm in diameter. Scale bar is 100 µm for A, B and D, and 5 µm for C.

hydrogel shrinkage; the lyophilisation process itself which likely increases pore size through the increased volume of ice over a given amount of water before sublimation; and the different imaging techniques, where hydrogel herein was imaged dry and in a vacuum versus hydrated and in a humidified chamber previously (Tronci et al., 2015).

Following the results indicating lyophilisation could retain pore structure and volume, a relevant consideration was the effect on mechanical properties. Rheograms of lyophilised and rehydrated collagen-GMA hydrogel (Fig. 7.10A) versus pre-hydrated collagen-GMA hydrogel (Fig. 7.10B) showed higher storage and loss modulus values following dehydration. For example, at an angular frequency of 0.1 rad s^{-1}, collagen-GMA hydrogel that was lyophilised and rehydrated versus pre-hydrated had a storage modulus of 509 ± 5 versus 255 ± 5 Pa, respectively, and a loss modulus of 99 ± 2 versus 36 ± 2 Pa, respectively. These combined to give complex shear modulus values of 608 Pa for lyophilised and rehydrated collagen-GMA hydrogel versus 291 Pa for pre-hydrated collagen-GMA hydrogel. As such, some stiffening was observed, with around a two-fold increase in shear modulus.

However, cell viability remained high for the lyophilised collagen-GMA hydrogel, as seen in the exemplary confocal images (Fig. 7.11A), and was calculated at 93 ± 4%; even higher than the 84 ± 2% for the cells encapsulated in collagen-GMA hydrogel-forming solution and UV-irradiated, as outlined in Chapter 6.3.1. Again, this was reinforced by the complete cell death of the positive control (Fig. 7.11B) and complete cell survival of the negative control (Fig. 7.11C), and well above the 70% recommended to indicate a non-cytotoxic effect (ISO, 2009). The increased cell viability for the cells seeded in the lyophilised collagen-GMA hydrogel versus the cells encapsulated in collagen-GMA hydrogel is likely due to the avoidance of UV-irradiation for the cells, as well as reduced handling and time spent in an environment without cell culture media.

Importantly, and despite seeding on the surface of lyophilised collagen-GMA hydrogel, cells were evenly distributed (Fig. 7.12A) throughout a 100 µm section (Fig. 7.12B), similar to cells encapsulated in collagen-GMA hydrogel-forming solution prior to UV-irradiation (Chapter 6.3.1, Fig. 6.2). Thus, cells could populate throughout

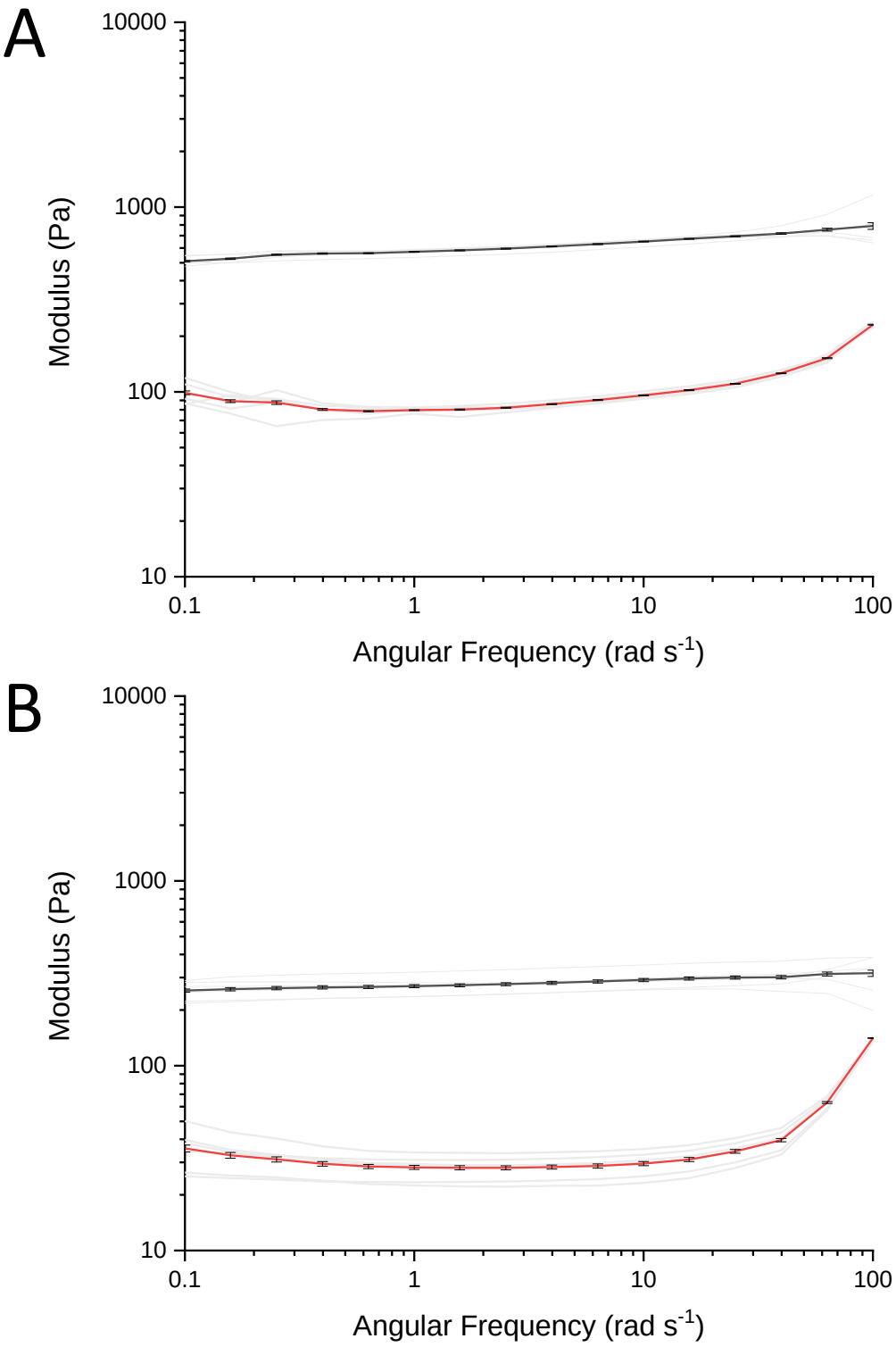

Figure 7.10 Mechanical properties in shear of collagen-GMA hydrogel lyophilised and rehydrated versus pre-hydrated. Frequency sweeps show (A) lyophilised and rehydrated collagen-GMA hydrogel and (B) pre-hydrated collagen-GMA hydrogel. The black and red lines show the mean storage and loss modulus for each experimental group (±SE), respectively. Grey lines depict actual measurements. Lyophilisation had a higher storage and loss modulus values compared to pre-hydrated collagen-GMA, indicating some stiffening had occurred. *n* = 6.

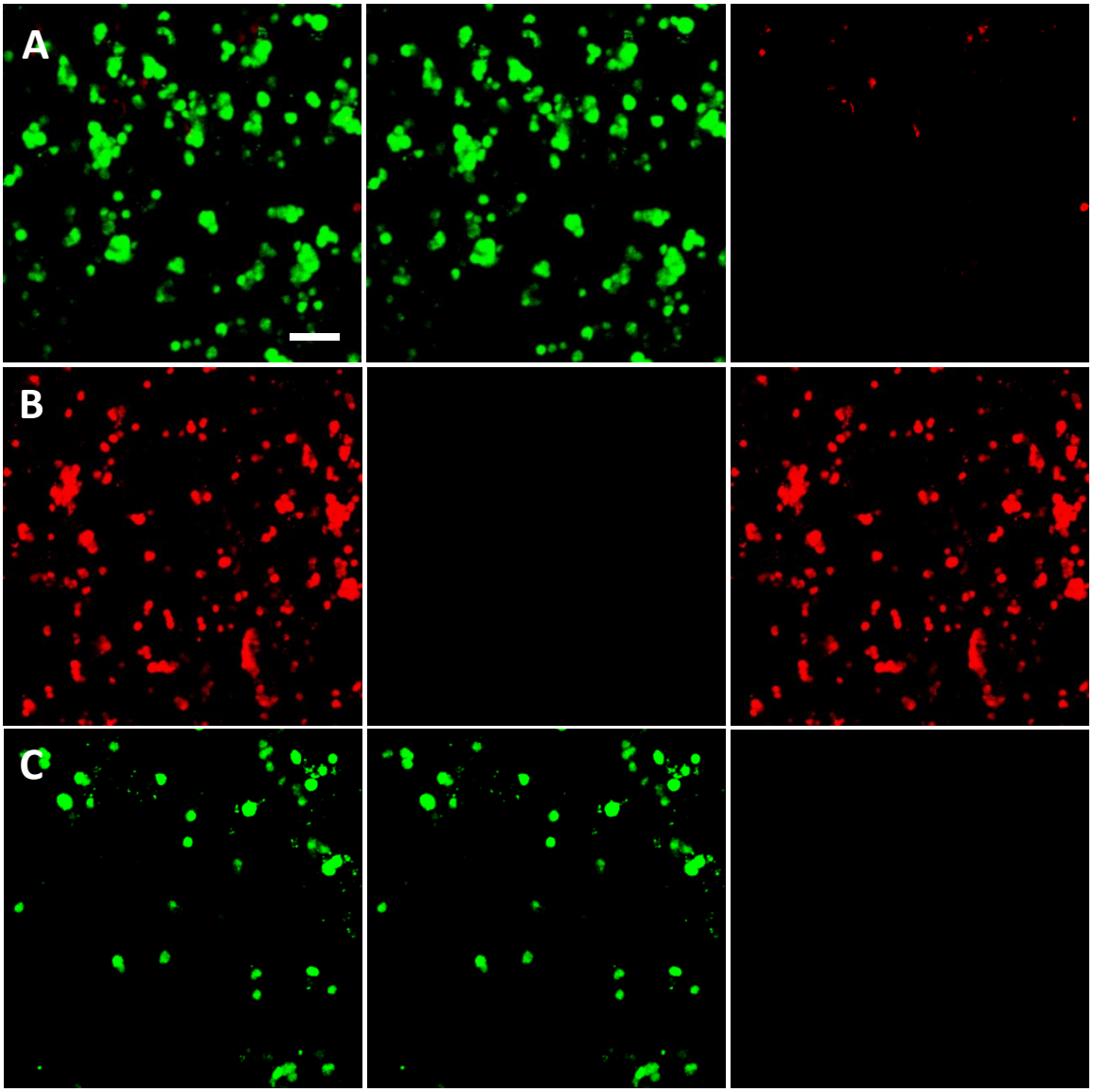

Figure 7.11 Cell viability of PC12 cells in lyophilised collagen-GMA hydrogel. (A) Exemplary confocal images show live (green) and dead (red) PC12 cells 48 hours after seeding on lyophilised collagen-GMA hydrogel. (B) PC12 cells 48 hours after seeding on lyophilised collagen-GMA hydrogel with DMSO added to cell culture media at 50% (v/v). (C) PC12 cells grown on glass coverslips coated in PDL as the negative control. Combined channels (left), as well as separate green (middle) and red (right) channels are shown for each image. Cell viability (±SD) was calculated at 93±4% for the lyophilised collagen-GMA hydrogel. Scale bar is 50 µm. *n* = 6.

the volume of the lyophilised collagen-GMA hydrogel and its space-filling and cell distribution functions were still retained.

In summary, after considering the clinical applicability of a combined composite nonwoven-hydrogel scaffold and the questionable feasibility of using pre-hydrated collagen-GMA hydrogel, work was undertaken to identify an appropriate means of

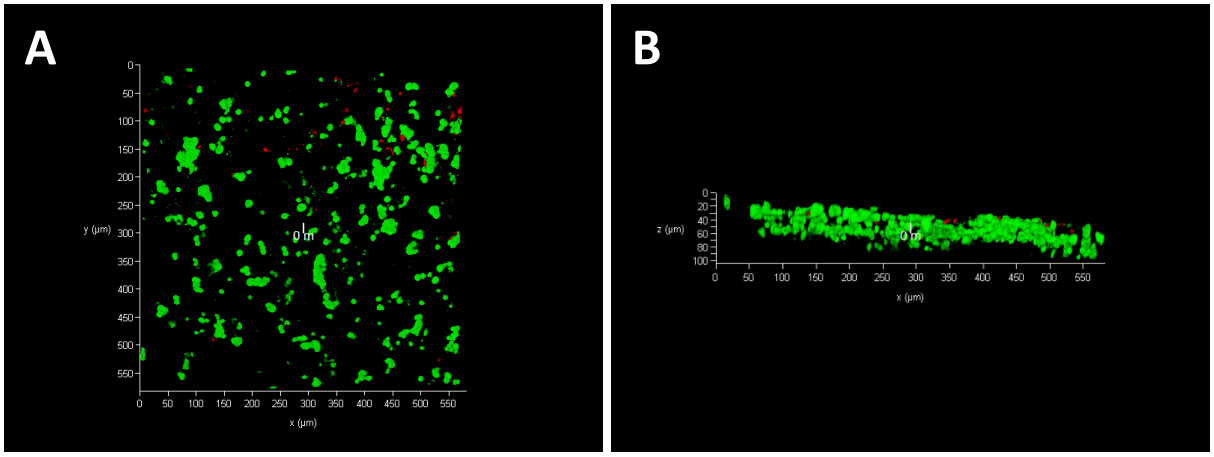

Figure 7.12 PC12 cells in lyophilised collagen-GMA hydrogel. Exemplary confocal images show live (green) and dead (red) PC12 cells, 48 hours after cell seeding. Viable cells can be seen (A) evenly distributed in the 600 x 600 µm section, and (B) throughout the 100 µm z-stack section.

dehydration that retained scaffold properties. Lyophilisation was determined as a means of maintaining volume and pore structure, as well as cell distribution throughout the hydrogel. Cell viability was even improved, likely due to the fact cells were no longer subject to a UV-irradiation dose at all. Whilst some stiffening of the scaffold was observed, the high cell viability, three-dimensional cell distribution and retained pore structure warranted further investigation of lyophilised collagen-GMA hydrogel as part of the composite nonwoven-hydrogel scaffold.

7.3.6 Refinement of Laser Ablation Parameters

As shown in Chapter 7.3.2, laser ablation introduced pores into the electrospun nonwoven that lead to an adequate and controllable degree of cell infiltration into the combined composite nonwoven-hydrogel scaffold. Prior to cell experiments, the laser ablation parameters were refined to understand both the link between power setting and the obtained output on the nonwoven from a manufacturing point of view, as well as the effects on the fibre surface from laser exposure.

Initially, the power setting was investigated for its capability to create pores, its effect on pore size once the minimum power setting had been determined, and any adverse effects from higher power settings. To do so, a series of pore arrays set at an inter-pore distance of 1.0, 1.5, 2.0, 3.0, 4.0, 5.0 and 10.0 mm were produced and the power setting set at 5, 10, 20, 50 and 100% (Fig. 7.13A). Following laser ablation, power settings of 50 and 100% lead to melting between pores on the

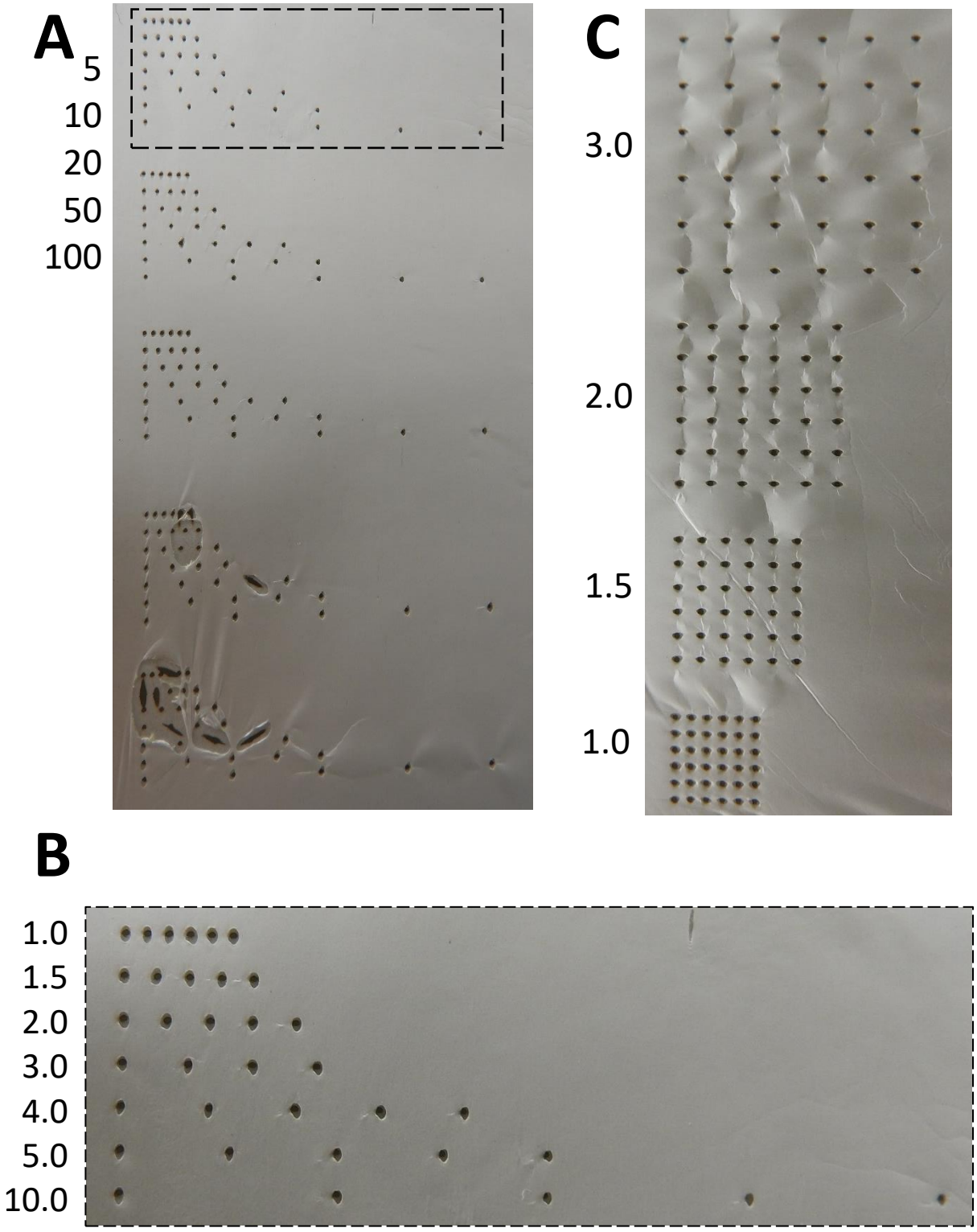

Figure 7.13 Laser ablation of electrospun PCL/P_{11}-8 nonwoven. Laser ablation was used to introduce pores into PCL/P_{11}-8 for improved cell infiltration past the nonwoven and into other layers of the nonwoven-hydrogel scaffold. (A) The effect of power setting at the macroscale indicated 50 and 100% would cause excessive melting, especially at smaller inter-pore distances, but 5, 10 and 20% did not. (B) Arrays and (C) matrices of pores set at different inter-pore distances between 1.0-10.0 mm could be produced.

nonwoven surface, and as such defined pores, especially at the lowest inter-pore distances, were not achieved. However, even the lowest power setting of 5% was able to achieve defined pores (Fig. 7.13B) and matrices (Fig. 7.13C), with little difference observed at the macroscale of nonwoven samples laser ablated with power settings of 5, 10 and 20%.

Taking a closer look at the electrospun nonwoven surface, SEM images of laser-ablated pores showed defined pores could be produced with an oval shape, likely due to the slight tension fibres were under (Fig. 7.14A). A ring of melted polymer

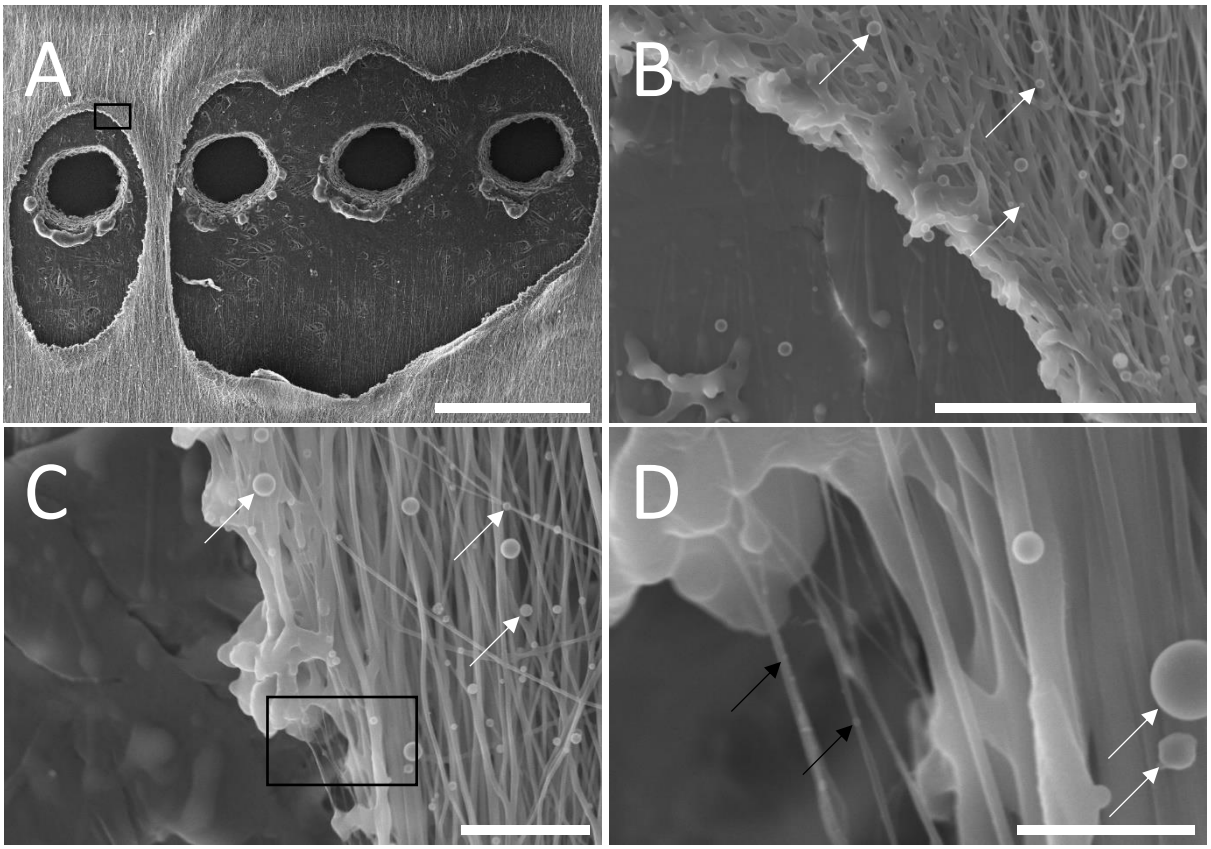

Figure 7.14 SEM images of laser-ablated PCL/P_{11}-8 electrospun nonwoven. (A) Defined oval-shaped pores were produced, likely from tension in the web. An inter-pore distance set at 0.5 mm lead to merging of pores at the lowest power setting of 5%, and thus 1.0 mm was determined as the minimum resolution for this system. (B) A ring of melted polymer-SAP defined the pore perimeter and (C) appeared to help maintain tension and alignment. (D) Despite melting at the pore perimeter, nanofibres were still visible and had not been totally destroyed. Of note, spherical debris was observed on the nonwoven surface, likely from the melting and scattering of polymer-SAP during ablation. Most of this appeared 1-2 μm in diameter (white arrows), but some evidence of much smaller debris 200 nm in diameter and below may have also been created (black arrows). Scale bar is 500, 50, 15 and 5 μm in A, B, C and D, respectively.

defined the pore perimeter (Fig. 7.14B) and appeared to help maintain tension and alignment of the nonwoven fibres (Fig. 7.14C). Further, increased magnification also showed nanofibres were still visible even at the immediate pore perimeter and had not been destroyed (Fig. 7.14D). However, spherical polymer debris could be seen on the polymer surface. Most of this appeared to be 1-2 μ m in diameter (white arrows), but some smaller debris 200 nm in diameter and below may have also been produced (black arrows).

Of note, following the successful laser-ablation at a power setting of 5%, the possibility of reducing the inter-pore distance to 0.5 mm was investigated. However, as seen in Fig. 7.14A, even at this low setting defined pores could not be created and a minimum resolution of 1.0 mm using this system was determined.

Other studies that have introduced laser-ablated pores into aligned electrospun nonwovens have been able to produce more spherical pores (Walthers et al., 2014; Petrigliano et al., 2015), and thus the likely reason for the oval shape herein is tension in the web, rather than any propagation of melting due to alignment. This does appear to be the first example of nanofibres in the region of a few tens of nanometres still being visible at the pore perimeter following laser ablation. Whilst lasers with much shorter optical pulse times are available which reduce the heat diffusion into the material preventing excess melting, such as femtosecond lasers (Rebollar et al., 2011; Lee et al., 2012; Kim et al., 2014; Adomavičiūtė et al., 2015), debris has still been noted even from these lasers (Lim et al., 2011). Whilst any effect on biocompatibility should be determined for individual systems, cell viability and adherence has not been hindered elsewhere (McCullen et al., 2011).

Whilst a power setting of 5% appeared to be sufficient in creating pores, the effect of power setting up to 20% was investigated for its effect on pore size. By increasing the power setting from 5 to 10 to 20%, pore area (± SE) increased from 0.329 ± 0.013 to 0.372 ± 0.017 to 0.402 ± 0.017 mm^2, respectively (Fig. 7.15A). As such, whilst an increase was observed, the effect of increased power setting seemed minimal on pore size and therefore a power setting of 5% was determined as both adequate and optimal for the system herein.

In contrast, other studies using other laser systems have seen up to a three-fold difference in pore diameter by altering pulse energy (Rebollar et al., 2011; Lee et al.,

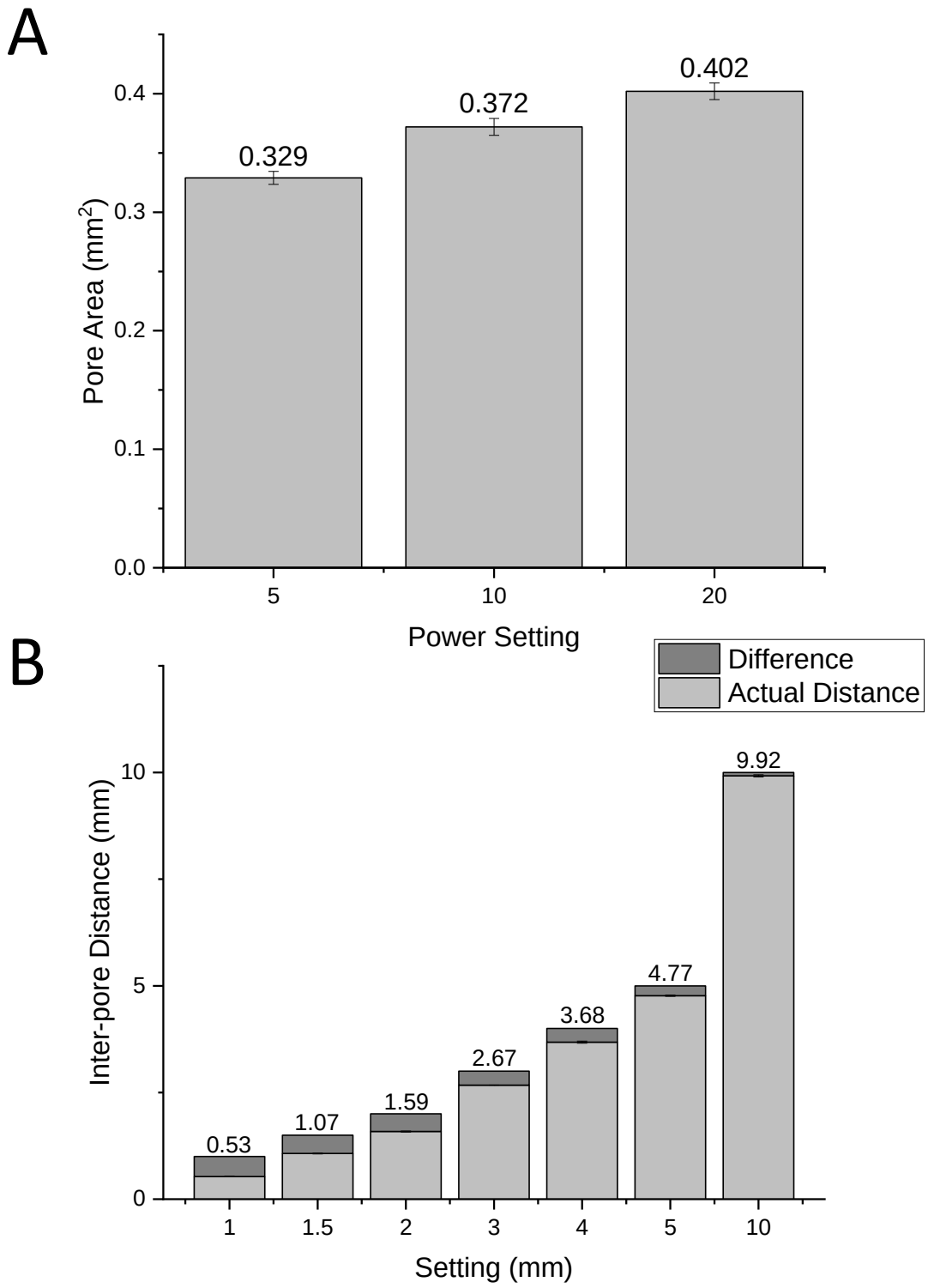

Figure 7.15 Effect of the laser power on pore area and the link between intended input and actual output for inter-pore distance. (A) Altering laser power setting from 5 to 10 to 20% lead to a pore area (±SE) of 0.329±0.013, 0.372±0.017 and 0.402±0.017, respectively. This negligible effect using the system herein lead to a power of setting of 5 being used for further experiments. (B) Inter-pore distances (±SE) set at 1.0, 1.5, 2.0, 3.0, 4.0, 5.0 and 10.0 mm had actual inter-pore distances of 0.53±0.02, 1.07±0.02, 1.59±0.03, 2.67±0.01, 3.68±0.06, 4.77±0.04 and 9.92±0.06, respectively. This was due to the material removal during laser ablation and the melting that defined the pore perimeter. *n* = 6.

2012; Jahnavi et al., 2017; Götze et al., 2019), duration (Rebollar et al., 2011; Kim et al., 2014), the number of pulses applied to the same spot (Adomavičiūtė et al., 2015; Götze et al., 2019), or the size of the aperture (McCullen et al., 2011). Whilst only pulse energy was varied here, it is clear that pore size as a parameter is affected by a number of factors that are system dependent and should be optimised for the system being used.

However, one of the main concerns, which does not appear to have been analysed elsewhere in the literature, was how the setting on the array and matrix would match the actual output on the nonwoven due to melting of the polymer. To investigate, the actual inter-pore distances were measured and compared to the intended input. Actual inter-pore distances (± SE) of 0.53 ± 0.02, 1.07 ± 0.02, 1.59 ± 0.03, 2.67 ± 0.01, 3.68 ± 0.06, 4.77 ± 0.04 and 9.92 ± 0.06 were measured for intended settings of 1.0, 1.5, 2.0, 3.0, 4.0, 5.0 and 10.0 mm (Fig. 7.15B). As such, the shorter the inter-pore distance, the greater the error between the intended input and actual output. This should be considered when using laser ablation as a manufacturing process and also optimised for the system being used.

In summary, the laser system used herein was investigated and optimised with regards to the power setting and the obtained output on the nonwoven. High power settings caused excessive melting and merging of pores, especially at shorter inter-pore distances. Whilst power setting had a negligible effect on pore size, even the lowest power setting was able to create pores in the nonwoven. Some debris was noted on the nonwoven surface from laser ablation, but importantly, nanofibres appeared to be retained even at the immediate pore perimeter. Together, a low power setting was determined as optimal for creating pores using the system herein and retaining the nanofibre features of the PCL/P_{11}-8 electrospun nonwoven.

7.4 Summary

The purpose of this chapter was to investigate the combination of electrospun PCL/P_{11}-8 and collagen-GMA hydrogel for the first time as a composite nonwoven-hydrogel scaffold, including cell infiltration and neurite alignment. It was confirmed that the combination of the materials occurred at the fibre level and did not disturb fibre alignment, and uptake of the hydrogel-forming solution was augmented by SAP,

both in total collagen mass and rate. This resulted in a composite nonwoven-hydrogel scaffold of electrospun PCL/P_{11}-8 and pre-hydrated collagen-GMA hydrogel that could control the direction of extending neurites. However, the clinical applicability and manufacturability of the scaffold in this embodiment was questioned. As such, a means of dehydrating the scaffold using lyophilisation was shown to retain pore structure and associated cell distribution, in contrast to air-drying, and also influence neurite alignment in an embodiment closer to the ideals of an off-the-shelf product. This was despite a slight increase in shear modulus, which is potentially addressed through altering the network architecture parameters of the hydrogel.

Further, one of the main design critiques of using a layered approach for combining nonwoven and hydrogel, namely cell infiltration past the dense nonwoven, was addressed using laser ablation. Whilst numerous methods could be used to do so, the work herein built on the defining benefits of laser ablation as a post-production technique, by highlighting its potential ability to modulate cell infiltration without significantly removing surface area, whilst retaining nanofibre features. It was further highlighted that error between the laser-ablation settings and results in the fibre web may occur due to fibre melting, depending on the system used, which should be taken into account during manufacture.

Further still, whilst another main design critique of using a layered approach, namely limiting directional cues to surface effects, was not addressed and is possibly augmented by dehydrating the scaffold, the benefits of a non-ablated electrospun outer barrier layer for preventing non-native cell infiltration was evaluated and shown to be feasible. This is of great importance considering the requirement to breach the meninges in order to implant any spinal cord scaffold, and further highlights the benefits of a layered approach.

Taken together, the results herein indicate the combination of electrospun PCL/P_{11}-8 and collagen-GMA hydrogel to form a composite nonwoven-hydrogel scaffold could likely form a space-filling scaffold with directional cues that overcome shortcomings of the materials on their own for spinal cord injury repair.

Chapter 8

Conclusion

8.1 General Conclusions

Composite nonwoven-hydrogel scaffolds are promising for spinal cord regeneration due to the mimicry of nanofibrous protein and hydrogel-like proteoglycans in spinal cord ECM (Haggerty et al., 2017). This includes white matter, where ECM and cells are aligned to facilitate information transmission between the CNS and periphery.

Whilst highly aligned nonwovens can impart cell guidance cues, they are considered two-dimensional at the cell scale and do not mimic the three-dimensional, hydrated and mechanical environment of tissue. Conversely, hydrogels are space-filling, homogeneous environments that support three-dimensional cell culture, but lack anisotropy to promote tissue alignment. Thus, it was theorised their combination would retain the individual benefits and overcome the individual shortcomings.

There have been limited investigations of composite nonwoven-hydrogel scaffolds and identifying materials and optimising for regeneration is still in its infancy. Thus, the purpose of the work herein was to evaluate electrospun PCL/P_{11}-8 nonwoven and collagen-GMA hydrogel for use as a spinal cord regenerative scaffold.

PCL/P_{11}-8 had previously been evaluated for bone tissue regeneration, displaying enhanced wetting, augmented degradation, and a fibre structure mimicking hierarchy in tissue (Gharaei et al., 2016; Gharaei, 2017; Gharaei et al., 2020). Further, control over crosslinking and biocompatibility with L929 cells had been demonstrated for collagen-GMA (Tronci et al., 2013; Tronci et al., 2015). This indicated they could be candidates for use in a composite nonwoven-hydrogel scaffold for SCI repair.

The purpose of Chapter 4 was to determine the feasibility of electrospinning aligned PCL/P_{11}-8. For the first time, aligned webs were produced using a rotating collector. A secondary network of nanoscale diameter fibres was observed coexisting with a

submicron network, the abundance correlating with the amount of SAP. The work herein confirmed a surface velocity of 30 m s^{-1} did not hinder nanofibre formation.

However, alignment in the MD was only observed for the submicron network and not the nanoscale network, which had a random orientation in high density and alignment in the CD between adjacent submicron fibres. Nanoscale fibres originating from and aligned orthogonal to submicron fibres provided evidence for the first time that some nanofibre formation was likely occurring post-deposition.

Further, an HPLC methodology for detecting and quantifying SAP was proposed. For the first time the distinguishable light-absorption of tryptophan was shown as a means of detecting and quantifying P_{11}-8, extendable to other SAPs or peptides.

Further still, electrospinning parameters were refined initially on PCL only. Collector velocities up to 15 m s^{-1} were found in the literature, but the results herein provide evidence a surface velocity of 30 m s^{-1} can align fibres without damage, and extends the phenomenon of fibre diameter reduction with increasing collector velocity.

The purpose of Chapter 5 was to physically characterise the web. Neurite extension was used as an *in vitro* proxy for aligned tissue regeneration. PC12 cells aligned neurites to the submicron network, despite the coexistence of nanoscale fibres. The results herein provide further evidence submicron fibres can preferentially influence cells, but this is true when submicron and nanoscale are present in the same space.

In contrast, the nanoscale network did affect web stiffness. Aligned nonwovens typically have poor mechanical properties in the CD, but the random and semi-orthogonal network resulted in higher Young's modulus, augmented by SAP amount.

The addition of SAP also reversed wetting properties, with a contact angle of 0°. This reduction is likely from the SAP, as similar results were observed in random webs (Gharaei et al., 2016), but rate augmented herein by capillary action from alignment.

Mechanical characterisation of the collagen-GMA hydrogel was also required, as a low modulus environment is optimal for neural cells. Thus, the purpose of Chapter 6 was to determine the feasibility of three-dimensional cell encapsulation and investigate mechanical properties. Cell encapsulation in a single-phase collagen-GMA hydrogel was achieved for the first time by altering the protocol to prioritise cell viability. Reduction in irradiation time to 10 min cured hydrogels and reduced UV

exposure. Prior, weight percent in the hydrogel-forming solution was shown to control shear modulus and 0.8 wt% closely matched the stiffness optimal for neural cells. Moreover, J-shaped stress-strain curves similar to native spinal cord tissue were observed during compression, and 0.8 wt% mimicked strain at break and maximum stress values of spinal cord tissue from published *in vivo* experiments.

Lastly, the purpose of Chapter 7 was to combine electrospun PCL/P_{11}-8 and collagen-GMA hydrogel for the first time and evaluate the composite scaffold. Layering was used and the manufacturing and implantation perspectives considered. Integration at the fibre level was observed, with SAP augmenting hydrogel uptake. Whilst aligned neurite extension was seen for cells in contact with the nonwoven, and cells surrounded by hydrogel extending neurites randomly, the value in layering for defining regions within a scaffold was considered.

Similar results were observed when the scaffold was lyophilised as an idealised off-the-shelf form and had a positive effect on cell viability, but stiffness did increase and cells did appear to take on a flatter morphology. Whilst stiffness may be addressable by reducing weight percent of the hydrogel, there appears to be both benefits and drawbacks associated with keeping the hydrogel in a hydrated or lyophilised form.

Regardless, cell distribution throughout the hydrogel was maintained. However, the small pore size in nonwovens is known to prevent cell infiltration. Laser ablation was used to introduce pores, and percentage porosity shown to augment infiltration up to around 25%, after which no difference was observed. This indicated it may be possible to optimise infiltration without removing more than 75% of the nonwoven. Further, the results herein show that even lasers which are not optimised to limit melting can result in defined pores and leave nanofibres intact at the pore perimeter.

The use of PCL/P_{11}-8 as a cell-impermeable barrier was also highlighted in a proof-of-principle experiment. This addresses one of the major clinical complications of non-native cell infiltration from the need to cut the meninges for implantation. Thus, the benefits of a layering were demonstrated again, using non-ablated PCL/P_{11}-8 as an outer barrier layer that excluded L929 cells, as a non-native cell model.

Taken together, the results herein present the first time an electrospun PCL/P_{11}-8 nonwoven and collagen-GMA hydrogel were combined for use as a spinal cord tissue regenerative scaffold. The results indicate P_{11}-8 SAP in the nonwoven

improved wetting, mechanical and associated properties. Further, combination with a mechanically optimised collagen-GMA hydrogel produced a space-filling, three-dimensional cell-culture scaffold capable of directing neurite outgrowth, which overcame shortcomings of the nonwoven and hydrogel components in isolation.

8.2 Recommendations for Further Work

To further understand the composite nonwoven-hydrogel scaffold of PCL/P_{11}-8 and collagen-GMA for spinal cord tissue repair, the following have been identified:

- Neurite extension and cell viability with primary neurons, astrocytes or OPCs.
- Implantation in an *in vivo* SCI model. Rats are commonly used, but can spontaneously recover. Thus, a complete transection model is recommended if assessing behaviour. Hemi- or partial section would suffice for histology.
- An organotypic slice model may also show regenerative effects in a complex environment, whilst reducing the number of animals required.
- Different combinations of PCL/P_{11}-8 and collagen-GMA to investigate spatial arrangement of fibre and hydrogel. For example, rolled up nonwoven placed in a conduit filled with hydrogel, or short cut fibres mixed with hydrogel. For the latter, it may be feasible to align the fibres using fluid flow through a filter.
- Molecular integration of fibres and hydrogel, which may augment structural integrity and degradation. For example, it may be possible to covalently crosslink methacrylated PCL with collagen-GMA.
- Addition of components to augment regeneration. For example, ChABC to reduce the spinal injury scar and NGF to promote regeneration. A temporal delivery schedule may be possible depending on location in the scaffold.

Further, the following are recommended for tissue regeneration outside spinal cord:

- Conversations with Rory O'Connor, Professor of Rehabilitation Medicine and Head of the Academic Department of Rehabilitation Medicine at the University of Leeds, indicated an aligned fibre scaffold may have utility for critical size defects in hard tissue repair by providing a direct path for regeneration.
- Other aligned soft tissues including peripheral nerves and skeletal muscle.

Further still, the following are recommended for exploring electrospinning PCL/P_{11}-8:

- Electrospinning PCL/P_{11}-8 using different setups, such as electrodes, to observe whether alignment of the nanoscale network can be initiated.
- Explore methods to decouple nanoscale fibre formation from electrospinning, possibly using evaporation of P_{11}-8 solution film from polymer fibres.

References

Abdelrazek, E.M., Hezma, A.M., El-khodary, A. and Elzayat, A.M. 2016. Spectroscopic studies and thermal properties of PCL/PMMA biopolymer blend. *Egyptian Journal of Basic and Applied Sciences*. **3**(1), pp.10–15.

Adomavičiūtė, E., Tamulevičius, T., Šimatonis, L., Fataraitė-Urbonienė, E., Stankevičius, E. and Tamulevičius, S. 2015. Micro-structuring of electrospun mats employing femtosecond laser. *Medziagotyra*. **21**(1), pp.44–51.

Afifi, A.M., Nakajima, H., Yamane, H., Kimura, Y. and Nakano, S. 2009. Fabrication of aligned poly(L-lactide) fibers by electrospinning and drawing. *Macromolecular Materials and Engineering*. **294**(10), pp.658–665.

Aggeli, A., Bell, M., Boden, N., Keen, J.N., Knowles, P.F., McLeish, T.C.B., Pitkeathly, M. and Radford, S.E. 1997. Responsive gels formed by the spontaneous self-assembly of peptides into polymeric β-sheet tapes. *Nature*. **386**(6622), pp.259–262.

Aggeli, A., Bell, M., Carrick, L.M., Fishwick, C.W.G., Harding, R., Mawer, P.J., Radford, S.E., Strong, A.E. and Boden, N. 2003. pH as a trigger of peptide β-sheet self-assembly and reversible switching between nematic and isotropic phases. *Journal of the American Chemical Society*. **125**(32), pp.9619–9628.

Aggeli, A., Nyrkova, I.A., Bell, M., Harding, R., Carrick, L., McLeish, T.C., Semenov, A.N. and Boden, N. 2001. Hierarchical self-assembly of chiral rod-like molecules as a model for peptide beta -sheet tapes, ribbons, fibrils, and fibers. *Proceedings of the National Academy of Sciences of the United States of America*. **98**(21), pp.11857–62.

Ahi, Z.B., Assunção-Silva, R.C., Salgado, A.J. and Tuzlakoglu, K. 2020. A combinatorial approach for spinal cord injury repair using multifunctional collagen-based matrices: Development, characterization and impact on cell adhesion and axonal growth. *Biomedical Materials (Bristol)*. **15**(5).

Ahvaz, H.H., Mobasheri, H., Bakhshandeh, B., Shakhssalim, N., Naji, M., Dodel, M. and Soleimani, M. 2013. Mechanical characteristics of electrospun aligned PCL/PLLA nanofibrous scaffolds conduct cell differentiation in human bladder tissue engineering. *Journal of Nanoscience and Nanotechnology*. **13**(7), pp.4736–4743.

Aimetti, A.A., Kirshblum, S., Curt, A., Mobley, J., Grossman, R.G. and Guest, J.D. 2019. Natural history of neurological improvement following complete (AIS A) thoracic spinal cord injury across three registries to guide acute clinical trial design and interpretation. *Spinal Cord*. **57**(9), pp.753–762.

Alizadeh, A., Dyck, S.M. and Karimi-Abdolrezaee, S. 2019. Traumatic Spinal Cord Injury: An Overview of Pathophysiology, Models and Acute Injury Mechanisms. *Frontiers in Neurology*. **10**, p.282.

Allen, N.J. and Eroglu, C. 2017. Cell Biology of Astrocyte-Synapse Interactions. *Neuron*. **96**(3), pp.697–708.

Ameer, J.M., Anil Kumar, P.R. and Kasoju, N. 2019. Strategies to tune electrospun scaffold

porosity for effective cell response in tissue engineering. *Journal of Functional Biomaterials*. **10**(3), p.30.

Arabi, A., Boggs, E., Patel, M.R., Zwiesler-Vollick, J., Maerz, T., Baker, K., Tuck, S., Corey, J. and Li, Y. 2014. Surface modification of electrospun polycaprolactone fibers and effect on cell proliferation. *Surface Innovations*. **2**(1), pp.47–59.

Aragon, J., Navascues, N., Mendoza, G. and Irusta, S. 2017. Laser-treated electrospun fibers loaded with nano-hydroxyapatite for bone tissue engineering. *International Journal of Pharmaceutics*. **525**(1), pp.112–122.

Ashammakhi, N., Kim, H.J., Ehsanipour, A., Bierman, R.D., Kaarela, O., Xue, C., Khademhosseini, A. and Seidlits, S.K. 2019. Regenerative Therapies for Spinal Cord Injury. *Tissue Engineering - Part B: Reviews*. **25**(6), pp.471–491.

Avraham, O., Feng, R., Ewan, E.E., Zhao, G. and Cavalli, V. 2020. Profiling sensory neuron microenvironment after peripheral and central axon injury reveals key pathways for axon regeneration. *bioRxiv*.

Bacakova, L., Filova, E., Parizek, M., Ruml, T. and Svorcik, V. 2011. Modulation of cell adhesion, proliferation and differentiation on materials designed for body implants. *Biotechnology Advances*. **29**(6), pp.739–767.

Bachstetter, A.D., Van Eldik, L.J., Schmitt, F.A., Neltner, J.H., Ighodaro, E.T., Webster, S.J., Patel, E., Abner, E.L., Kryscio, R.J. and Nelson, P.T. 2015. Disease-related microglia heterogeneity in the hippocampus of Alzheimer's disease, dementia with Lewy bodies, and hippocampal sclerosis of aging. *Acta neuropathologica communications*. **3**, p.32.

Bagher, Z., Azami, M., Ebrahimi-Barough, S., Mirzadeh, H., Solouk, A., Soleimani, M., Ai, J., Nourani, M.R. and Joghataei, M.T. 2016. Differentiation of Wharton's Jelly-Derived Mesenchymal Stem Cells into Motor Neuron-Like Cells on Three-Dimensional Collagen-Grafted Nanofibers. *Molecular Neurobiology*. **53**(4), pp.2397–2408.

Bak, L.K. and Walls, A.B. 2018. CrossTalk opposing view: lack of evidence supporting an astrocyte-to-neuron lactate shuttle coupling neuronal activity to glucose utilisation in the brain. *Journal of Physiology*. **596**(3), pp.351–353.

Baker, B.M., Gee, A.O., Metter, R.B., Nathan, A.S., Marklein, R.A., Burdick, J.A. and Mauck, R.L. 2008. The potential to improve cell infiltration in composite fiber-aligned electrospun scaffolds by the selective removal of sacrificial fibers. *Biomaterials*. **29**(15), pp.2348–2358.

Baklaushev, V.P., Bogush, V.G., Kalsin, V.A., Sovetnikov, N.N., Samoilova, E.M., Revkova, V.A., Sidoruk, K. V., Konoplyannikov, M.A., Timashev, P.S., Kotova, S.L., Yushkov, K.B., Averyanov, A. V., Troitskiy, A. V. and Ahlfors, J.E. 2019. Tissue Engineered Neural Constructs Composed of Neural Precursor Cells, Recombinant Spidroin and PRP for Neural Tissue Regeneration. *Scientific Reports*. **9**(1).

Balgude, A.P., Yu, X., Szymanski, A. and Bellamkonda, R.V. 2001. Agarose gel stiffness determines rate of DRG neurite extension in 3D cultures. *Biomaterials*. **22**(10), pp.1077–1084.

Banerjee, A., Arha, M., Choudhary, S., Ashton, R.S., Bhatia, S.R., Schaffer, D. V. and Kane,

R.S. 2009. The influence of hydrogel modulus on the proliferation and differentiation of encapsulated neural stem cells. *Biomaterials*. **30**(27), pp.4695–4699.

Barakat, N.A.M., Kanjwal, M.A., Sheikh, F.A. and Kim, H.Y. 2009. Spider-net within the N6, PVA and PU electrospun nanofiber mats using salt addition: Novel strategy in the electrospinning process. *Polymer*. **50**(18), pp.4389–4396.

Barnabé-Heider, F., Göritz, C., Sabelström, H., Takebayashi, H., Pfrieger, F.W., Meletis, K. and Frisén, J. 2010. Origin of new glial cells in intact and injured adult spinal cord. *Cell Stem Cell*. **7**(4), pp.470–482.

Barra, B., Conti, S., Perich, M.G., Zhuang, K., Schiavone, G., Fallegger, F., Galan, K., James, N.D., Barraud, Q., Delacombaz, M., Kaeser, M., Rouiller, E.M., Milekovic, T., Lacour, S., Bloch, J., Courtine, G. and Capogrosso, M. 2020. Electrical stimulation of the cervical dorsal roots enables functional arm and hand movements in monkeys with cervical spinal cord injury. *bioRxiv*.

Barros, L.F. and Weber, B. 2018. CrossTalk proposal: an important astrocyte-to-neuron lactate shuttle couples neuronal activity to glucose utilisation in the brain. *Journal of Physiology*. **596**(3), pp.347–350.

Bartlett, R.D., Choi, D. and Phillips, J.B. 2016. Biomechanical properties of the spinal cord: implications for tissue engineering and clinical translation. *Regenerative Medicine*. **11**(7), pp.659–673.

Bartnikowski, M., Dargaville, T.R., Ivanovski, S. and Hutmacher, D.W. 2019. Degradation mechanisms of polycaprolactone in the context of chemistry, geometry and environment. *Progress in Polymer Science*. **96**, pp.1–20.

Bashur, C.A., Dahlgren, L.A. and Goldstein, A.S. 2006. Effect of fiber diameter and orientation on fibroblast morphology and proliferation on electrospun poly(d,l-lactic-co-glycolic acid) meshes. *Biomaterials*. **27**(33), pp.5681–5688.

Bashur, C.A., Shaffer, R.D., Dahlgren, L.A., Guelcher, S.A. and Goldstein, A.S. 2009. Effect of fiber diameter and alignment of electrospun polyurethane meshes on mesenchymal progenitor cells. *Tissue engineering. Part A*. **15**(9), pp.2435–2445.

Baumann, N. and Pham-Dinh, D. 2001. Biology of oligodendrocyte and myelin in the mammalian central nervous system. *Physiological Reviews*. **81**(2), pp.871–927.

Beachley, V., Katsanevakis, E., Zhang, N. and Wen, X. 2012. Highly aligned polymer nanofiber structures: Fabrication and applications in tissue engineering. *Advances in Polymer Science*. **246**(1), pp.171–212.

Beachley, V. and Wen, X. 2009. Effect of electrospinning parameters on the nanofiber diameter and length. *Materials Science and Engineering C*. **29**(3), pp.663–668.

BEIS 2013. Research and analysis: Eight great technologies: infographics.

Bell, E. 2000. Tissue Engineering in Perspective *In*: R. Lanza, R. Langer and J. Vacanti, eds. *Principles of tissue engineering*. Academic Press, p.995.

Bell, E., Ivarsson, B. and Merrill, C. 1979. Production of a tissue-like structure by contraction

of collagen lattices by human fibroblasts of different proliferative potential in vitro. *Cell Biology*. **76**(3), pp.1274–1278.

Van Den Berg, M.E.L., Castellote, J.M., Mahillo-Fernandez, I. and De Pedro-Cuesta, J. 2010. Incidence of spinal cord injury worldwide: A systematic review. *Neuroepidemiology*. **34**(3), pp.184–192.

Bianchi, M.E. 2007. DAMPs, PAMPs and alarmins: all we need to know about danger. *Journal of Leukocyte Biology*. **81**(1), pp.1–5.

Del Bigio, M.R. 2010. Ependymal cells: Biology and pathology. *Acta Neuropathologica*. **119**(1), pp.55–73.

Bilston, L.E. and Thibault, L.E. 1996. The Mechanical Properties of the Human Cervical Spinal Cord In Vitro. *Annals of Biomedical Engineering*. **24**, pp.67–74.

Binder, C., Milleret, V., Hall, H., Eberli, D. and Lühmann, T. 2013. Influence of micro and submicro poly(lactic-glycolic acid) fibers on sensory neural cell locomotion and neurite growth. *Journal of Biomedical Materials Research - Part B Applied Biomaterials*. **101**(7), pp.1200–1208.

Biran, R., Noble, M.D. and Tresco, P.A. 2003. Directed nerve outgrowth is enhanced by engineered glial substrates. *Experimental Neurology*. **184**(1), pp.141–152.

Bjartmar, C., Karlsson, B. and Hildebrand, C. 1994. Cellular and extracellular components at nodes of Ranvier in rat white matter. *Brain Research*. **667**(1), pp.111–114.

BMJ 2016. Chronic spinal cord injury. [Accessed 25 February 2016]. Available from: http://bestpractice.bmj.com/best-practice/monograph/1176/basics/epidemiology.html.

Bölgen, N., Mencelo, Y.Z., Glu, ˘, Acatay, K., Vargel, ˙ I and Skin, E.P. 2005. In vitro and in vivo degradation of non-woven materials made of poly(ε-caprolactone) nanofibers prepared by electrospinning under different conditions. *J. Biomater. Sci. Polymer Edn*. **16**(12), pp.1537–1555.

Boys, C. V. 1887. On the production, properties, and some suggested uses of the finest threads. *Proceedings of the Physical Society of London*. **9**(1), pp.8–19.

Bradbury, E.J. and Burnside, E.R. 2019. Moving beyond the glial scar for spinal cord repair. *Nature Communications*. **10**(1).

Brännvall, K., Bergman, K., Wallenquist, U., Svahn, S., Bowden, T., Hilborn, J. and Forsberg-Nilsson, K. 2007. Enhanced neuronal differentiation in a three-dimensional collagen-hyaluronan matrix. *Journal of Neuroscience Research*. **85**(10), pp.2138–2146.

Broadhead, M.J., Bonthron, C., Arcinas, L., Bez, S., Zhu, F., Goff, F., Nylk, J., Dholakia, K., Gunn-Moore, F., Grant, S.G.N. and Miles, G.B. 2020. Nanostructural Diversity of Synapses in the Mammalian Spinal Cord. *Scientific Reports*. **10**(1).

Bronzino, J.D. and Peterson, D.R. 2015. *The Biomedical Engineering Handbook*.

Bruggeman, K.F., Wang, Y., Maclean, F.L., Parish, C.L., Williams, R.J. and Nisbet, D.R. 2017. Temporally controlled growth factor delivery from a self-assembling peptide hydrogel

and electrospun nanofibre composite scaffold. *Nanoscale*. **9**(36), pp.13661–13669.

Brun, P., Ghezzo, F., Roso, M., Danesin, R., Palù, G., Bagno, A., Modesti, M., Castagliuolo, I. and Dettin, M. 2011. Electrospun scaffolds of self-assembling peptides with poly(ethylene oxide) for bone tissue engineering. *Acta Biomaterialia*. **7**(6), pp.2526–2532.

Bryant, S.J., Nuttelman, C.R. and Anseth, K.S. 2000. Cytocompatibility of UV and visible light photoinitiating systems on cultured NIH/3T3 fibroblasts in vitro. *Journal of Biomaterials Science, Polymer Edition*. **11**(5), pp.439–457.

Bubnis, W.A. and Ofner, C.M. 1992. The determination of ϵ-amino groups in soluble and poorly soluble proteinaceous materials by a spectrophotometrie method using trinitrobenzenesulfonic acid. *Analytical Biochemistry*. **207**(1), pp.129–133.

Bundesen, L.Q., Scheel, T.A., Bregman, B.S. and Kromer, L.F. 2003. Ephrin-B2 and EphB2 regulation of astrocyte-meningeal fibroblast interactions in response to spinal cord lesions in adult rats. *The Journal of neuroscience : the official journal of the Society for Neuroscience*. **23**(21), pp.7789–7800.

Burke, J.L. 2011. *In Situ Engineering of Skeletal Tissues Using Self-assembled Biomimetic Scaffolds*.

Burnside, E.R. and Bradbury, E.J. 2014. Review: Manipulating the extracellular matrix and its role in brain and spinal cord plasticity and repair. *Neuropathology and Applied Neurobiology*. **40**(1), pp.26–59.

Busch, S.A., Horn, K.P., Cuascut, F.X., Hawthorne, A.L., Bai, L., Miller, R.H. and Silver, J. 2010. Adult NG2+cells are permissive to neurite outgrowth and stabilize sensory axons during macrophage-induced axonal dieback after spinal cord injury. *Journal of Neuroscience*. **30**(1), pp.255–265.

Canejo, J.P. and Godinho, M.H. 2013. Cellulose perversions. *Materials*. **6**(4), pp.1377–1390.

Capogrosso, M., Milekovic, T., Borton, D., Wagner, F., Moraud, E.M., Mignardot, J.-B., Buse, N., Gandar, J., Barraud, Q., Xing, D., Rey, E., Duis, S., Jianzhong, Y., Ko, W.K.D., Li, Q., Detemple, P., Denison, T., Micera, S., Bezard, E., Bloch, J. and Courtine, G. 2016. A brain–spine interface alleviating gait deficits after spinal cord injury in primates. *Nature*. **539**(7628), pp.284–288.

Carrick, L.M., Aggeli, A., Boden, N., Fisher, J., Ingham, E. and Waigh, T.A. 2007. Effect of ionic strength on the self-assembly, morphology and gelation of pH responsive β-sheet tape-forming peptides. *Tetrahedron*. **63**(31), pp.7457–7467.

Chandar, K. and Freeman, B.K. 2014. Spinal Cord Anatomy *In*: *Encyclopedia of the Neurological Sciences*., pp.254–263.

Chen, C., Tang, J., Gu, Y., Liu, L., Liu, X., Deng, L., Martins, C., Sarmento, B., Cui, W. and Chen, L. 2019. Bioinspired Hydrogel Electrospun Fibers for Spinal Cord Regeneration. *Advanced Functional Materials*. **29**(4).

Chen, W., Zhang, Y., Yang, S., Sun, J., Qiu, H., Hu, X., Niu, X., Xiao, Z., Zhao, Y., Zhou, Y., Dai, J. and Chu, T. 2020. NeuroRegen Scaffolds Combined with Autologous Bone Marrow

Mononuclear Cells for the Repair of Acute Complete Spinal Cord Injury: A 3-Year Clinical Study. *Cell Transplantation*. **29**.

Cheng, S., Clarke, E.C. and Bilston, L.E. 2008. Rheological properties of the tissues of the central nervous system: A review. *Medical Engineering and Physics*. **30**(10), pp.1318–1337.

Chow, W.N., Simpson, D.G., Bigbee, J.W. and Colello, R.J. 2007. Evaluating neuronal and glial growth on electrospun polarized matrices: Bridging the gap in percussive spinal cord injuries. *Neuron Glia Biology*. **3**(2), pp.119–126.

Christopherson, K.S., Ullian, E.M., Stokes, C.C.A., Mullowney, C.E., Hell, J.W., Agah, A., Lawler, J., Mosher, D.F., Bornstein, P. and Barres, B.A. 2005. Thrombospondins are astrocyte-secreted proteins that promote CNS synaptogenesis. *Cell*. **120**(3), pp.421–433.

Cnops, V., Chin, J.S., Milbreta, U. and Chew, S.Y. 2020. Biofunctional scaffolds with high packing density of aligned electrospun fibers support neural regeneration. *Journal of Biomedical Materials Research - Part A*. **108**(12), pp.2473–2483.

Colello, R.J., Chow, W.N., Bigbee, J.W., Lin, C., Dalton, D., Brown, D., Jha, B.S., Mathern, B.E., Lee, K.D. and Simpson, D.G. 2016. The incorporation of growth factor and chondroitinase ABC into an electrospun scaffold to promote axon regrowth following spinal cord injury. *Journal of Tissue Engineering and Regenerative Medicine*. **10**(8), pp.656–668.

Cooley, J.F. 1899. Apparatus for electrically dispersing fluids. *US Patent 692,631*. **693**(631), pp.1–6.

Corey, J.M., Lin, D.Y., Mycek, K.B., Chen, Q., Samuel, S., Feldman, E.L. and Martin, D.C. 2007. Aligned electrospun nanofibers specify the direction of dorsal root ganglia neurite growth. *Journal of Biomedical Materials Research - Part A*. **83**(3), pp.636–645.

Coull, J.A.M., Beggs, S., Boudreau, D., Boivin, D., Tsuda, M., Inoue, K., Gravel, C., Salter, M.W. and De Koninck, Y. 2005. BDNF from microglia causes the shift in neuronal anion gradient underlying neuropathic pain. *Nature*. **438**(7070), pp.1017–1021.

Cramer, G.D. and Darby, S.A. 2014. *Clinical Anatomy of the Spine, Spinal Cord, and ANS* [Online] Third. Available from: http://www.sciencedirect.com/science/article/pii/B9780323079549000050.

Cruz-Almeida, Y., Felix, E.R., Martinez-Arizala, A. and Widerström-Noga, E.G. 2012. Decreased spinothalamic and dorsal column medial lemniscus-mediated function is associated with neuropathic pain after spinal cord injury. *Journal of Neurotrauma*. **29**(17), pp.2706–2715.

Dabirian, F., Hosseini Ravandi, S.A., Pishevar, A.R. and Abuzade, R.A. 2011. A comparative study of jet formation and nanofiber alignment in electrospinning and electrocentrifugal spinning systems. *Journal of Electrostatics*. **69**(6), pp.540–546.

Danesin, R., Brun, P., Roso, M., Delaunay, F., Samouillan, V., Brunelli, K., Iucci, G., Ghezzo, F., Modesti, M., Castagliuolo, I. and Dettin, M. 2012. Self-assembling peptide-enriched electrospun polycaprolactone scaffolds promote the h-osteoblast adhesion and

modulate differentiation-associated gene expression. *Bone*. **51**(5), pp.851–859.

Datta, P. and Dhara, S. 2019. Engineering Porosity in Electrospun Nanofiber Sheets by Laser Engraving: A Strategy to Fabricate 3D Scaffolds for Bone Graft Applications. *Journal of the Indian Institute of Science*. **99**(3), pp.329–337.

Daud, M.F.B., Pawar, K.C., Claeyssens, F., Ryan, A.J. and Haycock, J.W. 2012. An aligned 3D neuronal-glial co-culture model for peripheral nerve studies. *Biomaterials*. **33**(25), pp.5901–5913.

Davalos, D., Grutzendler, J., Yang, G., Kim, J. V., Zuo, Y., Jung, S., Littman, D.R., Dustin, M.L. and Gan, W.B. 2005. ATP mediates rapid microglial response to local brain injury in vivo. *Nature Neuroscience*. **8**(6), pp.752–758.

Davies, R.P.W., Aggeli, A., Beevers, A.J., Boden, N., Carrick, L.M., Fishwick, C.W.G., McLeish, T.C.B., Nyrkova, I. and Semenov, A.N. 2006. Self-assembling β-sheet tape forming peptides. *Supramolecular Chemistry*. **18**(5), pp.435–443.

Davison, N.L., Barrère-de Groot, F. and Grijpma, D.W. 2014. Degradation of Biomaterials *In*: *Tissue Engineering: Second Edition*. Elsevier Inc., pp.177–215.

Deng, W.S., Ma, K., Liang, B., Liu, X.Y., Xu, H.Y., Zhang, J., Shi, H.Y., Sun, H.T., Chen, X.Y. and Zhang, S. 2020. Collagen scaffold combined with human umbilical cord-mesenchymal stem cells transplantation for acute complete spinal cord injury. *Neural Regeneration Research*. **15**(9), pp.1686–1700.

Dettin, M., Zamuner, A., Roso, M., Gloria, A., Iucci, G., Messina, G.M.L., D'Amora, U., Marletta, G., Modesti, M., Castagliuolo, I. and Brun, P. 2015. Electrospun Scaffolds for Osteoblast Cells: Peptide-Induced Concentration-Dependent Improvements of Polycaprolactone F. Gelain, ed. *PLOS ONE*. **10**(9), p.e0137505.

Ding, B., Li, C., Miyauchi, Y., Kuwaki, O. and Shiratori, S. 2006. Formation of novel 2D polymer nanowebs via electrospinning. *Nanotechnology*. **17**(15), pp.3685–3691.

Du, J., Liu, J., Yao, S., Mao, H., Peng, J., Sun, X., Cao, Z., Yang, Y., Xiao, B., Wang, Y., Tang, P. and Wang, X. 2017. Prompt peripheral nerve regeneration induced by a hierarchically aligned fibrin nanofiber hydrogel. *Acta Biomaterialia*. **55**, pp.296–309.

Dumont, R.J., Okonkwo, D.O., Verma, S., Hurlbert, R.J., Boulos, P.T., Ellegala, D.B. and Dumont, A.S. 2001. Acute spinal cord injury, part I: Pathophysiologic mechanisms. *Clinical Neuropharmacology*. **24**(5), pp.254–264.

Duncan, I.D., Radcliff, A.B., Heidari, M., Kidd, G., August, B.K. and Wierenga, L.A. 2018. The adult oligodendrocyte can participate in remyelination. *Proceedings of the National Academy of Sciences of the United States of America*. **115**(50), pp.E11807–E11816.

Dutta, D.J., Woo, D.H., Lee, P.R., Pajevic, S., Bukalo, O., Huffman, W.C., Wake, H., Basser, P.J., SheikhBahaei, S., Lazarevic, V., Smith, J.C. and Fields, R.D. 2018. Regulation of myelin structure and conduction velocity by perinodal astrocytes. *Proceedings of the National Academy of Sciences of the United States of America*. **115**(46), pp.11832–11837.

Edwards, M.D., Mitchell, G.R., Mohan, S.D. and Olley, R.H. 2010. Development of orientation

during electrospinning of fibres of poly(e-caprolactone). *European Polymer Journal*. **46**(6), pp.1175–1183.

Ellis-Behnke, R.G., Liang, Y.-X., You, S.-W., C Tay, D.K., Zhang, S., So, K.-F. and Schneider, G.E. 2006. *Nano neuro knitting: Peptide nanofiber scaffold for brain repair and axon regeneration with functional return of vision* [Online]. [Accessed 11 January 2020]. Available from: www.pnas.orgcgidoi10.1073pnas.0600559103.

Elmarco 2021. Elmarco.

Elsevier 2020. Biomaterials. [Accessed 29 November 2020]. Available from: https://www.journals.elsevier.com/biomaterials.

Engelberg, I. and Kohn, J. 1991. Physico-mechanical properties of degradable polymers used in medical applications: A comparative study. *Biomaterials*. **12**(3), pp.292–304.

Ewan, E.E., Avraham, O., Carlin, D., Gonçalves, T.M., Zhao, G. and Cavalli, V. 2021. Ascending dorsal column sensory neurons respond to spinal cord injury and downregulate genes related to lipid metabolism. *Scientific Reports*. **11**(1).

Fabris, G., Lucantonio, A., Hampe, N., Noetzel, E., Hoffmann, B., DeSimone, A. and Merkel, R. 2018. Nanoscale Topography and Poroelastic Properties of Model Tissue Breast Gland Basement Membranes. *Biophysical Journal*. **115**(9), pp.1770–1782.

Fahy, G.M. 2002. Dr. William Haseltine on regenerative medicine, aging and human immortality. *Life Extension*.

Fairbanks, B.D., Schwartz, M.P., Bowman, C.N. and Anseth, K.S. 2009. Photoinitiated polymerization of PEG-diacrylate with lithium phenyl-2,4,6-trimethylbenzoylphosphinate: polymerization rate and cytocompatibility. *Biomaterials*. **30**(35), pp.6702–6707.

Fan, J., Xiao, Z., Zhang, H., Chen, B., Tang, G., Hou, X., Ding, W., Wang, B., Zhang, P., Dai, J. and Xu, R. 2010. Linear Ordered Collagen Scaffolds Loaded with Collagen-Binding Neurotrophin-3 Promote Axonal Regeneration and Partial Functional Recovery after Complete Spinal Cord Transection. *Journal of Neurotrauma*. **27**(9), pp.1671–1683.

Fan, Z., Shen, Y., Zhang, F., Zuo, B., Lu, Q., Wu, P., Xie, Z., Dong, Q. and Zhang, H. 2013. Control of olfactory ensheathing cell behaviors by electrospun silk fibroin fibers. *Cell Transplantation*. **22**(SUPPL.1).

Faulkner, J.R., Herrmann, J.E., Woo, M.J., Tansey, K.E., Doan, N.B. and Sofroniew, M. V 2004. Reactive astrocytes protect tissue and preserve function after spinal cord injury. *The Journal of neuroscience : the official journal of the Society for Neuroscience*. **24**(9), pp.2143–55.

Filous, A.R., Tran, A., James Howell, C., Busch, S.A., Evans, T.A., Stallcup, W.B., Kang, S.H., Bergles, D.E., Lee, S. Il, Levine, J.M. and Silver, J. 2014. Entrapment via synaptic-like connections between NG2 proteoglycan + cells and dystrophic axons in the lesion plays a role in regeneration failure after spinal cord injury. *Journal of Neuroscience*. **34**(49), pp.16369–16384.

Fradet, L., Cliche, F., Petit, Y., Mac-Thiong, J.-M. and Arnoux, P.-J. 2016. Strain rate

dependent behavior of the porcine spinal cord under transverse dynamic compression. *Proceedings of the Institution of Mechanical Engineers, Part H: Journal of Engineering in Medicine*., p.954411916655373.

Frühbeis, C., Kuo-Elsner, W.P., Müller, C., Barth, K., Peris, L., Tenzer, S., Möbius, W., Werner, H.B., Nave, K.A., Fröhlich, D. and Krämer-Albers, E.M. 2020. Oligodendrocytes support axonal transport and maintenance via exosome secretion. *PLoS Biology*. **18**(12 December).

Fuller, K.P., Gaspar, D., Delgado, L.M. and Zeugolis, D.I. 2019. Development macro-porous electro-spun meshes with clinically relevant mechanical properties - A technical note. *Biomedical Materials (Bristol)*. **14**(2).

Gao, S., Guo, W., Chen, M., Yuan, Z., Wang, M., Zhang, Y., Liu, S., Xi, T. and Guo, Q. 2017. Fabrication and characterization of electrospun nanofibers composed of decellularized meniscus extracellular matrix and polycaprolactone for meniscus tissue engineering. *Journal of Materials Chemistry B*. **5**(12), pp.2273–2285.

Garaschuk, O. and Verkhratsky, A. 2019. Physiology of Microglia *In*: *Methods in Molecular Biology*., pp.27–40.

Garcia-Ovejero, D., Arevalo-Martin, A., Paniagua-Torija, B., Florensa-Vila, J., Ferrer, I., Grassner, L. and Molina-Holgado, E. 2015. The ependymal region of the adult human spinal cord differs from other species and shows ependymoma-like features. *Brain*. **138**(6), pp.1583–1597.

Gaumer, J., Prasad, A., Lee, D. and Lannutti, J. 2009. Structure-function relationships and source-to-ground distance in electrospun polycaprolactone. *Acta Biomaterialia*. **5**(5), pp.1552–1561.

Gelain, F., Bottai, D., Vescovi, A. and Zhang, S. 2006. Designer self-assembling peptide nanofiber scaffolds for adult mouse neural stem cell 3-dimensional cultures. *PLoS ONE*. **1**(1).

Gelain, F., Cigognini, D., Caprini, A., Silva, D., Colleoni, B., Donegá, M., Antonini, S., Cohen, B.E. and Vescovi, A. 2012. New bioactive motifs and their use in functionalized self-assembling peptides for NSC differentiation and neural tissue engineering. *Nanoscale*. **4**(9), pp.2946–2957.

Gentsch, R., Boysen, B., Lankenau, A. and Börner, H.G. 2010. Single-step electrospinning of bimodal fiber meshes for ease of cellular infiltration. *Macromolecular Rapid Communications*. **31**(1), pp.59–64.

Gentsch, R., Pippig, F., Schmidt, S., Cernoch, P., Polleux, J. and Börner, H.G. 2011. Single-step electrospinning to bioactive polymer nanofibers. *Macromolecules*. **44**(3), pp.453–461.

Gharaei, R. 2017. *Production and Properties of Fibre Webs Containing Self-Assembling Peptides for Promotion of Hard Tissue Repair*. PhD Thesis. University of Leeds.

Gharaei, R., Tronci, G., Davies, R.P.W., Gough, C., Alazragi, R., Goswami, P. and Russell, S.J. 2016. A structurally self-assembled peptide nano-architecture by one-step electrospinning. *J. Mater. Chem. B*. **4**(32), pp.5475–5485.

Gharaei, R., Tronci, G., Goswami, P., Davies, R.P.W., Kirkham, J. and Russell, S.J. 2020. Biomimetic peptide enriched nonwoven scaffolds promote calcium phosphate mineralisation. *RSC Advances*. **10**(47), pp.28332–28342.

Gottipati, M.K., D'Amato, A.R., Ziemba, A.M., Popovich, P.G. and Gilbert, R.J. 2020. TGFβ3 is neuroprotective and alleviates the neurotoxic response induced by aligned poly-L-lactic acid fibers on naïve and activated primary astrocytes. *Acta Biomaterialia*. **117**, pp.273–282.

Götze, M., Kürbitz, T., Krimig, O., Schmelzer, C.E.H., Heilmann, A. and Hillrichs, G. 2019. Investigation of Laser Processing of Biodegradable Nanofiber Nonwovens with Different Laser Pulse Durations. *JLMN-Journal of Laser Micro/Nanoengineering*. **14**(1).

Graham, H.K., Hodson, N.W., Hoyland, J.A., Millward-Sadler, S.J., Garrod, D., Scothern, A., Griffiths, C.E.M., Watson, R.E.B., Cox, T.R., Erler, J.T., Trafford, A.W. and Sherratt, M.J. 2010. Tissue section AFM: In situ ultrastructural imaging of native biomolecules. *Matrix Biology*. **29**(4), pp.254–260.

Griffiths, I., Klugmann, M., Anderson, T., Yool, D., Thomson, C., Schwab, M.H., Schneider, A., Zimmermann, F., McCulloch, M., Nadon, N. and Nave, K.A. 1998. Axonal swellings and degeneration in mice lacking the major proteolipid of myelin. *Science*. **280**(5369), pp.1610–1613.

Guest, J.D., Moore, S.W., Aimetti, A.A., Kutikov, A.B., Santamaria, A.J., Hofstetter, C.P., Ropper, A.E., Theodore, N., Ulich, T.R. and Layer, R.T. 2018. Internal decompression of the acutely contused spinal cord: Differential effects of irrigation only versus biodegradable scaffold implantation. *Biomaterials*. **185**, pp.284–300.

Guimarães, C.F., Gasperini, L., Marques, A.P. and Reis, R.L. 2020. The stiffness of living tissues and its implications for tissue engineering. *Nature Reviews Materials*. **5**(5), pp.351–370.

Guo, S.-Z., Ren, X.-J., Wu, B. and Jiang, T. 2010. Preparation of the acellular scaffold of the spinal cord and the study of biocompatibility. *Spinal Cord*. **48**, pp.576–581.

Haggerty, A.E., Marlow, M.M. and Oudega, M. 2017. Extracellular matrix components as therapeutics for spinal cord injury. *Neuroscience Letters*. **652**, pp.50–55.

Haider, A., Haider, S. and Kang, I.-K. 2015. A comprehensive review summarizing the effect of electrospinning parameters and potential applications of nanofibers in biomedical and biotechnology. *Arabian Journal of Chemistry*., pp.1–24.

Han, Q., Jin, W., Xiao, Z., Ni, H., Wang, J., Kong, J., Wu, J., Liang, W., Chen, L., Zhao, Y., Chen, B. and Dai, J. 2010. The promotion of neural regeneration in an extreme rat spinal cord injury model using a collagen scaffold containing a collagen binding neuroprotective protein and an EGFR neutralizing antibody. *Biomaterials*. **31**(35), pp.9212–9220.

Han, Q., Sun, W., Lin, H., Zhao, W., Gao, Y., Zhao, Y., Chen, B., Xiao, Z., Hu, W., Li, Y., Yang, B. and Dai, J. 2009. Linear Ordered Collagen Scaffolds Loaded with Collagen-Binding Brain-Derived Neurotrophic Factor Improve the Recovery of Spinal Cord Injury in Rats. *Tissue Engineering Part A*. **15**(10), pp.2927–2935.

Han, S., Wang, B., Jin, W., Xiao, Z., Li, X., Ding, W., Kapur, M., Chen, B., Yuan, B., Zhu, T.,

Wang, H., Wang, J., Dong, Q., Liang, W. and Dai, J. 2015. The linear-ordered collagen scaffold-BDNF complex significantly promotes functional recovery after completely transected spinal cord injury in canine. *Biomaterials*. **41**, pp.89–96.

Hasturk, O. and Kaplan, D.L. 2019. Cell armor for protection against environmental stress: Advances, challenges and applications in micro- and nanoencapsulation of mammalian cells. *Acta Biomaterialia*. **95**, pp.3–31.

Hawryluk, G.W.J., Rowland, J., Kwon, B.K. and Fehlings, M.G. 2008. Protection and repair of the injured spinal cord: a review of completed, ongoing, and planned clinical trials for acute spinal cord injury. *Neurosurgical FOCUS*. **25**(5), p.E14.

He, L., Liao, S., Quan, D., Ma, K., Chan, C., Ramakrishna, S. and Lu, J. 2010. Synergistic effects of electrospun PLLA fiber dimension and pattern on neonatal mouse cerebellum C17.2 stem cells. *Acta Biomaterialia*. **6**(8), pp.2960–2969.

Hennekinne, L., Colasse, S., Triller, A. and Renner, M. 2013. Differential control of thrombospondin over synaptic glycine and AMPA receptors in spinal cord neurons. *Journal of Neuroscience*. **33**(28), pp.11432–11439.

Holmes, T.C., De Lacalle, S., Su, X., Liu, G., Rich, A. and Zhang, S. 2000. Extensive neurite outgrowth and active synapse formation on self-assembling peptide scaffolds. *Proceedings of the National Academy of Sciences of the United States of America*. **97**(12), pp.6728–6733.

Horne, M.K., Nisbet, D.R., Forsythe, J.S. and Parish, C.L. 2010. Three-dimensional nanofibrous scaffolds incorporating immobilized bdnf promote proliferation and differentiation of cortical neural stem cells. *Stem Cells and Development*. **19**(6), pp.843–852.

Hsieh, A., Zahir, T., Lapitsky, Y., Amsden, B., Wan, W. and Shoichet, M.S. 2010. Hydrogel/electrospun fiber composites influence neural stem/progenitor cell fate. *Soft Matter*. **6**(10), pp.2227–2237.

Huang, D., Lin, C., Wen, X., Gu, S. and Zhao, P. 2016. A potential nanofiber membrane device for filling surgical residual cavity to prevent glioma recurrence and improve local neural tissue reconstruction. *PLoS ONE*. **11**(8).

Hudecki, A., Kiryczyński, G. and Los, M.J. 2019. Chapter 7 - Biomaterials, Definition, Overview *In*: *Stem Cells and Biomaterials for Regenerative Medicine*., pp.85–98.

Hung, T.K., Lin, H.S., Bunegin, L. and Albin, M.S. 1982. Mechanical and neurological response of cat spinal cord under static loading. *Surgical Neurology*. **17**(3), pp.213–217.

Hurtado, A., Cregg, J.M., Wang, H.B., Wendell, D.F., Oudega, M., Gilbert, R.J. and McDonald, J.W. 2011. Robust CNS regeneration after complete spinal cord transection using aligned poly-l-lactic acid microfibers. *Biomaterials*. **32**(26), pp.6068–6079.

Hynes, S.R., Rauch, M.F., Bertram, J.P. and Lavik, E.B. 2009. A library of tunable poly(ethylene glycol)/poly(L-lysine) hydrogels to investigate the material cues that influence neural stem cell differentiation. *Journal of Biomedical Materials Research - Part A*. **89**(2), pp.499–509.

Hyysalo, A., Ristola, M., Joki, T., Honkanen, M., Vippola, M. and Narkilahti, S. 2017. Aligned Poly(ε-caprolactone) Nanofibers Guide the Orientation and Migration of Human Pluripotent Stem Cell-Derived Neurons, Astrocytes, and Oligodendrocyte Precursor Cells In Vitro. *Macromolecular Bioscience*. **17**(7).

Iadecola, C. and Nedergaard, M. 2007. Glial regulation of the cerebral microvasculature. *Nature Neuroscience*. **10**(11), pp.1369–1376.

Ionescu, L.C., Lee, G.C., Sennett, B.J., Burdick, J.A. and Mauck, R.L. 2010. An anisotropic nanofiber/microsphere composite with controlled release of biomolecules for fibrous tissue engineering. *Biomaterials*. **31**(14), pp.4113–4120.

ISO 2009. ISO 10993-5:2009. *Biological evaluation of medical devices – Part 5: Tests for in vitro cytotoxicity*.

Jahnavi, S., Arthi, N., Pallavi, S., Selvaraju, C., Bhuvaneshwar, G.S., Kumary, T. V. and Verma, R.S. 2017. Nanosecond laser ablation enhances cellular infiltration in a hybrid tissue scaffold. *Materials Science and Engineering C*. **77**, pp.190–201.

Janmohammadi, M. and Nourbakhsh, M.S. 2019. Electrospun polycaprolactone scaffolds for tissue engineering: a review. *International Journal of Polymeric Materials and Polymeric Biomaterials*. **68**(9), pp.527–539.

Jirsak, O., Sanetrnik, F., Lukas, D., Kotek, V., Martinova, L. and Chaloupek, J. 2009. A method of nanofibres production from a polymer solution using electrostatic spinning and a device for carrying out the method. *US Patent*. [Online]. Available from: http://www.google.com/patents/US7585437.

Johansson, F., Carlberg, P., Danielsen, N., Montelius, L. and Kanje, M. 2006. Axonal outgrowth on nano-imprinted patterns. *Biomaterials*. **27**(8), pp.1251–1258.

Johnson, C.D., D'Amato, A.R., Puhl, D.L., Wich, D.M., Vesperman, A. and Gilbert, R.J. 2018. Electrospun fiber surface nanotopography influences astrocyte-mediated neurite outgrowth. *Biomedical Materials (Bristol)*. **13**(5).

Johnson, C.D.L., Ganguly, D., Zuidema, J.M., Cardinal, T.J., Ziemba, A.M., Kearns, K.R., McCarthy, S.M., Thompson, D.M., Ramanath, G., Borca-Tasciuc, D.A., Dutz, S. and Gilbert, R.J. 2019. Injectable, Magnetically Orienting Electrospun Fiber Conduits for Neuron Guidance. *ACS Applied Materials and Interfaces*. **11**(1), pp.356–372.

Jorba, I., Uriarte, J.J., Campillo, N., Farré, R. and Navajas, D. 2017. Probing Micromechanical Properties of the Extracellular Matrix of Soft Tissues by Atomic Force Microscopy. *Journal of Cellular Physiology*. **232**(1), pp.19–26.

Joshi, V.S., Lei, N.Y., Walthers, C.M., Wu, B. and Dunn, J.C.Y. 2013. Macroporosity enhances vascularization of electrospun scaffolds. *Journal of Surgical Research*. **183**(1), pp.18–26.

Jun, I., Han, H.S., Edwards, J.R. and Jeon, H. 2018. Electrospun fibrous scaffolds for tissue engineering: Viewpoints on architecture and fabrication. *International Journal of Molecular Sciences*. **19**(3), p.745.

Jun, I., Kim, K., Chung, Y.W., Shin, H.J., Han, H.S., Edwards, J.R., Ok, M.R., Kim, Y.C., Seok, H.K., Shin, H. and Jeon, H. 2018. Effect of spatial arrangement and structure of

hierarchically patterned fibrous scaffolds generated by a femtosecond laser on cardiomyoblast behavior. *Journal of Biomedical Materials Research - Part A*. **106**(6), pp.1732–1742.

Kabiri, M., Oraee-Yazdani, S., Dodel, M., Hanaee-Ahvaz, H., Soudi, S., Seyedjafari, E., Salehi, M. and Soleimani, M. 2015. Cytocompatibility of a conductive nanofibrous carbon nanotube/poly (L-lactic acid) composite scaffold intended for nerve tissue engineering. *EXCLI Journal*. **14**, pp.851–860.

Kadler, K.E., Holmes, D.F., Trotter, J.A. and Chapman, J.A. 1996. *Collagen fibril formation*.

Kamen, Y., Pivonkova, H., Evans, K.A. and Káradóttir, R.T. 2021. A Matter of State: Diversity in Oligodendrocyte Lineage Cells. *The Neuroscientist*., p.107385842098720.

Kanaka, C., Ohno, K., Okabe, A., Kuriyama, K., Itoh, T., Fukuda, A. and Sato, K. 2001. The differential expression patterns of messenger RNAs encoding K-Cl cotransporters (KCC1,2) and Na-K-2Cl cotransporter (NKCC1) in the rat nervous system. *Neuroscience*. **104**(4), pp.933–946.

Kaplan, M.R., Meyer-Franke, A., Lambert, S., Bennett, V., Duncan, I.D., Levinson, S.R. and Barres, B.A. 1997. Induction of sodium channel clustering by oligodendrocytes. *Nature*. **386**(6626), pp.724–728.

Karimi, A., Shojaei, A. and Tehrani, P. 2017. Mechanical properties of the human spinal cord under the compressive loading. *Journal of Chemical Neuroanatomy*. **86**, pp.15–18.

Karmiol, S., Manaster, E. and Ryan, J. 2008. Attachment and Matrix Factors. *Sigm-Aldrich Biofiles*.

Kárová, K., Urdzíková, L.M., Romanyuk, N., Svobodová, B., Kekulová, K., Kočí, Z., Jendelová, P. and Kubinová, Š. 2020. Tissue engineering and regenerative medicine in spinal cord injury repair *In*: *Handbook of Innovations in Central Nervous System Regenerative Medicine*., pp.291–332.

Kettenmann, H., Hanisch, U.-K., Noda, M. and Verkhratsky, A. 2011. Physiology of microglia. *Physiological reviews*. **91**(2), pp.461–553.

Kim, C.H., Khil, M.S., Kim, H.Y., Lee, H.U. and Jahng, K.Y. 2006. An improved hydrophilicity via electrospinning for enhanced cell attachment and proliferation. *Journal of Biomedical Materials Research Part B: Applied Biomaterials*. **78B**(2), pp.283–290.

Kim, K.D., Lee, K.S., Coric, D., Chang, J.J., Harrop, J.S., Theodore, N. and Toselli, R.M. 2021. A study of probable benefit of a bioresorbable polymer scaffold for safety and neurological recovery in patients with complete thoracic spinal cord injury: 6-month results from the INSPIRE study. *Journal of Neurosurgery: Spine*., pp.1–10.

Kim, M., Son, J., Lee, H., Hwang, H., Choi, C.H. and Kim, G. 2014. Highly porous 3D nanofibrous scaffolds processed with an electrospinning/laser process. *Current Applied Physics*. **14**(1), pp.1–7.

Kimelberg, H.K. and Nedergaard, M. 2010. Functions of Astrocytes and their Potential As Therapeutic Targets. *Neurotherapeutics*. **7**(4), pp.338–353.

Kimmer, D., Slobodiam, P., Petrás, D., Zatloukal, M., Olejnik, R. and Sáha, P. 2009. Polyurethane/multiwalled carbon nanotube nanowebs prepared by an electrospinning process. *Journal of Applied Polymer Science*. **111**(6), pp.2711–2714.

Kirk, J.S.L. 2018. *Development of a 3D in vitro spinal cord injury model to investigate how the mechanical properties of the matrix affect CNS cell behaviour*. University of Leeds.

Kissane, R.W.P., Wright, O., Al'Joboori, Y.D., Marczak, P., Ichiyama, R.M. and Egginton, S. 2019. Effects of treadmill training on microvascular remodeling in the rat after spinal cord injury. *Muscle and Nerve*. **59**(3), pp.370–379.

Ko, H.-Y., Park, J., Shin, Y. and Baek, S. 2004. Gross quantitative measurements of spinal cord segments in human. *Spinal Cord*. **42**(1), pp.35–40.

Kowalczyk, T. 2020. Functional micro- and nanofibers obtained by nonwoven post-modification. *Polymers*. **12**(5).

Krawczyk-Marc, I., Wawrzyniak, A., Luszczewska-Sierakowska, I., Babicz, M. and Orkisz, S. 2019. Oligodendrocytes: Morphology, functions and involvement in neurodegenerative diseases. *Medycyna Weterynaryjna*. **75**(8), pp.465–471.

Krishnamoorthy, T., Thavasi, V., Akshara, V., Kumar, A.S., Pliszka, D., Mhaisalkar, S.G. and Ramakrishna, S. 2011. Direct deposition of micron-thick aligned ceramic TiO 2 nanofibrous film on FTOs by double-needle electrospinning using air-turbulence shielded disc collector. *Journal of Nanomaterials*. **2011**.

Kroeker, S.G., Morley, P.L., Jones, C.F., Bilston, L.E. and Cripton, P.A. 2009. The development of an improved physical surrogate model of the human spinal cord-Tension and transverse compression. *Journal of Biomechanics*. **42**(7), pp.878–883.

Kubotera, H., Ikeshima-Kataoka, H., Hatashita, Y., Allegra Mascaro, A.L., Pavone, F.S. and Inoue, T. 2019. Astrocytic endfeet re-cover blood vessels after removal by laser ablation. *Scientific Reports*. **9**(1).

Kuntz Willits, R. and Skornia, S.L. 2004. Effect of collagen gel stiffness on neurite extension. *Journal of Biomaterials Science Polymer Edition J. Biomater. Sci. Polymer Edn*. **1512**(12), pp.1521–1531.

Kwansa, A.L. and Freeman, J.W. 2015. Ligament tissue engineering *In*: *Regenerative Engineering of Musculoskeletal Tissues and Interfaces*., pp.161–193.

Kwok, J.C.F., Dick, G., Wang, D. and Fawcett, J.W. 2011. Extracellular matrix and perineuronal nets in CNS repair. *Developmental Neurobiology*. **71**(11), pp.1073–1089.

Lam, C.X.F., Hutmacher, D.W., Schantz, J.-T., Woodruff, M.A. and Teoh, S.H. 2009. Evaluation of polycaprolactone scaffold degradation for 6 months in vitro and in vivo. *Journal of Biomedical Materials Research Part A*. **90A**(3), pp.906–919.

Lampe, K.J., Antaris, A.L. and Heilshorn, S.C. 2013. Design of three-dimensional engineered protein hydrogels for tailored control of neurite growth. *Acta Biomaterialia*. **9**, pp.5590–5599.

Lampe, K.J., Mooney, R.G., Bjugstad, K.B. and Mahoney, M.J. 2010. Effect of macromer

weight percent on neural cell growth in 2D and 3D nondegradable PEG hydrogel culture. *Journal of Biomedical Materials Research - Part A*. **94**(4), pp.1162–1171.

Lang, B.T., Cregg, J.M., Depaul, M.A., Tran, A.P., Xu, K., Dyck, S.M., Madalena, K.M., Brown, B.P., Weng, Y.L., Li, S., Karimi-Abdolrezaee, S., Busch, S.A., Shen, Y. and Silver, J. 2015. Modulation of the proteoglycan receptor PTPσ promotes recovery after spinal cord injury. *Nature*. **518**(7539), pp.404–408.

Langer, R. and Vacanti, J.P. 1993. Tissue engineering. *Science*. **260**(5110), pp.920–926.

Lau, L.W., Cua, R., Keough, M.B., Haylock-Jacobs, S. and Yong, V.W. 2013. Pathophysiology of the brain extracellular matrix: a new target for remyelination. *Nature reviews. Neuroscience*. **14**(10), pp.722–9.

Layer, R.T., Ulich, T.R., Coric, D., Arnold, P.M., Guest, J.D., Heary, R.H., Hsieh, P.C., Jenkins, A.L., Kim, K.D., Lee, K.S., Masuoka, L.K., Neff, K.M., Ray, W.Z., Theodore, N. and Fehlings, M.G. 2017. New Clinical-Pathological Classification of Intraspinal Injury Following Traumatic Acute Complete Thoracic Spinal Cord Injury: Postdurotomy/Myelotomy Observations from the INSPIRE Trial *In*: *Clinical Neurosurgery*., pp.105–109.

Lee, B.A., Leiby, B.E. and Marino, R.J. 2016. Neurological and functional recovery after thoracic spinal cord injury. *Journal of Spinal Cord Medicine*. **39**(1), pp.67–76.

Lee, C.H., Lim, Y.C., Powell, H.M., Farson, D.F. and Lannutti, J.J. 2012. Electrospun vascular graft properties following femtosecond laser ablation. *Journal of Applied Polymer Science*. **124**(3), pp.2513–2523.

Lee, J.Y., Bashur, C.A., Gomez, N., Goldstein, A.S. and Schmidt, C.E. 2010. Enhanced polarization of embryonic hippocampal neurons on micron scale electrospun fibers. *Journal of biomedical materials research. Part A*. **92**(4), pp.1398–406.

Lee, S., Yun, S., Park, K.I. and Jang, J.H. 2016. Sliding Fibers: Slidable, Injectable, and Gel-like Electrospun Nanofibers as Versatile Cell Carriers. *ACS Nano*. **10**(3), pp.3282–3294.

Lee, S.J., Nowicki, M., Harris, B. and Zhang, L.G. 2017. Fabrication of a Highly Aligned Neural Scaffold via a Table Top Stereolithography 3D Printing and Electrospinning. *Tissue Engineering - Part A*. **23**(11–12), pp.491–502.

Lee, Y.S., Wu, S., Arinzeh, T.L. and Bunge, M.B. 2017. Enhanced noradrenergic axon regeneration into schwann cell-filled PVDF-TrFE conduits after complete spinal cord transection. *Biotechnology and Bioengineering*. **114**(2), pp.444–456.

Li, D., Wang, Y. and Xia, Y. 2003. Electrospinning of polymeric and ceramic nanofibers as uniaxially aligned arrays. *Nano Letters*. **3**(8), pp.1167–1171.

Li, W.-J., Mauck, R.L., Cooper, J.A., Yuan, X. and Tuan, R.S. 2007. Engineering controllable anisotropy in electrospun biodegradable nanofibrous scaffolds for musculoskeletal tissue engineering. *Journal of Biomechanics*. **40**(8), pp.1686–1693.

Li, X., Floriddia, E.M., Toskas, K., Fernandes, K.J.L., Guérout, N. and Barnabé-Heider, F. 2016. Regenerative Potential of Ependymal Cells for Spinal Cord Injuries Over Time. *EBioMedicine*. **13**, pp.55–65.

Li, X., Han, J., Zhao, Y., Ding, W., Wei, J., Han, S., Shang, X., Wang, B., Chen, B., Xiao, Z. and Dai, J. 2015. Functionalized Collagen Scaffold Neutralizing the Myelin-Inhibitory Molecules Promoted Neurites Outgrowth in Vitro and Facilitated Spinal Cord Regeneration in Vivo. *ACS Appl. Mater. Interfaces*. **7**(25), pp.13960–13971.

Li, X., Li, M., Sun, J., Zhuang, Y., Shi, J., Guan, D., Chen, Y. and Dai, J. 2016. Radially Aligned Electrospun Fibers with Continuous Gradient of SDF1α for the Guidance of Neural Stem Cells. *Small*. **12**(36), pp.5009–5018.

Li, X., Li, M., Tian, L., Chen, J., Liu, R. and Ning, B. 2020. Reactive Astrogliosis: Implications in Spinal Cord Injury Progression and Therapy. *Oxidative Medicine and Cellular Longevity*. **2020**.

Li, X., Xiao, Z., Han, J., Chen, L., Xiao, H., Ma, F., Hou, X., Li, X., Sun, J., Ding, W., Zhao, Y., Chen, B. and Dai, J. 2013. Promotion of neuronal differentiation of neural progenitor cells by using EGFR antibody functionalized collagen scaffolds for spinal cord injury repair. *Biomaterials*. **34**(21), pp.5107–5116.

Li, X., Yang, C., Li, L., Xiong, J., Xie, L., Yang, B., Yu, M., Feng, L., Jiang, Z., Guo, W. and Tian, W. 2015. A therapeutic strategy for spinal cord defect: Human dental follicle cells combined with aligned PCL/PLGA electrospun material. *BioMed Research International*. **2015**.

Li, Z. and Wang, C. 2013. Effects of Working Parameters on Electrospinning *In*: *One-Dimensional Nanostructures* [Online]., pp.15–28. Available from: http://link.springer.com/10.1007/978-3-642-36427-3_2.

Liang, H., Russell, S.J., Wood, D.J. and Tronci, G. 2018a. A hydroxamic acid-methacrylated collagen conjugate for the modulation of inflammation-related MMP upregulation. *Journal of Materials Chemistry B*. **6**(22), pp.3703–3715.

Liang, H., Russell, S.J., Wood, D.J. and Tronci, G. 2018b. Monomer-Induced Customization of UV-Cured Atelocollagen Hydrogel Networks. *Frontiers in Chemistry*. **6**(DEC), p.626.

Liddelow, S.A., Guttenplan, K.A., Clarke, L.E., Bennett, F.C., Bohlen, C.J., Schirmer, L., Bennett, M.L., Münch, A.E., Chung, W.S., Peterson, T.C., Wilton, D.K., Frouin, A., Napier, B.A., Panicker, N., Kumar, M., Buckwalter, M.S., Rowitch, D.H., Dawson, V.L., Dawson, T.M., Stevens, B. and Barres, B.A. 2017. Neurotoxic reactive astrocytes are induced by activated microglia. *Nature*. **541**(7638), pp.481–487.

Lim, Y.C., Johnson, J., Fei, Z., Wu, Y., Farson, D.F., Lannutti, J.J., Choi, H.W. and Lee, L.J. 2011. Micropatterning and characterization of electrospun poly(ε-caprolactone)/gelatin nanofiber tissue scaffolds by femtosecond laser ablation for tissue engineering applications. *Biotechnology and Bioengineering*. **108**(1), pp.116–126.

Lin, H., Chen, B., Wang, B., Zhao, Y., Sun, W. and Dai, J. 2006. Novel nerve guidance material prepared from bovine aponeurosis. *Journal of Biomedical Materials Research Part A*. **79A**(3), pp.591–598.

Liu, L. and Dzenis, Y.A. 2008. Analysis of the effects of the residual charge and gap size on electrospun nanofiber alignment in a gap method. *Nanotechnology*. **19**(35), p.355307.

Liu, T., Houle, J.D., Xu, J., Chan, B.P. and Chew, S.Y. 2012. Nanofibrous collagen nerve

conduits for spinal cord repair. *Tissue Engineering - Part A*. **18**(9–10), pp.1057–1066.

Liu, W., Thomopoulos, S., Xia, Y., Liu, W., Thomopoulos, S. and Xia, Y. 2012. Electrospun Nanofi bers for Regenerative Medicine. . **1**, pp.10–25.

Lubetzki, C., Sol-Foulon, N. and Desmazières, A. 2020. Nodes of Ranvier during development and repair in the CNS. *Nature Reviews Neurology*. **16**(8), pp.426–439.

Ma, C., Chang, B., Jing, Y., Kim, H., Liu, X., Ma, C., Chang, B., Liu, X., Jing, Y. and Kim, H. 2018. CommuniCation Bio-Inspired Micropatterned Platforms Recapitulate 3D Physiological Morphologies of Bone and Dentinal Cells.

Man, A.J., Davis, H.E., Itoh, A., Leach, J.K. and Bannerman, P. 2011. Neurite outgrowth in fibrin gels is regulated by substrate stiffness. *Tissue Engineering - Part A*. **17**(23–24), pp.2931–2942.

Manwaring, M.E., Walsh, J.F. and Tresco, P.A. 2004. Contact guidance induced organization of extracellular matrix. *Biomaterials*. **25**(17), pp.3631–3638.

Martins-Franchetti, S.M., Campos, A., Egerton, T.A. and White, J.R. 2008. Structural and morphological changes in Poly(caprolactone)/poly(vinyl chloride) blends caused by UV irradiation. *Journal of Materials Science*. **43**(3), pp.1063–1069.

MASCIP 2020. Spinal Cord Injury Centres. Available from: http://www.mascip.co.uk/sci-charities/list-other-sci-organisations-links/.

Mata, A., Hsu, L., Capito, R., Aparicio, C., Henrikson, K. and Stupp, S.I. 2009. Micropatterning of bioactive self-assembling gels. *Soft Matter*. **5**(6), pp.1228–1236.

Maude, S., Miles, D.E., Felton, S.H., Ingram, J., Carrick, L.M., Wilcox, R.K., Ingham, E. and Aggeli, A. 2011. De novo designed positively charged tape-forming peptides: self-assembly and gelation in physiological solutions and their evaluation as 3D matrices for cell growth. *Soft Matter*. **7**(18), p.8085.

McClure, M.J., Sell, S.A., Ayres, C.E., Simpson, D.G. and Bowlin, G.L. 2009. Electrospinning-aligned and random polydioxanone-polycaprolactone-silk fibroin-blended scaffolds: Geometry for a vascular matrix. *Biomedical Materials*. **4**(5).

McCullen, S.D., Gittard, S.D., Miller, P.R., Pourdeyhimi, B., Narayan, R.J. and Loboa, E.G. 2011. Laser ablation imparts controlled micro-scale pores in electrospun scaffolds for tissue engineering applications. *Annals of Biomedical Engineering*. **39**(12), pp.3021–3030.

McMurtrey, R.J. 2014. Patterned and functionalized nanofiber scaffolds in three-dimensional hydrogel constructs enhance neurite outgrowth and directional control. *Journal of Neural Engineering*. **11**(6), p.66009.

Meco, E. and Lampe, K.J. 2018. Microscale architecture in biomaterial scaffolds for spatial control of neural cell behavior. *Frontiers in Materials*. **5**.

Meletis, K., Barnabé-Heider, F., Carlén, M., Evergren, E., Tomilin, N., Shupliakov, O. and Frisén, J. 2008. Spinal cord injury reveals multilineage differentiation of ependymal cells. *PLoS Biology*. **6**(7), pp.1494–1507.

Menezes, R., Hashemi, S., Vincent, R., Collins, G., Meyer, J., Foston, M. and Arinzeh, T.L. 2019. Investigation of glycosaminoglycan mimetic scaffolds for neurite growth. *Acta Biomaterialia*. **90**, pp.169–178.

Milbreta, U., Huong Nguyen, L., Diao, H., Lin, J., Wu, W., Sun, C.-Y., Wang, J. and Yian Chew, S. 2016. Three-Dimensional Nanofiber Hybrid Scaffold Directs and Enhances Axonal Regeneration after Spinal Cord Injury. *ACS Biomater. Sci. Eng*. **2**, pp.1319–1329.

Milbreta, U., Lin, J., Pinese, C., Ong, W., Chin, J.S., Shirahama, H., Mi, R., Williams, A., Bechler, M.E., Wang, J., ffrench-Constant, C., Hoke, A. and Chew, S.Y. 2019. Scaffold-Mediated Sustained, Non-viral Delivery of miR-219/miR-338 Promotes CNS Remyelination. *Molecular Therapy*. **27**(2), pp.411–423.

Miller, R.J., Chan, C.Y., Rastogi, A., Grant, A.M., White, C.M., Bette, N., Schaub, N.J. and Corey, J.M. 2018. Combining electrospun nanofibers with cell-encapsulating hydrogel fibers for neural tissue engineering. *Journal of Biomaterials Science, Polymer Edition*. **29**(13), pp.1625–1642.

Mironi-Harpaz, I., Wang, D.Y., Venkatraman, S. and Seliktar, D. 2012. Photopolymerization of cell-encapsulating hydrogels: Crosslinking efficiency versus cytotoxicity. *Acta Biomaterialia*. **8**(5), pp.1838–1848.

Mitsuhashi, K., Ghosh, S. and Koibuchi, H. 2018. Mathematical Modeling and Simulations for Large-Strain J-Shaped Diagrams of Soft Biological Materials.

Moore, S.A. 2016. The Spinal Ependymal Layer in Health and Disease. *Veterinary Pathology*. **53**(4), pp.746–753.

Morton, W.J. 1900. Method of dispersing fluids. *US Patent 705, 691*. **28**(2), pp.131–134.

National Pressure Ulcer Advisory Panel, European Pressure Ulcer Advisory Panel and Pan Pacific Pressure Injury Alliance 2014. *Prevention and Treatment of Pressure Ulcers: Quick Reference Guide* [Online]. [Accessed 10 November 2016]. Available from: http://www.npuap.org/wp-content/uploads/2014/08/Updated-10-16-14-Quick-Reference-Guide-DIGITAL-NPUAP-EPUAP-PPPIA-16Oct2014.pdf.

Nature 2020. Subjects: Regenerative Medicine. Available from: https://www.nature.com/subjects/regenerative-medicine.

Nave, K.A. 2010. Myelination and the trophic support of long axons. *Nature Reviews Neuroscience*. **11**(4), pp.275–283.

New, P.W., Cripps, R. a and Bonne Lee, B. 2014. Global maps of non-traumatic spinal cord injury epidemiology: towards a living data repository. *Spinal Cord*. **52**(2), pp.97–109.

Nguyen, D.N., Hwang, Y. and Moon, W. 2016. Electrospinning of well-aligned fiber bundles using an End-point Control Assembly method. *European Polymer Journal*. **77**, pp.54–64.

Nguyen, K.T. and West, J.L. 2002. Photopolymerizable hydrogels for tissue engineering applications. *Biomaterials*. **23**(22), pp.4307–4314.

Nguyen, L.H., Gao, M., Lin, J., Wu, W., Wang, J. and Chew, S.Y. 2017. Three-dimensional aligned nanofibers-hydrogel scaffold for controlled non-viral drug/gene delivery to

direct axon regeneration in spinal cord injury treatment. *Scientific Reports*. **7**.

NHS 2017. Paralysis. [Accessed 4 November 2020]. Available from: https://www.nhs.uk/conditions/paralysis/.

Nicodemus, G.D. and Bryant, S.J. 2008. Cell encapsulation in biodegradable hydrogels for tissue engineering applications. *Tissue Engineering - Part B: Reviews*. **14**(2), pp.149–165.

Niederöst, B., Oertle, T., Fritsche, J., McKinney, R.A. and Bandtlow, C.E. 2002. Nogo-A and myelin-associated glycoprotein mediate neurite growth inhibition by antagonistic regulation of RhoA and Rac1. *Journal of Neuroscience*. **22**(23), pp.10368–10376.

Nimmerjahn, A., Kirchhoff, F. and Helmchen, F. 2005. Neuroscience: Resting microglial cells are highly dynamic surveillants of brain parenchyma in vivo. *Science*. **308**(5726), pp.1314–1318.

Nirmala, R., Nam, K.T., Park, S.J., Shin, Y.S., Navamathavan, R. and Kim, H.Y. 2010. Formation of high aspect ratio polyamide-6 nanofibers via electrically induced double layer during electrospinning. *Applied Surface Science*. **256**(21), pp.6318–6323.

Norenberg, M.D., Smith, J. and Marcillo, A. 2004. The Pathology of Human Spinal Cord Injury: Defining the Problems. *Journal of Neurotrauma*. **21**(4), pp.429–440.

NSCISC 2013. Spinal cord injury facts and figures at a glance. *The journal of spinal cord medicine*. **36**(1), pp.1–2.

Nune, M., Krishnan, U.M. and Sethuraman, S. 2015. Decoration of PLGA electrospun nanofibers with designer self-assembling peptides: a 'Nano-on-Nano' concept. *RSC Adv.* **5**(108), pp.88748–88757.

Nune, M., Krishnan, U.M. and Sethuraman, S. 2016. PLGA nanofibers blended with designer self-assembling peptides for peripheral neural regeneration. *Materials Science and Engineering: C*. **62**, pp.329–337.

Nune, M., Subramanian, A., Krishnan, U.M., Kaimal, S.S. and Sethuraman, S. 2017. Self-assembling peptide nanostructures on aligned poly(lactide-co-glycolide) nanofibers for the functional regeneration of sciatic nerve. *Nanomedicine*. **12**(3), pp.219–235.

Nune, M., Subramanian, A., Krishnan, U.M. and Sethuraman, S. 2019. Peptide nanostructures on nanofibers for peripheral nerve regeneration. *Journal of Tissue Engineering and Regenerative Medicine*. **13**(6), pp.1059–1070.

O'Connor, R. 2016. Private discussion on treatment pathway for SCI pateints, 21st October.

Obara, M., Szeliga, M. and Albrecht, J. 2008. Regulation of pH in the mammalian central nervous system under normal and pathological conditions: Facts and hypotheses. *Neurochemistry International*. **52**(6), pp.905–919.

Oh, H.J., Pant, H.R., Kang, Y.S., Jeon, K.S., Pant, B., Kim, C.S. and Kim, H.Y. 2012. Synthesis and characterization of spider-web-like electrospun mats of meta-aramid. *Polymer International*. **61**(11), pp.1675–1682.

Omidinia-Anarkoli, A., Boesveld, S., Tuvshindorj, U., Rose, J.C., Haraszti, T. and De Laporte, L.

2017. An Injectable Hybrid Hydrogel with Oriented Short Fibers Induces Unidirectional Growth of Functional Nerve Cells. *Small*. **13**(36).

Osteopore 2020. Osteoplug™ and Osteomesh™. Available from: https://www.osteopore.com/products.html.

Oyinbo, C.A. 2011. Secondary injury mechanisms in traumatic spinal cord injury: A nugget of this multiply cascade. *Acta Neurobiologiae Experimentalis*. **71**(2), pp.281–299.

Pant, H.R., Bajgai, M.P., Nam, K.T., Chu, K.H., Park, S.J. and Kim, H.Y. 2010. Formation of electrospun nylon-6/methoxy poly(ethylene glycol) oligomer spider-wave nanofibers. *Materials Letters*. **64**(19), pp.2087–2090.

Pant, H.R., Bajgai, M.P., Nam, K.T., Seo, Y.A., Pandeya, D.R., Hong, S.T. and Kim, H.Y. 2011. Electrospun nylon-6 spider-net like nanofiber mat containing TiO2 nanoparticles: A multifunctional nanocomposite textile material. *Journal of Hazardous Materials*. **185**(1), pp.124–130.

Pant, H.R., Bajgai, M.P., Yi, C., Nirmala, R., Nam, K.T., Baek, W. Il and Kim, H.Y. 2010. Effect of successive electrospinning and the strength of hydrogen bond on the morphology of electrospun nylon-6 nanofibers. *Colloids and Surfaces A: Physicochemical and Engineering Aspects*. **370**(1–3), pp.87–94.

Parajuli, D.C., Bajgai, M.P., Ko, J.A., Kang, H.K., Khil, M.S. and Kim, H.Y. 2009. Synchronized polymerization and fabrication of poly(acrylic acid) and nylon hybrid mats in electrospinning. *ACS Applied Materials and Interfaces*. **1**(4), pp.750–757.

Parakalan, R., Jiang, B., Nimmi, B., Janani, M., Jayapal, M., Lu, J., Tay, S.S.W., Ling, E.A. and Dheen, S.T. 2012. Transcriptome analysis of amoeboid and ramified microglia isolated from the corpus callosum of rat brain. *BMC Neuroscience*. **13**(1).

Park, S.H., Hong, J.W., Shin, J.H., Yang, D.-Y., Park, S.H., Hong, J.W., Shin, J.H. and Yang, D.-Y. 2011. Quantitatively Controlled Fabrication of Uniaxially Aligned Nanofibrous Scaffold for Cell Adhesion. *Journal of Nanomaterials*. **2011**, pp.1–9.

Park, S.H. and Yang, D.-Y. 2010. Fabrication of aligned electrospun nanofibers by inclined gap method. *Journal of Applied Polymer Science*. **120**(3), pp.1800–1807.

Partheniadis, I., Nikolakakis, I., Laidmäe, I. and Heinämäki, J. 2020. A mini-review: Needleless electrospinning of nanofibers for pharmaceutical and biomedical applications. *Processes*. **8**(6).

Pascual, O., Achour, S. Ben, Rostaing, P., Triller, A. and Bessis, A. 2012. Microglia activation triggers astrocyte-mediated modulation of excitatory neurotransmission. *Proceedings of the National Academy of Sciences of the United States of America*. **109**(4).

Pasterkamp, R.J., Giger, R.J., Ruitenberg, M.J., Holtmaat, a J., De Wit, J., De Winter, F. and Verhaagen, J. 1999. Expression of the gene encoding the chemorepellent semaphorin III is induced in the fibroblast component of neural scar tissue formed following injuries of adult but not neonatal CNS. *Molecular and cellular neurosciences*. **13**(2), pp.143–166.

Patel, H.N., Vohra, Y.K., Singh, R.K. and Thomas, V. 2020. HuBiogel incorporated fibro-

porous hybrid nanomatrix graft for vascular tissue interfaces. *Materials Today Chemistry*. **17**.

Pérez-Cerdá, F., Sánchez-Gómez, M.V. and Matute, C. 2015. Pío del Río hortega and the discovery of the oligodendrocytes. *Frontiers in Neuroanatomy*. **9**(July).

Petrigliano, F.A., Arom, G.A., Nazemi, A.N., Yeranosian, M.G., Wu, B.M. and McAllister, D.R. 2015. In vivo evaluation of electrospun polycaprolactone graft for anterior cruciate ligament engineering. *Tissue Engineering - Part A*. **21**(7–8), pp.1228–1236.

Phelps, C.H. 1972. Barbiturate-induced glycogen accumulation in brain. An electron microscopic study. *Brain Research*. **39**(1), pp.225–234.

Philips, T. and Rothstein, J.D. 2017. Oligodendroglia: Metabolic supporters of neurons. *Journal of Clinical Investigation*. **127**(9), pp.3271–3280.

Pitt, C. and Schindler, A. 1984. Capronor--a biodegradable delivery system for levonorgestrel. *In*: *Long-acting contraceptive delivery systems* [Online]., pp.48–63. Available from: http://www.popline.org/node/418115.

Pitt, C.G., Chasalow, F.I., Hibionada, Y.M., Klimas, D.M. and Schindler, A. 1981. Aliphatic polyesters. I. The degradation of poly(ϵ-caprolactone) in vivo. *Journal of Applied Polymer Science*. **26**(11), pp.3779–3787.

Plantman, S., Patarroyo, M., Fried, K., Domogatskaya, A., Tryggvason, K., Hammarberg, H. and Cullheim, S. 2008. Integrin-laminin interactions controlling neurite outgrowth from adult DRG neurons in vitro. *Molecular and Cellular Neuroscience*. **39**(1), pp.50–62.

Polyganics 2020. NEUROLAC®. Available from: https://polyganics.com/portfolio/peripheral-nerve-repair/neurolac/.

Pritchard, C.D., Slotkin, J.R., Yu, D., Dai, H., Lawrence, M.S., Bronson, R.T., Reynolds, F.M., Teng, Y.D., Woodard, E.J. and Langer, R.S. 2010. Establishing a model spinal cord injury in the African green monkey for the preclinical evaluation of biodegradable polymer scaffolds seeded with human neural stem cells. *Journal of neuroscience methods*. **188**(2), pp.258–69.

Purves, D., Augustine, G. and Fitzpatrick, D. 2001. *Increased Conduction Velocity as a Result of Myelination*.

Qu, J., Wang, D., Wang, H., Dong, Y., Zhang, F., Zuo, B. and Zhang, H. 2013. Electrospun silk fibroin nanofibers in different diameters support neurite outgrowth and promote astrocyte migration. *Journal of Biomedical Materials Research - Part A*. **101 A**(9), pp.2667–2678.

Quigley, A.F., Bulluss, K.J., Kyratzis, I.L.B., Gilmore, K., Mysore, T., Schirmer, K.S.U., Kennedy, E.L., O'Shea, M., Truong, Y.B., Edwards, S.L., Peeters, G., Herwig, P., Razal, J.M., Campbell, T.E., Lowes, K.N., Higgins, M.J., Moulton, S.E., Murphy, M.A., Cook, M.J., Clark, G.M., Wallace, G.G. and Kapsa, R.M.I. 2013. Engineering a multimodal nerve conduit for repair of injured peripheral nerve. *Journal of Neural Engineering*. **10**(1).

Ramón y Cajal, S. 1928. Degeneration and regeneration of the nervous system. *Oxford University Press*.

Raspa, A., Marchini, A., Pugliese, R., Mauri, M., Maleki, M., Vasita, R. and Gelain, F. 2016. A biocompatibility study of new nanofibrous scaffolds for nervous system regeneration. *Nanoscale*. **8**(1), pp.253–265.

Readhead, C., Schneider, A., Griffiths, I. and Nave, K.A. 1994. Premature arrest of myelin formation in transgenic mice with increased proteolipid protein gene dosage. *Neuron*. **12**(3), pp.583–595.

Rebollar, E., Cordero, D., Martins, A., Chiussi, S., Reis, R.L., Neves, N.M. and León, B. 2011. Improvement of electrospun polymer fiber meshes pore size by femtosecond laser irradiation. *Applied Surface Science*. **257**(9), pp.4091–4095.

Ricard-Blum, S. 2011. The Collagen Family. *Cold Spring Harbor Perspectives in Biology*. **3**(1), pp.1–19.

Rodríguez, K., Sundberg, J., Gatenholm, P. and Renneckar, S. 2014. Electrospun nanofibrous cellulose scaffolds with controlled microarchitecture. *Carbohydrate Polymers*. **100**, pp.143–149.

Roman, J.A., Reucroft, I., Martin, R.A., Hurtado, A. and Mao, H.Q. 2016. Local Release of Paclitaxel from Aligned, Electrospun Microfibers Promotes Axonal Extension. *Advanced Healthcare Materials*. **5**(20), pp.2628–2635.

Román, J.T., Fuenmayor, C.A., Dominguez, C.M.Z., Clavijo-Grimaldo, Di., Acosta, M., García-Castañeda, J.E., Fierro-Medina, R. and Rivera-Monroy, Z.J. 2019. Pullulan nanofibers containing the antimicrobial palindromic peptide LfcinB (21-25)Pal obtained: Via electrospinning. *RSC Advances*. **9**(35), pp.20432–20438.

Rose, J.C., Cámara-Torres, M., Rahimi, K., Köhler, J., Möller, M. and De Laporte, L. 2017. Nerve Cells Decide to Orient inside an Injectable Hydrogel with Minimal Structural Guidance. *Nano Letters*. **17**(6), pp.3782–3791.

Rose, J.C., Gehlen, D.B., Omidinia-Anarkoli, A., Fölster, M., Haraszti, T., Jaekel, E.E. and De Laporte, L. 2020. How Much Physical Guidance is Needed to Orient Growing Axons in 3D Hydrogels? *Advanced Healthcare Materials*. **9**(21).

Ruiz-Cantu, L., Gleadall, A., Faris, C., Segal, J., Shakesheff, K. and Yang, J. 2020. Multi-material 3D bioprinting of porous constructs for cartilage regeneration. *Materials Science and Engineering C*. **109**, p.110578.

Russell, S.J. 2006. *Handbook of Nonwovens*.

Sabantina, L., Mirasol, J.R., Cordero, T., Finsterbusch, K. and Ehrmann, A. 2018. Investigation of needleless electrospun PAN nanofiber mats *In*: *AIP Conference Proceedings*.

Sagner, A. and Briscoe, J. 2019. Establishing neuronal diversity in the spinal cord: A time and a place. *Development (Cambridge)*. **146**(22).

Saha, S., Yang, X.B., Wijayathunga, N., Harris, S., Feichtinger, G.A., Davies, R.P.W. and Kirkham, J. 2019. A biomimetic self-assembling peptide promotes bone regeneration in vivo: A rat cranial defect study. *Bone*. **127**, pp.602–611.

Sakaguchi, H., Amoroso, N.J. and Wagner, W.R. 2014. Engineering Electrospun Scaffolds to

Encourage Cell Infiltration *In*:, pp.75–94. [Accessed 27 September 2020]. Available from: http://link.springer.com/10.1007/978-4-431-55139-3_4.

Saliani, A., Perraud, B., Duval, T., Stikov, N., Rossignol, S. and Cohen-Adad, J. 2017. Axon and myelin morphology in animal and human spinal cord. *Frontiers in Neuroanatomy*. **11**.

Sarrazin, S., Lamanna, W.C. and Esko, J.D. 2011. Heparan sulfate proteoglycans. *Cold Spring Harbor Perspectives in Biology*. **3**(7), pp.1–33.

Schnell, E., Klinkhammer, K., Balzer, S., Brook, G., Klee, D., Dalton, P. and Mey, J. 2007. Guidance of glial cell migration and axonal growth on electrospun nanofibers of poly-ε-caprolactone and a collagen/poly-ε-caprolactone blend. *Biomaterials*. **28**(19), pp.3012–3025.

Schwab, M.E. and Strittmatter, S.M. 2014. Nogo limits neural plasticity and recovery from injury. *Current Opinion in Neurobiology*. **27**, pp.53–60.

Seidlits, S.K., Khaing, Z.Z., Petersen, R.R., Nickels, J.D., Vanscoy, J.E., Shear, J.B. and Schmidt, C.E. 2010. The effects of hyaluronic acid hydrogels with tunable mechanical properties on neural progenitor cell differentiation. *Biomaterials*. **31**(14), pp.3930–3940.

Seifert, G., Schilling, K. and Steinhäuser, C. 2006. Astrocyte dysfunction in neurological disorders: a molecular perspective. *Nature reviews. Neuroscience*. **7**(3), pp.194–206.

Semino, C.E., Kasahara, J., Hayashi, Y. and Zhang, S. 2004. Entrapment of Migrating Hippocampal Neural Cells in Three-Dimensional Peptide Nanofiber Scaffold *In*: *Tissue Engineering*., pp.643–655.

Serwanski, D.R., Jukkola, P. and Nishiyama, A. 2017. Heterogeneity of astrocyte and NG2 cell insertion at the node of ranvier. *Journal of Comparative Neurology*. **525**(3), pp.535–552.

Seyednejad, H., Gawlitta, D., Kuiper, R. V., De Bruin, A., Van Nostrum, C.F., Vermonden, T., Dhert, W.J.A. and Hennink, W.E. 2012. In vivo biocompatibility and biodegradation of 3D-printed porous scaffolds based on a hydroxyl-functionalized poly(ε-caprolactone). *Biomaterials*. **33**(17), pp.4309–4318.

Shapiro, J.M. and Oyen, M.L. 2013. Hydrogel Composite Materials for Tissue Engineering Scaffolds. *JOM*. **65**(4), pp.505–516.

Shelke, N.B., Lee, P., Anderson, M., Mistry, N., Nagarale, R.K., Ma, X.-M., Yu, X. and Kumbar, S.G. 2016. Neural tissue engineering: nanofiber-hydrogel based composite scaffolds. *Polymers for Advanced Technologies*. **27**(1), pp.42–51.

Sheng, D., Li, J., Ai, C., Feng, S., Ying, T., Liu, X., Cai, J., Ding, X., Jin, W., Xu, H., Chen, J. and Chen, S. 2019. Electrospun PCL/Gel-aligned scaffolds enhance the biomechanical strength in tendon repair. *Journal of Materials Chemistry B*. **7**(31), pp.4801–4810.

Sierra, A., Encinas, J.M., Deudero, J.J.P., Chancey, J.H., Enikolopov, G., Overstreet-Wadiche, L.S., Tsirka, S.E. and Maletic-Savatic, M. 2010. Microglia shape adult hippocampal neurogenesis through apoptosis-coupled phagocytosis. *Cell Stem Cell*. **7**(4), pp.483–495.

Sierra, A., Paolicelli, R.C. and Kettenmann, H. 2019. Cien Años de Microglía: Milestones in a Century of Microglial Research. *Trends in Neurosciences*. **42**(11), pp.778–792.

Silva, G.A., Czeisler, C., Niece, K.L., Beniash, E., Harrington, D.A., Kessler, J.A. and Stupp, S.I. 2004. Selective Differentiation of Neural Progenitor Cells by High-Epitope Density Nanofibers. *Science*. **303**(5662), pp.1352–1355.

Silver, J. and Miller, J.H. 2004. Regeneration beyond the glial scar. *Nature reviews. Neuroscience*. **5**(2), pp.146–56.

Simard, M. and Nedergaard, M. 2004. The neurobiology of glia in the context of water and ion homeostasis. *Neuroscience*. **129**(4), pp.877–896.

Sinha, R.P. and Häder, D.P. 2002. UV-induced DNA damage and repair: A review. *Photochemical and Photobiological Sciences*. **1**(4), pp.225–236.

Slaughter, B. V., Khurshid, S.S., Fisher, O.Z., Khademhosseini, A. and Peppas, N.A. 2009. Hydrogels in regenerative medicine. *Advanced Materials*. **21**(32–33), pp.3307–3329.

Sofroniew, M. V. 2015. Astrogliosis. *Cold Spring Harbor Perspectives in Biology*. **7**(2).

Sofroniew, M. V. and Vinters, H. V. 2010. Astrocytes: Biology and pathology. *Acta Neuropathologica*. **119**(1), pp.7–35.

Sorushanova, A., Delgado, L.M., Wu, Z., Shologu, N., Kshirsagar, A., Raghunath, R., Mullen, A.M., Bayon, Y., Pandit, A., Raghunath, M. and Zeugolis, D.I. 2019. The Collagen Suprafamily: From Biosynthesis to Advanced Biomaterial Development. *Advanced Materials*. **31**(1).

Sparrey, C.J., Choo, A.M., Liu, J., Tetzlaff, W. and Oxland, T.R. 2008. The distribution of tissue damage in the spinal cord is influenced by the contusion velocity. *Spine*. **33**(22), pp.E812–E819.

Sparrey, C.J. and Keaveny, T.M. 2011. Compression behavior of porcine spinal cord white matter. *Journal of Biomechanics*. **44**(6), pp.1078–1082.

Sparrey, C.J., Manley, G.T. and Keaveny, T.M. 2009. Effects of white, grey, and pia mater properties on tissue level stresses and strains in the compressed spinal cord. *Journal of Neurotrauma*. **26**(4), pp.585–595.

Spector, R., Robert Snodgrass, S. and Johanson, C.E. 2015. A balanced view of the cerebrospinal fluid composition and functions: Focus on adult humans. *Experimental Neurology*. **273**, pp.57–68.

Spinal Research 2015. *Annual Review*.

Stabenfeldt, S.E. and LaPlaca, M.C. 2011. Variations in rigidity and ligand density influence neuronal response in methylcellulose–laminin hydrogels. *Acta Biomaterialia*. **7**(12), pp.4102–4108.

Stankus, J.J., Guan, J., Fujimoto, K. and Wagner, W.R. 2006. Microintegrating smooth muscle cells into a biodegradable, elastomeric fiber matrix. *Biomaterials*. **27**(5), pp.735–744.

Stellwagen, D., Beattie, E.C., Seo, J.Y. and Malenka, R.C. 2005. Differential regulation of

AMPA receptor and GABA receptor trafficking by tumor necrosis factor-α. *Journal of Neuroscience*. **25**(12), pp.3219–3228.

Stellwagen, D. and Malenka, R.C. 2006. Synaptic scaling mediated by glial TNF-α. *Nature*. **440**(7087), pp.1054–1059.

Stence, N., Waite, M. and Dailey, M.E. 2001. Dynamics of microglial activation: A confocal time-lapse analysis in hippocampal slices. *GLIA*. **33**(3), pp.256–266.

Stifani, N. 2014. Motor neurons and the generation of spinal motor neuron diversity. *Frontiers in Cellular Neuroscience*. **8**(OCT).

Streit, W.J., Xue, Q.S., Tischer, J. and Bechmann, I. 2014. Microglial pathology. *Acta Neuropathologica Communications*. **2**(1).

Sugiyama, T., Lama, S., Gan, L.S., Maddahi, Y., Zareinia, K. and Sutherland, G.R. 2018. Forces of tool-tissue interaction to assess surgical skill level *In*: *JAMA Surgery*. American Medical Association, pp.234–242.

Sun, H., Mei, L., Song, C., Cui, X. and Wang, P. 2006. The in vivo degradation, absorption and excretion of PCL-based implant. *Biomaterials*. **27**(9), pp.1735–1740.

Sun, Z., Deitzel, J.M., Knopf, J., Chen, X. and Gillespie, J.W. 2012. The effect of solvent dielectric properties on the collection of oriented electrospun fibers. *Journal of Applied Polymer Science*. **125**(4), pp.2585–2594.

Sundararaghavan, H.G., Monteiro, G.A., Firestein, B.L. and Shreiber, D.I. 2009. Neurite growth in 3D collagen gels with gradients of mechanical properties. *Biotechnology and Bioengineering*. **102**(2), pp.632–643.

Suwantong, O. 2016. Biomedical applications of electrospun polycaprolactone fiber mats. *Polymers for Advanced Technologies*. **27**(10), pp.1264–1273.

Swindle-Reilly, K.E., Paranjape, C.S. and Miller, C.A. 2014. Electrospun poly(caprolactone)-elastin scaffolds for peripheral nerve regeneration. *Progress in Biomaterials*. **3**(1), p.20.

TA Instruments 2013. *Understanding Rheology of Structured Fluids* [Online]. Available from: http://www.tainstruments.com/pdf/literature/AAN016_V1_U_StructFluids.pdf.

Tan, E.P.S. and Lim, C.T. 2006. Mechanical Characterization of a Single Nanofiber *In*: *Nanomechanics of Materials and Structures*. Springer-Verlag, pp.121–137.

Tang, A.H., Chen, H., Li, T.P., Metzbower, S.R., MacGillavry, H.D. and Blanpied, T.A. 2016. A trans-synaptic nanocolumn aligns neurotransmitter release to receptors. *Nature*. **536**(7615), pp.210–214.

Taylor, G. 1964. Disintegration of water drops in an electric field. *Proceedings of the Royal Society of London. Series A. Mathematical and Physical Sciences*. **280**(1382), pp.383–397.

Taylor, G. 1969. Electrically driven jets. *Proceedings of the Royal Society of London. A. Mathematical and Physical Sciences*. **313**(1515), pp.453–475.

Taylor, G. 1966. The force exerted by an electric field on a long cylindrical conductor.

Proceedings of the Royal Society of London. Series A. Mathematical and Physical Sciences. **291**(1425), pp.145–158.

Telano, L.N. and Baker, S. 2018. *Physiology, Cerebral Spinal Fluid (CSF)* [Online]. Available from: http://www.ncbi.nlm.nih.gov/pubmed/30085549.

Teng, Y.D., Lavik, E.B., Qu, X., Park, K.I., Ourednik, J., Zurakowski, D., Langer, R. and Snyder, E.Y. 2002. Functional recovery following traumatic spinal cord injury mediated by a unique polymer scaffold seeded with neural stem cells. *Proceedings of the National Academy of Sciences of the United States of America*. **99**(5), pp.3024–9.

Thayer, P.S., Verbridge, S.S., Dahlgren, L.A., Kakar, S., Guelcher, S.A. and Goldstein, A.S. 2016. Fiber/collagen composites for ligament tissue engineering: influence of elastic moduli of sparse aligned fibers on mesenchymal stem cells. *Journal of Biomedical Materials Research - Part A*. **104**(8), pp.1894–1901.

The Electrospinning Company 2021. The Electrospinning Company. Available from: https://www.electrospinning.co.uk/.

Theodore, N., Hlubek, R., Danielson, J., Neff, K., Vaickus, L., Ulich, T.R. and Ropper, A.E. 2016. First Human Implantation of a Bioresorbable Polymer Scaffold for Acute Traumatic Spinal Cord Injury. *Neurosurgery*. **79**(2), pp.E305–E312.

Thermo Fisher Scientific 2017. Protein Measurements. *T032-TECHNICAL BULLETIN*. [Online]. [Accessed 3 March 2021]. Available from: https://assets.thermofisher.com/TFS-Assets/CAD/manuals/T032-NanoDrop-2000-2000c-Protein-Measurements.pdf.

Thermo Fisher Scientific 2015. User Guide: Qubit Protein Assay Kits. Available from: https://tools.thermofisher.com/content/sfs/manuals/Qubit_Protein_Assay_UG.pdf.

Thomas, V., Jose, M. V., Chowdhury, S., Sullivan, J.F., Dean, D.R. and Vohra, Y.K. 2006. Mechano-morphological studies of aligned nanofibrous scaffolds of polycaprolactone fabricated by electrospinning. *Journal of Biomaterials Science, Polymer Edition*. **17**(9), pp.969–984.

Tomal, W. and Ortyl, J. 2020. Water-soluble photoinitiators in biomedical applications. *Polymers*. **12**(5).

Tomaszewski, W., Kudra, M., Ciechanska, D., Szadkowski, M. and Gutowska, A. 2012. Electrospinning of aligned fibrous materials on an inner rapidly rotating cone surface. *Fibres and Textiles in Eastern Europe*. **96**(6 B), pp.44–51.

Tortora, G.J. and Derrickson, B. 2014. *Principles of Anatomy & Physiology 14th Edition*.

Tran, A.P., Warren, P.M. and Silver, J. 2018. The biology of regeneration failure and success after spinal cord injury. *Physiological Reviews*. **98**(2), pp.881–917.

Trawczynski, M., Liu, G., David, B.T. and Fessler, R.G. 2019. Restoring Motor Neurons in Spinal Cord Injury With Induced Pluripotent Stem Cells. *Frontiers in Cellular Neuroscience*. **13**.

Tronci, G., Grant, C.A., Thomson, N.H., Russell, S.J. and Wood, D.J. 2016. Influence of 4-vinylbenzylation on the rheological and swelling properties of photo-activated collagen

hydrogels. *MRS Advances*. **1**(8), pp.533–538.

Tronci, G., Grant, C.A., Thomson, N.H., Russell, S.J. and Wood, D.J. 2015. Multi-scale mechanical characterization of highly swollen photo-activated collagen hydrogels. *Journal of the Royal Society, Interface / the Royal Society*. **12**.

Tronci, G., Russell, S.J. and Wood, D.J. 2013. Photo-active collagen systems with controlled triple helix architecture. *Journal of Materials Chemistry B*. **1**, pp.3705–3715.

Tronci, G., Yin, J., Holmes, R.A., Liang, H., Russell, S.J. and Wood, D.J. 2016. Protease-sensitive atelocollagen hydrogels promote healing in a diabetic wound model. *Journal of Materials Chemistry B*. **4**(45), pp.7249–7258.

Tseng, H., Puperi, D.S., Kim, E.J., Ayoub, S., Shah, J. V., Cuchiara, M.L., West, J.L. and Grande-Allen, K.J. 2014. Anisotropic Poly(Ethylene Glycol)/Polycaprolactone Hydrogel–Fiber Composites for Heart Valve Tissue Engineering. *Tissue Engineering Part A*. **20**(19–20), pp.2634–2645.

Valipour M., N., Birjandi, F.C. and Sargolzaei, J. 2014. Super-non-wettable surfaces: A review. *Colloids and Surfaces A: Physicochemical and Engineering Aspects*. **448**(1), pp.93–106.

Vashisth, P., Kar, N., Gupta, D. and Bellare, J.R. 2020. Three dimensional quercetin-functionalized patterned scaffold: Development, characterization, and in vitro assessment for neural tissue engineering. *ACS Omega*. **5**(35), pp.22325–22334.

Venero, J.L., Vizuete, M.L., Ilundáin, A.A., Machado, A., Echevarria, M. and Cano, J. 1999. Detailed localization of aquaporin-4 messenger RNA in the CNS: Preferential expression in periventricular organs. *Neuroscience*. **94**(1), pp.239–250.

Verkhratsky, A. and Nedergaard, M. 2014. Astroglial cradle in the life of the synapse. *Philosophical Transactions of the Royal Society B: Biological Sciences*. **369**(1654).

Vile, G.F., Tanew-Iliitschew, A. and Tyrrell, R.M. 1995. ACTIVATION OF NF-KB IN HUMAN SKIN FIBROBLASTS BY THE OXIDATIVE STRESS GENERATED BY UVA RADIATION. *Photochemistry and Photobiology*. **62**(3), pp.463–468.

Visakh, P.M., Markovic, G. and Pasquini, D. 2016. *Recent Developments in Polymer Macro, Micro and Nano Blends: Preparation and Characterisation*.

Vleggeert-Lankamp, C.L.A.M., De Ruiter, G.C.W., Wolfs, J.F.C., Pêgo, A.P., Van Den Berg, R.J., Feirabend, H.K.P., Malessy, M.J.A. and Lakke, E.A.J.F. 2007. Pores in synthetic nerve conduits are beneficial to regeneration. *Journal of Biomedical Materials Research - Part A*. **80**(4), pp.965–982.

Walser, J., Stok, K.S., Caversaccio, M.D. and Ferguson, S.J. 2016. Direct electrospinning of 3D auricle-shaped scaffolds for tissue engineering applications. *Biofabrication*. **8**(2).

Walsh, J.F., Manwaring, M.E. and Tresco, P.A. 2005. Directional neurite outgrowth is enhanced by engineered meningeal cell-coated substrates *In*: *Tissue Engineering*., pp.1085–1094.

Walthers, C.M., Nazemi, A.K., Patel, S.L., Wu, B.M. and Dunn, J.C.Y. 2014. The effect of

scaffold macroporosity on angiogenesis and cell survival in tissue-engineered smooth muscle. *Biomaterials*. **35**(19), pp.5129–5137.

Wang, C., Yue, H., Feng, Q., Xu, B., Bian, L. and Shi, P. 2018. Injectable Nanoreinforced Shape-Memory Hydrogel System for Regenerating Spinal Cord Tissue from Traumatic Injury. *ACS Applied Materials and Interfaces*. **10**(35), pp.29299–29307.

Wang, H.B., Mullins, M.E., Cregg, J.M., McCarthy, C.W. and Gilbert, R.J. 2010. Varying the diameter of aligned electrospun fibers alters neurite outgrowth and Schwann cell migration. *Acta Biomaterialia*. **6**(8), pp.2970–2978.

Wang, J., Ye, R., Wei, Y., Wang, H., Xu, X., Zhang, F., Qu, J., Zuo, B. and Zhang, H. 2012. The effects of electrospun TSF nanofiber diameter and alignment on neuronal differentiation of human embryonic stem cells. *Journal of Biomedical Materials Research - Part A*. **100 A**(3), pp.632–645.

Wang, T.Y., Bruggeman, K.F., Kauhausen, J.A., Rodriguez, A.L., Nisbet, D.R. and Parish, C.L. 2016. Functionalized composite scaffolds improve the engraftment of transplanted dopaminergic progenitors in a mouse model of Parkinson's disease. *Biomaterials*. **74**, pp.89–98.

Wang, X., Ding, B., Yu, J. and Yang, J. 2011. Large-scale fabrication of two-dimensional spider-web-like gelatin nano-nets via electro-netting. *Colloids and Surfaces B: Biointerfaces*. **86**(2), pp.345–352.

Wang, Y., Wang, G., Chen, L., Li, H., Yin, T., Wang, B., Lee, J.C.M. and Yu, Q. 2009. Electrospun nanofiber meshes with tailored architectures and patterns as potential tissue-engineering scaffolds. *Biofabrication*. **1**(1).

Watson, C. and Kayalioglu, G. 2009. The Organization of the Spinal Cord *In*: *The Spinal Cord*., pp.1–7.

Wawrzyniak-Gacek, A. 2002. Distribution of various types of oligodendrocytes and cellular localisation of iron in the frontal cortex of the adult rat. *Folia Morphologica*. **61**(2), pp.115–121.

Waxman, S.G. 1997. Axon-glia interactions: Building a smart nerve fiber. *Current Biology*. **7**(7).

Wee-Eong Teo 2013. Comparison of common electrospun aligned fiber membrane construction methods. *ElectrospinTech*. [Online]. [Accessed 22 November 2016]. Available from: http://electrospintech.com/alignfibercom.html#.WDQltS2LSUk.

Wee-Eong Teo 2014. Mechanical Movement. *ElectrospinTech*. [Online]. [Accessed 22 November 2016]. Available from: http://electrospintech.com/mechanical-movement.html#.WDQivC2LSUk.

Wei, L., Sun, R., Liu, C., Xiong, J. and Qin, X. 2019. Mass production of nanofibers from needleless electrospinning by a novel annular spinneret. *Materials and Design*. **179**.

Weightman, A.P., Jenkins, S., Pickard, M., Chari, D. and Yang, Y. 2014. Alignment of multiple glial cell populations in 3D nanofiber scaffolds: Toward the development of multicellular implantable scaffolds for repair of neural injury. *Nanomedicine:*

Nanotechnology, Biology, and Medicine. **10**(2), pp.291–295.

Weightman, A.P., Pickard, M.R., Yang, Y. and Chari, D.M. 2014. An in vitro spinal cord injury model to screen neuroregenerative materials. *Biomaterials*. **35**(12), pp.3756–3765.

WHO 2013. *International Perspectives on Spinal Cord Injury* [Online]. Available from: http://apps.who.int/iris/bitstream/10665/94190/1/9789241564663_eng.pdf.

Williams, C.G., Malik, A.N., Kim, T.K., Manson, P.N. and Elisseeff, J.H. 2005. Variable cytocompatibility of six cell lines with photoinitiators used for polymerizing hydrogels and cell encapsulation. *Biomaterials*. **26**(11), pp.1211–1218.

De Winter, F., Oudega, M., Lankhorst, A.J., Hamers, F.P., Blits, B., Ruitenberg, M.J., Pasterkamp, R.J., Gispen, W.H. and Verhaagen, J. 2002. Injury-induced class 3 semaphorin expression in the rat spinal cord. *Experimental Neurology*. **175**(1), pp.61–75.

Wong, D.Y., Ranganath, T. and Kasko, A.M. 2015. Low-Dose, Long-Wave UV Light Does Not Affect Gene Expression of Human Mesenchymal Stem Cells C. Chan, ed. *PLOS ONE*. **10**(9), p.e0139307.

Woodruff, M.A. and Hutmacher, D.W. 2010. The return of a forgotten polymer—Polycaprolactone in the 21st century. *Progress in Polymer Science*. **35**(10), pp.1217–1256.

Woodward, S.C., Brewer, P.S., Moatamed, F., Schindler, A. and Pitt, C.G. 1985. The intracellular degradation of poly(ε-caprolactone). *Journal of Biomedical Materials Research*. **19**(4), pp.437–444.

Wu, S., Chen, M.S., Maurel, P., Lee, Y.S., Bunge, M.B. and Arinzeh, T.L. 2018. Aligned fibrous PVDF-TrFE scaffolds with Schwann cells support neurite extension and myelination in vitro. *Journal of Neural Engineering*. **15**(5).

Xia, H., Sun, X., Liu, D., Zhou, Y. and Zhong, D. 2016. Oriented growth of rat Schwann cells on aligned electrospun poly(methyl methacrylate) nanofibers. *Journal of the Neurological Sciences*. **369**, pp.88–95.

Xia, H. and Xia, Y. 2018. An in vitro study of non-aligned or aligned electrospun poly(methyl methacrylate) nanofibers as primary rat astrocytes-loading scaffold. *Materials Science and Engineering C*. **91**, pp.228–235.

Xiao, Z., Tang, F., Tang, J., Yang, H., Zhao, Y., Chen, B., Han, S., Wang, N., Li, X., Cheng, S., Han, G., Zhao, C., Yang, X., Chen, Y., Shi, Q., Hou, S., Zhang, S. and Dai, J. 2016. One-year clinical study of NeuroRegen scaffold implantation following scar resection in complete chronic spinal cord injury patients. *Science China Life Sciences*. **59**(7), pp.647–655.

Xiao, Z., Tang, F., Zhao, Y., Han, G., Yin, N., Li, X., Chen, B., Han, S., Jiang, X., Yun, C., Zhao, C., Cheng, S., Zhang, S. and Dai, J. 2018. Significant Improvement of Acute Complete Spinal Cord Injury Patients Diagnosed by a Combined Criteria Implanted with NeuroRegen Scaffolds and Mesenchymal Stem Cells. *Cell Transplantation*. **27**(6), pp.907–915.

Xing, H., Yin, H., Sun, C., Ren, X., Tian, Y., Yu, M. and Jiang, T. 2019. Preparation of an acellular spinal cord scaffold to improve its biological properties. *Molecular Medicine*

Reports. **20**(2), pp.1075–1084.

Xue, J., Wu, T., Dai, Y. and Xia, Y. 2019. Electrospinning and electrospun nanofibers: Methods, materials, and applications. *Chemical Reviews*. **119**(8), pp.5298–5415.

Yang, F., Murugan, R., Wang, S. and Ramakrishna, S. 2005. Electrospinning of nano/micro scale poly(l-lactic acid) aligned fibers and their potential in neural tissue engineering. *Biomaterials*. **26**(15), pp.2603–2610.

Yao, L., O'Brien, N., Windebank, A. and Pandit, A. 2009. Orienting neurite growth in electrospun fibrous neural conduits. *Journal of Biomedical Materials Research - Part B Applied Biomaterials*. **90 B**(2), pp.483–491.

Yao, S., He, F., Cao, Z., Sun, Z., Chen, Y., Zhao, H., Yu, X., Wang, X., Yang, Y., Rosei, F. and Wang, L.N. 2020. Mesenchymal Stem Cell-Laden Hydrogel Microfibers for Promoting Nerve Fiber Regeneration in Long-Distance Spinal Cord Transection Injury. *ACS Biomaterials Science and Engineering*. **6**(2), pp.1165–1175.

Yao, S., Liu, X., Yu, S., Wang, X., Zhang, S., Wu, Q., Sun, X. and Mao, H. 2016. Co-effects of matrix low elasticity and aligned topography on stem cell neurogenic differentiation and rapid neurite outgrowth. *Nanoscale*. **8**(19), pp.10252–10265.

Yao, S., Yang, Y., Wang, X. and Wang, L. 2017. Fabrication and characterization of aligned fibrin nanofiber hydrogel loaded with PLGA microspheres. *Macromolecular Research*. **25**(6), pp.528–533.

Yao, S., Yu, S., Cao, Z., Yang, Y., Yu, X., Mao, H.Q., Wang, L.N., Sun, X., Zhao, L. and Wang, X. 2018. Hierarchically aligned fibrin nanofiber hydrogel accelerated axonal regrowth and locomotor function recovery in rat spinal cord injury. *International Journal of Nanomedicine*. **13**, pp.2883–2895.

Yokota, K., Kubota, K., Kobayakawa, K., Saito, T., Hara, M., Kijima, K., Maeda, T., Katoh, H., Ohkawa, Y., Nakashima, Y. and Okada, S. 2019. Pathological changes of distal motor neurons after complete spinal cord injury. *Molecular Brain*. **12**(1).

Yu, X. and Bellamkonda, R. V. 2001. Dorsal root ganglia neurite extension is inhibited by mechanical and chondroitin sulfate-rich interfaces. *Journal of Neuroscience Research*. **66**(2), pp.303–310.

Yuan, H., Zhou, Q. and Zhang, Y. 2017. Improving fiber alignment during electrospinning.

Zalc, B. 2000. Origins of Vertebrate Success. *Science*. **288**(5464), p.271c–271.

Zamani, F., Amani-Tehran, M., Latifi, M., Shokrgozar, M.A. and Zaminy, A. 2014. Promotion of spinal cord axon regeneration by 3D nanofibrous core-sheath scaffolds. *Journal of Biomedical Materials Research - Part A*. **102**(2), pp.506–513.

Zamanian, J.L., Xu, L., Foo, L.C., Nouri, N., Zhou, L., Giffard, R.G. and Barres, B.A. 2012. Neurobiology of Disease Genomic Analysis of Reactive Astrogliosis.

Zariffa, J., Kramer, J.L.K., Fawcett, J.W., Lammertse, D.P., Blight, A.R., Guest, J., Jones, L., Burns, S., Schubert, M., Bolliger, M., Curt, A. and Steeves, J.D. 2011. Characterization of neurological recovery following traumatic sensorimotor complete thoracic spinal cord

injury. *Spinal Cord*. **49**(3), pp.463–471.

Zavvarian, M.M., Hong, J. and Fehlings, M.G. 2020. The Functional Role of Spinal Interneurons Following Traumatic Spinal Cord Injury. *Frontiers in Cellular Neuroscience*. **14**.

Zhang, S., Greenfield, M.A., Mata, A., Palmer, L.C., Bitton, R., Mantei, J.R., Aparicio, C., De La Cruz, M.O. and Stupp, S.I. 2010. A self-assembly pathway to aligned monodomain gels. *Nature Materials*. **9**(7), pp.594–601.

Zhang, T., Chen, H., Zhang, Y., Zan, Y., Ni, T., Liu, M. and Pei, R. 2019. Photo-crosslinkable, bone marrow-derived mesenchymal stem cells-encapsulating hydrogel based on collagen for osteogenic differentiation. *Colloids and Surfaces B: Biointerfaces*. **174**, pp.528–535.

Zhao, Y., Tang, F., Xiao, Z., Han, G., Wang, N., Yin, N., Chen, B., Jiang, X., Yun, C., Han, W., Zhao, C., Cheng, S., Zhang, S. and Dai, J. 2017. Clinical Study of NeuroRegen Scaffold Combined with Human Mesenchymal Stem Cells for the Repair of Chronic Complete Spinal Cord Injury. *Cell Transplantation*. **26**(5), pp.891–900.

Zhao, Y., Zhu, R., Song, X., Ma, Z., Chen, S., Wu, D., Liu, F., Ouyang, S., Zhang, J., Ramakrishna, S., Zhu, X. and He, L. 2018. Assembly Pathway Selection of Designer Self-Assembling Peptide and Fabrication of Hierarchical Scaffolds for Neural Regeneration. *ACS Applied Materials & Interfaces*. **10**(31), pp.26128–26141.

Zholudeva, L. V., Qiang, L., Marchenko, V., Dougherty, K.J., Sakiyama-Elbert, S.E. and Lane, M.A. 2018. The Neuroplastic and Therapeutic Potential of Spinal Interneurons in the Injured Spinal Cord. *Trends in Neurosciences*. **41**(9), pp.625–639.

Zhong, S., Teo, W.E., Zhu, X., Beuerman, R.W., Ramakrishna, S. and Yung, L.Y.L. 2006. An aligned nanofibrous collagen scaffold by electrospinning and its effects on in vitro fibroblast culture. *Journal of Biomedical Materials Research - Part A*. **79**(3), pp.456–463.

Zong, X., Kim, K., Fang, D., Ran, S., Hsiao, B.S. and Chu, B. 2002. Structure and process relationship of electrospun bioabsorbable nanofiber membranes. *Polymer*. **43**(16), pp.4403–4412.

Zuidema, J.M., Desmond, G.P., Rivet, C.J., Kearns, K.R., Thompson, D.M. and Gilbert, R.J. 2015. Nebulized solvent ablation of aligned PLLA fibers for the study of neurite response to anisotropic-to-isotropic fiber/film transition (AFFT) boundaries in astrocyte-neuron co-cultures. *Biomaterials*. **46**, pp.82–94.

Zuidema, J.M., Hyzinski-García, M.C., Van Vlasselaer, K., Zaccor, N.W., Plopper, G.E., Mongin, A.A. and Gilbert, R.J. 2014. Enhanced GLT-1 mediated glutamate uptake and migration of primary astrocytes directed by fibronectin-coated electrospun poly-l-lactic acid fibers. *Biomaterials*. **35**(5), pp.1439–1449.

Zussman, E., Rittel, D. and Yarin, A.L. 2003. Failure modes of electrospun nanofibers. *Applied Physics Letters*. **82**(22), pp.3958–3960.